EXPERIMENTAL INVESTIGATION ON THE FATE OF ETHANOL-BLENDED FUELS IN THE SUBSURFACE

by

Jarod Michael Devries

B.Sc., The University of Western Ontario, 2013

A THESIS SUBMITTED IN PARTIAL FULFILLMENT OF

THE REQUIREMENTS FOR THE DEGREE OF

MASTER OF SCIENCE

in

THE FACULTY OF GRADUATE AND POSTDOCTORAL STUDIES

(Geological Sciences)

THE UNIVERSITY OF BRITISH COLUMBIA

(Vancouver)

June 2017

Abstract

Currently, the North American market for motor fuels is distributing E10 (gasoline with an ethanol content up to 10%). Recent legislature is promoting a range of higher ethanol content fuels to be introduced into the market. The result is an increased risk of accidental release of these higher ethanol content fuels. A comprehensive understanding of the fate of ethanol-blended fuels, including interactions between its constituents (e.g. ethanol, benzene and toluene), degradation products (e.g. VFAs, CO_2, CH_4) and potential secondary water quality impacts (e.g. Mn^{2+},Fe^{2+}), is lacking. Eight large columns were constructed to evaluate the impacts of fuel blends of varying ethanol contents on biodegradation, and to determine the effect of soil type on gas generation and migration. In each scenario, approximately 2L of fuel was injected into the lower quarter of the column, approximately 30cm above the water table. The saturated zone was analyzed for dissolved Mn and Fe, as well as EtOH and VFAs. Vadose zone analysis focused on measuring surficial CO_2 and CH_4 fluxes, in-situ soil gas concentrations of CO_2, CH_4, O_2, N_2, and Ar, as well as benzene and toluene. Isotopic analysis of vadose zone CO_2 was also completed.

The results confirm that ^{13}C isotopic analysis is well suited for identifying the predominant microbial substrate undergoing biodegradation. Fuel blends with higher ethanol content showed more elevated levels of dissolved Mn and Fe, demonstrating that metal mobilization occurs more readily in spills with higher ethanol content. Additionally, fuels with a higher ethanol content exhibited signs of elevated microbial stress through the increased production of butyric acids. Benzene and toluene measured near surface, and the surficial effluxes of CO_2 or CH_4 did not indicate a significant SVI risk in any of the scenarios tested, under the conditions studied.

Lay Summary

Recently, governmental policy is promoting an increase of the ethanol content in fuel for a variety of environmental and economic reasons. Risks for accidental spills or leaks into the ground have since increased. Once a spill has entered the ground, native soil microbes begin degrading the fuel. This process, known as biodegradation, can remove the fuel from the ground. However, the process of biodegradation is complicated and may lead to unintended side-effects, which may also be harmful to the environment. To address this issue, this study examined biodegradation of fuels with varying ethanol content in different soils. Findings of this work include that elevated ethanol contents negatively affect water quality by increasing metal concentrations and by accumulating intermediate biodegradation products. However, for the experimental conditions examined, the results suggest that emissions of volatile fuel compounds and methane at the ground surface were insignificant, independent of ethanol content and soil type.

Preface

This thesis is original unpublished work. Experimental design was completed by Dr. K. Ulrich Mayer, Dr. N. Sihota and the author. All samples were collected by the author with help from Jannel Robertson, Eva Marcy, Bissultan Umbet and Laura Stewart. Samples were analyzed by the author with help from Jannel Robertson, Eva Marcy, Bissultan Umbet and Laura Stewart, or in commercial laboratories. Data interpretation was conducted by the author under guidance from Dr. K. Ulrich Mayer. All chapters were written by the author and edited by Dr. K. Ulrich Mayer.

Table of Contents

List of Tables

List of Figures

List of Acronyms

Acronym	Definition
BOD	Biological oxygen demand
BT	Benzene, toluene
BTEX	Benzene, toluene, ethylbenzene, xylene
CSIA	Compound specific isotopic analysis
DFE	Denatured fuel-grade ethanol
E10	10% ethanol, 90% gasoline
E15	15% ethanol, 85% gasoline
E20	20% ethanol, 80% gasoline
E85	85% ethanol, 15% gasoline
E95	95% ethanol, 5% gasoline
E100	100% ethanol
EA	Electron acceptor
EPA	Environmental Protection Agency
EtOH	Ethanol
GC	Gas chromatograph
IHT	Interspecies hydrogen transfer
IRGA	Infra-red gas analyzer
ITRC	Interstate Technology and Regulatory Council
LCFA	Long chained fatty acid
MP	Matric potential
MTBE	Methyl tertiary butyl ether
NA	Natural attenuation
NAPL	Non-aqueous phase liquid
p	Pearson correlation coefficient
RFG	Reformulated gasoline
SCFA	Short chained fatty acid
SVI	Soil vapour intrusion
SWSS	Soil water solution sampler
TEAP	Terminal electron acceptor processes
v/v%	Percent by volume
VFA	Volatile fatty acid
VWC	Volumetric water content
XRD	X-ray diffraction

Acknowledgements

Thank you to Uli for your guidance, mentorship, sense of humor and of course your unending patience.

Thanks to Roger Beckie for being on my advisory committee and helping me along the way. In addition, I would also like to thank Sean Crowe for being a part of my committee.

Thanks to Ramon Aravena for your advice with data interpretation.

Thank you to my family, and in particular my parents Carl and Nancy. Thank you for your constant encouragement and support, both morally and financially.

I would also like to thank Joern Unger for the construction of the columns, column exhaust line, and other assistance. I would like to thank David Jones, Sukhi Hundal, and Charles Krzysik for their help with software, hardware and programming issues. Thanks to Daniele Pedretti for help with Matlab. Thanks to Eva Marcy, Jannel Robertson, Laura Stewart, and Bissultan Umbet for their lab work.

Thanks to Laura Laurenzi for always being there to bounce ideas off of. Our conversations were motivating, thank you for everything.

Thanks to all of my fellow grad students for being such amazing and supportive people. It is because of you that I can reflect on my time at UBC with such fondness. I wish you all my very best.

To Susan, you have helped and supported me in so many ways and I cannot thank you enough.

Funding for this work was provided by the American Petroleum Institute, NSERC (Discovery Grant), NSERC (Discovery Accelerator Supplement), and a NSERC (Strategic Grant) held by K.U. Mayer. The author would like to acknowledge Shell for provision of the soils required to carry out the experiments.

Chapter 1: Introduction

1.1 Background

The emergence of biofuels, such as ethanol-blended fuels, onto the global market for use as a motor fuel has become increasingly popular among countries worldwide. The increased use of ethanol-blended fuels in North America is in response to several political decisions in the U.S., and stemming from two main initiatives (Powers et al., 2001). Firstly, ethanol is a renewable resource that can aid in reducing the demand for fossil fuels, particularly when the price of crude oil is high. Biofuels can also be marketed as a more environmentally friendly, and renewable energy source alternative, as opposed to gasoline derived purely from petroleum hydrocarbons. Secondly, ethanol is an oxygenate that is replacing the much more environmentally damaging *methyl tertiary butyl ether* (MTBE). Oxygenates are hydrocarbon compounds that contain oxygen, and the addition of these compounds to fuels will increase their octane and contribute to a cleaner burn, thus resulting in a reduction of air pollution from vehicle emissions (Blue Ribbon Panel (BRP), 1999). In 1990 under the Clean Air Act Amendments in the U.S., the decision was made by policy makers to incorporate oxygen-containing organic compounds into motor fuels to reduce air pollution, and the Federal Reformulated Gasoline Program was established and implemented in 1995. Requirements under the Clean Air Act state that reformulated gasoline (RFG) must contain 2 percent oxygen by weight. An estimated 85% of the RFG initially produced contained the oxygenate MTBE (Blue Ribbon Panel (BRP), 1999). This regulatory decision to integrate MTBE into fuels had been severely scrutinized since it was revealed that MTBE is a ubiquitous contaminant in surface and groundwater (Gullick and LeChevallier, 2000; Moran et al., 1999). Governmental agencies turned to ethanol as a safer replacement to MTBE, and since then ethanol utilization in the U.S. has been on the rise resulting from a biofuel utilization mandate put in place by the Energy Independence and Security Act of 2007 (EISA), (Sluder and West, 2011). The

statutory responsibility to implement the EISA mandates through the promulgation of the Renewable Fuel Standard, were given to the United States Environmental Protection Agency (EPA), (Sluder and West, 2011). During the same time, the Canadian government announced a new $1.5 billion dollar ecoEnergy for Biofuels initiative, which provided investments over a 9-year span to boost Canada's production of biofuels (Natural Resources Canada, 2016). This commitment made under Canada's Renewable Fuels Strategy is aligned with the U.S. Renewable Fuel Standard, and aims to expand the production and use of cleaner renewable fuels such as ethanol and biodiesel (Department of the Environment, 2010). Therefore, many changes happening in the U.S. surrounding renewable fuels have also been reciprocated in Canada's governmental policies. This trend among renewable fuel requirements have long been on the rise in other international jurisdictions such as Brazil, the European Union (EU), Japan, India, China, Mexico, Russia and South Africa (Department of the Environment, 2010; Elbehri et al., 2012). Currently the North American market is commonly served with E10, a fuel that contains up to 10% ethanol. However, recent legislation is promoting a range of higher percentage ethanol-blended fuels. The U.S. Department of Energy undertook a series of tests which evaluated the impact from the use of mid-level blends ranging from 10 to 20% ethanol to the legacy fleet. Results from the study have shown no significant catalyst degradation associated with aging vehicles using fuels containing 15% ethanol (Sluder and West, 2011). These findings prompted the EPA to announce in January 2011 a partial waiver, making E15 legal for use in vehicles from model year 2001 through 2006 (EPA, 2011). Due to the increasing financial and political incentives to stimulate growth of the ethanol-fuel market, the likelihood of accidental releases of these higher-percentage biofuels to the environment will increase. Assessing the potential frequency of accidental releases is dependent upon the likely points of exposure due to release within the biofuel

supply chain infrastructure, as well as the current and future projections of consumption, which are expected to increase. According to the ITRC (2011), denatured fuel ethanol (DFE or E95) is transported from manufacturing facilities to depots/supply terminals mostly by tanker truck, railcar, and tank barges, while conventional petroleum is mostly transported via extensive networks of pipelines. Releases in the supply chain during transport are primary release scenarios, and are typically most significant. Additionally, secondary release scenarios may arise from the misuse of incompatible materials in storage tanks, hosing, piping, dispensers, etc. The current supply chain infrastructure illustrates the potential for accidental release of biofuels, in addition to the increased likelihood of accidental releases resulting solely from increased production and distribution. To assess these potential impacts to the environment, a comprehensive understanding of the fate of ethanol-blended fuels in the subsurface is needed.

1.2 Current State of Affairs

The search for sustainable fuel alternatives has led to the increased production and use of a variety of biofuels. Particularly, the increased interest in ethanol as a promising fuel alternative has transformed government policies worldwide. Despite being chosen as the clean alternative to MTBE, and the renewable nature that ethanol-blended fuels provide, ethanol-blended fuels are not without challenges from an environmental perspective. Governments and regulatory bodies have invested in research initiatives to study the effects of ethanol-blended fuels in the subsurface, particularly focusing at the potential impact on the environment in the event of an accidental spill, or leakage from underground storage tanks. These studies have been gaining traction over the past 20 years and researchers have made considerable advances in the past decade, improving the understanding of the biogeochemical interactions during the degradation of ethanol-blended fuels

by indigenous microorganisms. More recently, researchers have been using metagenomics to advance the quantitative understanding of the dynamics and functional diversity of microbial communities, which have been modified by exposure to ethanol-blended fuels (Ma et al., 2013). Studies conducted on ethanol-blended fuels over the last two decades have discovered a number of potential environmental drawbacks. The significance of these drawbacks; however, remains unclear and continues to be investigated with different approaches to determine potential effects on the environment and on health risks that may be posed to the human population.

Once a site is contaminated, understanding and quantifying the rate of biodegradation and natural attenuation processes are of high importance when evaluating remediation strategies for sites that are impacted by ethanol-blended fuels. Recent studies have focused on the effects of ethanol on the biodegradation processes in microcosm studies (Chen et al., 2008; Corseuil et al., 1998a; Freitas et al., 2010; Österreicher-Cunha et al., 2009) and pilot scale aquifer tanks (Cápiro et al., 2007; Ma et al., 2011, 2015; Österreicher-Cunha et al., 2009). As well, field studies investigating the effects of ethanol on biodegradation were conducted in a sandy aquifer in Brazil (Corseuil et al., 2011), a former fuel service station at the Vandenberg Air Force Base, CA (Mackay et al., 2006), and the CFB Borden Aquifer in Ontario, Canada (Freitas and Barker, 2011). The majority of the studies to date have focused on the saturated zone, leaving a void of information regarding processes occurring in the vadose zone as a result of biodegradation. Processes affecting the fate of ethanol-blended fuels in the vadose zone are still poorly understood (Österreicher-Cunha et al., 2009) and the impact of these alternative fuels on vadose zone geochemistry and gas composition remains unclear.

1.3 Literature Review: Concerns with Ethanol-Blended Fuels

Research on the environmental impact of ethanol-blended fuels has gained considerable traction in the past 20 years. Although ethanol itself poses no significant environmental risk, initial studies have discovered concerns associated with the highly labile nature of ethanol in biofuels, and its ability to quickly render an environment anaerobic. The rapid consumption of electron acceptors (EA's) and nutrients in the presence of ethanol diminishes the capacity for degradation of harmful BTEX compounds (Corseuil et al., 1998b), leaving benzene refractory in denitrifying, sulfidogenic, and methanogenic microcosms. Chen et al., (2008) also concluded that BTEX biodegradation was completely shut off in the presence of high ethanol concentrations. Since BTEX compounds are degraded using inducible enzymes, the BTEX substrate is often secondarily preferred to more easily degradable substrates such as ethanol (Duetz et al., 1994, 1996), which utilizes thermodynamically favorable constitutive enzymes through central metabolic pathways (Corseuil et al., 1998a). This preferential utilization of ethanol might result in increased lag times of in-situ microbial degradation of BTEX (Corseuil et al., 1998a). Elevated ethanol levels promote microbial activity which can rapidly impose a significant biological oxygen demand (BOD) within the soil, leading to the development of anaerobic conditions, and as a result a reduced capacity for biodegradation. This was also confirmed in two field studies, where Mackay et al., (2006) determined that the presence of ethanol resulted in reduced biodegradation rates of aromatic fuel components in the subsurface, and a 10 year field study conducted by Corseuil et al., (2011), who found that benzene degradation remained inhibited as long as highly reducing conditions persisted. Along with a an inhibitory effect on BTEX degradation, it was noted that the presence of ethanol above 10% can produced a cosolvency effect that enhances BTEX dissolution into the saturated zone (Powers et al., (2001). A study conducted in the U.S. Midwest addressed the apparent impacts

of ethanol-amended fuels on BTEX plumes, and discovered that the median length of a benzene plume in an aquifer previously amended with ethanol-blended fuels was almost twice as long as the benzene plume at a site where ethanol amended fuel was never used (Ruiz-Aguilar et al., 2003). In summary, high ethanol concentrations in groundwater can shut off BTEX degradation and increase the solubility of BTEX in groundwater resulting in longer and more persistent plumes. This is of particular importance as all 6 BTEX compounds have been found to depress the central nervous system, and can cause leukemia in extreme cases of chronic benzene exposure (Federal Register, 1985).

High ethanol concentrations of 5,000 mg/L also revealed slower degradation rates when compared to lower concentrations of 500 mg/L where ethanol degraded rapidly and substantial CH_4 was produced (Chen et al., 2008). These experiments point to ethanol toxicity of the microbial community when exposed to elevated ethanol concentrations. Chen et al., (2008), also found that systems exposed to these high concentrations produced unidentified volatile fatty acids (VFA), likely butyrate and propionate, and less CH_4 was generated. Under these high ethanol conditions, butyric and propionic acids may be formed until the stressed conditions recede prompting the reverse reaction to acetic acid (Wu and Hickey, 1996). In a pilot scale aquifer study, (Ma et al., 2015) found that once the dissolved ethanol concentration decreased below toxicity levels (~2000 mg/L), fermentation activity was stimulated, and ethanol metabolites, CH_4 and VFA concentrations increased. Therefore, systems stressed resulting from microbial toxicity towards ethanol, will delay the onset of CH_4 generation which has implications towards risk assessment of sites contaminated by higher ethanol content fuels.

Concerning the vadose zone, when compared to petroleum hydrocarbon spills, ethanol-blended fuels have a substantially higher potential to develop anoxic environments, and increased

rates of CO_2 and CH_4 production. If ethanol decomposition goes to completion, the generation of CO_2 and CH_4 is produced at a ratio of 1:3, thereby producing significant CH_4 levels which may dominate soil gas composition. Aerobic degradation of CH_4 consumes the available O_2 which is needed for degradation of other harmful hydrocarbons such as BTEX. Jewell and Wilson, (2011) highlighted the risks of completing a vapor intrusion pathway for benzene and other concerning hydrocarbons, as O_2 is consumed via CH_4 oxidation reactions. In a study of a denatured ethanol (E95) fuel spill, Spalding et al., (2011) noted very high methane concentrations in the vadose zone (>50% locally), and observed approximately 2-3% CH_4 in surficial collection cells several years after the release. They also found that dissolved CH_4 concentrations exceeded the solubility limits, highlighting ethanol's significant potential for CH_4 generation. The human risks associated with soil vapor intrusion (SVI) of CH_4, or other hydrocarbons of concern are amplified owing to the fact that underground/above ground storage tanks are typically found in urban environments.

There are many benefits of having motor fuels amended with ethanol, with the strongest environmental arguments stemming from a cleaner atmosphere and the complete discontinuation of the use of MTBE. Regardless, researchers have also discovered a few potential drawbacks regarding the use of ethanol-blended fuels. Scientist must fill in the knowledge gaps where they exists, in order to determine the potential impacts to both the environment and society.

1.4 Research Objectives

This thesis is based on a series of laboratory experiments designed to represent a cross-sectional (1-D) slice of a shallow unconfined aquifer located downgradient of an ethanol-blended fuel release (Figure 1-1). The study focuses on vadose zone and saturated zone impacts and attenuation processes. The overarching scope of the study is broken down into three main

investigations: 1) assessment of soil type on the biodegradation of ethanol-blended (E20) fuels, 2) evaluation of varying ethanol-content on biodegradation processes in comparison to a standard gasoline spill, and 3) assessment of releasing ethanol-blended fuel (E20) into an aquifer already contaminated by standard gasoline and comparison of the results to those of an E20 fuel spill onto clean sediments. Each of these objectives addresses the effect of fuel degradation in the saturated zone and vadose zone.

In this context, the saturated zone is the region that extends approximately 20cm upwards from the base of each column. The saturated zone analysis focuses on the examination of VFAs, dissolved metals, and dissolved ethanol to determine the following:

i) Is there a potential for the development of toxicity affecting microbial activity, related to specific ethanol fuel blends?

ii) How does soil type and fuel blend affect invasion of ethanol into the saturated zone?

iii) Can substantial metal mobilization occur in ethanol-blended fuel spill zones, and does ethanol content play a role?

iv) What are the dominant redox conditions likely to be found in the saturated zone within the plume zone of an ethanol-blended fuel spill?

The vadose zone of each column extends from the water table located at an elevation of 20 cm to 185 cm where the interface between the soil surface and column headspace exists. The vadose zone represents the longest section of the column. The vadose zone analysis focuses on the use of gas profiles based on continuous and snapshot soil gas measurements, isotopic analysis, surficial CH_4 and CO_2 fluxes, and benzene and toluene soil gas measurements to evaluate the following research questions:

i) Can the use of stable isotopes aid in identifying the specific hydrocarbon sources predominantly undergoing biodegradation?

ii) Is there an effect on the biodegradation of benzene and toluene in the presence of varying ethanol contents?

iii) Is there a potential for increased risk of soil vapor intrusion (SVI) for sites with specific soils and/or certain ethanol-blended fuels?

iv) How do the biodegradation rates compare to previous studies?

These research goals were addressed through the implementation of eight large and heavily instrumented column experiments with each column standing 2m in height and 30cm in diameter. The soils used for the experiments were obtained from the vadose zone at a local site in Burnaby, B.C. Canada, and retained their indigenous microbial population. The evaluation of vadose zone gas composition, stable isotopes, surficial CO_2 and CH_4 fluxes, as well as saturated zone water chemistry was used to investigate natural attenuation processes occurring in the different scenarios.

The simulated scenario, in which the plume has extended beyond its source and migrated along the surface of the water table, interacting with the capillary fringe and the saturated zone, required that the columns have a water table near the base of each column (~20 cm from the base). The remainder of the column above the water table includes the capillary fringe and unsaturated soils, permitting gas exchange with the atmosphere. The fuels were released through an injection coil emplaced at 50cm above the base of the column, allowing infiltration of the fuel down to the capillary fringe region. Releasing the fuel beneath ground surface simulated a scenario in which the fuel had migrated beneath the ground surface along the water table, overlain by uncontaminated aquifer material. Investigating the effects of soil media on biodegradation of ethanol-blended fuels

involved the construction of sand and silty-sand columns. Differences in soil material allow evaluating the dependence of gas generation and migration in media with differing soil-gas permeability. Additionally, to investigate the scenario of an E20 fuel blend on a previously gasoline contaminated soil, two columns with different soil types underwent a primary gasoline spill, followed by a delayed spill of E20 fuel 8 weeks later. Ethanol content in blended fuels is believed to have a direct impact on the concentrations of ethanol found in the groundwater succeeding a spill/leak event. To investigate this, the present study compares the effects of biodegradation in sand columns containing gasoline, E10, E20 and E85 fuels.

Evaluating biodegradation required an analysis approach based on multiple lines of evidence. The analysis included final, intermediate and byproducts generated from biodegradation of the ethanol-blended fuels, specifically CH_4, CO_2, volatile fatty acids (VFAs), and dissolved Mn and Fe. In addition, assessing dominant reaction pathways required a more in-depth study of the geochemical evolution of each column, as well as the isotopic composition of the degradation end products. The analysis of dissolved metal concentrations in the saturated zone and O_2 concentrations in the vadose zone provided additional insights into the redox evolution of the column, while ^{13}C isotopic composition of degradation products CO_2 aided in the assessment of the contributing source compounds (gasoline vs ethanol). Surficial CO_2 and CH_4 fluxes were measured to quantify depth-integrated biodegradation rates and to assess potential risks for soil vapor intrusion of CH_4 and CO_2 into nearby structures. Finally, monitoring of benzene and toluene concentrations within the vadose zone provided the necessary data to improve our understanding of BTEX degradation in the presence of ethanol.

1.5 Figures

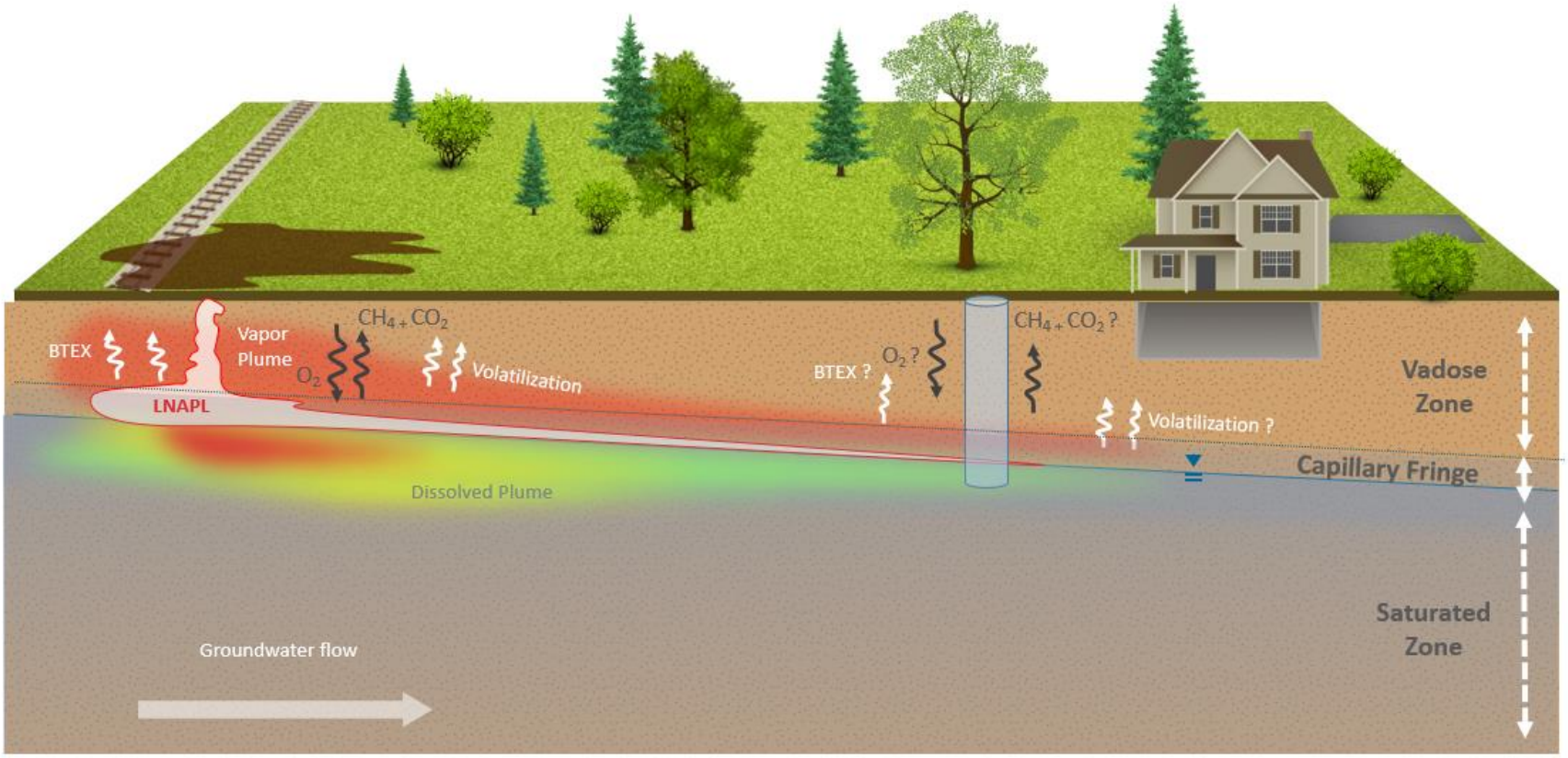

Figure 1-1 Conceptual model of an ethanol-blended fuel spill with emphasis on the region downgradient from a source zone. Figure made using Health Canada Contaminated Sites Division's Conceptual Model Builder.

Chapter 2 : Methodology

2.1. Overview

To study the fate of ethanol-blended fuels downgradient from a source zone, with an emphasis on the gas and vapor migration in the vadose zone during biodegradation, 8 large columns were designed and constructed to represent a 1-D slice of an unconfined aquifer (Figure 1-1). With the aim to provide insight into vadose zone processes in response to biodegradation of the fuel, the majority of the column length was designated to be unsaturated, with a much smaller representation of the saturated zone. This column study was designed to target specific regions within the soil column; just below the water table, within the spill zone/capillary region, and higher up within the unsaturated zone. Each of the 8 columns were dedicated to a specific combination of fuel blend and soil material as outlined in the research objectives section.

2.2. Experimental Design

2.2.1 Column Design Overview

A vertical 1-D soil profile was created by constructing 8 large columns with each column standing 2 meters tall and approximately 30 cm in diameter (Figure 2-1). The large dimension of the columns was selected to provide a realistic representation of vadose zone processes for soils with water table depths > 1m. The column dimensions contribute to the novelty of the experiments, as there has not been another study with columns comparable in size. The columns consist of three main parts; (1) transparent-blue acrylic tube (Length = 2 m, I.D. = 30 cm, wall thickness = 1 cm), (2) Polyvinyl chloride (PVC) base, and a PVC cap (3). The transparency of the columns allows to observe the location and transient evolution of the released biofuel, which was dyed for

visualization purposes. All materials were chosen to be compatible with ethanol and gasoline. The columns were strapped to a customized cradle to help secure the 2 m tall columns.

2.2.1.1. Column Tubing

The column tube was designed to contain the soil material while providing an opportunity for data collection from in-situ sensor equipment and sample collection along the length of the column through a series of access ports. Each individual column tube was designed to have the ability to access the vertical soil profile at 10cm intervals. 18 holes were drilled to create a vertical profile of gas or water sampling ports at 10 cm intervals, starting from the base (0 cm) to the top of the soil (180 cm). To accommodate the sensors, holes were drilled at 5 locations along the vertical soil profile – 40 cm, 60 cm, 100 cm, 140 cm, and 160 cm. At the same vertical locations, holes were drilled to house a soil water solution sampler (SWSS) and a pressure sampling port. Preventing/limiting the amount of leakage from the sampling ports required that each sensor/sampler was installed to have a circular PVC spacer wedged into the column with a smaller hole in the spacer designed to host the respective sensor wire or sampling tubing. Both the spacer and the sampling tubing/sensor wire were sealed in place using PVC glue and epoxy. To provide the necessary plumbing required to measure hydraulic head and to set the water table within the column, a 1/2 “ hole was drilled near the base of the column, and fitted with a PVC ball valve (Figure 2-2). A clear tube connected to the ball valve acted as a manometer which also functioned also as a basal recharge port, allowing the maintenance of a water table to counteract the effects of water loss from the column by evaporation and other processes.

2.2.1.2. Column Base

The PVC base was fabricated to provide a socket-type fit around one end of the acrylic tubing. The base was then sealed to the acrylic tube via an O-ring and PVC cement. A bead of silicone

was also added to the connection between the PVC base and the acrylic tube to provide a water tight seal. The radius of the column base is 3 cm greater than that of the column itself.

2.2.1.3. Column Cap

In order to replicate the conditions found in an unsaturated aquifer downgradient of a fuel spill, it was important to maintain the column headspace aerobic. Due to laboratory safety concerns, it was necessary to collect the hazardous gases and fumes exiting at the soil surface and route these gases to a fume hood. To this end, the column cap was designed to prevent all gases from exiting the column into the lab space, while maintaining near atmospheric conditions in the column headspace. This was achieved through a venting system consisting of an inlet port to facilitate ingress of lab air into the headspace to maintain oxic conditions, and a small diaphragm pump connected to a customized stainless steel exhaust line, delivering the exhaust to the fume hood (Figure 2-3). The diaphragm pump was connected via stainless steel quick-connect devices (Figure 2-3). A water infiltration system was also constructed to simulate rainfall events within the columns. With the aim to mimic natural rainfall events, and to prevent preferential flow, emphasis was placed on developing a "rain" system to distribute water evenly across the soil surface. To achieve this, each column was outfitted with a small coiled-up soaker hose buried immediately below the surface of the soil (Figure 2-4). The coil was attached to a special two-way connector mounted and sealed on the inside of the PVC cap, and then attached to a Masterflex® hose on the external side of the cap. A peristaltic pump can be connected to the Masterflex® hose and water can be distributed across the surface of the soil through the soaker hose. A similar stainless steel version of the infiltration system was placed in the lower part of the column for administration of the controlled fuel releases.

2.2.2 Sampling Ports

Each column was constructed with narrowly-spaced sampling ports to provide high resolution depth-discrete information. The columns required three different sampling port styles to accommodate the sampling of gas, pressure and water samples (Figure 2-5). In total, there are 16 gas sampling ports (GP), 5 pressure sampling ports (Pres.), and 7 soil water solution sampling ports (SWSS) (Figure 2-1). Polyether ether ketone (PEEK) tubing was used to construct all sampling ports. This material was chosen because of its high chemical resistivity and gas impermeability. Gas sampling ports consisted of a FDA luer lock polycarbonate stop cock (1/8" ID) connected to a needle epoxied to a PEEK tube (0.06" ID, 0.125" OD), which was screened with fine mesh at the sampling end. Pressure sampling ports utilized the screened PEEK tube connected to a 1/8" NPT 2-way ball valve with nylon tube connectors fitted with a 1/4 " Puresep-T septa™. Water sampling ports were comprised of a FDA luer lock polycarbonate stop cock (1/8" ID) connected to a needle epoxied into a PEEK tube (0.06" ID, 0.125" OD), which was fitted with a ceramic porous cup at the sampling end.

2.2.3 Data Logging and Sensors

In each column, there are four main sensor types emplaced at five vertical levels; two gas sensors to measure O_2 levels (%) and CO_2 levels (%), respectively, and two hydraulic sensors to measure volumetric water content (VWC) and matric potential (MP), respectively (Figure 2-1). The O_2 and CO_2 gas sensors are analog sensors, and required the use of an analog Labjack ™- U3-LV device (Figure 2-6), whereas the VWC and MP sensors are digital and required a connection to an Arduino® MEGA digital microcontroller (Figure 2-7). Both data acquisition devices communicate directly with a dedicated lab computer. The moisture sensors were programmed to

collect a measurement every 35 seconds, while the gas sensors recorded concentrations every two minutes. Appendix C provides the codes for controlling the sensors and data acquisition.

2.2.3.1. Analog Sensors

Soil gas O_2 content was measured by an Apogee SO-200 sensor, which has a range from 0-100% O_2 and operates by generating an electrical current from the electrochemical reaction that occurs as O_2 contacts an electrolyte within the galvanic cell (Apogee Instruments, 2015). To protect the Apogee sensor against water/fuel damage, a gas permeable polytetrafluoroethylene (PTFE) membrane was secured onto the sensor head with a cable tie and sealed with silicone. Carbon dioxide concentrations were measured using a Dynament CO_2 sensor, which uses a tungsten infrared light source and an infrared detector to quantify CO_2 gas as it diffuses into the optical cavity (Dynament, 2011). An initial warm-up period of up to 1 minute is required for the sensor to indicate the correct gas reading (Dynament, 2011). To avoid any unnatural soil temperature increases due to the heat generated from a constantly functioning CO_2 sensor, the sensor was controlled using an Arduino® MEGA microcontroller and was scheduled to turn on every 15 minutes for a period of 5 minutes, allowing for a proper warm-up and reading (Figure 2-6). Data from the CO_2 sensors was collected continuously for ease of operation. A filtering algorithm was used to eliminate the data during the time periods when the sensor was off. To accomplish this, the microcontroller was wired into a solid state relay connected to the positive lead of the CO_2 sensor, and the positive lead from the power source. Each sensor head was shrouded with a PTFE membrane to protect the sensor from damage by exposure to water and fuel, sealed with silicone against the sensor cable. In an attempt to maintain optimal measurement precision throughout the soil profile within the column, multiple ranges of CO_2 sensors were chosen. Sensors with ranges between 0-30% were placed at elevations of 40 and 60 cm, i.e. within

the area expected to have the highest CO_2 concentrations (in the spill zone). A CO_2 sensor with a range from 0-20% was placed at the midway point (100 cm), and the top two sensors at 140 cm and 160 cm consisted of CO_2 sensors with ranges from 0-10% and 0-2%, respectively.

2.2.3.2. Digital Sensors

The soil moisture and soil water potential sensors (Decagon GS3 and MPS-2, respectively) located at 40, 60, 100, 140 and 160 cm, provide continuous in-situ data on volumetric soil water content and soil matric potential. The Decagon GS3 also reports soil temperature, and uses the soil electrical conductivity to determine the volumetric water content (VWC, Decagon, 2011). The MPS-2 uses the soil dielectric water potential to report the soil water potential (MP) (Decagon, 2011). Measurements are based on the physical properties of water, therefore it is it likely that sensors at 40 cm, located within the spill zone, were affected by the presence of the fuel. The factory calibration was used for both sensors types. The GS3 has an accuracy of ± 5% in mineral soils with low organic content (Decagon, 2011), and the MPS-2 is accurate within ± 25% from -5kPa to -100kPa (Decagon, 2011).

2.3. Soil Characterization

Soil material chosen for the column experiments represented an important aspect of the study to determine the effects of gas permeability on soil gas migration, concentration build-up near the base of the columns (CO_2 and CH_4) and ingress of O_2 from the top of the columns. Uncontaminated sand and silt obtained from a local site in Burnaby, BC, Canada was used for all 8 column experiments. All material was collected from the vadose zone several meters above the regional water table. The two different types of soil were characterized to understand differences

in soil properties that might affect gas migration, and to understand geochemical conditions defined by each soil type. Additionally, soil characterization revealed that the silt was too impermeable to be used in the column experiments directly. The information gained from soil characterization helped to define the fractions of silt and sand needed to create the lower permeable material that was used in the columns.

2.3.1. Grain Size Analysis

Both the silt and sand material were analyzed for their respective grain size distributions. Grain size for the sand and silt material was tested using a nest of U.S. Std. sieves, and a sieve shaker. However, the silts required a further step as the grain size was too small to be determined using this method. In order to obtain the full grain size distribution of the silts, a wet sieve technique was applied, followed by the use of a *Malvin Mastersizer 2000* particle size analyzer to analyze the proportion of grains which were <417 μm (U.S. std. Sieve No. 35). A general purpose analysis model was utilized in the Hydro 2000SS (A) software, and the diffraction parameters used include a particle refractive index (RI) of 1.680, dispersant RI of 1.330 (water) and an obscuration of 28.8%. Once the sediments passed through the wet sieves, the remaining fines were placed in a glass beaker with water, and stirred using a magnetic stirrer to mix the sample. Once a homogeneous slurry was created, a representative aliquot from the sample grains (<417 μm) was taken and then injected into the sampling port of the Mastersizer for analysis. The Mastersizer utilizes an ultrasonic pulse to detach grains from one another, and then uses a method of laser diffraction to determine the grain size of the sample passing through a detector array in the optical bench. For optimal results, each sample underwent a period of ultrasonic treatment for 3 minutes. The procedure was run in triplicate to compare results and to ensure that the results were not skewed by the sampling technique. The results from the Mastersizer were then combined with the

results from the sieve shaker to provide a full profile of the silt grain size distribution. The grain size analysis revealed that, according to the Udden-Wentworth scale, the majority of the sand material lies within the fine sand - medium sand range (Figure A-1) and is quite well distributed. The silt material is characterized by a fine sand - silt composition (Figure A-2), with approximately 20% clay content.

2.3.2. Mineralogy

Two sand samples and one silt sample were used for quantitative X-ray analysis to determine the mineralogical composition (Klassen, 2014). The analysis must meet grain size requirements of the equipment. To obtain the optimal grain size for the analysis, each sample underwent a process of grain size reduction by grinding under ethanol in a vibratory McCrone Micronising Mill for 7 minutes. Step-scan X-ray powder-diffraction data were collected over a range 3-80° 2θ with CoKα radiation on a Bruker D8 Focus Bragg-Brentano diffractometer equipped with an Fe monochromator foil, 0.6mm (0.3°) divergence slit, incident and diffracted-beam Soller slits, and a LynxEye detector. The long fine-focus Co X-ray tube was operated at 35 kV and 40 mA, using a take-off angle of 6°. The X-ray diffractograms were analyzed using the International Centre for Diffraction Database PDF-4 and Search-Match Software by Bruker. Refinement of the X-ray powder diffraction data was achieved through a Rietveld refinement analysis. Results represents the relative amounts of crystalline phases normalized to 100% (Klassen, 2014). Sands primarily consist of Quartz (44 - 45%) and Plagioclase (38.9 - 39.3%), with minor amounts of K-feldspar (4.8 - 6.0%), Actinolite (3.5 – 4.3%), and Illite-Muscovite (3.1 – 4.2%) (Klassen, 2014). Conversely, the plagioclase content for the silts is greater than that of the sands (42%), and the Quartz content is lower (36.1%); however, the contents of minor minerals are similar to those in the sands, with K-feldspar, Actinolite, and Illite-Muscovite accounting for 5.7%, 6.4% and 4.9%,

respectively (Klassen, 2014). Detailed results of the XRD-analyses are provided in the Appendix (**Table A-5 Soil mineralogical data obtained through XRD analysis.**Table A-5).

2.4. Hydrogeological Characterization

2.4.1. Soil Bulk Density and Porosity

Bulk density ρ_b and porosities φ for the sand and silty-sand were determined by saturating each soil in a steel cylinder with a known volume. The sediments were tightly packed into the cylinder and were weighed when completely saturated and re-weighed after they were oven dried overnight. The difference in weight was attributed to the removal of water from the pore space in the soil. The volume of water was calculated, which represented the total volume of water that occupied the pore space when completely saturated. Assuming complete saturation, the calculated volume of water equates to the total porosity φ of each soil type. The silty-sand has a ρ_b ranging from 1.69 – 1.70 (g/cm^3), and φ ranging from 0.33-0.36 (cm^3/cm^3). The sand material is less dense; ρ_b ~1.49 (g/cm^3), and has a slightly higher porosity ranging from 0.35-0.41 (cm^3/cm^3). The lower porosity of the silty-sand is likely a result of the smaller silt and clay grains occupying the gaps between the compacted sand grains, which will have an effect on the permeability of the soil. See Table B-4 for a detailed summary of these results.

2.4.2. Saturated Hydraulic Conductivity

Saturated hydraulic conductivities were determined for both materials, and the hydraulic conductivity differences were utilized as a proxy to characterize the differences in the dry gas

permeabilities for each soil type. The type of fluid used in both hydraulic conductivity experiments were the same (water), therefore the differences in hydraulic conductivity (K_w) is related solely to the differences of the intrinsic permeability of the soil material (k_i). Intrinsic permeability is a property of the porous medium only, not the fluid, therefore the differences in pneumatic (gas) conductivity (K_g) between the two soils is a direct function of the intrinsic permeability differences of the soil – assuming soils are completely dry. It must be noted that effective pneumatic conductivity is a direct function of gas content, and is therefore strongly affected by the moisture retention capacity of the material. Differences in the dry pneumatic conductivity between the soils can be inferred from differences between their intrinsic permeabilities, given that the density ρ_g, and the viscosity μ_g of the gas remains equal for both soil types. The relationships relating hydraulic and pneumatic conductivities to intrinsic permeability are described by the following equations.

$$K_w = k_i \frac{\rho_w g}{\mu_w}$$

$$K_g = k_i \frac{\rho_g g}{\mu_g}$$

where K_w is the saturated hydraulic conductivity, k_i is the intrinsic permeability, g is gravitational acceleration, ρ_w is the density of water, and μ_w is the viscosity of water. Similarly, K_g is the pneumatic conductivity in dry soil, ρ_g is the density of gas, and μ_g is the viscosity of gas. Note that this approach only provides an estimate for dry gas permeability. Differences in effective gas permeabilities will be higher between the two materials, because of higher moisture retention capacity of the finer grained material, and associated lower gas contents, which reduce effective gas permeability and diffusivity.

A difference of 2 orders of magnitude was chosen to evaluate the effect of permeability on the fate of ethanol-blended fuels. In order to achieve a permeability difference of 2 orders of magnitude, it was determined experimentally that the silt had to be blended with the sand at a sand-silt ratio of 19:1.

Due to the substantial differences between the permeabilities of the two soil types, two separate methods were used to determine the saturated hydraulic conductivity of the sand and silty-sand mixture. A constant head permeameter test was performed on the sands, whereas a falling head permeameter test was performed on the silty-sand. The saturated hydraulic conductivity (K_{sat}) for sand was calculated by applying Darcy's law to the constant head data, based on the equation shown below:

$$q = -K_w \frac{\Delta h}{\Delta l}$$

where q is the specific discharge (cm/s), K_w is the saturated hydraulic conductivity in units of cm/s, and Δh is the head drop across the sample over the length Δl (Figure 2-9). The saturated hydraulic conductivity for the silty-sand was calculated by using and a modified version of Darcy's law for the falling head data (Todd, 1959).

$$K_w = 2.3 \left(\frac{aL}{At}\right) log \left(\frac{h_0}{h_1}\right)$$

where a is the cross sectional area of the standpipe (cm^2), A is the cross sectional area of the sample (cm^2), L is the length of the sample (cm), h_0 is the initial water level in the standpipe (relative to the datum) at the start of the experiment (cm), h_1 is the water level in the standpipe at the end of the experiment (cm), and t is the elapsed time (s) (Figure 2-10). The results from the hydraulic

conductivity tests are given in Appendix B (Table B-3). The average K_w calculated for the sand and silty-sand was 1.2E-4 m/s, and 1.2E-6 m/s, respectively.

2.4.3. Soil Water Retention Curves and Unsaturated Hydraulic Conductivity

Soil water characteristic curves were determined with Tempe cell tests on the sand material using a technique described by Fredlund and Rahardjo (1993). The curves for the silty-sand material could not be completed in this study due to an unresolved disruption of the tests by a process known as "ventilation" (Fredlund and Rahardjo, 1993), which is a direct consequence of the large amounts of suction needed to conduct tests on the low-permeability silty-sand. The water retention curve describes the relationship between the soil water content θ, and soil water suction ψ (matric potential), and is strongly dependent upon soil properties such as texture and soil structure (Klute, 1986). Soil matric suction was created through the gravitational potential differences of water in the soil and at the outflow location (Figure 2-11). Lowering the outflow tube generated more matric suction causing water to drain from the sediments. Once equilibrated, the cells were weighed to back calculate the saturation level at each matric potential. This process was repeated to obtain the necessary data points to obtain a full drainage curve. Once the curves were plotted, the water retention curve parameters were determined by fitting the (TH., 1980) empirical model to the experimental data from the Tempe cell tests (see Appendix B -Figure B-1,Figure B-2). The van Genuchten curve fitting parameters for the sand show a good fit between the model and the measured data, with an $R^2 \sim 0.991$ (Appendix B-Table B-2). The combined experimental data and model results allow the determination of the unsaturated hydraulic conductivity K_{unsat} as a function of relative hydraulic conductivity K_r, through the relationship derived by (TH., 1980):

$$K_r(\psi) = \frac{1 - (\alpha\psi)^{(n-2)}[1 + (\alpha\psi)^n]^{-1+\frac{1}{n}}}{[1 + (\alpha\psi)^n]^{2(1-\frac{1}{n})}}$$

where $K_r(\psi)$ is the relative hydraulic conductivity [$K_r(\psi) = K(\psi)/K_{sat}$), ψ is the matric potential expressed as tension (kPa), α is a water retention curve fitting parameter (kPa $^{-1}$) which relates to the air entry pressure, and n is a dimensionless curve fitting parameter which relates to the slope of the water retention curve. The relationship between K_r and soil matric potential ψ are summarized in Appendix B (Table B-1).

2.5. Column Filling

Two types of soil columns can theoretically be used in laboratory column experiments: columns containing packed (disturbed) sediments, or columns containing monolithic (undisturbed) soil material (Lewis and Sjöstrom, 2010). The choice of methodology is important because the results will be impacted from one methodology to another (Lewis and Sjöstrom, 2010). Considering the size of the experiments and the nature of the instrumentation, only the "packed" methodology was possible. Although less representative of field conditions, packed columns have the advantage of having a better reproducibility (Lewis and Sjöstrom, 2010). In the literature it has been found that packed columns, using sieved, homogenized soils tend to have fewer macropores, which explains the increased reproducibility (Lewis and Sjöstrom, 2010).

2.5.1. Sediment and Column Preparation

Soil characterization tests provided the information required to identify a suitable sediment mixing ratio for the silty-sand columns, to generate the desired permeability differences between the two experimental soils. The lower permeable soil was created by homogenizing a mixture of

95 wt% sand with 5 wt% silt in a cement mixer. The sediments were combined and mixed inside the cement mixer for a period of approximately 5 minutes, while small amounts of water were added to break down silt and clay aggregates and promote mixing of the silt into the sand. Both the sand and the silty-sand mixtures were sieved with a 3/8" U.S. Std sieve to remove larger pebbles and cobbles from the sediment, before the sediment was placed into the columns. Prior to filling, the inside walls of the columns were roughed up with sand paper. This strategy was used to prevent/limit preferential fluid migration along the column walls (Smajstrla, 1985), which is a common problem associated with packed soil columns (Corwin, 2000; Ghodrati et al., 1999; Sentenac et al., 2001).

2.5.2. Filling

The aim of packing was to produce a homogeneous soil column with a bulk density and porosity similar to sediments found naturally at a field site. The most common method of packing a column is known as dry packing, as cited by Lewis and Sjöstrom (2010), which involves loading small amounts of soil, known as "lifts" into the column and tamping down the soil carefully with a type of pestle or ram. Oliviera et al. (1996) demonstrated that lifts of 0.2 cm produced the best results for creating homogenous packed sand experiments; however, such a resolution was impractical to achieve for the 2 m tall columns used here and the prepared sediments were loaded into the column in discrete 10cm lifts. At each stage of filling, the individual lifts were tamped down with a large 2 meter metal rod equipped with a cylindrical PVC cap ~ 10 cm in diameter. After compaction, the top surface was scarified lightly, which is a method found to help maintain similar hydraulic conductivity between the layers and across the interface (Plummer et al., 2004; Seol and Lee, 2001). Once the top surface was roughened, the necessary sensors or samplers were installed at the level above, and epoxied into place. This process was repeated until each column

was fully constructed. Once the filling of the columns was completed, caps were placed on the top of the columns via O-rings, and subsequently sealed with silicone around the edges. A silicone bead was also applied at the bottom of the columns between the column base and the tube.

2.6. Baseline Water Analysis

Water used for infiltration tests and to generate and maintain the water table was collected from the taps in the EIL laboratory. Chlorination and chloramination are two of the most widely used practices for bacterial disinfection in water treatment systems (AWWA, 2006), therefore it was necessary to amend the Vancouver tap water with 5 ppm of Nutrafin®, which is a water conditioner that removes both chlorine and chloramine. Analysis of treated water was performed approximately 10 months into the experiment. Analysis of dissolved metals in the treated water was performed on an ICP-OES and the results are presented in Table 2-5. Infiltration water collected was also analyzed for pH and conductivity. An Oakton pH 11 series meter calibrated using a 3-point method (pH 4, 7, and 10) and a Thermo Orion 115 conductivity using an automated temperature correction were used to determine the pH and conductivity of Vancouver tap water. Results for baseline pH and conductivity can also be found in Table 2-5. The composition of the injected water can be described as very dilute, low in major cations, and low in conductivity. The pH of the water is slightly less than neutral, around pH = 5.8. Although the analysis was not performed for the tap water that was used to establish the initial groundwater table, it is representative, considering that the composition of Vancouver tap water remains consistent over time and is very dilute in nature (collected from reservoirs).

2.7. In-Situ Testing and Baseline Monitoring

A series of in-situ sensor calibrations, testing and baseline monitoring was performed before deploying the columns. The first aim of the tests was to identify unresponsive sensors that were damaged during the construction of the column. In addition, the tests provided data to generate the appropriate calibration equations for each individual sensor. Baseline monitoring provided the initial environmental conditions inside the columns.

2.7.1. Water Infiltration Tests

Tap water treated with Nutrafin® was pumped into the water infiltration system at a constant rate until 4 L of water had been pumped onto the soil surface in the sand column, and 2 L in the silty sand column. The water infiltrated into the sandy soil without ponding, and there was no sign of sidewall flow or excessive fingering. Conversely, the low permeability silty-sand columns began to pond immediately and some columns showed signs of sidewall flow (Figure D-1). As the water infiltrated into the columns, responses of the factory-calibrated moisture sensors were data logged, (an example can be viewed in Appendix D – Figure D-2). In this context, the moisture sensor data was evaluated to determine sensor functionality. The infiltrating water pooled at the base of the column, developing a water table. The water table was supplemented with Nutrafin®-treated water through the basal manometer until the desired water table level of ~ 15 cm was achieved. All columns facilitated the infiltration of water along the entire vertical length of the column with pooling at the base, except for the silty-sand column "GAS-SS" (Gasoline application – silty sand medium), which developed a perched water table at an elevation of approximately 100 cm (Figure D-3). The perched water table developed despite consistent blending procedures of sand and silt media and persisted throughout the entirety of the GAS-SS column experiment, disallowing direct comparison of results from this column with the other experiments.

2.7.2. Gas Injection Tests

An in-situ, 2-point calibration of the O_2 and CO_2 sensors was achieved through gas injection tests at each sensor level. A gas with known composition was injected into the column until the sensor output stabilized (Figure D-4). Once stabilized, the sensor output in volts (V) was recorded and the process was repeated with a gas of different composition. The data was gathered into a table and plotted to obtain a linear regression equation for the 2-point calibration. The linear regression equation was then inputted into the Lab-Jack™ U3-LV to convert voltages into real-world gas concentrations. An example can be found in Appendix D (Figure D-5). Once the tests were completed, the data was compiled and malfunctioning sensors were identified. Subsequently, the columns were allowed to return to oxic conditions. After testing, approximately 1 in 7 of these sensors were diagnosed as unresponsive, implying a success rate of > 85%.

2.7.3. Baseline Monitoring

After sensor testing and calibration, the columns were monitored for a week prior to injection to observe and characterize baseline conditions within the columns before the fuel injection. Initial O_2 and CO_2 composition within the columns remained near atmospheric with measured O_2 concentrations ranging between 18.3 and 21.9%, and CO_2 concentrations ranging from 0 to 2.4% (Table D-1). Columns showing lower O_2 concentrations showed a correspondingly higher initial CO_2 concentration, indicating that columns had differing microbial activities prior to the fuel releases. The soil CO_2 flux was also measured using a LI-COR® LI-8100A, utilizing the column headspace as a custom chamber for measurements. The initial soil CO_2 effluxes are interpreted to represent bacterial degradation of detrital carbon within the soil. The efflux is not related to root respiration which typically takes place in soils that are hosting plants. Baseline results are

presented in Appendix D (Table D-2), with baseline fluxes ranging from 0.07 – 1.3 µmol m^{-2} s^{-1}). The columns with the higher baseline soil CO_2 effluxes correspond to the columns that showed higher CO_2 concentrations and lower O_2 concentrations, relative to the atmosphere. Together, these data provide an indication of differing baseline microbial activities within the columns.

2.8. Fuel Preparation and Analysis

The fuels used in this experiment are ethanol and gasoline, both of which were purchased locally in Vancouver, BC. Shell V-power Nitro purchased from a gas station in Vancouver, BC, Canada, was amended with 100mg/L Sudan 7B dye. Sudan 7B is a non-polar dye that is commonly used to visualize non-polar organic compounds typically found in gasoline (Griffin and Watson, 2002; McDowell and Powers, 2003). The addition of Sudan 7B turned the gasoline bright red (Figure 2-12), facilitating the visualization of the spill distribution within the transparent acrylic column. 100% ethanol (pure un-denatured grade, 200 proof) was purchased from GreenField Specialty Alcohols. Fluorescein, a synthetic organic compound that is soluble in alcohol, was added to the ethanol and mixed to a final concentration of 10 mg/L, causing the ethanol to appear bright yellow (Figure 2-13). The dyed fuels were mixed together to form the desired fuel blend for each experiment in preparation for injection into the column. A summary of the total proportions of fuels added to each mixture, as well as total injected volumes can be found in Table 2-3. Prior to the injection events, aliquots from each fuel type were taken for laboratory analysis to provide a geochemical baseline of each source type. Gasoline samples were taken for analysis of BTEX composition, ^{13}C and ^{2}H isotopes in benzene and toluene compounds, and ethanol samples were analyzed for ^{13}C and ^{2}H isotopes. The compositional results show that there is significantly more toluene than benzene in the gasoline. The average concentration of toluene was 44,287 ppm,

whereas the average concentration of benzene was 9,667 ppm (Table 2-6). The ratio of benzene to toluene in the gasoline is approximately 1:4. The isotopic results show that ethanol is enriched in ^{13}C, with a $\delta^{13}C$ value of -11 ‰, which represents the typical isotopic signature of C4 plants (corn) from which the ethanol was derived (Aelion et al., 2009). C4 plants undergo a different photosynthetic pathway compared to their C3 plant relatives, and it is this difference that determines the amount of ^{13}C fractionation of CO_2 during photosynthesis (Aelion et al., 2009). The ^{13}C isotopic signature of the gasoline components benzene and toluene consisted of $\delta^{13}C$ values of -30‰ and -28‰, and a ^{2}H isotopic signature of -163‰ and - 34‰, respectively. These results are consistent with other studies, which have found that the $^{13}C/^{12}C$ isotopic ratio in fossil fuels lies within a narrow range between -23 to -28.6‰ (Smallwood et al., 2002; Widory, 2006). The results are summarized in Table 2-4, and illustrate the distinct isotopic signatures associated with gasoline fuel components and ethanol. Radiocarbon analysis of the ethanol confirmed its plant-derived modern signature ($F^{14}C$ 1.02). Radiocarbon analysis of the gasoline was not performed; however, a radiocarbon-dead signature can be assumed safely, considering that the gasoline is derived from petroleum.

2.9. Fuel Injection

Injection of the fuels took place in two stages. The first stage involved injections into all of the columns, and the second stage was dedicated exclusively to the delayed spill columns, in which blended fuel was applied on top of a pre-existing gasoline spill. The first stage was completed over a two-week period, when gasoline injections were applied to the columns dedicated to investigate "pure gasoline" spills and the response to a "delayed E20" release. These releases were completed on May 21st 2015. The first stage was completed by releasing ethanol-blended fuels into the

remaining columns a week later on May 28th 2015. The second stage involved the final release of E20 fuel on July 15th 2015, into the delayed spill columns, which was roughly 8 weeks after the initial release of gasoline during the first stage.

Injecting the fuels was administered via a gravity drainage method, where an elevated reservoir containing fuel was connected to an insertion coil located 50cm above the base of the column. The coil was fabricated from stainless steel tubing, and formed to a maximum diameter of 15cm, just half the diameter of the column itself. As previously discussed, the design was similar to that of the water infiltration coil near the top of the column. To allow for an even dispersal of fuel inside the column, the coil was pierced approximately 10 times in an even distribution around the entire segment of the coil. During injection, the elevated reservoir was connected to the coil and the fuels were then released into the columns through the coil. Observations on infiltration times for each column were recorded. As the infiltrating fuel reached the water table, an increase in fluid pressure could be observed in the manometers of the columns. In general, the injections were successful; however, a few columns developed leaks which occurred either during injection or within the following week. For the columns that experienced leaks, the fluid loss was estimated based on leaked volumes and leaks were sealed. Subsequently, it was attempted to re-administer missing fuel volumes. However, these attempts were not completely successful for select columns as subsequent leaks developed, resulting in a reduced total fuel volume inside some columns. The total administered fuel volumes for all columns are summarized in Table 2-3. The internal distribution of the spill zones was identified through visual observations of the dyes inside the column. A powerful lamp was needed to visualize the dyes through the blue transparent columns (Figure 2-15).

2.10. Column Sampling and Analysis

A suite of samples was collected over a time period in excess of one year to evaluate the geochemical conditions in both the vadose zone and the saturated zone of the columns. The sampling schedule focused some sampling events to be collected early on while others were more temporally distributed throughout the duration of the year-long experiment. A full list of the vadose zone analytes is described in Table 2-1, and the list of saturated zone analytes can be found in Table 2-2. All saturated zone and vadose zone sampling techniques involved purging of the sampling line prior to sample collection. Note, vadose zone soil water solution samplers (SWSS) were not used due to strong interference with vadose zone gas chemistry.

2.10.1. Vadose Zone Gas Concentration and Pressure

All gas concentration samples were collected with Hamilton GASTIGHT® syringes. 10 ml gas samples were taken and analyzed immediately after collection using a Varian CP-4900 dual channel gas chromatograph, equipped with a Molsieve 5A PLOT column to separate out Ar, N_2 and O_2 gases, and a PoraPLOT U column to separate CH_4 and CO_2 from the gas sample. The required operating temperatures for each column are 110°C and 50°C, respectively. Collected samples were pumped into the GC columns via a helium carrier stream pressurized to 50 psi. The GC was calibrated using a calibration gas (20% CO_2, 20% CH_4 balanced with N_2) and atmospheric air (20.95% O_2, 78.09% N_2, 0.93% Ar, and 0.039% CO_2). Calibration occurred periodically to ensure accuracy of the results. Vadose zone pressure measurements were taken using a Dwyer® handheld digital manometer with range of +/- 1" H_2O.

2.10.2. Vadose Zone CH_4 and CO_2 Stable Isotopes

Gas samples for stable isotope analyses in CH_4 and CO_2 were collected from the columns and stored in 12 ml Labco Exetainers®. The samples were over pressurized by 1 atm and stored in a laboratory fridge until they were shipped to their respective destinations. Samples for methane isotope analysis were shipped to UC Davis, and were analyzed for stable isotope ratios of carbon ($\delta^{13}C$) and hydrogen ($\delta^{2}H$) using a ThermoScientific Precon concentration unit interfaced to a ThermoScientific Delta V Plus isotope ratio mass spectrometer (UC Davis). Samples for carbon dioxide isotope analysis were shipped to the University of Waterloo, Ontario, and were analyzed for carbon stable isotope ratios ($\delta^{13}C$) with a GC-C-IRMS system using a Micromass IsoPrime isotope-ratio mass spectrometer. The results from both labs are provided using standard del notation, which is a common method to compare measured isotopic ratios to those found in a reference sample:

$$\partial^{13}C = \frac{N\,(^{13}C)_{co_2} / N\,(^{12}C)_{co_2} - N\,(^{13}C)_{std} / N\,(^{12}C)_{std}}{N\,(^{13}C)_{std} / N\,(^{12}C)_{std}}$$

where $\delta^{13}C$ represents the difference in isotopic ratio between the sample and the international standard, $N(^{13}C)_{CO2} / N\,(^{12}C)_{CO2}$ is the isotopic ratio of the CO_2 sample, $N(^{13}C)_{std} / N\,(^{12}C)_{std}$ is the isotopic ratio of the standard. The reference material for carbon is V-PDB (Vienna Pee Dee Belemnite) and V-SMOW (Vienna Standard Mean Ocean Water) for hydrogen.

2.10.3. Soil CO_2 and CH_4 Efflux

CO_2 and CH_4 fluxes were measured using an infra-red gas analyzer (IRGA) from LI-COR, model series LI-8100 and an LGR Greenhouse Gas Analyzer, following methods described in Sihota et al. (2013). Here, the column headspace was used as a custom chamber and equipped with quick-connections on the column cap, providing an attachment for the LICOR-LGR

sampling lines. The gas stream was routed through the gas analyzers to measure headspace concentrations over time. To calculate the CO_2 and CH_4 effluxes, a standard equation developed by LI-COR was utilized (LI-COR, 2007):

$$F = \frac{10VP_0\left(1 - \frac{W_0}{1000}\right)}{RA(T_0 + 273.15)}\frac{\partial C}{\partial t}$$

where F is the gas efflux in μmol $m^{-2}s^{-1}$, V is the total volume of the system (chamber, tubing, and analyzers), P_0 is the initial pressure (kPa), W_0 is the initial water vapor mole fraction (mmol mol^{-1}), R is the gas constant (3.314 [Pa m^3 K^{-1} mol^{-1}]), A is the area of the soil surface (cm^2), T_0 is the initial air temperature (°C), and $\partial C/\partial t$ is the rate of change in gas concentration of a selected gas species over the measurement period - corrected for water vapor (μmol mol^{-1} s^{-1} , or ppm_v s^{-1}). A measurement period of 2 minutes was determined to be the optimal length of time to allow for chamber mixing and measurement of soil gas flux. The early time data was discarded as the elevated gas concentrations in the headspace during initial measurements did not accurately reflect gas flux from the soil surface. The raw data was imported into SoilFluxPro™ and flux was computed by fitting a linear flux model to the data. The linear flux model was fitted to specified segments of the raw data, usually by simply omitting the initial mixing data, which generally resulted in a fit to the concentration data with an R^2 >95%.

2.10.4. Saturated Zone Dissolved Metals, VFA and EtOH

Sampling techniques for ethanol and VFAs from the basal region of the column were generally the same. Water samples were extracted from the column and filtered using a 22 μm filter, capped and subsequently stored in a laboratory freezer. The VFA samples were shipped to UBC Okanagan for analysis of acetic, butyric and propionic acids, using an Agilent 7890A GC equipped with a 25

m Agilent 19091F-112 column, a flame ionization detector (FID) as well as an auto-sampler (Agilent Technologies). Aqueous ethanol samples were taken and analyzed by injecting 100 μL of sample into a SRI 310 GC with a Haysep D column and flame ionization detector (FID). The instrument was calibrated using various standards composed of 100% ethanol and DDI H_2O to ensure measurement accuracy (Abbott, 2016) Samples for dissolved metal analysis were taken from the saturated zone and passed through a 22 μm filter into a 5ml falcon tube. The sample was then preserved with 2% HNO_3, and then stored inside a laboratory fridge. The samples were analyzed using a Varian 725-ES-ICP-OES along with multi element standards and blanks to ensure accuracy.

2.11 Figures

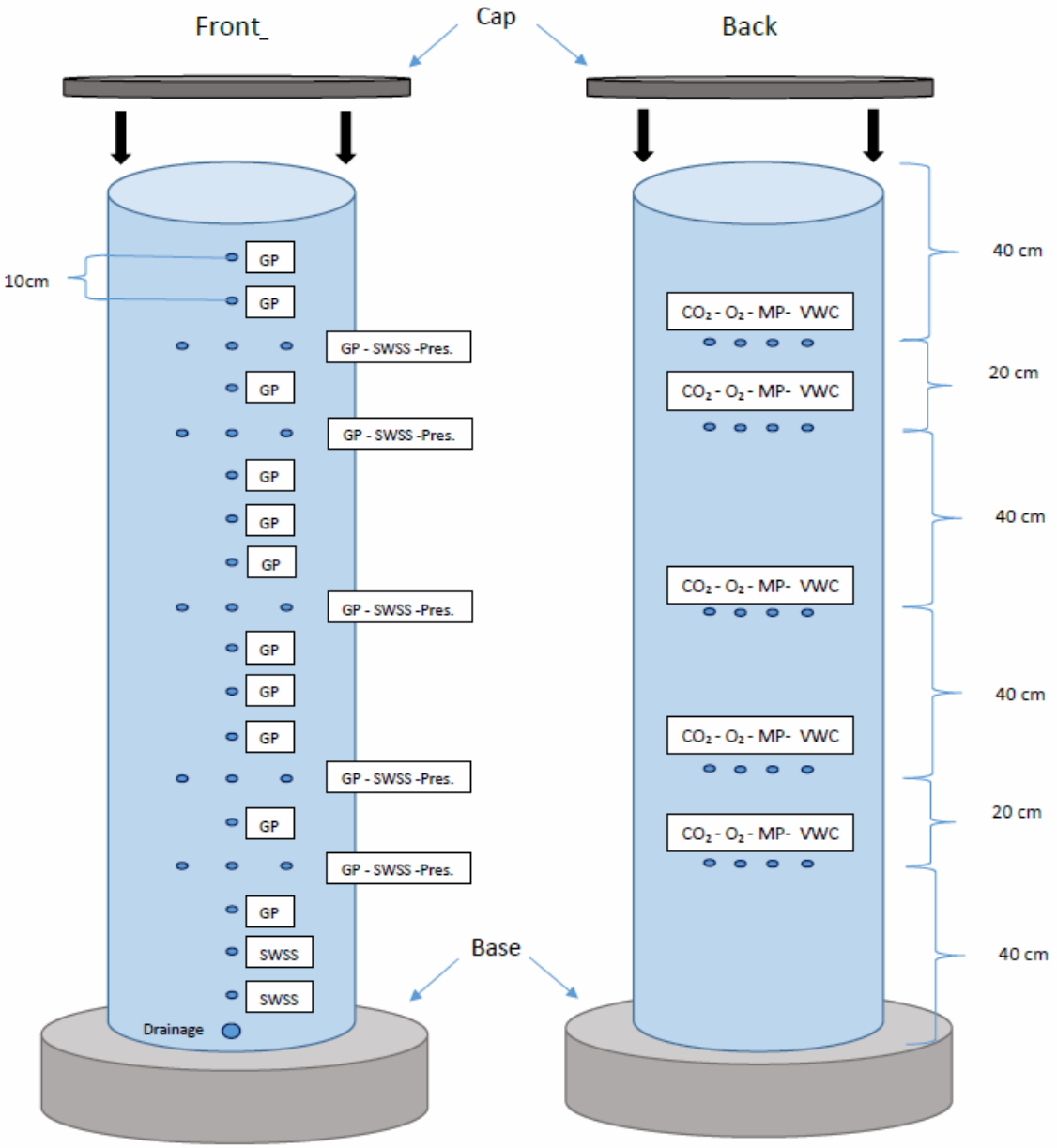

Figure 2-1: Schematic of experimental set-up including location and type of monitoring ports (GP = gas port, SWSS = soil water solution sampler, Pres = pressure port, MP = matric potential sensor, VWC = volumetric water content sensor, CO_2 = CO_2 sensor, O_2 = O_2 sensor, column height = 2 m)

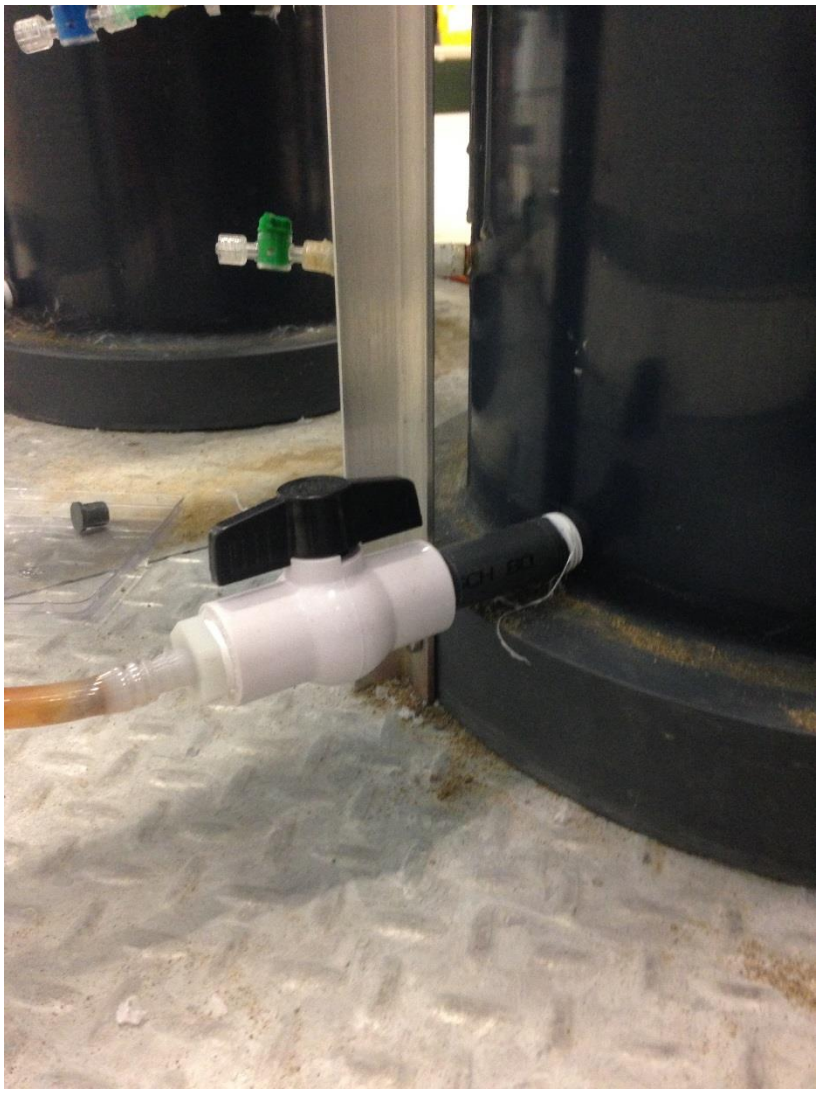

Figure 2-2 Column Base. Drainage port fitted with a PVC ball valve and connected to Tygon® tubing which makes up the manometer.

Figure 2-3 Column cap equipped with the headspace air circulation unit, and an infiltration coil which connects externally to Tygon ® tubing for optional delivery of water. A close-up of the exhaust line shows the diaphragm pump that pulls air into the column headspace and delivers the exhaust to a manifold system which leads to a fume hood.

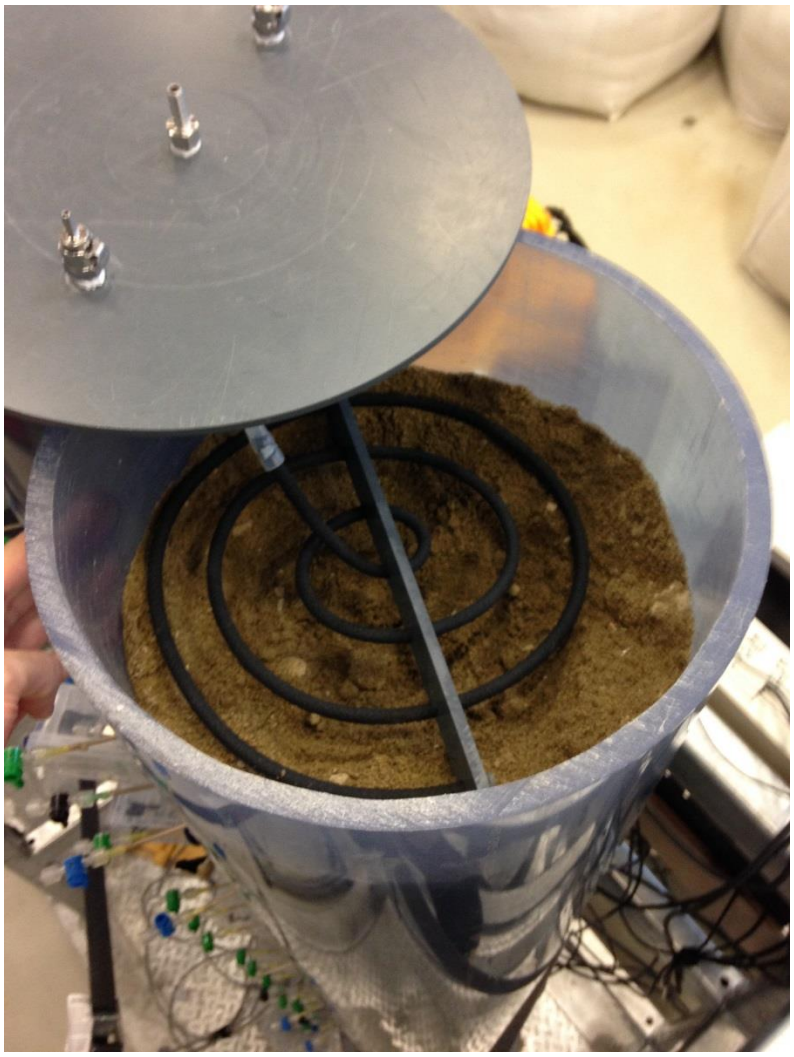

Figure 2-4 Infiltration coil to simulate recharge events. Similar infiltration coils were installed in the lower section of the columns for administration of the fuel releases.

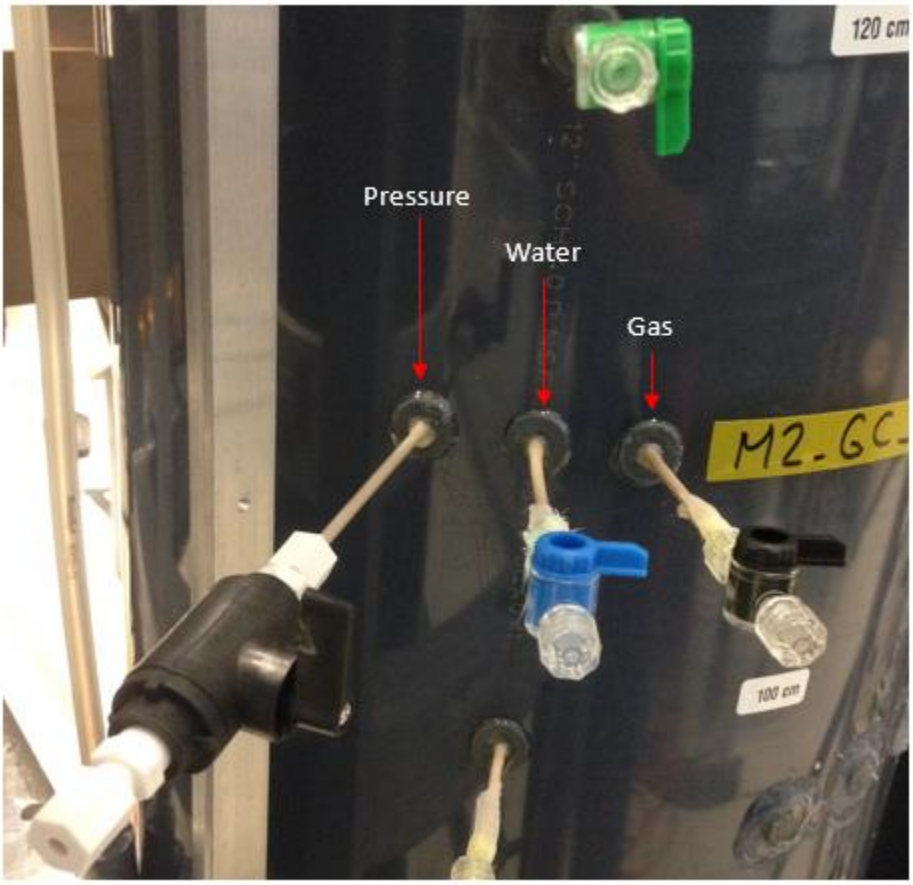

Figure 2-5 Column monitoring port for pressure and sampling ports for water and gas. The water sampling port is connected to a soil water solution sampler (SWSS).

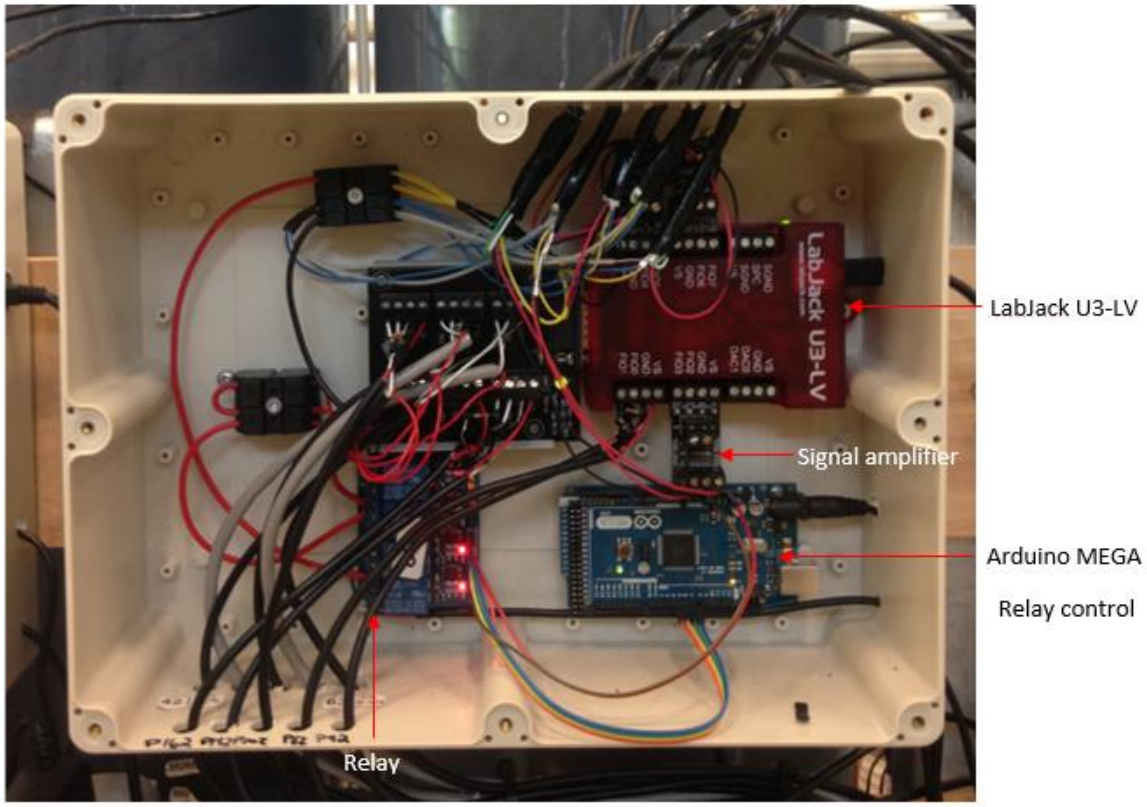

Figure 2-6 LabJack U3-LV data acquisition device for O_2 and CO_2 gas sensors. Arduino MEGA programmed for relay control of the CO_2 sensors which are connected to a solid state relay.

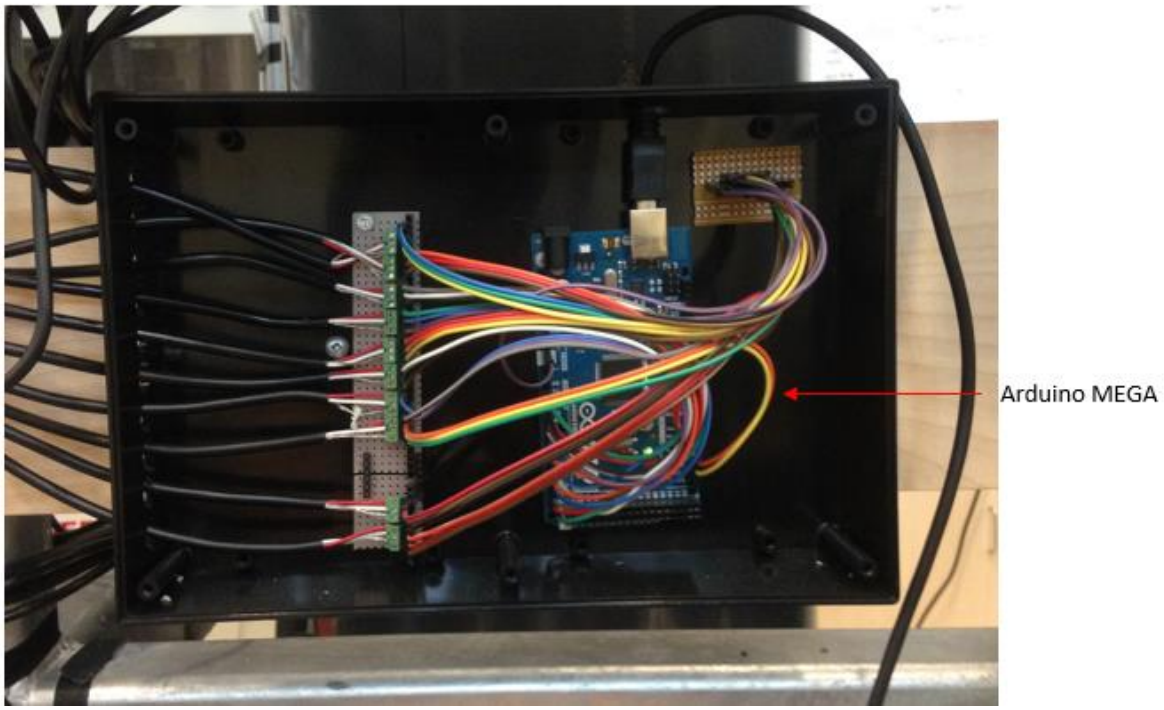

Figure 2-7 Arduino MEGA programmed for digital data acquisition for the GS3 (VWC) and MPS-2 (MP) sensors. The Arduino USB communication is connected to a dedicated lab computer.

Figure 2-8 Wet sieving of sediments prior to filling of columns

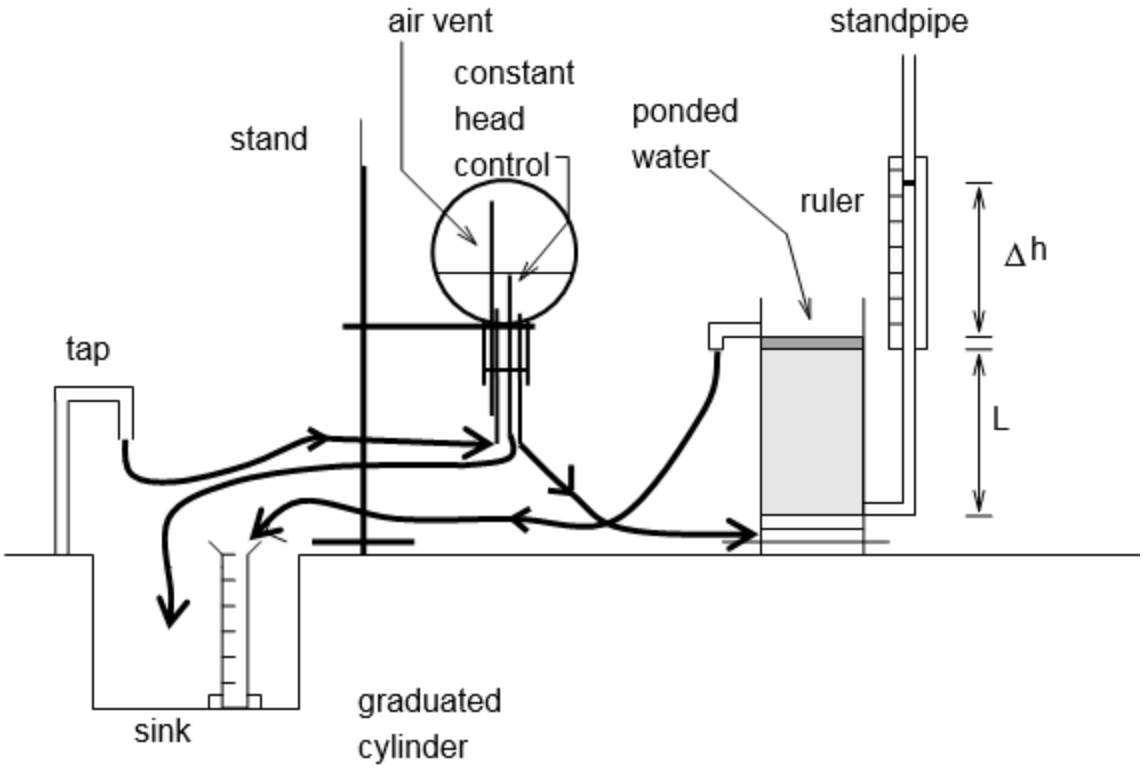

Figure 2-9 Constant head apparatus used to quantify hydraulic conductivity of sand. The water flows out of the tap into the constant head reservoir, and then into the permeameter through the sample of length L (cm). The head difference Δh is kept constant through the positioning of the constant head reservoir, and the flow is measured from the outlet port on the permeameter q (cm/s). Figure copied with permission of Roger Beckie (UBC).

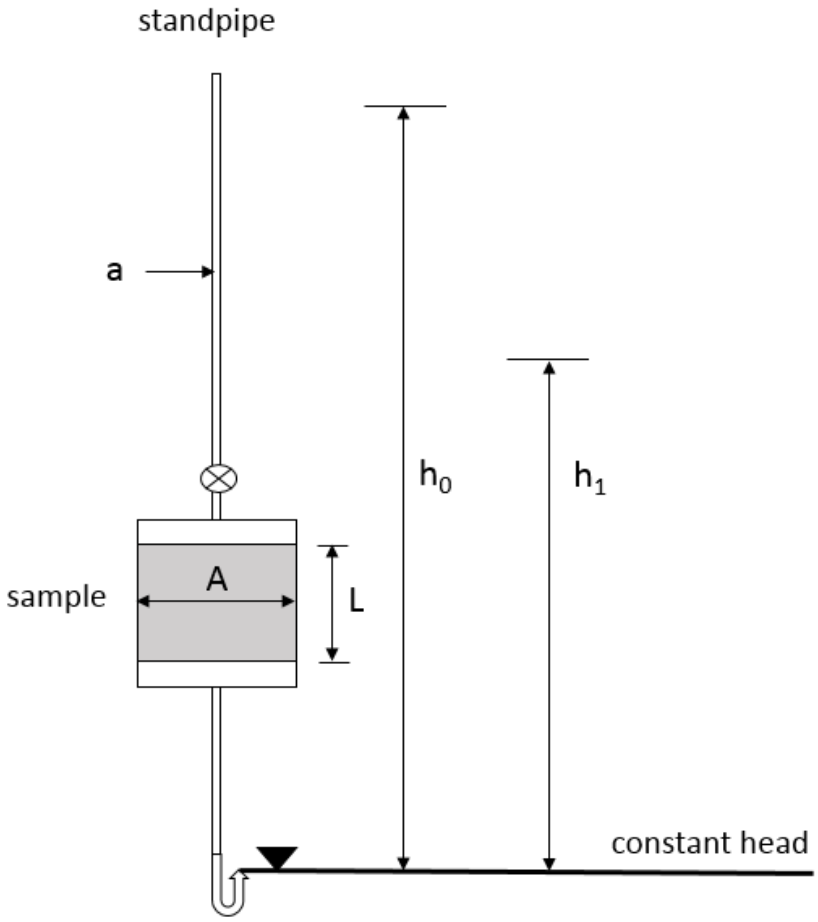

Figure 2-10 Falling head apparatus used to test hydraulic conductivity of the silty-sand material. Water flows down through the standpipe, into the sample, and exits through the outflow tube which is set up to keep a constant head. Two measurements are taken at h_0 and h_1 over a time period Δt (s). The length of the sample L (cm), cross sectional area (cm^2) of the standpipe a, and the sample A are inputted into a modified Darcy's law equation to determine hydraulic conductivity.

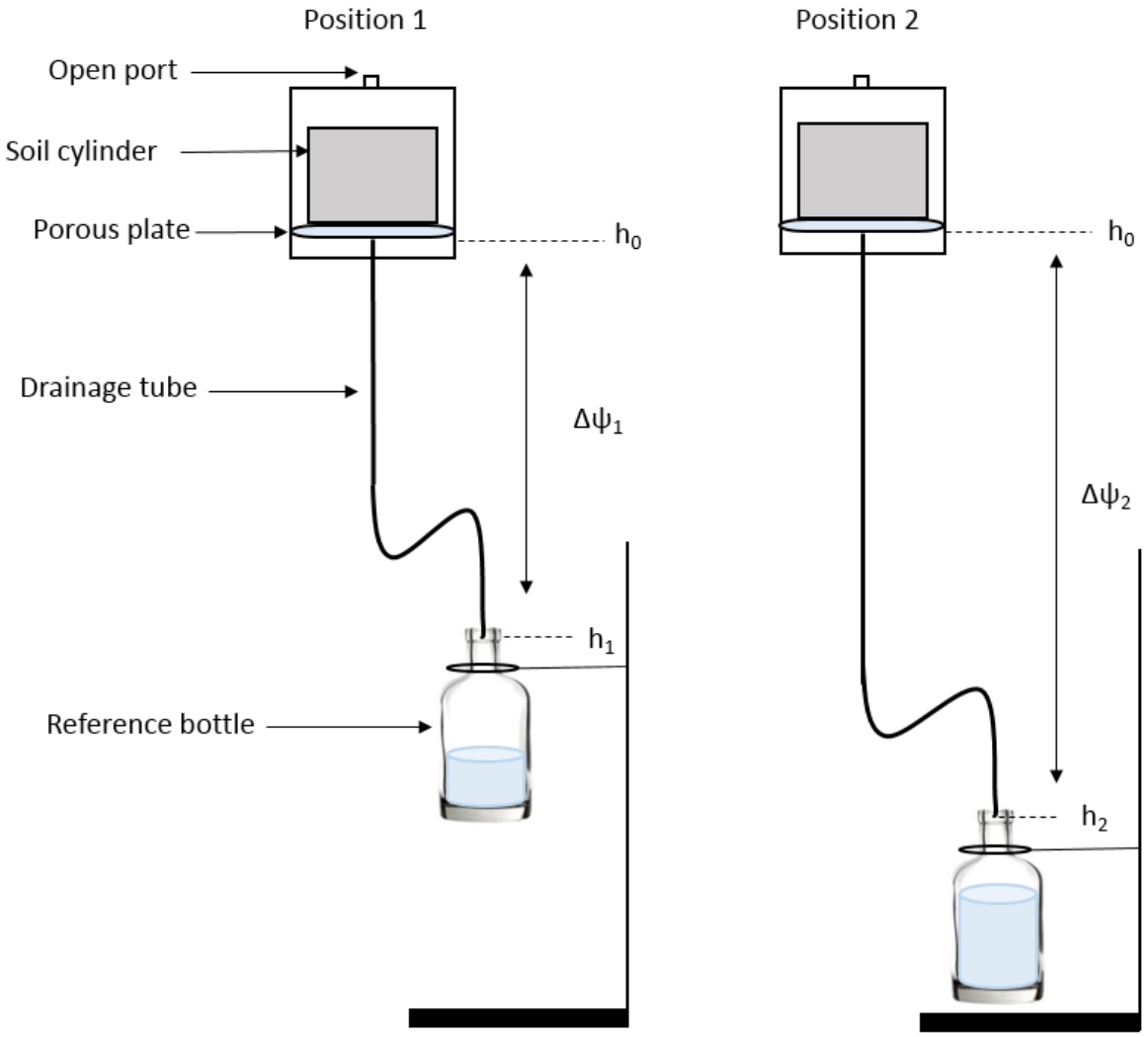

Figure 2-11 Tempe cell apparatus to determine soil water characteristic curves. Soil material is packed inside the soil cylinder and saturated. Once fully saturated the drainage tube is lowered and allowed to drain until equilibrium is reached. Once equilibrium is reached, the soil is then weighed and the height of the reference bottle is recorded. The process is repeated to obtain multiple data points to produce a distinct soil water characteristic curve.

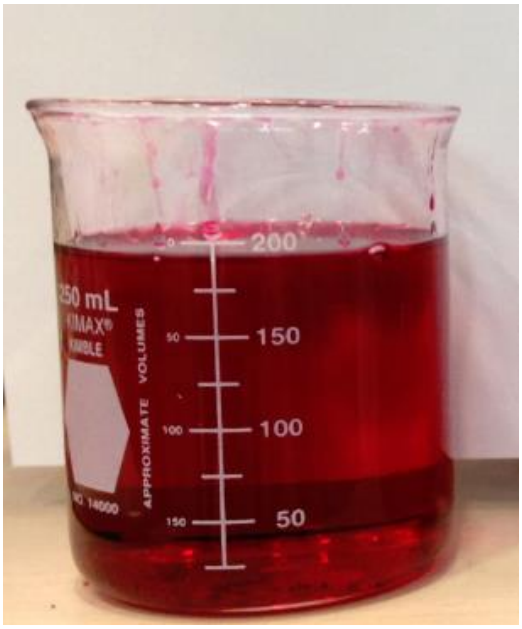

Figure 2-12 Shell V-power Nitro amended with 100mg/L Sudan IV dye. The dye aided in the visualization of the gasoline within the column

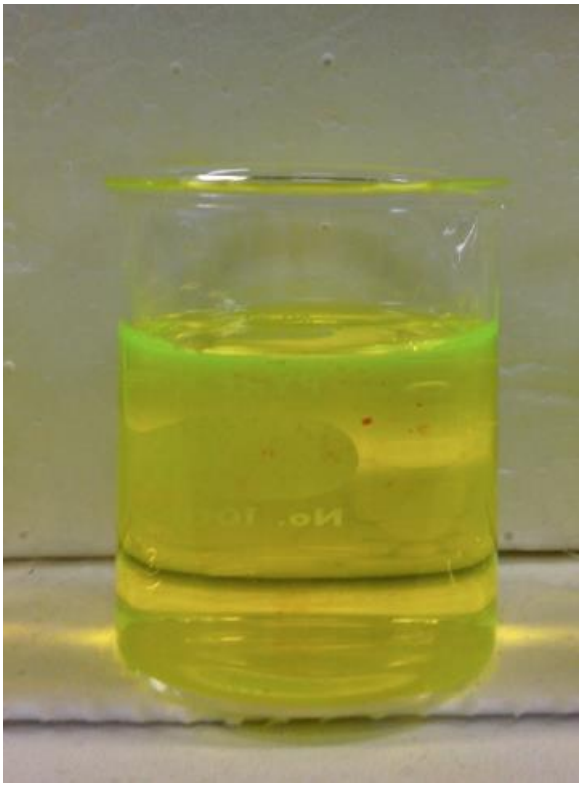

Figure 2-13 Ethanol amended with 10mg/L of fluorescein appears bright yellow after mixing.

Figure 2-14 Fuels being injected using a gravity assisted method. Fuels from reservoir drain into the column through the infiltration coil.

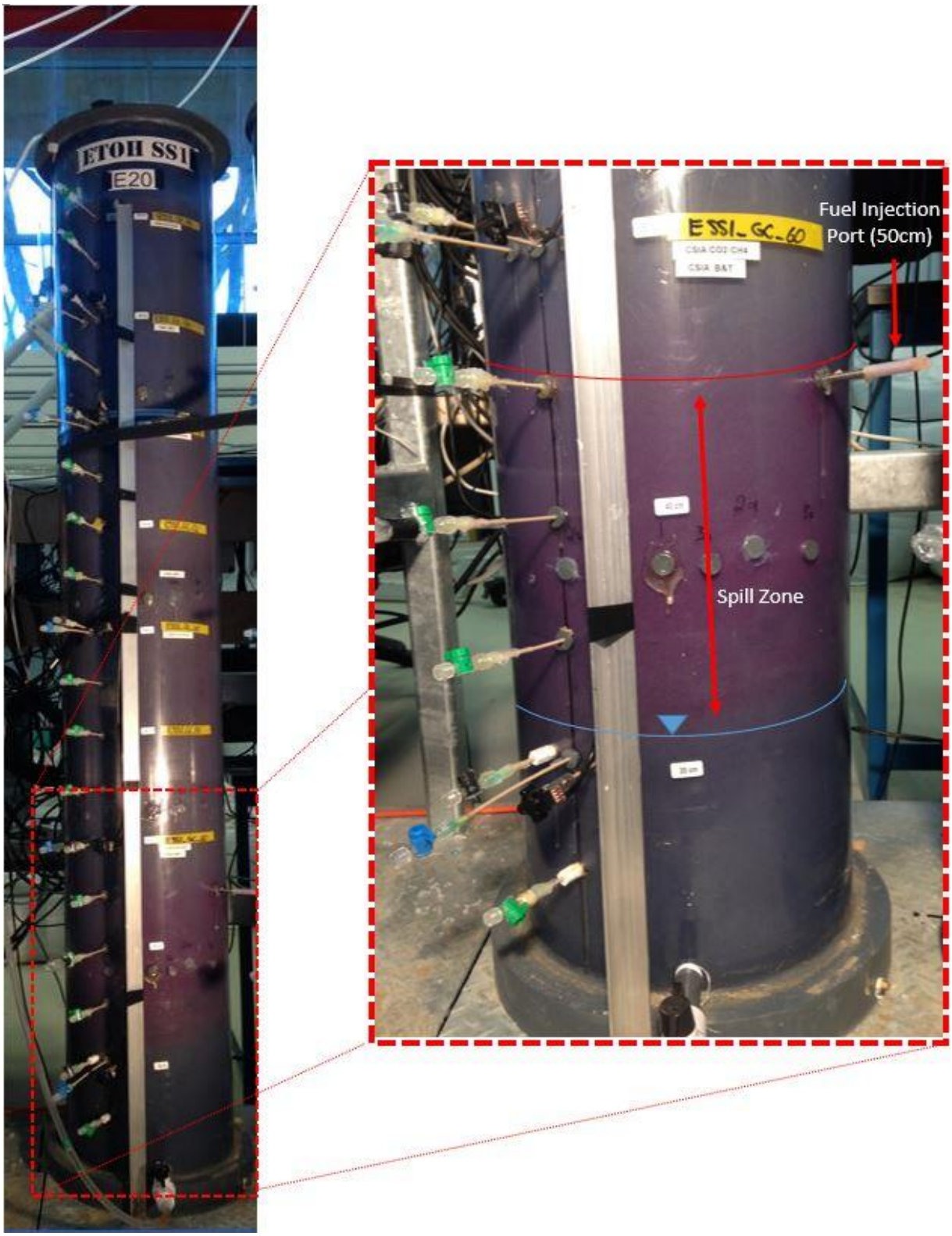

Figure 2-15 Visualization of the injected fuel (dyed red). The close up shows the fuel resting on top of the water table.

2.12 Tables

Table 2-1 A summary of vadose zone analytes taken at various locations along the vertical profile of the column

Vadose zone analytes		
Analysis Type	Target Compounds	Location (cm above base)
	O_2 , CO_2, CH_4, Ar, N_2	60, 80, 100, 120, 140, 160, 180
Gas composition		60, 110, 160
	Benzene, Toluene	
Pressure	N/A	60, 100, 140, 160
^{13}C (CSIA)	Benzene, Toluene	60, 110, 160
^{13}C (CSIA)	CH_4, CO_2	60, 100, 140, 180
^{2}H (CSIA)	Benzene, Toluene	60, 110, 160
^{2}H (CSIA)	CH_4,	60, 100, 140, 180

Table 2-2 A summary of the saturated zone analytes.

Saturated Zone Analytes		
Analysis type	Target compounds	Location (cm above base)
Aqueous concentration	Benzene, Toluene , Ethanol	10
	Dissolved: Fe, Mn, Mg, Ca, Na, K, Si	10
Volatile Fatty Acids (VFA's)	Acetic, Butyric, Propionic	10
^{13}C (CSIA)	CH_4, Benzene, Toluene	10
^{2}H (CSIA)	CH_4, Benzene, Toluene	10

Table 2-3 A summary of the fuel mixtures and volume of controlled fuel releases for each experimental column. The table provides a breakdown of the proportions of each fuel constituent and the total amount released into each column. Note that E20-D-SS, GAS-SS and E10-S all experienced leaks and the total administered volumes were less than 2L. For these columns, administered volumes were estimated from applied volumes and the volume of leaked free product.

Fuel Mixtures							
Column	**Total "Spilled" Quantity (L)**	**EtOH Proportion (%)**	**Gasoline Proportion (%)**	**Quantity of EtOH (L)**	**Quantity of Gasoline (L)**	**Fuel Blend**	**Description**
E20-S	2	20	80	0.4	1.6	***E20***	E20 release
E20-D-S	2	20	80	0.2	1.8	***E20***	Gasoline with delayed E20 release (1L gas + 1L E20)
GAS-S	2	0	100	0	2	***none***	Gasoline
E20-SS	2	20	80	0.4	1.6	***E20***	E20 release
E20-D-SS	2	20	80	0.2	1.8	***E20***	Gasoline with delayed E20 release (1L gas + 1L E20)
GAS-SS	1.6	0	100	0	1.6	***none***	Gasoline
E85-S	2	85	15	1.7	0.3	***E85***	E85 release
E10-S	1.9	10	90	0.19	1.71	***E10***	E10 release

Table 2-4 Stable isotopic results of EtOH, Benzene and Toluene feedstock. Benzene and toluene isotopic compositions are reflective of typical isotopic compositions in gasoline. The data shows distinct isotopic signatures from each fuel source.

	PDB ± 0.2‰		VSMOW ± 0.5‰	
Sample	δ13C- Result	δ13C -Repeat	δ2H- Result	δ2H -Repeat
EtOH	-11.03	-10.98	-198.72	-195.58
Benzene	-30.29	-30.14	-163.47	-163.56
Toluene	-28.28	-28.36	33.31	34.53

Table 2-5 Baseline water composition results of major cations, pH and conductivity.

Sample Date	Sample Labels	Ca (ppm)	Fe (ppm)	K (ppm)	Mg (ppm)	Mn (ppm)	Na (ppm)	Si (ppm)	pH	Conductivity (µS/cm)
April 4th 2016	injection water	2.59	0.19	0.19	0.38	0.00	9.11	1.05	--	--
March 17th 2016	injection water	2.59	0.00	0.19	0.38	0.00	9.11	1.05	--	--
June 17th 2016	injection water	--	--	--	--	--	--	--	5.88	65

Table 2-6 Analysis of the benzene and toluene composition of the shell v-power gasoline used in this experiment. The data shows there is significantly more toluene than benzene, with an average ratio of 4.6:1, respectively.

Sample ID	Date	Benzene (ppm)	Toluene (ppm)
Shell V-Power Gasoline	30-Jun-15	10650.0	42400.0
Shell V-Power Gasoline (DUP)	30-Jun-15	9650.0	44565.8
Shell V-Power Gasoline (TRP)	30-Jun-15	8700.0	45896.5
Shell V-Power Gasoline (AVG)		9666.7	44287.4
Average Ratio		1.0	4.6

Chapter 3 - Results and Discussion

3.1 Introduction

The total operational lifetime for the column experiments were approximately a year and a half (~ 530 days). The data collected during this time is presented and discussed in this chapter. This introduction outlines the outcome of the experiments and provides context for the results and framework of this chapter. The experiments were successful in providing information on the evolution of biodegradation of motor fuels in the subsurface. The continual sensor monitoring of soil O_2 and CO_2 in combination with the column sampling program were successful in characterizing both the vadose zone and saturated zone with sufficient resolution of data.

3.1.1 Limitations

It is necessary to acknowledge experimental issues that arose during the life of the experiments because they had an effect on the ability of this study to accomplish the objectives set out in the introduction chapter

In the later stages of the experiment, evaluation of the data revealed inconsistencies in expected soil gas composition in many of the columns. It was discovered that there was a problem associated with the design of the headspace venting system. This system was intended to capture and direct harmful volatiles entering the headspace from the sediment column into the fume hood, while simultaneously sustaining an oxygenated headspace. However, the small opening in the air inlet port proved to be overly restrictive, and consequently, resisted the air inflow into the column creating a negative pressure inside the headspace, relative to the pressure outside of the column. Despite efforts to seal all locations of potential air ingress including sampling ports and sensor installation ports, some locations were inadequately sealed and allowed outside air to ingress along the length of the columns - driven by the pressure gradient between the column headspace and lab air generated by the pump. As a result, a few columns were affected to varying degrees by this

inadvertent air ingress. The columns that were affected the greatest resulted in compromised vadose zone data sets as a consequence of the long lasting effects on the soil gas profile produced by the continual ingress of lab air, effectively leading to partial venting of the sediment column. During the initial stages of the experiment, the pumping rates were increased as it was discovered that fuel volatiles were escaping through the air inlet port into the lab. This increased pumping rate likely caused the air ingress, and this effect was noticeable in a few of the columns, as carbon dioxide concentrations decreased and oxygen increased along the length of the columns.

Procedural error also contributed to short term interruptions, which affected the natural soil gas composition in certain columns. During the operational life of the column experiment, many samples were collected from various locations along the length of the columns. Analysis of the data suggests that some columns were affected by accidental air-ingress due to improper closure of sampling ports. In general, these short interruptions did not have a lasting effect on the overall behavior of the evolved soil gas profile, and only existed as temporary disturbances in operational soil gas profiles.

In conclusion, due to the issues described above, the results for two columns (E10-S, E20-D-S, and E20-D-SS) are not suitable to address the original project objectives and cannot be included in this context, and ultimately the vadose zone analysis is limited to the following columns:

- E85 Sand Column – E85-S
- E20 Sand Column – E20
- Gasoline Sand Column – Gas-S
- Gasoline Silty-Sand Column – Gas-SS
- E20 Silty-Sand Column – E20-SS

In contrast, saturated zone data remained mostly unaffected by the unintentional air-ingress into the vadose zone of the columns. Thus, the saturated zone data set is not considered to be compromised for any of the column experiments and analysis of all eight columns is possible, as listed below:

- E10 Sand Column – E10-S
- E85 Sand Column – E85-S
- Gasoline Sand Column – Gas-S
- E20 Sand Column – E20-S
- E20-Delay Sand Column – E20-D-S
- Gasoline Silty-Sand Column – Gas-SS
- E20 Silty-Sand Column – E20-SS
- E20-Delay Silty-Sand Column – E20-D-SS

In addition, the original sampling plans also included sample collection from soil water solution samplers in the vadose zone. However, this sampling could not be conducted, because it disturbed vadose gas concentrations substantially. It was found that the significant suction that must be applied during sample collection does not allow collection of water samples from the vadose zone in the laboratory.

3.2 Chapter Overview

This chapter is divided into three main sections: conceptual model, results and discussion. The conceptual model section focuses on the reaction network describing the biodegradation of the fuels used in the column experiments, providing the foundation for the results and discussion sections.

The results section presents the data for each column experiment and the discussion section integrates the results by addressing the research questions outlined in the research objectives. The results section is divided into a description of the geochemical evolution in the columns followed by a section on the isotopic characterizations. Results on the column geochemistry combine the data sets from the saturated zone and the vadose zone.

3.3 Conceptual Model

The major biodegradation pathways can be summarized into two main categories: 1) aerobic and 2) anaerobic degradation. These degradation processes can be distinguished based on the energy yield associated with different terminal electron accepting processes (TEAPs) in bacterial respiration. The high energy yield from reducing O_2 during cellular respiration is what distinguishes aerobic degradation from anaerobic degradation which utilizes terminal electron acceptors (TEAP's) with a lower energy yield, such as NO_3^-, Mn^{4+}, Fe^{3+}, SO_4^{2-}, and CH_4 fermentation (Appelo and Postma, 2005). Biological degradation of hydrocarbons had long been considered a strictly aerobic process, dependent on molecular oxygen as a co-substrate in the metabolism of bacteria, and it was not until the late 1980's, when it was discovered that bacteria had the capacity for respiration in the absence of oxygen (Heider et al., 1998). The following

section provides a summary of the aerobic and anaerobic biodegradation pathways relevant to this experiment.

3.3.1 Aerobic Degradation

The aerobic biodegradation of the fuels, both ethanol and gasoline, requires oxygen to be the sole terminal electron acceptor. Aerobic respiration is the most efficient biodegradation pathway due to the high energy yield of oxygen during cellular respiration (Lovley and Chapelle, 1995). The aerobic degradation of ethanol is described below.

$$CH_3CH_2OH + 3O_2 \rightarrow 2HCO_3^- + H_2O + 2H^+ \qquad (1)$$

The overall aerobic degradation of ethanol is shown to consume oxygen and produce carbon dioxide and water. The ratio between O_2 consumption and CO_2 production is 1:1.

The aerobic degradation of gasoline is more complex owing to the fact gasoline is a highly complex mixture of more than 150 chemicals (ATSDR, 1995), including alkanes, cycloalkanes, alkenes and aromatic compounds. The proportions of these chemicals change with the source of crude petroleum, manufacturer, and the time of year (ATSDR, 1995). For example, a study conducted by (Air Force, 1989) analyzed a gasoline sample and revealed that gasoline contains 49 wt.% of alkanes (*n*-alkanes and branched alkanes), 30.5 wt.% aromatics, 5 wt. % cycloalkanes and 1.8 wt.% olefins, amongst various other compounds. The majority of the gasoline components were alkanes and aromatics, making up around 79.5 wt. % of the gasoline. As a result, it is logical to use a simplified alkane compound as well as the two important aromatic compounds; benzene and toluene, to describe the overall behavior of gasoline degradation. Alkanes were found to typically range from C_5-C_{13} (Air Force, 1989). For simplicity, this study will focus on the degradation of octane (C_8H_{18}), which represents a chemical formula within the range of typical alkanes found in gasoline. Aromatics like benzene and toluene are relatively stable molecules, and

degradation of these components are primarily accomplished aerobically. These compounds, in particular benzene, and relatively resistant to degradation under anaerobic conditions (Foght, 2008). The aerobic degradation of octane, as well as aromatic compounds of benzene and toluene are described below, respectively.

$$2C_8H_{18} + 25O_2 \rightarrow 16HCO_3^- + 2H_2O + 16H^+ \quad (2)$$

$$C_6H_6 + 3H_2O + 7.5O_2 \rightarrow 6HCO_3^- + 6H^+ \quad (3)$$

$$C_7H_8 + 9O_2 + 3H_2O \rightarrow 7HCO_3^- + 7H^+ \quad (4)$$

Overall, aerobic gasoline degradation reactions consume a significant amount of oxygen, and produce a substantial amount of acidity and bicarbonate.

Lastly, it is important to note that methane produced by methanogenic degradation in anaerobic regions of the column, is readily oxidized in the presence of O_2 by methanotrophs. Methane can migrate into oxic regions, because it is a relatively insoluble gas, prone to exsolution.This reaction is described below.

$$CH_4 + 2O_2 \rightarrow HCO_3^- + H^+ + H_2O \quad (5)$$

Methane oxidation occurs as methane diffuses into the vadose zone and encounters O_2. Carbon dioxide and acidity are generated in the process.

3.3.2 Anaerobic Degradation

Anaerobic degradation of hydrocarbons is more complex, may involve multiple TEAPs and includes fermentation processes during each stage of anaerobic degradation. It is important to keep in mind that depending on the availability of terminal electron acceptors, organic matter may be

mineralized completely without ever entering into methanogenesis. The stages of degradation are presented below.

3.3.2.1 Hydrolysis

This first stage is important in the breakdown of large and complex hydrocarbons into smaller constituents (Lovley and Chapelle, 1995; Ostrem and Themelis, 2004). Hydrolysis is relevant only to the breakdown of the gasoline portion of the fuel blend, as ethanol is more readily degradable. If the substrate is complex, then the hydrolysis stage is slow (Ostrem and Themelis, 2004).The products of hydrolysis include long-chained fatty acids, formate, and glucose. Below is an example of the hydrolysis of octane to glucose (Lovley and Chapelle, 1995).

$$3C_8H_{18} + 24H_2O \rightarrow 4C_6H_{12}O_6 + 27H_2 \qquad (6)$$

The products from the hydrolysis stage, which include simple sugars, long chained fatty acids (LCFA), hydrogen gas and aromatics are then utilized in the next stage of degradation.

3.3.2.2 Acidification

Immediately after the hydrolysis stage, fermenters and oxidizers further break down the organic material. Oxidizers may play an important role in completely mineralizing the organic compounds, given there is no limitation regarding the supply of terminal electron acceptors. These reactions involve the use of NO_3^-, Mn^{4+}, Fe^{3+} and SO_4^{2-} TEAPs. The bacterial consortium responsible for this oxidation step include NO_3^--, Mn- and Fe-reducers (Lovley and Phillips, 1988), as well as SO_4^{2-} reducers (Atlas and Bartha, 1998). These oxidizers depend on the availability of these terminal electron acceptors. Based on the mineral characterization of the sand and silt presented in the methods chapter, as well as the dissolved metals reported in the results section, Mn^{4+} and Fe^{3+} are important terminal electron acceptors. There are no known sources for nitrate

or sulphate in the system and therefore there is no indication that either NO_3^- or SO_4^{2-} reduction are important processes. However, the presence of Fe and Mn as electron acceptors is important because the energy yield provided by these TEAPs may result in the complete mineralization of the aromatics, LCFAs and SCFAs, provided there is no inhibition of Mn^{4+} or Fe^{3+} supply. This was shown by (Cozzarelli et al., 1994) and (Lovley and Phillips, 1987) who found that groundwater concentrations of acetate were lower where iron reduction was the major degradation pathway.

Fermenters degrade the products of hydrolysis into simple short-chained fatty acids (e.g., propionic, butyric, formic acids), alcohols (e.g., ethanol, methanol), hydrogen gas and carbon dioxide (Ostrem and Themelis, 2004; Powers et al., 2001). At the same time LCFA and aromatic oxidizers degrade the aromatics and LCFAs produced through hydrolysis. Again, this stage is only relevant to the breakdown of the gasoline portion of the fuel blend. These byproducts are variable and depend on the type of bacteria, as well as the pH and temperature (United Tech ,Inc., 2003).

The following equations represent the fermentation reactions involving the acidification of glucose to propionic acid, butyric acid and ethanol, respectively.

$$C_6H_{12}O_6 + 2H_2 \rightarrow 2CH_3CH_2COOH + 2H_2O \qquad (7)$$

$$2C_6H_{12}O_6 + 6H_2 \rightarrow 3CH_3CH_2CH_2COOH + 6H_2O \qquad (8)$$

$$C_6H_{12}O_6 + 2H_2O \rightarrow 2CH_3CH_2OH + 2HCO_3^- + 2H^+ \qquad (9)$$

VFA data collected from the saturated zone show the presence of acetic, butyric and in some cases propionic acids.

While fermenters generate ethanol, propionate and butyrate from glucose, LCFA and aromatic oxidizers break down aromatics, and long chained fatty acids. In addition, SCFA oxidizers may consume the SCFAs produced by fermenters shown in Eqns (7, 8).

Aromatic oxidizers can completely mineralize aromatic compounds such as benzene and toluene through reduction of Mn^{4+} and Fe^{3+}, producing carbon dioxide and dissolved metal cations. Examples of Fe reduction combined with benzene and toluene oxidation are shown below, respectively.

$$C_6H_6 + 30Fe(OH)_3 + 54H^+ \rightarrow 6HCO_3^- + 30Fe^{2+} + 72H_2O \quad (10)$$

$$C_7H_8 + 36Fe(OH)_3 + 65H^+ \rightarrow 36Fe^{2+} + 7HCO_3^- + 87H_2O \quad (11)$$

The aromatic oxidation reactions are shown to consume a significant amount of acidity, and produce dissolved metal concentrations. The oxidation of ethanol and SCFA through Fe and Mn reduction are demonstrated below, with the degradation of ethanol and further degradation of acetate.

$$CH_3CH_2OH + 2MnO_2 + 3H^+ \rightarrow 2Mn^{2+} + CH_3COO^- + 3H_2O \quad (12)$$

$$CH_3COO^- + 4MnO_2 + 7H^+ \rightarrow 4Mn^{2+} + 2HCO_3^- + 4H_2O \quad (13)$$

$$CH_3CH_2OH + 4Fe(OH)_3 + 7H^+ \rightarrow 4Fe^{2+} + CH_3COO^- + 11H_2O \quad (14)$$

$$CH_3COO^- + 8Fe(OH)_3 + 17H^+ \rightarrow 8Fe^{2+} + 2HCO_3^- + 20H_2O + 2H^+ \quad (15)$$

The series of oxidation reactions above reveal the steps involved in ethanol and acetate mineralization. These ethanol and SCFA mineralization reactions consume acidity and produce bicarbonate, and result in elevated dissolved Mn^{2+} and Fe^{2+} concentrations.

The reactions above are typically related to the reduction of amorphous minerals. The mineralogical data provided by the XRD analysis of the soil material is limited to crystalline minerals, and therefore amorphous minerals were not detected. However, it is probable that these minerals occur in the sediments and contribute to acetate formation and/or acetate mineralization, as well as the accumulation of $Fe^{2+}$and Mn^{2+}. However, elevated dissolved Mn and Fe concentrations may also originate from the dissolution of an ankerite-dolomite mineral phase, which was identified in the XRD analysis (Table A-5). The dissolution reaction of ankerite is provided below:

$$Ca(Fe^{2+}, Mn, Mg)(CO_3)_2 + 2H^+ \leftrightarrow Ca^{2+} + (Fe, Mn, Mg)^{2+} + 2HCO_3^- \qquad (16)$$

If Mn^{4+} and Fe^{3+} become depleted, the redox conditions develop into a more reducing environment, and degradation of benzene and toluene, LCFAs, SCFAs and ethanol proceeds by acetogenesis through proton-reducing acetogens.

3.3.2.3 Acetogenesis

There are multiple pathways that are involved in the production of acetate. The main reactants in acetogenesis are ethanol and VFAs. The bacterial consortium responsible for acetogenesis include Mn and Fe reducers (Lovley and Phillips, 1988), SO_4^{2-} reducers, as well as proton reducing acetogens, which oxidize butyrate, propionate, ethanol and other compounds to acetate, H_2 and CO_2 (Powers et al., 2001). Another group of bacteria, called homacetogens, can generate acetate by consuming H_2 and CO_2 (Madigan et al., 1997). Acetogenesis through Mn and Fe reduction was

discussed in the previous section and is described by equations 12 and 14, whereby ethanol was oxidized to acetate. This reaction will likely proceed to complete mineralization of acetate due to the presence of Mn^{4+} and Fe^{3+} (as shown in equations 13 and 15). Therefore, this section will focus on the acetogenic processes leading to methanogenesis. In the absence of Mn and Fe reduction, the two main pathways for acetogenesis include oxidation by proton-reducing acetogens and homoacetogens.

The proton-reducing acetogens utilize water derived protons which are generally in abundance as H_2O or H^+ ions are consumed to produce H_2. These organisms degrade aromatics, such as benzene and toluene, as well as ethanol, LCFAs and SCFAs (Lovley and Chapelle, 1995). Below are the acetogenic reactions involving the degradation of butyric acid, propionic acid and ethanol by proton-reducing acetogens.

$$CH_3CH_2CH_2COO^- + 2H_2O \rightarrow 2CH_3COO^- + 2H_2 + H^+ \qquad (17)$$

$$CH_3CH_2COO^- + 3H_2O \rightarrow CH_3COO^- + HCO_3^- + 3H_2 + H^+ \qquad (18)$$

$$CH_3CH_2OH + H_2O \rightarrow 2H_2 + CH_3COO^- + H^+ \qquad (19)$$

The reactions above are shown to degrade SCFAs and ethanol, to acetate and H_2, producing acidity in the process. Under standard conditions, these reactions are not thermodynamically feasible due to excess H_2 (Conrad et al., 1985; Wolin and Miller, 1982; Wu and Hickey, 1996). A crucial link in the anaerobic food chain is a process called interspecies hydrogen transfer (IHT), which involves the consumption of H_2 by hydrogen scavenging bacteria (Ferry, 2011; Powers et al., 2001). In the literature, this process is generally described through a symbiotic relationship between acetogens and hydrogenotrophic methanogens. However, the conversion of bicarbonate

and H_2 to acetate by homoacetogens provides similar benefits. Depending on the environmental conditions the reaction below occurs.

$$H^+ + 2HCO_3^- + 4H_2 \rightarrow CH_3COO^- + 4H_2O \qquad (20)$$

It is important to note that the factors affecting this reaction are not well understood, and the importance of this reaction in IHT is not certain (Wolfe, 1983). Due to the abundance of water-derived protons, it is expected that these reactions can take place uninhibited.

3.3.2.4 Methanogenesis

Methane is produced through two primary methanogenic pathways; acetate fermentation and carbon dioxide reduction (Whiticar, 1999; Whiticar et al., 1986). Acetate fermentation accounts for approximately two thirds of the methane production, while carbon dioxide reduction accounts for one third (Whiticar et al., 1986). The acetate fermentation pathway requires acetoclastic methanogens to convert acetate and hydrogen into methane and carbon dioxide, as shown below.

$$CH_3COO^- + H_2O \rightarrow CH_4 + HCO_3^- \qquad (21)$$

The reaction consumes water and acetate to produce methane and bicarbonate in a 1:1 ratio.

The CO_2 reduction pathway is utilized by hydrogenotrophic bacteria. This consortium reduces dissolved CO_2, oxidizes H_2 and produces CH_4. As previously mentioned, this step is critical in limiting H_2 concentrations which are generated through acetogenesis. The decline in the partial pressure of H_2 through IHT allows for the acetogenesis reactions (Eqn. 17, 18, and 19) to become exergonic (releasing energy) and thermodynamically feasible (Conrad et al., 1985). The hydrogenotrophic reaction is presented below.

$$H^+ + HCO_3^- + 4H_2 \rightarrow CH_4 + 3H_2O \qquad (22)$$

This reaction consumes bicarbonate, acidity, and hydrogen gas to produce methane and water.

The reactions presented here, characterize the biodegradation pathways, which dictate the fate of biofuels in the subsurface and will provide the basis for the presentation and discussion of the results.

3.4 Results

The results presented in this chapter are divided into two main sections:

1. Geochemical evolution in soil gas and pore water
2. Isotope geochemistry

Spatial locations indicated on the figures relate to elevation in the column, i.e. 0 cm refers to the base of the column, 200 cm refers to the top of the column.

3.4.1 Geochemical Evolution in Soil Gas and Pore Water

The results for the geochemical evolution and pressure distribution in the individual columns is presented in this section. The data presented here provides the majority of the geochemical information in both the vadose zone and saturated zone for each column experiment. The isotopic results are presented in the following section. The saturated zone geochemistry results focus on the analysis of volatile fatty acids (VFAs), dissolved ethanol (EtOH) and dissolved metals. Both the VFAs and dissolved metals are important identifiers of anaerobic degradation, redox conditions and provide a window into microbial conditions (Bekins et al., 2001; Chen et al., 2008; Powers et al., 2001). Dissolved ethanol reveals the infiltration of ethanol and, combined with VFA data, provides a greater comprehension of microbial conditions.

The measurement of soil gas concentrations of O_2, CO_2, CH_4, Ar, N_2, benzene and toluene, as well as surficial soil flux measurements of CO_2 and CH_4, are important for the characterization of the vadose zone geochemical evolution. It is important to note that observed gas concentrations show in almost every case that the O_2 measured with the GC is higher than the O_2 measured with the sensors, and that CO_2 measured with the GC is lower than concentrations determined by the CO_2 sensors. This observation indicates contamination by atmospheric air occurred at some point between the collection of the samples and analysis with the GC. However, the samples are generally affected in a systematic fashion. Therefore, the GC measurements are used to corroborate trends, but are considered less useful for quantifying absolute gas concentrations. Gas phase pressure measurements were performed in the columns; however, due to the prevalence of leaks, these measurements were mostly utilized to locate and assess the impact of the leaks on the experiments, rather than to assess the potential for pressure-driven advection, as was originally intended. In addition, Ar and N_2 data was affected by the leaks which caused the development of artificial pressure gradients which overprinted naturally occurring pressure gradients. Therefore, advection interpretations based on Ar and N_2 concentrations could not be performed in all columns.

The vadose zone data set provides a one-dimensional vertical soil gas profile of the aforementioned analytes. By developing a vertical profile of soil gas from the spill zone to the soil surface, attenuation processes and the risk of soil vapor intrusion (SVI) of aromatics can be assessed for the different scenarios. Analysis of soil gas for the presence of benzene and toluene (BT) provides insight into the fate of BT in the subsurface in the presence of different fuels. The vertical soil gas profile of O_2 presented in this study reveals the redox conditions, allowing to differentiate between aerobically dominated biodegradation regions and anaerobically dominated

biodegradation regions. As the final product of biodegradation, CO_2 plays an important role in gauging the biodegradation rates of each experimental scenario. By this virtue, the measurements of soil gas CO_2 and surficial CO_2 fluxes (Sihota and Mayer, 2012) are essential metrics in the determination of the rate of biodegradation in each column. Non-reactive gases Ar and N_2 were used to detect advection based on the principles described in Amos et al., (2005).Soil gas measurements of CH_4 were also attempted along the vertical profile of the column; however, the concentrations were generally below the detection limit of the gas chromatograph. In some cases, atmospheric contamination affected redox conditions in the columns and methane concentrations in the soil gas. Soil gas measurements and soil surface CH_4 flux measurements provided the basis for discussing the potential for CH_4 SVI risk, whenever possible.

Surficial soil effluxes of CO_2 and CH_4 represent degraded fuel leaving the columns as completely mineralized CO_2 and CH_4. Using these soil fluxes, estimations of the mass loss in %, of total fuel degraded over time were made. The mass loss is calculated by estimating the amount of total carbon leaving the system through soil surface fluxes using the surface CO_2 and CH_4 flux measurements, and comparing them to the estimated total mass of C injected as fuel. It is important to note that this calculation is approximate as fuel may also leave the columns as vapors (e.g. as benzene or toluene). In addition, carbon contained in biodegradation intermediates, as well as carbon sequestered to biomass, or released due to mineral dissolution, are all processes which are not accounted for in the estimation of mass loss. Therefore, the estimation provides a conservative baseline estimate for the mass loss due to degradation of the biofuel.

3.4.1.1 E10 Sand Column – “E10-S “

The data for the geochemical characterization of the E10-S experiment are shown in Figure 3-1. It is important to note that much of the vadose zone data for this column was affected by

unintentional venting due to leak issues. Venting had an effect on the quality of data, as it affects hydrocarbon volatilization, biodegradation processes, soil gas concentrations of O_2, CO_2 and BT, as well as the surficial fluxes of CO_2 and CH_4. Vertical soil gas measurements of O_2 and CO_2 reveal the presence of a leak at 60 cm, where the concentrations of O_2 and CO_2 shift towards atmospheric levels between weeks 11 and 21 (Figure 3-9F, G). Pressure measurements corroborate the presence of a modest leak near the base of the column through the observation of a small pressure gradient generated from a slightly higher pressure at the base between weeks 11 and 21 (Figure 3-13D). An increase in the pressure gradient and a positive internal pressure shift (closer to the external pressure) indicates that the leak worsened between weeks 40 and 61 (Figure 3-13D), which is reflected in the nearly atmospheric O_2 and CO_2 concentrations during this time period (Figure 3-9F, G).The affected periods are highlighted in red in Figure 3-1.

The O_2 and CO_2 soil gas profiles (Figure 3-1B and 1C) show a significant degree of variation during the first 9 weeks of column operation. This is a result of operational changes and various leaks requiring maintenance. The major spike in soil gas around week 4 could be traced to column maintenance, whereby the gasoline injection port located at 50 cm was temporarily opened and then sealed with epoxy. The momentary event resulted in increased air ingress, leading to a short-term change in the column soil gas composition.

Generally, the O_2 gas profile (Figure 3-1B) shows considerable decreases in soil O_2 concentrations starting at week 9 and lasting until approximately week 25. The vertical O_2 profile shows that during this time, oxygen was completely depleted from the column at 100cm and 140 cm while the uppermost O_2 sensor at 160cm (just 20 cm from the soil surface) reported only 10% O_2 (v/v). Vertical soil O_2 measurements generally corroborate this trend; however, the data reveals the presence of a modest leak at 60 cm, resulting an increase in soil O_2 at the base. The CO_2 soil

gas profile (Figure 3-1C) shows a similar but opposite trend, whereby significant CO_2 concentrations developed during periods of O_2 consumption. At both 100 cm and 140 cm, CO_2 concentrations reached ~10 % v/v (note that sensor range was limited to 10% CO_2 v/v and that concentrations may have been higher), and a decline in CO_2 concentrations at 60 cm due to accidental air ingress (Figure 3-9G). During the period of significant O_2 decline and CO_2 increase, the soil gas flux measurements reported CO_2 fluxes of substantial magnitude across the surface (Figure 3-1A**)**. Peak soil CO_2 fluxes were measured around 35-40 µmol m^{-2} s^{-1}. Furthermore, a soil surface flux of CH_4 was detected, also peaking during this time period (Figure 3-1A**)**. These results are indicative of rapid and mostly aerobic degradation of the biofuel as described by Eqns. 1, 2, 3 and 4. Based on concentration data alone, it remains uncertain which component of fuel (ethanol or gasoline) was degrading the fastest. However, it is clear from the surficial methane flux that methanogenesis occurred a few weeks after the significant decline in O_2. During the period of elevated methane fluxes, soil methane concentrations showed the presence of methane throughout the column (week 21), with concentrations as high as ~0.1% v/v at 60 cm (Figure 3-9H). The soil methane data collected during this period seems to suggest a diffusion dominated and uninhibited methane flux based on the linear slope of the methane concentration profile. This seems logical due to the substantial depletion of O_2 throughout the column, which would limit methanotrophic activity. Based on these data, aerobic degradation was accompanied by anaerobic degradation in some regions of the column. Around 25 weeks post-spill of the 2L of E10, the soil gas O_2 and CO_2 concentrations started to return to atmospheric levels, and soil CO_2 and CH_4 fluxes declined. This observation was made despite the fact that around week 25 only approximately 33 % of the total fuel was degraded in the E10-S column (Figure 3-14). The flux data suggests that the rate of degradation begins to slow after week 30, coinciding with the increase in O_2 and decrease in CO_2

in the soil column. However, observed changes in gas effluxes were not as dramatic as the observed changes for the soil gas concentrations. More in-depth analysis of the data suggests that a leak affected the data quality and results of the geochemical evolution in the vadose zone between weeks 25 and 72. After week 72, the venting system was modified to avoid the development of reduced pressure in the headspace, resulting in some decrease of O_2 concentrations and increases in CO_2 concentrations. However, concentrations did not return to the levels observed earlier during the experiment (weeks 9-25), suggesting that much of the hydrocarbons had been degraded or vented by week 72.

In addition, the headspace pump failed at week 53 causing a short-term O_2 decrease, and slight CO_2 increase. The sudden drop in O_2 concentrations around week 48 is due to sensor-failure. However, these observations are of secondary importance, because these events occurred after week 25, only affecting data that was already compromised by leaks in the column.

The highest benzene concentrations in the vadose zone were found at 60 cm, staying below 350 μg L^{-1} (100 ppm) (Figure 3-15D and Figure 3-1D). Toluene concentrations were much higher than benzene concentrations, with the highest detected concentrations exceeding 9500 μg L^{-1} (2,500 ppm) just above the spill at 60 cm (Figure 3-16D and Figure 3-1D). The vertical cross section of benzene (Figure 3-15D) and toluene (Figure 3-16D) show that, in general, there is a substantial decrease in benzene and toluene concentrations between 60 cm and 100 cm, while the decline in concentration from 100cm to 160 cm is more subtle. This suggests that microbial degradation of benzene and toluene is primarily occurring in the first 50cm above the spill zone.

The results show that there is substantially more toluene present in soil gas than benzene (Figure 3-16D and Figure 3-15D, respectively). The initial analysis of benzene and toluene in the gasoline showed that there was considerably more toluene than benzene in the gasoline sample.

The ratio between benzene and toluene in the gasoline is approximately 1:4.6, respectively (Table 2-6 gas data). Therefore, the results of higher toluene are likely affected by the differences in initial benzene and toluene concentrations of the gasoline. However, the raw data shown in Table E-1 illustrate that the ratio of toluene to benzene in the soil gas is much higher than the initial baseline ratio in the gasoline. In general, benzene and toluene concentrations during the first two weeks were lower, while concentrations increased later during the experiment. These initial lower concentrations during weeks 2, 5 and 8 occurred when oxygen was more abundant in comparison to weeks 16, 25, and 35. This data suggests more limited benzene and toluene attenuation during periods of substantial O_2 depletion.

In the saturated zone, Figure 3-1F shows the presence of VFAs, indicating that anaerobic metabolic pathways were active in the degradation process (Powers et al., 2001); in this case the degradation of the E10 fuel. Acetic acid remained below the detection limit for the first 19 weeks of the experiment. Concentrations of acetic acid were minor, typically ranging from 5-10ppm, with concentrations reaching a peak of 14 ppm 47 weeks post-spill. Observed increases of acetic acid coincided with the appearance of a soil methane flux at the surface, suggesting a link between acetogenesis and methanogenesis. Butyric acid was detected only slightly above detection limits (~1 ppm) nearly four weeks post-spill. Butyric acid concentrations hovered slightly above the detection limit for the remainder of the experiment. The overall trend of VFAs in the E10-S column showed a slight increase in concentration, followed by a decline in concentrations.

Dissolved Mn^{2+} and Fe^{2+} observed within the saturated zone of the E10-S column were found to be relatively limited in concentration. In contrast, dissolved Ca was much more significant. Concentrations of Mn and Fe increased consistently throughout the duration of the experiment, and reached a peak of 19 and 18 ppm at week 72, respectively (Figure 3-1E). Ca concentrations;

however, were more significant with concentrations reaching 356ppm by the 72nd sampling week. The presence of significant concentrations of Ca is likely a result of ankerite dissolution, shown in Eq. (16). Increases in dissolved Fe and Mn concentrations in groundwater may also be due to the dissolution of ankerite or are due to the reductive dissolution of Fe and Mn oxides. It is also possible that the sediments contain calcite below the detection limit of XRD analysis, contributing to elevated Ca concentrations:

$$CaCO_3 + 2H^+ \rightarrow Ca^{2+} + CO_2 + H_2O \qquad (23)$$

Both the dissolution of ankerite and calcite can act to buffer the decreases in pH resulting from aerobic respiration (Eqns. 1, 2, 3, and 4), as well as acetogenesis (Eqns.17, 18, and 19).

Mn was detected in the first sampling round at week 7; however, Fe was detected approximately 8 weeks later, and only slightly above the detection limit of ~1 ppm. The temporally discordant appearance of Mn and Fe further suggests that ankerite is not the sole source for these metals and that reductive dissolution reactions involving Mn- and Fe-oxides leading to anaerobic degradation of the fuel were also active (e.g. Eqns. 14 and 12). Initial Mn concentrations were higher than Fe concentrations; however, there was a slightly steeper increase in Fe concentrations throughout the duration of the experiment, resulting in roughly equal concentrations of both Fe and Mn for the final water sample.

Ethanol was largely undetectable in the saturated zone and had only been detected on one occasion with a concentration of 1.9 ppm at week 47 of the experiment (Figure 3-1F). The appearance of dissolved ethanol around week 48 suggests that ethanol may persist in the groundwater for prolonged periods of time, even for limited ethanol contents in the fuel.

In summary, the data for this column suggests that the majority of the E10 biodegradation was aerobic in nature. However, degradation and volatilization was likely enhanced due to unintentional venting of the column after week 25 of the experiment. Degradation of benzene and toluene in the vadose zone of the column is likely responsible for substantially reducing surficial benzene and toluene concentrations and emissions. In addition, the dissolved metals and VFA data, combined with the surficial CH_4 flux data prove that anaerobic oxidation and methanogenesis are occurring concurrently with aerobic oxidation on the scale of the full column.

3.4.1.2 E85 Sand Column – "E85-S"

The results for the geochemical evolution in the E85 Sand Column are depicted in Figure 3-2. It is important to note, that the sudden change in soil gas compositions around week 55 are likely due to a leak, that continued to affect geochemical processes in the vadose zone until week 71, when the headspace venting system was modified. Vertical pressure measurements at weeks 11, 21, 40 and 61 do not show the presence of a pressure gradient, indicating diffusion dominated transport. In addition, these results also demonstrate that this column was not affected by leaks during this time period (Figure 3-13H). Vertical soil gas measurements during the same weeks also indicate that there were no leaks present (Figure 3-9A,B), with the exception of the week 40 60 cm sample which shows a small CO_2 decline at the base (Figure 3-9B). The time period affected by accidental air ingress is highlighted in red (Figure 3-2). However, for this column, much of the data was unaffected by the headspace pumping issue outlined in previous sections.

Vadose zone soil gas concentrations of O_2 (Figure 3-2B) and CO_2 (Figure 3-2C) illustrate that the O_2 concentrations and CO_2 throughout the length of the column remain near atmospheric levels until roughly 27 weeks post-spill. Somewhat surprisingly, the lowest working O_2 sensor at 60 cm (located 10cm above the spill zone), as well as the lowest working CO_2 sensors at 40cm (located

directly within the spill zone), did not record significant changes in the soil gas composition after the spill until approximately week 27. By week 27; however, there is a modest decline in soil O_2 concentrations and an equal, but opposite, increase in soil CO_2 concentrations at depth. Vertical concentrations of O_2 and CO_2 illustrate this slight increase in biodegradation activity observed during weeks 21, 40 and 61 (Figure 3-9A, B). This trend is interrupted by the leak event commencing during week 55. Upon resolution of the problem, the trend of increasing CO_2 and decreasing O_2 continued, with concentrations returning to levels similar to those prior to the leak event. By week 73 soil O_2 at 60 cm had dropped to roughly 10%, and CO_2 at 40 cm had increased to approximately 8%. Near the soil surface, there was virtually no change in the soil gas O_2 and CO_2 concentrations (i.e. 160cm). Soil surficial CO_2 fluxes are relatively low, reflecting the lack of CO_2 in the subsurface. Maximum CO_2 fluxes reached approximately 5 µmol m^{-2} s^{-1} (Figure 3-2A). There was a notable spike in soil surface CH_4 flux to approximately 0.5 µmol m^{-2} s^{-1} between week 27 and week 36, which subsequently disappeared. Soil methane concentrations sampled during week 40 were able to capture a vertical profile of the methane during the tail end of the methane flux event (Figure 3-9C). This vertical profile suggest that methane oxidation is actively occurring between 100 cm and 120 cm. Soil gas concentrations of O_2 and CO_2 combined with the soil surficial flux data reveals that in general there was not much consumption of oxygen and production of carbon dioxide was limited. This observation suggests that degradation of the E85 fuel was inhibited, possibly due to toxicity.

Soil gas toluene concentrations were significantly greater than benzene concentrations (Figure 3-2D, Figure 3-15H, Figure 3-16H). This is likely due to the composition of the initial gasoline sample, containing more toluene than benzene by approximately a factor of 4.5. Maximum concentrations for benzene occurred at 60 cm during week 12 and was less than 800 µg/L (250

ppm). Maximum toluene concentrations also occurred at 60 cm and was approximately 2,010 μg L^{-1} (525 ppm). With the exception of the week 12 sampling event, benzene concentrations throughout the column were typically <40 μg L^{-1} (12 ppm). However, toluene appears to persist at the 100 cm level (Figure 3-15E). As well, there seems to be a pronounced decline in toluene concentrations between 100 cm and 160cm (Figure 3-16E). The data suggests that microbial attenuation is occurring within the top 100 cm of the column, but may be inhibited below 100cm. Benzene and toluene concentration near the top of the column substantially decreased to <12 μg L^{-1}(3.7 ppm), <115 μg L^{-1}(30 ppm), respectively. The last two sampling rounds revealed further diminished BT concentrations in the vadose zone.

In the saturated zone of the E85-S column, volatile fatty acids were detected at significant concentrations (Figure 3-2F). Acetic acid was detected first during week 10, followed by butyric acid 3 weeks later. Less significant concentrations of propionic acids were detected (<6ppm). The initial behavior of acetic acid concentrations showed a sharp increase from below detection in the week 7 water samples, to 450 ppm at week 11, and then declined to 16 ppm by week 15. After this sharp decline, acetic acid concentrations slowly began to rebound at a rate of ~45 ppm/month. The final water sample collected during week 71 contained ~ 490 ppm of acetic acid. Substantial and sustained butyric acid concentrations were observed starting during week 11, with the highest concentrations observed during weeks 13-47. At early time, butyric acid concentrations rose sharply reaching a maximum concentration of ~ 920 ppm after 27 weeks, followed by a steep decline to 337 ppm by week 39. Subsequently, the butyric acid concentrations levelled off to between 170 and 400 ppm. The appearance and increase in butyric acid concentrations was correlated with the observed decline in acetic acid concentrations (Figure 3-2F). During acetogenesis, acetate is formed through multiple pathways, one of which is through the

transformation of butyric acid (butyrate) to acetic acid (acetate) as described by (Ferry, 2011) (Eqn.17). However, as pointed out by (Freitas et al., 2010; Kim et al., 1994), under severe environmental stress, such as severe ethanol loadings, the acetogenic reactions are reversible, whereby butyrate and propionate may be produced in a feedback loop until the stressed conditions recede (Smith and McCarty, 1989). In this case, due to the high ethanol content of the E85 blend (85% ethanol), butyrate is likely produced through the reverse reaction defined by Eqn.17, which is shown below.

$$2CH_3COO^- + H^+ + 2H_2 \leftrightarrow CH_3CH_2CH_2COO^- + 2H_2O \qquad (24)$$

The production of butyrate occurs during stressed conditions; however, after week 27 the butyric acid concentrations decline, indicating that butyric acid degradation gained importance over time. The data only show a slight increase in acetate, and does not appear to represent the transition between butyric and acetic acid at first glance. However, shortly after butyric acid concentrations began to decline, a significant peak of methane flux was observed, likely explaining the lack of acetic acid build-up. Observed methane effluxes are likely a result of the conversion of the acetate, produced by the degradation of butyrate, to CH_4 (shown below).

$$CH_3COO^- + H_2O \rightarrow CH_4 + HCO_3^- \qquad (21)$$

The data suggests that the active methanogenesis pathway is through acetate fermentation (as described above). Due to conversion of butyrate to acetate, the supply of acetate was high and promoted the rapid conversion of acetate to methane. For acetate concentrations to remain low, methanogenesis must have occurred at similar rates than the conversion of butyrate to acetate.

Dissolved metal concentrations detected within the saturated zone of the E85-S column show elevated concentrations. An increase in Ca, Fe and Mn concentrations was observed through the

majority of the study, lasting from week 7 through week 47, followed by a slight decline in all dissolved metal concentrations measured in the final groundwater samples collected in week 71 (Figure 3-2E). Ca concentrations were much higher than Fe and Mn concentrations during each period. Elevated Ca is likely due to the dissolution of ankerite (Eqn. 16) and/or calcite (Eqn. 23), which buffer the decrease in pH brought on by acetogenesis and other acid generating reactions. Aqueous Mn was detected during the first sampling event 7 weeks post-spill; however, only slightly above detection at approximately 1 ppm. Dissolved Fe was detected in samples collected during the second sampling event 8 weeks later. In general, aqueous Fe in the saturated zone was greater than Mn throughout the experiment with the E85 fuel. Peak Fe and Mn concentrations reached 205 ppm and 125 ppm, respectively, whereas Ca concentrations peaked at 860 ppm. It is important to note that initially both Mn and Fe concentrations were similar, 46 ppm and 58 ppm, respectively. Overall, the results indicate that reductive dissolution of Mn-oxides occurs first, but that reductive dissolution of Fe-oxides gains importance over time.

Ethanol was present in the earliest water samples taken at week 14, at a concentration of 100 ppm (Figure 3-2F). The concentration of dissolved ethanol in the saturated zone hovered between 50 ppm and 140 ppm until 27 weeks post-spill when noticeably higher concentrations of ethanol were detected in the groundwater. The analysis of the week 27 water samples showed the groundwater had an ethanol concentration of ~775 ppm. Further analysis of succeeding water samples showed the ethanol concentrations were increasing at a significant rate. Week 41 groundwater samples showed ethanol concentrations had increased to ~14,000 ppm. Peak ethanol concentrations were measured in the final groundwater samples. At week 69 and week 75, the ethanol concentration had reached 45,000 ppm and 46,570 ppm, respectively. The delay of the

appearance of ethanol at the saturated zone basal port is due to mass transfer limitations, but indicates persistence of EtOH beyond the duration of the experiment.

In summary, the impact on vadose zone oxygen and carbon dioxide concentrations above the spill was limited, suggesting that biodegradation was relatively slow. (McDowell and Powers, 2003) conducted a test to compare the infiltration of gasoline and gasoline mixed with 10% ethanol. They found that the ethanol in the E1O fuel preferred to partition into the vadose zone, while the gasoline continued to infiltrate. It is possible that the large ethanol fraction of the E85 fuel was held in the capillary region, resulting in an inhibition of aerobic degradation owing to ethanol microbial toxicity localized to the upper portion of the spill zone. Benzene soil gas concentrations are low in comparison to toluene. Vertical attenuation of toluene appears to occur in the region spanning 100 cm to 160 cm, whereas toluene degradation in the lower half of the column was limited. The attenuation of both benzene and toluene is significant, decreasing benzene and toluene soil gas concentrations near the surface significantly. Beneath the spill zone, the groundwater concentrations for dissolved metals and VFAs were quite substantial, indicative of anaerobic degradation processes beneath the water table. The results show substantial butyric acid build-up mid-way through the experiment with a subsequent decline, likely due to the development of microbially stressed conditions. In addition, a substantial increase in dissolved ethanol was observed in the later stages of the experiment. This delay is likely a result of the hydrophilic nature of ethanol (McDowell and Powers, 2003), which causes the ethanol to almost completely partition into the aqueous phase of the capillary region, followed by slow diffusive transport of ethanol into the saturated zone. Overall, mass balance calculations suggest that biodegradation of the E85 fuel in the sand column was limited. The cumulative mass degradation

of the E85 biofuel spill was estimated to have only been ~12 % near the end of the experiment at week 70 (Figure 3-14).

3.4.1.3 Gasoline Sand Column – "Gas-S"

The results for the geochemical evolution in the Gasoline Sand Column are depicted in Figure 3-3. Large fluctuations in soil O_2 and CO_2 during the first week occur largely due to a leak and maintenance following the gasoline injection. The leak was fixed and gasoline was re-injected. This resulted in erratic fluctuations of the initial soil gas composition. In addition, another leak occurred around week 60 leading to the ingress of lab air and inadvertent venting of the column, likely a result of improper closure of a vadose zone sampling port. This event is also observed in the column pressure data, which shows a substantial pressure gradient at week 61 (Figure 3-13A). As a result, the flushing of air through the column lasting until week 72, when the headspace venting system was modified. Vertical soil gas measurements show a dramatic shift towards atmospheric concentrations during this time (week 61) (Figure 3-10A, B).Questionable data collected during the gasoline leak/re-injection and the air leak are highlighted in red (Figure 3-3). However, much of the data was unaffected by issues related to headspace venting.

Vadose zone soil gas data illustrates an immediate response to the gasoline injection (Figure 3-3A, B). Column oxygen levels dropped very quickly, with oxygen being completely consumed at and below 100 cm, halfway up the column (Figure 3-3A). Carbon dioxide generated from aerobic degradation was significant, and mirrors the oxygen profile (Figure 3-3B) (Figure 3-10A,B). Rapid consumption of oxygen indicates that the aerobic respiration leads to the degradation of the injected gasoline at significant rates. Aerobic respiration was sustained throughout the entirety of the experiment (with the exception of the leak event), with only a slight decrease in the O_2 consumption and CO_2 production over time. Only minor differences in the soil

gas composition can be observed before and after the leak event, which lasted from week 60 to week 71. The data suggests that after the flushing event, the system rebounded and the rate of aerobic degradation remained similar to conditions present prior to the leak. The surficial CO_2 effluxes show a steady flux of around 8-12 μmol m^{-2} s^{-1} throughout the experiment, accompanied by a small CH_4 flux <0.025 μmol m^{-2} s^{-1}. This small CH_4 flux indicates that anaerobic degradation is occurring in the column; however, the vertical profiles show methane detected at 60 cm is very low (<0.025% v/v), and often below the detection limit, suggesting limited methanogenesis (Figure 3-10C).

Analysis of benzene and toluene revealed the presence of elevated benzene and toluene concentrations in the vadose zone, just above the spill zone (60 cm) (Figure 3-15A and Figure 3-16A). Toluene concentrations were much higher than benzene as a result of the higher ratio of toluene to benzene in the initial gasoline sample. Initial benzene and toluene concentrations were limited; however, after week 18, the benzene and toluene concentrations at the base of the column increased substantially reaching a maximum concentration of ~700 μg L^{-1} (220 ppm) and ~ 7800 μg L^{-1}(2,040 ppm), respectively. The fuel injected was pure gasoline, explaining the high concentrations of the aromatics. As a result, the Gas-S column showed higher basal benzene and toluene concentrations in comparison to the other columns with ethanol-blended fuel releases. Lastly, despite the significant decrease of O_2 in soil gas (Figure 3-3B), vertical benzene and toluene migration was substantially attenuated between 60 cm and 100 cm. Maximum concentrations of benzene and toluene at 160 cm was 11 μg/L and 143 μg/L, respectively.

VFAs analyzed in the groundwater revealed that throughout the experiment VFA concentrations remained low, generally <15 ppm (Figure 3-3F). The highest acetic acid concentrations were observed in the last three samples taken at week 47, week 65 and week 69, all

of which contained approximately 13 ppm acetic acid. During this time, the highest CH_4 fluxes were measured, likely a result of the degradation of acetate to methane (Eqn. 21). Butyric acid stayed consistently below 5 ppm throughout the experiment, and propionic acid was not detected in the groundwater.

Dissolved metal analysis of the groundwater samples indicated a slight increase in concentrations over time; however, concentrations of Fe and Mn remained below 25 ppm, while Ca concentrations reached a maximum of 335 ppm (Figure 3-3E). Dissolved Mn appeared 21 weeks before Fe; however, both cations were comparable in concentration during subsequent sampling events.

In conclusion, the data suggests that anaerobic degradation is limited in the Gas-S column, considering that aqueous Fe, Mn and VFA concentrations remained low throughout the experiment. Substantial aerobic degradation was observed in the vadose zone leading to consumption of O_2 and elevated CO_2 effluxes, resulting in approximately 28% of the fuel being degraded during the 72 week experiment (Figure 3-14). In addition, benzene and toluene declined substantially between 60cm and 100cm resulting in significantly reduced concentrations near the soil surface.

3.4.1.4 E20 Sand Column – "E20-S"

The results of the geochemical evolution in the E20 Sand Column are depicted in Figure 3-4. Vadose zone soil gas composition prior and after modification of the headspace venting system are comparable. This indicates that the column was largely unaffected by unintentional air ingress caused by reduced pressures in the headspace. This is confirmed by the vertical pressure gradients, which were effectively zero through weeks 11, 21 and 40; however, the week 61 data shows an internal column pressure shift towards the external column pressures indicating the high likelihood

of a leak during the later stages of the experiment (Figure 3-13B). Near the end of the experiment, O_2 and CO_2 sensors malfunctioned linked to a disruption in the LabJack data logger. Time periods with questionable data are highlighted in red (Figure 3-4).

An initial decline of O_2 in soil gas occurred immediately after the spill most clearly seen at the lowest monitoring location; however, a corresponding increase in CO_2 was not observed. The O_2 decline may be associated with oxygen displacement due to volatilization immediately after the spill and/or development of nearly saturated conditions around the sensor, temporarily limiting O_2 ingress (Figure 3-4B). However, in general the oxygen and carbon dioxide composition in the vadose zone largely remained unaffected by the spill for the entire duration of the 1.5 year experiment (Figure 3-4B and Figure 3-4C), and can also be seen in the vertical O_2 and CO_2 plots (Figure 3-12A and Figure 3-12B), respectively. The CO_2 flux measured at the soil surface was very small (Figure 3-4A) and typically ranged from 0.07 to 2.3 µmol m^{-2} s^{-1}. The pre-spill baseline CO_2 flux measurement was approximately 0.1 µmol m^{-2} s^{-1}, which is a result of a small amount of biodegradation of natural organic matter present in the soil. Vertical soil gas measurements did not show the presence of methane at depth throughout in the week 11, 21, 40 and 61 samples; however, during the later stages of degradation, a flux of CH_4 was measured between week 63 and 71. This indicates that methanogenesis produced a measurable surficial methane flux during the late stages of the experiment.

Soil concentrations of benzene and toluene were initially relatively low; however, around week 25 toluene concentrations increased substantially to concentrations of 7,313 (1,915 ppm) and 6,656 µg L^{-1} (1,740 ppm) at 60 cm and 100 cm (Figure 3-4D, Figure 3-16B). The final two samples (weeks 25 and 35) show that the benzene and toluene concentrations were declined to concentrations below 1000 µg L^{-1}(300 and 260 ppm, respectively). The vertical distribution of benzene and toluene in the

vadose zone showed diminishing concentrations with proximity to the soil surface. This decline in benzene concentrations; however, may not be due to microbial degradation, but may be related to diffusive transfer towards the surface, supported by the predominately linear concentration gradients (Figure 3-15B). There is evidence of attenuation of toluene between 100 cm and 160 cm, as there is a significant increase in the concentration gradient in the upper half of the column (Figure 3-16B). Toluene degradation is described by the aerobic degradation reaction represented by Eqn. 4. Lastly, consistent with other experiments, toluene concentrations were much higher than benzene concentrations, owing to the higher proportion of toluene in the original gasoline.

In the saturated zone, acetic acid and butyric acid were detected 10 weeks post-spill. Groundwater acetic and butyric acid concentrations rose sharply and by week 21 concentrations had reached a peak of 580 and 625 ppm, respectively (Figure 3-4F). A slight decline of butyric and acetic acid was observed in the week 39 samples. Subsequent groundwater samples showed an increase and stabilization of acetic acid concentrations, whereas butyric acid concentrations stabilized between 300-400 ppm. Less significant amounts of propionic acid were detected (<30 ppm) with no observable trend. The significant concentrations of acetic and butyric acid indicates anaerobic activity below the water table (Powers et al., 2001). Once again, the substantial levels of butyric acid is likely caused by toxicity issues, as described by (Freitas et al., 2010).

Aqueous Fe^{2+} and Mn^{2+} were identified in the groundwater approximately 15 weeks after the fuel spill (Figure 3-4E). Aqueous Fe^{2+} concentrations were observed to be higher than Mn^{2+} throughout the ~1.5 year experiment. Dissolved Fe concentrations reached peak values of 125 ppm in the 37^{th} week of the experiment, whereas peak Mn^{2+} concentrations were not observed until week 48, when Mn^{2+} reached 85 ppm. Aqueous sample analysis of dissolved metals also revealed that the Ca concentrations were on average 4-5 times higher than Fe and Mn, and reached a maximum

concentration of ~690 ppm 47 weeks post spill. This is likely due to the dissolution of calcite and/or ankerite. Both Fe and Mn declined slightly near the end of the experiment; however, the concentrations remained elevated.

Only minor concentrations of ethanol were detected in the first four groundwater samples (Figure 3-4F). Subsequent samples showed a continual increase in concentration until maximum concentrations were reached at ~ 76 weeks. The dissolved ethanol concentrations measured in the final weeks of the experiment showed concentrations of ~ 12,000 ppm. This illustrates the mass transfer limitations affecting the ingress of ethanol into the saturated zone.

In summary, observations of the E20-S experiment showed substantial acetic and butyric acid concentrations, notably during the early to mid-stages of the experiment indicating active anaerobic bacterial degradation. As noted in (Powers et al., 2001), acetic acid build-up may occur in a poorly buffered system, as methanogens are sensitive to pH and are generally inhibited when the pH decreases below 6 (McCarty, 1964). Reductive dissolution of Mn- and Fe-oxides are likely contributing to the groundwater concentrations of dissolved Mn^{2+} and Fe^{2+}.

Surprisingly, aerobic respiration of the E20 fuel appears to be substantially inhibited. It is well known that hydrocarbon degradation processes are inhibited under nutrient limiting conditions (Atlas and Bartha, 1972; Head et al., 2006); however, this did not seem to be an issue in the other experiments described in this thesis. Notably, the same sediments were used in all experiments. The reason for slow degradation in this column remains currently unknown. Persistent leak issues were also considered as a potential explanation for the observed behavior; however, leaks tend to enhance degradation and sustain significant CO_2 effluxes, which were not observed in this experiment. It can therefore be concluded that leaks did not play a significant role in this experiment.

Mass balance calculations suggest that the fraction of E20 degraded during the 71 week experiment was only 0.4% (Figure 3-14). In addition, the data also illustrates mass transfer limitations with respect to ethanol into the saturated zone. These results are consistent with (McDowell and Powers, 2003) and (Cápiro et al., 2007), who showed ethanol preferentially partitioning in the capillary region and reported a delay in the ethanol infiltration into the groundwater.

3.4.1.5 E20 Delay Sand Column – "E20-D-S"

The results for the geochemical evolution in the E20 Delay Sand Column are depicted in Figure 3-5. A significant change occurred in the vadose zone gas concentrations after the headspace venting system was modified during week 71 (Figure 3-5-B, and C). The data shows that an appreciable amount of O_2 ingress occurred due to leaks, affecting O_2, CO_2 and BT concentrations for much of the study (affected data is highlighted in red). Although the impact seems more limited between weeks 7 and 25, O_2 sensor measurements at an elevation of 100 cm show the lowest values after week 71, indicating that O_2 ingress also occurred between week 7 and 25. Vertical soil O_2 and CO_2 data also shows the presence of a substantial leak at 100 cm, present during week 11, 21, 40 and 61 (Figure 3-11A, B). In addition, the pressure measurements show an increase in the pressure gradient between 100 cm and 140 cm (Figure 3-13C), thereby corroborating the findings on the leak location using the vertical soil gas profile. In conclusion, vadose zone concentrations above 100 cm are questionable until week 71 of the experiment.

Despite these experimental issues, vadose zone O_2 and CO_2 concentrations show two separate events of substantial CO_2 production and O_2 consumption (Figure 3-5B, C). The first event occurred during the first week of the experiment and is in direct response to the 1L injection of gasoline. The second event at week 7 is the response of the delayed 1L E20 injection. In both cases, the response

to the fuel injections illustrate the immediate aerobic degradation of the fuel, which significantly consumes O_2 and produces a CO_2 at a substantial rate. As mentioned previously, the headspace venting rate was increased to better capture escaping volatiles from the column. In doing so, the enhanced pressure gradient between the headspace of the column and lab air, resulted in the air ingress and flushing of the column, as can be seen in the data between weeks 2 and 7. This data further illustrates the susceptibility of the experimental setup towards leaks. After the delayed spill of E20, O_2 concentrations decreased again, accompanied by an increase of CO_2 concentrations. Over time the production of CO_2 and consumption of O_2 declined, indicating a slowing of aerobic processes, and much of the basal region of the column remained anoxic. However, it has to be kept in mind, that the observed concentration pattern is likely overprinted by the leak issues discussed above. In addition, methane was detected in low concentrations at the base of the column during weeks 21 and 40 (week 21 data is overprinted by week 40 data because concentrations are exactly the same) and 61 (Figure 3-11C).The vertical methane profile illustrates that methane concentrations decrease below detection at 100 cm, likely due to artificially enhanced oxidation resulting from the leak at 100cm.

A substantial soil efflux of CO_2 was observed (ranging between 10 - 20 µmol m^{-2} s^{-1}), most notably after the delayed E20 spill (Figure 3-5A). As well, a moderate efflux of CH_4 was observed between week 20 and 42, when fluxes ranged from 0.1 to 0.25 µmol m^{-2} s^{-1}. However, the methane flux disappears when O_2 concentrations begin to rebound suggesting that methanotrophic activity is increasing permitted by the presence of oxygen (Eqn. 5) (Figure 3-5A, B).The significant consumption of oxygen and the presence of methane indicates that both aerobic and anaerobic processes are occurring within the column.

Soil gas concentrations of benzene and toluene generally remained below 1,000 μg L^{-1} (300 and 260 ppm, respectively) (Figure 3-5-D). In general, concentrations of toluene remained below 700 μg L^{-1} (180 ppm). There was no observable trend, over time, as indicated by temporal fluctuations of toluene concentrations. Toluene was present at higher concentrations than benzene, as expected due to the increased proportion of toluene in the gasoline. The data shows a change in the vertical concentration gradient of both benzene and toluene between 60 cm and 100 cm, which is likely owing to the leak which was identified at 100 cm (Figure 3-15C, Figure 3-16C). Unintentional advective flushing of benzene and toluene in the gas phase is the most likely explanation for the non-linear vertical concentration gradient. At the uppermost sampling port at 160 cm maximum benzene and toluene concentrations of 11 μg L^{-1} (3.4 ppm) and 150 μg L^{-1} (40 ppm) were measured, respectively.

Below the water table, relatively low concentrations of acetic and butyric acids were observed, with no detection of propionic acid (Figure 3-5F). Acetic acid concentrations were found to be slightly higher than butyric acid. A maximum acetic acid concentration of 21 ppm was observed in week 71. Butyric acid concentrations only reached 14 ppm in week 47 of the experiment.

Slight increases in the concentrations of dissolved Fe and Mn were observed as the experiment progressed (Figure 3-5E). Mn^{2+} concentrations were detected already during the first sampling event (week 7), while Fe^{2+} was detected approximately 16 weeks later. This data suggests that Mn- and Fe-reduction processes may be contributing to the dissolved Fe and Mn. Dissolved Ca was observed to be significantly higher (an order of magnitude difference), possibly due to ankerite and/or calcite dissolution. The final sampling event revealed the peak concentrations of 19 ppm and 17 ppm for Fe and Mn cations, respectively; while Ca reached a peak concentration of 354 ppm during week 40 of the experiment.

Ethanol was only detected on three occasions, with concentrations only slightly above the detection limit (Figure 3-5F). The delayed detection of ethanol below the water table is consistent with the other sand columns injected with an ethanol-blended fuel.

In summary, the vadose zone of this column was affected to various degrees by unintentional air ingress which occurred at 100 cm. However, after the delayed injection of the E20 fuel, the system stabilized providing strong evidence for active biodegradation processes. The total estimated mass degraded by week 71 is roughly 40% (Figure 3-14). It is possible that degradation was enhanced due to unintentional bioventing of the column. VFAs, Fe, Mn and ethanol were present in the groundwater, but at relatively low concentrations. In contrast, concentrations of Ca were found to be much more abundant in the groundwater. Attenuation of benzene and toluene was significant, resulting in limited concentrations of these compounds near the surface of the column; however, this was likely augmented by enhanced oxidation capabilities due to the leak identified at 100 cm.

3.4.1.6 Gas Silty-Sand Column – "Gas-SS"

The results for geochemical evolution of the Gas Silty-Sand column are shown in Figure 3-6. Oxygen and carbon dioxide vertical soil gas profiles provide no evidence that this column was affected inadvertently by headspace venting (Figure 3-10F, G). This is validated by the column pressure measurements, which do not show any artificial pressure gradients inside the column, except for measurements between 60 and 100 cm, which illustrates the development of a low-permeability layer at 80 cm (Figure 3-13E). Pressure data indicates that below 80 cm the column is largely unaffected by the negative pressure induced through headspace pumping, illustrating the resistance to gas migration through this layer). Upon water infiltration, a perched water table developed at approximately 100 cm. The presence of saturated conditions in this region has major

implications for the biodegradation and soil gas distribution inside the Gas-SS column. The spill zone was effectively cut off from the upper vadose zone, and gas exchange between the top and bottom of the column was blocked. Strongly inhibited gas exchange is evident in the carbon dioxide data in Figure 3-6C. It can be seen that CO_2 sensors below 100 cm are measuring significant levels of CO_2, whereas above the perched water table the CO_2 signature in soil gas remained close to atmospheric. During the injection of gasoline into the base of the column, several leaks occurred, and lost gasoline was subsequently re-injected. Each leak/injection cycle generated significant fluctuations in the carbon dioxide content at 40 cm (highlighted in red in Figure 3-6). However, these disturbances were short lived and only affected the first few weeks of the experiment.

Vadose zone gas compositions showed strong vertical gradients due to the presence of the perched water table. All O_2 and CO_2 sensors above the perched water table measured roughly atmospheric levels of O_2 and CO_2 (Figure 3-6B, C). The O_2 sensor below the perched water table show that oxygen was consumed rapidly and that anoxic conditions persisted throughout the experiment (sensor data at bottom left of Figure 3-6B). The CO_2 sensors showed significant production of CO_2 below 80 cm, indicative of anaerobic respiration below the perched water table. Carbon dioxide concentrations increased from week 9 to week 27 and remained stable for the remainder of the 1.5 year experiment. Maximum CO_2 concentrations were observed near the base of the column (at an elevation of 40 cm), reaching up to 25% v/v. A persistent CO_2 gradient towards the overlying sensor suggests some CO_2 loss across the perched water table; however, soil flux measurements of CO_2 at the surface were low, and CH_4 effluxes were not detected (Figure 3-6A), suggesting that biodegradation in this column is limited. However, the presence of methane at 60 cm during weeks 21 and 40 shows that methanogenesis is occurring (Figure 3-10H).

Benzene and toluene were detected above the low permeability layer at 100cm (Figure 3-15E, Figure 3-16E). Benzene (19 μg L^{-1} [5 ppm]) and toluene (254 μg L^{-1} [78 ppm)) were detected at 160 cm around week 35. Concentrations below an elevation of 100 cm were significantly higher, producing a substantial concentration gradient between the bottom half and upper half of the column. Benzene and toluene near the base of the column (60 cm) reached a maximum concentration of 565 μg L^{-1} (175 ppm) and 2,975 μg L^{-1} (780 ppm), respectively. Soil gas concentrations appear to increase in concentration through time. Lastly, toluene soil gas concentrations were generally higher than benzene concentrations, owing to the fact that the original gasoline contained a higher proportion of toluene than benzene.

VFAs were present in groundwater at low concentrations and persisted throughout the experiment (Figure 3-6F). In general, concentrations of acetic acid were greater than butyric acid; however, only slightly. Acetic acid and butyric acid concentrations were consistently below 30 ppm, and 10 ppm, respectively. Propionic acids were not detected.

Dissolved Ca-concentrations remained relatively low and constant throughout the experiment; similar observations were made for Fe and Mn (Figure 3-6E). Aqueous Ca concentrations consistently hovered around 50 ppm. Aqueous Mn measured consistently higher than Fe. Mn concentrations were below 5 ppm and Fe concentrations were below 2 ppm. These results are indicative of limited ankerite dissolution, possibly due to limited generation of acidity due to a lack of aerobic respiration. However, because pH was not measured, this interpretation remains speculative.

In summary, aerobic degradation rapidly consumed oxygen in the basal region of the column. Aerobic degradation was inhibited once the oxygen was consumed and the primary degradation pathway became anaerobic, leading to an increase of CO_2 concentrations to levels > 25%v/v.

Groundwater samples showed limited accumulation of VFAs and dissolved metals. These data suggest that anaerobic degradation was active; however, degradation was occurring at a sluggish rate. Mass loss calculations based on the gas effluxes suggest that less than 2% of the injected hydrocarbons have been degraded (Figure 3-14).

3.4.1.7 E20 Silty-Sand Column – "E20-SS"

Results describing the geochemical evolution in the E20 Silty-Sand Column are shown in Figure 3-7. Initial vadose zone O_2 and CO_2 concentrations are affected by the increased headspace venting rates during the first week (Figure 3-7B, C). Vertical O_2 and CO_2 concentrations show a small leak at 100 cm, which had a minor effect on the concentration during weeks 11 and 21; however during weeks 40 and 61, the data suggests that another leak developed at a lower elevation, as gas concentrations at 60 cm shifted slightly towards that of atmospheric composition (Figure 3-12F, G). Just prior to week 27, BT samples were collected and the ports were not closed properly allowing for air ingress into the column. This likely caused the development of the new leak, disrupting vadose zone soil gas between weeks 27 and week 71. Column pressure measurements show a pressure gradient throughout the column during weeks 11, 21, 40 and 60, indicating the presence of a leak. Time periods of elevated concern with data quality are highlighted in red (Figure 3-7).

Immediately after the spill, O_2 concentrations declined rapidly, accompanied by a gradual increase in soil CO_2 concentrations (Figure 3-7B, C). Data suggest that there was a period of microbial acclimatization before aerobic respiration began. By week 5, soil gas concentrations stabilized. During this time, the data shows that the oxygen content at 160 cm was around 10%, while at 100 cm and below, oxygen was depleted completely. At the same time, the CO_2 sensor

at 140 cm reached the sensor's maximum detectable concentration of 10%, while the CO_2 sensors below reported concentrations close to 15%. Significant O_2 consumption and CO_2 production illustrates that biodegradation is active in the column. Soil methane was detected during weeks 21 and 40 (Figure 3-12H). Methane was detected throughout the column during week 21, which coincides with the elevated methane fluxes observed at the surface. The week 40 vertical methane profile shows the disappearance of methane around 100 cm, which is likely a result of oxidation occurring as a result of an increase in O_2 at 100 cm during that time.

During this time, soil CO_2 fluxes reflect high biodegradation rates indicated by O_2 consumption and CO_2 built-up observed by the vadose zone gas sensors (Figure 3-7A). Interestingly, there is a high degree of variation in the surficial CO_2 fluxes. Reasons for these fluctuations are unknown. In addition, significant surficial CH_4 fluxes were observed between weeks 20 and 38, indicating that methanogenesis was occurring.

Analysis of vadose zone benzene and toluene gas concentrations provide evidence of vertical attenuation of benzene and toluene (Figure 3-7D). Vertical profiles of benzene and toluene show non-linear concentration gradients, pointing towards microbial attenuation. The vertical benzene profile suggests that attenuation may be important between 100 cm and 160 cm (Figure 3-15F), while toluene appears to be attenuated between 60 cm and 100 cm (Figure 3-16F). The highly variable soil gas concentrations during the later part of the experiment and concentration declines may be affected by leaks and unintentional air ingress occurring at the base of the column between 40 and 60 cm. Nevertheless, attenuation is evident, since maximum benzene and toluene concentrations at 160 cm (20 cm below the soil surface), are 51 $\mu g\ L^{-1}$ (16 ppm) and 353 $\mu g\ L^{-1}$ (92 ppm), respectively. Soil gas concentrations of toluene were much higher than benzene

concentrations, which is expected considering there was a higher proportion of toluene in the gasoline. The most significant toluene concentrations was observed at 60 cm, just above the injection zone, where a maximum concentration of 4,481 μg L^{-1} (1,174 ppm) was measured.

In the saturated zone, significant VFA concentrations were observed early during the experiment, reaching maximum concentrations by week 21, followed by an immediate decline-virtually disappearing from the groundwater by week 38 (Figure 3-7F). From weeks 9 through 38, elevated rates of anaerobic degradation are indicated by the lack of oxygen at the base of the column and the substantial buildup of VFAs in the saturated zone. The concentrations of acetic and butyric acid reached 760 ppm and 850 ppm, respectively. Dissolved concentrations of acetic and butyric acids were roughly equal during the period of significant VFA production; however, at early time the VFA production was dominated by butyric acid, while acetic acid dominated towards the end of the experiment. The production of VFAs was succeeded by methanogenesis as indicated by the elevated methane fluxes in Figure 3-7A. The decline in these anaerobic degradation intermediates coincides with the accidental air ingress starting around week 27. Therefore, it is likely that air ingress shifted the redox conditions towards more oxic conditions resulting in the inhibition of anaerobic degradation.

Dissolved metals observations show a trend of increasing Mn^{2+} and Fe^{2+} generation, followed by a significant decline in concentrations (Figure 3-7E). Mn^{2+} and Fe^{2+} concentrations rose to a maximum of 52 ppm and 46 ppm, respectively. Fe and Mn subsequently declined gradually to below 15 ppm by week 40. During the initial stages, the redox indicator Mn dominated the groundwater in comparison to Fe, indicating that there was a clear dominant redox regime of Mn^{4+} reduction to Mn^{2+}, possibly through Eqn. (**Error! Reference source not found.**) and Eqn. (**Error!**

ference source not found.). Subsequent groundwater sampling revealed that dissolved Fe began to increase approximately 10 weeks later, representing a switch from Mn^{4+} reduction to Fe^{3+} reduction, possibly through Eqn. (14) and/ or Eqn. (13).Following the decline of Fe and Mn, residual dissolved concentrations of Fe and Mn were comparable during the second half of the experiment. This decline in reduced Mn^{2+} and Fe^{2+} also coincides with the accidental air-ingress just prior to week 27. These data suggest that air ingress resulted in a shift in the redox conditions in the saturated zone to more oxic conditions, thereby re-oxidizing dissolved Mn^{2+} and Fe^{2+} to Mn^{4+} and Fe^{3+}, resulting in the precipitation of amorphous Mn and Fe minerals. Examples of these reactions are shown below.

$$Mn^{2+} + \frac{1}{2}O_2 + H_2O \rightarrow MnO_2 + 2H^+ \quad (25)$$

$$2Fe^{2+} + \frac{1}{2}O_2 + 5H_2O \rightarrow 2Fe(OH)_3 + 4H^+ \quad (26)$$

Elevated dissolved Ca was measured in the saturated zone throughout the experiment, which is likely a result of ankerite dissolution, shown in Eqn.(16). Increases in dissolved Fe and Mn concentrations in groundwater may also be due to the dissolution of ankerite. At its highest, Ca reached ~460 ppm 22 weeks post spill. Ca declined slowly during the later stages of the experiment, and the final groundwater sample contained approximately 280 ppm Ca. The temporally discordant arrival of Mn and Fe suggests that reductive dissolution is occurring alongside ankerite dissolution. Without pH data this interpretation remains speculative.

Ethanol was not seen in most of the groundwater samples. Only two samples, collected during week 22 and week 27 showed the presence of ethanol above the detection limit of 1 ppm (Figure 3-7F).

In summary, vadose zone data suggest that aerobic respiration is effectively degrading E20. The data also shows that the unintentional air ingress significantly affected the soil gas profile within the column, leading to an artificially increased aerobic degradation rate. The mass-loss calculation estimates reveal that by the end of the experiment almost 40% of the released fuel had been degraded (Figure 3-14). In addition, the substantial decline in oxygen near the base of the column during early stages of the experiment illustrates a shift towards anaerobically dominated degradation, as shown in the groundwater results. Groundwater observations reveal substantial amounts of dissolved metals and VFAs between weeks 15 and 30, indicating the activity of anaerobic degradation of the E20 fuel. The high concentrations of butyric acid could signal a stressed microbial community (Freitas et al., 2010). The presence of a methane soil flux combined with a decline in acetic acid suggests that acetogenic methanogenesis was occurring. The bell-shaped concentration trend (increase, followed by a decline) of VFAs was also observed for the redox indicators Fe and Mn.

3.4.1.8 E20- Delay Silty-Sand Column – "E20-D-SS"

Results for the geochemical evolution in the E20-Delay Silty Sand Column are presented in Figure 3-8. The E20-D-SS column experienced the same operational difficulties as the E20-SS column, whereby the initial soil O_2 and CO_2 gas composition was disturbed soon after the injection of 1L of gasoline (Figure 3-8B, C). The disturbance, highlighted in red, was caused by changes to the headspace venting rates to ensure that volatiles exiting the column were routed to the fume hood. Just prior to week 27, benzene and toluene samples were collected and the ports were not closed properly, allowing for air ingress into the column affecting data in the vadose zone between weeks 27 and week 71. Vertical O_2 and CO_2 concentrations show the presence of a leak around 100 cm, for weeks, 11, 21, 40 and 61 (Figure 3-11F,G). Pressure measurements verified the

presence of a leak at 100 cm through a pressure gradient above 100 cm (Figure 3-13G). Leaks persisted until the headspace venting system was modified during week 71. Time periods with questionable data quality areas are highlighted in red (Figure 3-8).

After the initial injection of 1 litre of gasoline, the soil O_2 concentration decreased sharply while the soil CO_2 concentration increased abruptly in response (Figure 3-8-B, C). An adjustment to the headspace venting rate was made about a week after the injection, resulting in an increase in soil O_2 and a decrease in soil CO_2. The delayed injection of 1L E20 occurred around week 7, and resulted in the substantial decrease in O_2 and increase in CO_2 concentrations from the increased rates of aerobic degradation. The second leak developed just before week 27, resulting in a reduced CO_2 concentration. The surficial soil CO_2 flux does not seem to be affected by the decrease in the CO_2 gradient and a soil CH_4 flux was detected after the oxygen concentration in the soil increased between weeks 36 and 68 (Figure 3-8A). The vertical methane profile shows the appearance of subsurface methane during the period of methane flux (week 40 and 61) (Figure 3-11H). Despite the significant amount of oxygen located in the upper half of the column, the GC data reveals measurable methane concentrations until 160 cm, just 25 cm below the soil surface (Figure 3-11H).

Maximum benzene and toluene concentrations 20 cm below the ground surface were 33 $\mu g\ L^{-1}$ (10 ppm) and 63 $\mu g\ L^{-1}$ (17 ppm), respectively (Figure 3-15G, Figure 3-16G). Toluene concentrations were higher than benzene due to the increased proportion of toluene within the fuel (Figure 3-8D). A maximum toluene concentration of 3,117 $\mu g\ L^{-1}$ (47 ppm) was detected 10 cm above the fuel injection zone (Figure 3-8D). In general, slightly stronger concentration gradients of benzene and toluene exist between 60 cm and 100 cm likely a result of a leak which was identified at 100cm.

The groundwater VFA data provided in Figure 3-8F show a substantial buildup in acetic acid concentrations from week 17 to week 31. Acetic acid concentrations during this time reached a maximum concentration of 740 ppm. Declining acetic acid concentrations were observed by week 31, when concentrations remained generally below 150 ppm. In comparison, butyric acid concentrations were much lower; however, still significant. Substantial amounts of butyric acid (>200ppm) were detected by week 27, after the buildup of acetic acid. In subsequent groundwater samples, the butyric acid and acetic acid concentrations declined to comparable levels. The decline in acetic acid concentration coincides with the time of the accidental air ingress, and the increase in groundwater ethanol (Figure 3-8F). The data suggests that redox conditions in the saturated zone may have become increasingly aerobic, which resulted in a decrease in ethanol degradation from acetogenesis Eqn. (19).

Dissolved metal data presented in Figure 3-8E reveal a bell-shaped trend of Mn^{2+} and Fe^{2+} concentrations throughout time. Concentrations of Fe^{2+} and Mn^{2+} remained relatively low, generally below 30 ppm. Mn^{2+} appeared to be slightly higher in concentration initially, followed by a sharper increase of dissolved Fe^{2+} at week 32, likely a result from shifting dominant redox conditions from an Mn^{4+} reducing to a Fe^{3+} reducing environment. Both redox indicators (Fe, Mn) subsequently declined gradually. Concentrations in the final groundwater samples of Fe and Mn corresponded to 12 ppm and 14 ppm, respectively. The decline in Mn^{2+} and Fe^{2+} seemed to occur during the period of increased soil oxygen concentrations from the accidental air ingress prior to week 27. This suggests that re-oxidation of Mn^{2+} and Fe^{2+} likely occurred, causing the precipitation of Mn and Fe amorphous minerals (Eqns.25, 26). Ca showed a similar trend compared to Fe and Mn cations; however, concentrations of Ca were much higher than Fe and Mn.

Ethanol was present in the groundwater in the earliest collected groundwater samples, generally below 25ppm (Figure 3-8F). However, the presence of ethanol increased during weeks 35-47 when concentrations rose above 340 ppm, and then fell below detection by week 75.

In summary, early vadose zone data largely unaffected by the leak showed significant consumption of O_2 due to aerobic respiration. The data also illustrates the delay in arrival of substantial concentrations of ethanol, followed by its disappearance in the final sample. The events of acetic acid decline, Mn^{2+} and Fe^{2+} decline, as well as increase in dissolve ethanol appear to occur within the same timeframe, therefore suggesting that a redox shift towards more oxic conditions inhibited acetogenesis resulting in an inhibition of ethanol degradation (Eqn. 19), and forced Mn and Fe out of solution through oxidation (Eqns. 25, 26) Methanogenesis appears to occur, despite the period of accidental gas ingress into the column. Microbial attenuation of benzene and toluene between 60 and 100 cm results in minor soil surface concentrations of benzene and toluene.

3.4.2 Isotopic Results

Stable and radioisotopic methods provide tools which are often used to study natural attenuation (NA) processes (Aelion et al., 2009).

Natural isotopic intermolecular variation provides the basis for the application of stable isotope analysis to assess microbial degradation reactions and pathways. In carbon, the two stables isotopes are ^{12}C (98.93%), and ^{13}C (1.074%), which occur naturally with varying proportions within nature (Aelion et al., 2009). In microbial reactions, the rate constant depends on whether the heavy isotope (^{13}C) or the light isotopes (^{12}C) is at the reactive position, resulting in what is known as the kinetic isotope effect. A molecule containing a heavy carbon (^{13}C) has slightly

stronger bonds than a molecule that contains bonds with the lighter carbon (^{12}C) (Aelion et al., 2009). Therefore, molecules with the lighter isotope of carbon at the reactive position will react more quickly relative to the reactions involving the heavier bond due to the lower energy cost associated with breaking intra-molecular bonds (Kendall and Caldwell, 1998). As a result, the isotopes become unevenly distributed among the reactants and products of biodegradation. This process is called isotopic fractionation. While stable isotopes have long been considered a powerful tool in assessing NA processes (e.g., methanogenesis), and reaction pathways (e.g., acetate fermentation) (Sihota and Mayer, 2012), they can also be used for the identification of source material undergoing NA. This is attributable to the two fuel components in ethanol-blended fuels, ethanol and gasoline, which have distinct stable isotopic carbon signatures. The isotopic results show that ethanol is enriched in ^{13}C, with a $\delta^{13}C$ value of -11 ‰, which represents the typical isotopic signature of C4 plants (corn) from which the ethanol was derived (Aelion et al., 2009). C4 plants undergo a different photosynthetic pathway compared to their C3 plant relatives, and it is this difference that determines the amount of ^{13}C fractionation of CO_2 during photosynthesis (Aelion et al., 2009). The ^{13}C isotopic signature of the gasoline components benzene and toluene consisted of $\delta^{13}C$ values of -30‰ and -28‰, and a ^{2}H isotopic signature of -163‰ and - 34‰, respectively. These results are consistent with other studies, which have found that the $^{13}C/^{12}C$ isotopic ratio in fossil fuels lies within a narrow range between -23 to -28.6‰ (Smallwood et al., 2002; Widory, 2006). The results for the source materials are summarized in the Methods chapter (Table 2-4) and illustrate the distinct isotopic signatures associated with gasoline fuel components and ethanol.

Radiocarbon (^{14}C) can be used to identify carbon sources of biodegradation by analyzing CO_2 produced by either natural soil respiration, or contaminated soil respiration (Aelion et al., 2009; Conrad et al., 1997; Sihota and Mayer, 2012). Naturally occurring radiocarbon is continually produced in the atmosphere through a nuclear reaction between nitrogen (^{14}N) nuclei and cosmic rays which ejects a proton from ^{14}N to produce an unstable ^{14}C atom (Aelion et al., 2009). These ^{14}C atoms become oxidized into CO_2 and enter the carbon cycle through photosynthesis. This results in an equilibrium of the ^{14}C in the atmosphere with both living animals and plants, until death when the reincorporation of atmospheric ^{14}C into the cellular structure ceases (Aelion et al., 2009). Since ^{14}C is unstable, it begins to decay in the dead biological tissues with a half-life of 5730 (±40) years. As ethanol is produced from modern corn crops, the amount of time for radioactive decay to occur is relatively insignificant resulting in a modern radiocarbon signature which resembles the current atmospheric ^{14}C signal [~114% modern carbon (pMC)] (Aelion et al., 2009). In contrast, carbon present in petroleum (fossil fuel) has undergone decay of multiple half-lives. Radiocarbon in petroleum is significantly depleted in ^{14}C (effectively radiocarbon dead) and can easily be distinguished from modern sources such as ethanol. Radiocarbon analysis of the ethanol confirmed its plant-derived modern signature and is represented as a fraction of modern carbon ($F^{14}C$ 1.02). Radiocarbon analysis of the gasoline was not performed; however, a radiocarbon-dead signature can be assumed safely, considering that the gasoline is derived from petroleum. Consequently, CO_2 derived by biodegradation of ethanol is easily distinguishable from CO_2 derived through biodegradation of gasoline.

The isotopic analysis as previously mentioned in the methods chapter, outlined the collection and analysis of ^{13}C and ^{2}H isotopes in benzene, toluene, CO_2 and CH_4. However, due to issues at

different isotopic labs, as well as problems analyzing methane isotopes at low concentrations and in the presence of ethanol, the focus of the stable isotopic results will be narrowed down to the analysis of ^{13}C in CO_2. Radiocarbon results of ^{14}C in the CO_2 produced during biodegradation are included as well. Furthermore, the results for both stable and radio isotopes are presented together in sections separated by fuel type rather than by each individual column.

3.4.2.1 E85 Fuel – 15% Gasoline / 85% Ethanol

The discussion of biodegradation of E85 fuel is based on isotopic results in the E85-S column. The ^{13}C signature of CO_2 in soil gas varies significantly throughout the duration of the experiment (Figure 3-18A). Initial samples of CO_2 collected from weeks 14 and 22 (post-spill), were isotopically light, with $\delta^{13}C$ values ranging from ~ -30‰ to -25‰. However, a significant shift in the isotopic composition of the CO_2 occurred between weeks 22 and 32. Samples collected during weeks 32, 37 and 55 contained isotopically heavier CO_2, with $\delta^{13}C$ values ranging from ~ -13.5‰ to -17‰. Figure 3-17A shows that the initial CO_2 samples collected during weeks 14 and 22 are quite similar to the ^{13}C signature of the benzene and toluene, and by extension the gasoline. In contrast, the CO_2 samples collected during weeks 32, 37, and 55 contain a ^{13}C signature that approaches that of the ethanol ($\delta^{13}C$ ~ -11‰). Radiocarbon analysis of the week 55 CO_2 samples confirm the presence of a significant fraction of modern carbon, with a $F^{14}C$ value of ~0.9 (Figure 3-20A. This indicates that 90% of the carbon in carbon dioxide is derived from a modern source, in this case the ethanol. Therefore the isotopic data confirms that initial biodegradation was predominately of the gasoline portion of the fuel; however, the system shifted towards utilization of ethanol as the primary substrate after 30 weeks post-spill.

3.4.2.2 E10 Fuel – 90% Gasoline / 10% Ethanol

The discussion of biodegradation of the E10 fuel is based on the isotopic results of the E10-S column. The ^{13}C isotopic signature of the CO_2 does not vary much with time; however, there appears to be a minor trend of decreasing $\delta^{13}C$ values over time (Figure 3-17B). Carbon dioxide isotope samples collected during weeks 14, 22 and 32 have a $\delta^{13}C$ signature ranging from -25‰ to -20‰, approximately. The $\delta^{13}C$ signature of the CO_2 lies in between that of the ethanol and gasoline (B.T.). However, week 37 and week 55 samples become isotopically lighter and approach the signature of the gasoline ($\delta^{13}C$ -30‰), with week 55 $\delta^{13}C$ values of around -28‰. This data suggests that during the initial 30 weeks, degradation of both ethanol and gasoline occurred, resulting in the intermediate isotopic signature. The data suggests, as the experiment progressed, the proportion of gasoline degradation increased resulting in a much lighter isotopic signal by the end (week 55). Considering the fuel blend contains "only" 10% ethanol, it is possible that ethanol had been completely degraded during the initial 30 weeks of the experiment, causing the ^{13}C signal to shift from a "mixed" signal to a gasoline dominated signal.

3.4.2.3 Gasoline

Isotopic results related to the biodegradation of the gasoline fuel are discussed based on the isotopic results of the Gas-S and the Gas-SS columns. The isotopic signatures during progressing biodegradation of the gasoline are very similar between the sand and silty-sand columns (Figure 3-18A and Figure 3-18D, respectively).

For the Gas-SS column, there appears to be significant fractionation as a function of elevation in the 100cm and 160cm sampling ports (Figure 3-18D); however, it is important to note that these locations are both above the perched water table. Carbon dioxide concentration measurements

reveal extremely low concentrations of CO_2 at both 100cm and 160 cm (<1%) (Figure E-2). Since atmospheric CO_2 concentrations in ambient air are around ~0.04% (~400ppm), a significant proportion of the CO_2 is derived from the atmosphere. According to (Friedli et al., 1986), atmospheric CO_2 has a $\delta^{13}C$ signature of ~ -7.8‰. Therefore, it is likely that this observed fractionation is a result of mixed CO_2 sources; atmospheric and hydrocarbon. To test this, a mixing model was developed which accounted for the proportions of CO_2 derived from gasoline biodegradation vs. the proportion of atmospherically derived CO_2. The proportions were then used in a weighted average calculation to determine the overall $\delta^{13}C$ of the "mixed" composition. This model does not account for isotopic fractionation but rather it is useful for determining the amount of ^{13}C enrichment that will occur from atmospheric CO_2 contamination at low CO_2 levels. The data is plotted with the "actual" data and generally agrees with the levels of ^{13}C enrichment as the proportion of atmospheric CO_2 increases vertically (Figure 3-19). These results confirm that the apparent vertical fractionation is a result of atmospheric mixing, and further provides confidence in the ability to identify the influence of atmospheric CO_2 on the overall CO_2 generated from biodegradation.

Fortunately, the samples at 60cm provides a data set directly reflecting the biodegradation of the gasoline. Interestingly, the trends in the isotopic signature of CO_2 are very similar between the sand and silty sand gasoline columns. Further examination of the 60cm data shows the biological induced fractionation of the gasoline degradation. Initial CO_2 samples in both columns are depleted in ^{13}C relative to the initial gasoline source (~ -30‰). This is because of the kinetic isotope effect, which results in the faster degradation of lighter isotopes within the gasoline. As microbial degradation proceeds, the CO_2 signature becomes heavier in weeks 32 and 37 and 55, due to the

progressive depletion of the lighter ^{12}C isotopes in the source. Despite there being a substantial difference in the permeability between the sand and silty-sand column, as well as the inclusion of a perched water table in Gas-SS, the data between the sand and silty-sand column are in good agreement, suggesting a direct link between time, reaction progress and degree of isotopic fractionation in CO_2.

3.4.2.4 E20 Fuel – 80% Gasoline / 20% Ethanol

Discussion of the isotopic fractionation during biodegradation of the E20 fuel is based on the isotopic results of the E20-S and the E20-SS columns. Initial $\delta^{13}C$ values for the sand and silty-sand columns are similar, however the overall evolution appears to be quite different (Figure 3-18B and Figure 3-18E, respectively). There is an enrichment of ^{13}C in the CO_2 in the sand column, whereas there is an overall depletion in ^{13}C in the CO_2 in the silty-sand column. Carbon dioxide concentrations between the two columns differ greatly; 0.4% to 0.8% in the E20-S column, and 2-8% in the E20-SS column (Figure E-2). It is therefore likely, that the observed enrichment of ^{13}C in the CO_2 for the sand column is because of increased mixing with atmospheric CO_2. Low contaminant degradation rates and low CO_2 concentrations lead to a greater influence of atmospheric CO_2, as the proportion of atmospheric derived CO_2 in the mixture is higher. Since the CO_2 in ambient air has a heavy $\delta^{13}C$ signature (-7.8‰), the resulting mixed CO_2 signature becomes heavier. Therefore, the E20-S column does not reliably show the evolution of the isotopic composition of the microbially derived CO_2 from an E20 fuel spill. The silty-sand column; however, does not suffer from atmospheric CO_2 influence on the isotopic values of CO_2. Carbon dioxide samples collected from E20-SS during the first few weeks of the experiment (weeks 14, 22, and 32) present an isotopic signature that lies in between ethanol and gasoline (Figure 3-18E). The evolution of the isotopic signature of CO_2 shows a depletion in ^{13}C through weeks 37 and 55,

resulting in a signature that approaches that of the gasoline. Therefore, the data show that during the first 30 weeks there was a significant influence of ethanol-derived CO_2, suggesting that a significant portion of the 20% ethanol was degraded along with the gasoline during this time. Furthermore, the shift in the $\delta^{13}C$ during weeks 37 and 55 reflects a source dominated predominately by gasoline, indicating that the microbial community has shifted towards utilization of gasoline. Examination of the ^{14}C in CO_2 during week 55 shows that the fraction of modern carbon in the CO_2 is very low ($F^{14}C \sim 0.1$), which confirms the lack of ethanol contribution to the CO_2 generated through biodegradation (Figure 3-20).

3.4.2.5 Gasoline + E20 Delay - 90% Gasoline / 10% Ethanol

Discussion of the E20 delayed experiments are focused on the E20-D-S and E20-D-SS columns. The E20 delay experiment involved a 1L injection of gasoline followed by an injection of 1L of E20 at week 8, two months after the gasoline injection. Early CO_2 samples for both sand and silty-sand columns were taken during week 14, approximately 6 weeks after the delayed injection of the E20 fuel. These early CO_2 samples are depleted in ^{13}C, showing a signature similar to gasoline. It appears that CO_2 in the silty-sand column is slightly more depleted in ^{13}C (Figure 3-18F) compared to the sand column (Figure 3-18C). The initial $\delta^{13}C$ values for the silty-sand column range between -32‰ to -30‰, while the initial $\delta^{13}C$ values for the sand range between -27‰ to -24‰. The initial $\delta^{13}C$ CO_2 signature in both columns reflect predominately a gasoline source, although the slightly heavier initial carbon isotopic signature in the sand column suggests a slightly stronger influence of ethanol relative to the silty-sand column. Both sand and silty-sand columns are identical in their evolution, whereby there is a brief enrichment in ^{13}C as the CO_2 isotopic signal becomes progressively heavier until week 32, when subsequent CO_2 samples collected during week 37 and week 55 show a progressively lighter CO_2 trend. This data suggests

that initially microbial degradation of the gasoline portion of the fuel is dominating, which is succeeded by a progressively increasing proportion of ethanol degradation, and then finally returning to a more gasoline dominated source. Radiocarbon isotopes from CO_2 samples taken on week 55 show that the fraction of modern carbon is low in the sand column ($F^{14}C$ ~0.08), while the fraction of modern carbon is higher in the silty-sand column ($F^{14}C$ ~ 0.3) (Figure 3-20). Radiocarbon analysis confirms the presence of an increased proportion of ethanol derived carbon in the silty-sand column, relative to the sand column in the later stages of the experiment (week 55). Interestingly, despite the minor differences in the proportion of ethanol derived carbon between the two columns, there appears to be a distinct and delayed shift from a predominately gasoline dominated source to a source with a higher ethanol fraction, approximately 6 weeks after the E20 injection. This data suggests that the microbial community established during the initial gasoline spill was resistant to change substrates to ethanol following the E20 spill at week 8.

3.5 Discussion

This section provides an analysis of the data focusing the discussion around the research goals of the study. The discussion integrates the vadose zone and saturated zone results as they pertain to each particular research goal.

3.5.1 Is There a Potential for the Development of Toxicity Affecting Microbial Activity, Related to Specific Ethanol Fuel Blends?

Microbial toxicity was assessed based on two criteria. First, microbial toxicity to ethanol will result in either; a reduced capacity for degradation, or a complete shutdown of biodegradation processes. This occurs primarily by disruption/disintegration of the cellular membrane as ethanol

dissolves the phospholipids (Ingram and Buttke, 1985). As this process progresses, ethanol can enter the cell, and inhibits the synthesis of DNA (Osztovics et al., 1980), stunting the growth of microbial communities. In addition, once inside the cell, ethanol inhibits RNA (Mitchell and Lucas-Lenard, 1980) and proteins, which are essential to catabolic functions, leading to a reduction/inhibition of biodegradation (biosynthesis) of organic chemicals. The effects of inhibition are visible in the overall output of CO_2, through soil vadose zone CO_2 measurements and soil CO_2 fluxes. Secondly, studies have demonstrated that highly stressed microbial communities undergoing anaerobic degradation undergo reversible reactions, whereby butyric acid may be formed and then degraded to acetate as the stressed conditions recede (Chen et al., 2008; Freitas et al., 2010; Kim et al., 1994; Wu and Hickey, 1996). Data collected in this study show a trend of increasing butyric acid concentrations as the total applied ethanol content increased (Table 3-2). Figure 3-23 shows the evolution of butyric acid column-by-column. This graph shows that the columns with the highest and in general- most persistent butyric acid concentrations, are those with higher applied ethanol content. Figure 3-23 shows that there was a significant correlation ($p = < 0.05$) between average butyric acid concentration and applied ethanol. According to these results, elevated butyric acid concentrations were correlated with higher applied ethanol content, indicating an increase in microbial toxicity with the ethanol content of the biofuel.

Carbon dioxide isotopic results from four of the six ethanol-blended fuel columns, show a progressive enrichment of ^{13}C during the later stages of the experiment, indicating that microbial degradation shifted towards a more ethanol dominated substrate late in the experiments (Figure 3-17A, Figure 3-18B,C,F), suggesting that there was an initial microbial acclimation period possibly resulting from varying levels of ethanol toxicity. Of the two column experiments that did

not follow this trend, E10-S and E20-SS, the data seems to suggest that only the E20-SS experienced microbial toxicity. The E20-SS VFA data, in combination with the isotopic data shows that significant levels of butyric acid were detected from weeks 14- 30 (Figure 3-7F), during the same time of ^{13}C CO_2 enrichment, suggesting that a significant portion of the ethanol was being degraded, despite evidence towards microbial toxicity (Figure 3-18B). Dissolved ethanol was only detected slightly above the detection limit during this time, and concentrations subsequently returned to below detection (Figure 3-7F). Combining all data, it appears that despite signs of ethanol toxicity issues, the microbial community was able to degrade ethanol effectively, leaving behind the gasoline portion of the fuel. This behavior was not seen in other higher ethanol content fuels such as; E20-S and E85-S, suggesting differences in the natural variations in microbial communities which may have an effect on the capacity to degrade ethanol, or by variability in the ethanol partitioning and infiltration. Since the soils came from the same site, these differences in behavior may be a result of unique ethanol partitioning. Differences in ethanol partitioning could lead to either a complete separation of the two phases (ethanol and gasoline), further exacerbating the toxicity issues, or conversely a more blended infiltration front may lead to more manageable concentration levels for microbial degradation.

When comparing average butyric acid concentrations in the columns to the calculated mass loss based on CO_2 surficial efflux measurements, there is a general trend towards decreasing mass loss (decreasing biodegradation), and increasing butyric acid concentrations, suggesting that biodegradation rates become slower for higher butyric acid concentrations and ethanol fractions (Figure 3-22). Although the data is slightly outside of our criteria for statistical significance (p = 0.06) whereby p must be less than α (0.05), it is important to consider that the mass loss data is undoubtedly affected by the unintentional air ingress in some columns, thereby having a varied

effect on the calculated mass loss related to the level of toxicity (as indicated by the presence of butyric acid) experienced by each column.

In brief, there appears to be a greater propensity towards a decrease in biodegradation rates with columns possessing high butyric acid concentrations, which was demonstrated in this study to be the case for columns with higher ethanol content. In conclusion, this study suggests that there is a link between an increasing ethanol content and a diminished biodegradation capability resulting from microbially stressed conditions likely attributed to increasing ethanol concentrations.

3.5.2 How Does Soil Type and Fuel Blend Affect Invasion of Ethanol Into the Saturated Zone?

Data relating ethanol abundance and distribution to soil type collected from the saturated zone (10 cm above the base of the column) are presented in Table 3-3. The data shows that the time of first detection of EtOH was varied and did not depend on soil type. In some columns, ethanol was detected during the first sampling week (week 14), while ethanol was not detected in other columns until much later in the experiment (week 48). In general, substantial ethanol concentrations were not observed until much later in the experiments, which indicates that a significant portion of the ethanol was initially retained in the capillary region and slowly diffused into the saturated portion of the column. These results corroborate findings from a study by McDowell and Powers (2003), who conducted a large 2D sand tank experiment to illustrate how gasohols, specifically E10, partitions into the vadose zone. They found that during infiltration, 99% of the ethanol was initially retained in the vadose zone due to the hydrophilic nature of ethanol. Interestingly, the delay in ethanol diffusion to the sampling port did not appear to be affected by the soil type or fuel type. The differences in infiltration and diffusion rates are likely attributed to column-specific

macroscopic soil properties resulting in unique ethanol partitioning, as well as microbial activity, as discussed in the previous section. As expected; however, ethanol concentrations are typically the greatest for fuel blends with the highest ethanol content (Table 3-3). In conclusion, the influencing factors on the infiltration of ethanol into the groundwater appear to depend on microbial activity and unique ethanol partitioning, which is surprisingly not dependent on soil type.

3.5.3 Can Substantial Metal Mobilization Occur in the Ethanol Blended Fuel Spill Zones, and Does Ethanol Content Play a Role?

There are two main metal mobilizing pathways identified in this study: 1) ankerite dissolution, and 2) reductive dissolution of metal oxides. In the case of ankerite dissolution, acidity generated from aerobic oxidation of ethanol and gasoline, as well as VFAs produced through anaerobic degradation can lower the pH sufficiently to dissolve ankerite ($Ca(Mn,Mg,Fe)(CO_3)_2$ and release Ca^{2+}, Mg^{2+}, Mn^{2+} and Fe^{2+} into the groundwater. Reductive dissolution processes; however, involve microbial reactions, which degrade the fuel components. Reductive dissolution of Fe and Mn-oxides strongly consume acidity, while producing Fe^{2+} and Mn^{2+}.

The data collected provides insight into the processes involved and the role ethanol plays in metal mobilization. The detection of Ca^{2+} in groundwater provides evidence towards ankerite dissolution. Cross plots representing moles of Ca vs. moles of Mg, Mn, and Fe combined, were created to examine the process of ankerite dissolution. The data reveals that within each column data set, there is a clear and significant trend ($p < 0.05$) between the moles of Ca vs. moles of Mg, Mn, and Fe (Figure 3-24). If all of the Ca, Mg, Mn, and Fe came from ankerite dissolution, the slope of the cross-plots would be 1, based on the ankerite stoichiometry ($Ca(Mn,Mg,Fe)(CO_3)_2$); however, the slope for all of the graphs are less than 1 (higher ratio of Ca moles to Mg, Mn and Fe

moles). This data may indicate that there is the presence of another source of Ca (possibly calcite), or a sink for Mg, Mn, or Fe. When examining the slopes between sediment types, the data reveals that they are quite similar. Since the fraction of clay is higher in the silty-sand (SS) columns, it would be expected that Mn, Mg, or Fe, would adsorb more readily. Since this is not observed, it is believed that adsorption of Mg, Fe and Mn is unlikely responsible for the slope of <1. As well, the presence of VFAs in the saturated zone are indicative of anaerobic degradation in anoxic environments. As a result, it is not likely that the Mn and Fe oxidation provides a likely sink for these metals. Therefore, the most probable explanation for the elevated Ca is the presence of another Ca source, likely calcite, as was presented in the results section.

Furthermore, there appears to be a correlation between increasing slopes and applied ethanol content (Figure 3-24). The slopes for the cross-plots reveal that the sand and silty-sand gasoline columns have the smallest slope, indicating lesser amounts of dissolved Mn, Fe and Mg (Figure 3-24A, B). The slope of the line increases as the applied ethanol content increases from approximately 200 mL for E10-S (Figure 3-24G), E20-D-S (Figure 3-24C) and E20-D-SS (Figure 3-24D), to 400ml of ethanol in the E20-S (Figure 3-24E)and E20-SS (Figure 3-24F) columns, and finally the E85-S column (Figure 3-24H) with 1,700 ml of applied ethanol, indicating an increase in the relative proportion of Mn, Fe and Mg to Ca as the applied ethanol content increases. Taking a closer look at the average dissolved Fe and Mn in each column with respect to applied ethanol content, the data reveals a significant correlation ($p < 0.05$) with the amount of ethanol applied to the column and the amount of metal mobilization (Figure 3-25). The anaerobic degradation pathway is much different than the aerobic pathways, in that anaerobic microbes require a more complex consortium to oxidize a wide range of organic compounds. In addition, microbes are often limited to certain types of organic compounds (Lovley, 1995, 1991). For example, Fe-reducers can

only oxidize simple organic acids, LCFA's, monoaromatic compounds (Lovley and Chapelle, 1995) and ethanol (Lovley and Phillips, 1988). Therefore, the correlation between increasing ethanol content and dissolved metals (Mn and Fe) is likely a result of the increase in available substrate for microbial Mn-oxide and Fe-oxide reductions to occur. Since the higher ethanol-blended fuels contain a higher fraction of simple organic molecules, i.e. ethanol, these reduction reactions are more likely to occur, producing elevated groundwater concentrations of Fe^{2+} and Mn^{2+}. In addition, the arrival of Mn before Fe is generally consistent throughout the experiments and in-line with the redox sequence, providing further support for microbial reductive dissolution reactions involving Mn-oxides, and Fe oxides.

In conclusion, both ankerite dissolution and microbially mediated reductive dissolution reactions are likely contributing to the dissolved metal content in groundwater; however, without pH data it is difficult to determine the relevance of ankerite dissolution compared to Mn-oxide and Fe-oxide reduction. In addition, increasing the ethanol content in fuels resulted in an increase in groundwater Mn and Fe mobilization, likely occurring from increased microbial reduction activity of Mn-oxides and Fe-oxides reacting to the increase in available substrate.

3.5.4 What are the Dominant Redox Conditions Likely to be Found Within the Plume Zone of an Ethanol-Blended Fuel Spill?

In general, there was a significant vertical oxygen decline in most columns, despite a constant source of atmospheric oxygen in the headspace. This decline in O_2 is related to the consumption of O_2 through aerobic respiration. In general, there was a significant decline in column O_2 suggesting that aerobic respiration was an important pathway in almost every column, with the exception of E85-S and E20-S. The columns that did not show an oxygen decline are the same columns that showed the highest levels of butyric acid (Figure 3-2F, Figure 3-7F), i.e. the columns

possessing the largest fraction of ethanol. As previously mentioned, butyric acid is an indicator for microbially stressed conditions, therefore the data suggests that the aerobes were negatively affected by the ethanol resulting in a decline of aerobic respiration relative to the other columns. It should be noted that for the columns that showed minimal aerobic respiration, the total calculated mass loss was significantly lower than for the columns with a significant decline in O_2 from aerobic activity (Figure 3-14), suggesting that aerobic degradation was the dominant degradation pathway.

The saturated zone data provided evidence towards anaerobic degradation via the presence of VFAs, dissolved Mn^{2+} and Fe^{2+}. Other indicators such as SO_4^{2-} and NO_3^- were not sampled for as there were no known sources of sulphate, or nitrate in the sediments. As previously mentioned, the occurrences of these anaerobic indicators occurred to a greater degree in columns with higher ethanol content, suggesting a greater capacity for anaerobic degradation in ethanol blended fuels. Methanogenic activity appeared to be higher in the ethanol blended fuel columns compared to the pure gasoline columns. Surprisingly, there did not appear to be a correlation between methanogenic activity and ethanol content, nor was there a correlation between methanogenic activity and acetate content.

Combining the results from the vadose and saturated zones, illustrates that methanogenic conditions can exist within an LNAPL ethanol-blended fuel spill, despite having an entirely oxic vadose zone. Therefore, the existence of a strong redox gradient and/or the development of micro-niches results in a variety of redox conditions on the scale of centimeters.

3.5.5 Can the Use of Stable Isotopes Aid in Identifying the Specific Hydrocarbon Sources Predominantly Undergoing Biodegradation?

The $^{13}C - CO_2$ results reveal that stable isotopic analysis is well suited for identifying CO_2 originating from either ethanol or gasoline biodegradation. Since the stable isotopic signature

changes over time due to kinetic isotopic fractionation, it is difficult to determine the exact proportion of CO_2 resulting from ethanol biodegradation, for instance, as both gasoline and ethanol sources are continually evolving isotopically. In this case, the gasoline isotopic CO_2 data provided an expected baseline for the level of fractionation, allowing for a more precise understanding of the influence of ethanol-derived CO_2 and vice versa. The results from the study revealed shifts in the prevailing microbial substrates, proving to be valuable when assessing toxicity related concerns as a function of ethanol content. These results were corroborated with ^{14}C data, which aided in determining the proportion of modern carbon stemming from ethanol degradation. Although not intended, stable isotopes were also able to identify the influence of atmospheric contamination on the $^{13}CO_2$ signature produced through biodegradation of the gasoline in the Gas-SS column. The utility of this method is limited to scenarios when there are only two main sources of carbon with distinctively different isotopic signatures undergoing biodegradation. In the case of ethanol blended fuel spills, this technique proved to be invaluable in determining the evolution of the primary microbial substrate. These isotopic techniques can also be a useful tool in site assessment.

3.5.6 Is There an Effect on the Biodegradation of Benzene and Toluene in the Presence of Varying Ethanol Contents?

Benzene and toluene concentration data were collected between week 2 and week 35 during this study. Due to laboratory issues, benzene and toluene concentrations were not measured for the remainder of the 72 week experiment. Maximum and average benzene and toluene concentrations both near the spill (120 cm below the soil surface) and near the surface (25 cm below the soil surface) were plotted against the applied ethanol contents of the fuel. There was no apparent trend between ethanol content and surficial concentrations of benzene and toluene (Figure 3-26, Figure 3-15,Figure 3-16). Near spill concentrations did not show a trend when examining the benzene

and toluene vs applied ethanol content (Figure 3-26). Vertical toluene profiles did not show a correlation with near spill vadose zone concentrations and ethanol content (Figure 3-16); however, upon closer inspection of Figure 3-15, benzene concentrations are noticeably higher near the spill in the gasoline columns, compared to the ethanol-blended fuel columns. Presumably, since the gasoline columns contain a greater benzene and toluene content, higher levels of benzene and toluene would be expected just above the surface. This is true for benzene, surprisingly; however, toluene does not appear to be significantly higher in the gasoline columns.

The experimental observations of vadose zone benzene and toluene near the soil surface, provide information on the potential for human health risks from a shallow subsurface ethanol-blended fuel release. According to Health Canada, human exposure to benzene at elevated levels between 700 to 3,000 ppm for periods longer than a minute has been linked to dizziness, tremors, nausea, vomiting, headache and drowsiness (Health Canada, 2014). Sub-chronic to chronic exposure to benzene concentrations as low as <1 ppm can lead to progressive deterioration in hematopoietic function including bone marrow damage, changes in circulating blood cells as well as altered immune response (ATSDR, 2007). Benzene has been shown to affect the blood-forming system at low levels of occupational exposure ≤ 1 ppm, and has been classified as a carcinogen (Environment Canada and Health and Welfare Canada, 1993; US EPA, 1998). Similarly, toluene has been demonstrated to cause negative health effects prompting Health Canada to issue guidelines for residential maximum exposure limits for both short-term and long-term exposure. To avoid neurologically-related symptoms such as; headaches, dizziness, and feelings of intoxication, Health Canada recommends that the toluene exposure limit be 4 ppm for short-term exposure, and 0.6 ppm for long-term exposure (Health Canada, 2011).

Table 3-5 provides data on the near-surface maximum and average concentrations of benzene and toluene located approximately 25 cm below the ground surface. Based on these results, there is a potential risk of long-term benzene exposure in the E20 fuel blend columns as 7/7 of the E20-S samples, and 6/7 of the E20-SS samples contained levels of benzene >1 ppm which span weeks 2 to 35 of the experiment. However, it must be kept in mind that these data were collected below the ground surface and that additional dilution occurs during egress to the surface or intrusion into buildings. None of the maximum concentrations observed were remotely close to the exposure limit for short-term benzene exposure, which ranges between 700 to 3,000 ppm according to Health Canada. In contrast, the results of the study conclude that the majority of near surface toluene concentrations (with the exception of the Gas-SS column) exceed both the long-term exposure limit of 1 ppm, and the short term exposure limit of 4 ppm set out in the guidelines for residential indoor toluene concentrations set out by Health Canada. Again, these concentrations are measured below the ground surface and additional dilution will occur during egress towards the surface or soil vapor intrusion into buildings. In conclusion, the study reveals the highest risk for long-term benzene exposure for the E20 fuel columns, while both short-term and long-term toluene exposure limits were exceeded in soil gas for the majority of the columns spanning several fuel blends (gasoline, E10, E20-delay and E20 fuels).

3.5.7 Is There a Potential for Increased Risk of Soil Vapor Intrusion (SVI) for Sites with Specific Soils and/or Certain Ethanol-Blended Fuels?

The risk for SVI will depend greatly on the amount of CH_4 and CO_2 generated and the ability for these gases to migrate to the surface into a potential receptor such as a basement. Migration of gases occurs primarily through diffusion; however, in some cases advection may occur if gas generation is significant enough to produce a pressure gradient. As previously mentioned,

accidental air ingress produced an internal pressure gradient resulting in an artificially induced advection in some columns, which would have overprinted evidence of a naturally produced pressure gradient. In addition, varying levels of accidental air ingress resulted in enhanced biodegradation through bioventing, producing more CO_2. However, oxygen ingress will dampen the CO_2 concentration gradient. The resulting outcome on the column efflux from the sum of these two effects in the affected columns can be examined in the individual column geochemistry data sets post week 71, when the headspace pumping system was modified to remove the internal pressure gradients leading to the accidental air ingress. In the affected columns; E20-D-S, E20-D-SS, E10-S, and E20-SS, the data reveals an increase in basal column CO_2 concentrations ranging from factors of approximately 2 to 3. Therefore, column effluxes could be 2 to 3 times greater for these columns, if based solely on diffusion. Since the historical effects of the leaks cannot be quantified, our flux estimates for the affected columns can only be described as a conservative baseline.

To put the soil CO_2 and CH_4 fluxes into perspective, Table 3-6 provides the results from this study and compares them to results from previous field studies where CO_2 and CH_4 fluxes were measured directly in the spill zone. The three sites include soil fluxes from: a) the Bemidji, Minnesota site, where approximately 1,700,000 L of crude oil was spilled due to a pipeline rupture in 1979 (Warren et al., 2014) , b) the Balaton Minnesota site, which saw the accidental release of ~ 150,000L of denatured fuel grade ethanol (DFE), an E95 blend (Sihota et al., 2013), as well as c) the Cambria Minnesota site, where approximately 95,000 L of E95 (DFE) fuel spilled into the subsurface following a train car derailment (Sihota et al., 2013). Despite a major clean-up at both the Bemidji site, an estimated 25% of the oil has remained and infiltrated into the subsurface, forming an oil body approximately 3,200 m^2 (Essaid et al., 2011; Warren et al., 2014). Based on

this observation, it can be estimated that for every square meter of the oil body contains approximately 133 L of crude oil. Similarly, following a site clean-up at the Balaton site and Cambria site, (Spalding et al., 2011) estimated that approximately 38,000L and 50,000L of DFE remained in the soil and aquifer, respectively. Based on the report by Spalding et al. (2011), the spill footprint at the Balaton site is approximately 2,500 m^2, therefore for every square meter of soil there was approximately 15 L of E95. In the same report Spalding et al. (2011) delineated a spill zone with an approximate area of 2,700 m^2 between the two pools of E95 at the Cambria site, resulting in approximately 18.5 L of E95 for every square meter of affected soil. In contrast, the columns received ~2L of fuel, and based on the column diameter, the calculated volume of fuel per square meter of surface area ranged from 23 to 28 L. Based on this observation, the loading per unit area in the column spill is comparable to that of both the DFE spills in Balaton and Cambria. Interestingly; however, the column surficial fluxes of CO_2 are significantly smaller than the fluxes measured 6 and 8 years after the initial spill at both the Cambria and Balaton site, respectively. In addition, the high ethanol content in the DFE spills (E95) did not appear to affect the amount of CO_2 and CH_4 generation. This suggests that, while the field studies showed significant rates of CO_2 production, our study showed significant inhibition of biodegradation capacity within the first year and a half due to ethanol toxicity. Therefore, it may take years before soil vapor intrusion of CO_2 or CH_4 may be a problem at sites with a significant source of high ethanol content fuels. In addition, it is possible that soil fluxes of CO_2 at the DFE spill sites may be comparable to the columns affected the most by the leaks; however, this remains speculative.

Additionally, given the rather distinct behavior in select columns (i.e. development of a perched water table in Gas-SS, and an increased toxicity effect in the E20-S column), the discussion related to soil type and gas migration is focused only on the E20-delay sand and silty-

sand columns. Regarding the benzene and toluene near-surface data, the average concentrations remain largely the same between the sand and the silty sand columns (Table 3-5). In addition, the CO_2 soil effluxes for the sand (10-25 μmol m^{-2} s^{-1}) are comparable to the silty-sand column (10-20 μmol m^{-2} s^{-1}) (Table 3-6). In summary, based on the current experimental results, there does not appear to be a significant difference in the risk for SVI in columns with an order of magnitude difference in soil permeability.

Lastly, the development of a perched water table in the Gas-SS column provided insights into soil gas migration when there is an impermeable layer above a gasoline spill. As expected, there was a significant reduction in the aerobic biodegradation capability. The lack of VFAs and dissolved metals, which was also found in the Gas-S column points towards a limit in anaerobic biodegradation capacity. Therefore, gasoline spills with overlying impermeable units may be more difficult to degrade using natural attenuation methods, possibly resulting in longer-term contamination problems.

3.5.8 How Do the Biodegradation Rates Compare to Previous Studies?

Biodegradation rates for the columns were calculated based on average measured CO_2 effluxes and an assumed spill zone thickness of 30 cm. Calculated rates are presented in (Table 3-7). Rates derived from the column experiments are compared with biodegradation rates calculated from ethanol laboratory microcosms conducted by Corseuil et al. (1998b) and Wilson et al. (2016), as well as rates from field studies involving DFE spills (Sihota et al., 2013) and crude oil (Sihota and Mayer, 2012). Columns affected by accidental air ingress produced the greatest average biodegradation rates ranging from 45.4 μmol C m^{-3} s^{-1} to 110.0 μmol C m^{-3} s^{-1}, which clearly demonstrates the efficacy of biodegradation through unintended bioventing (Table 3-7). In

contrast, the effect of oxygen exclusion on the Gas-SS column produced one of the lowest rates of biodegradation, further illustrating the important role of aerobic degradation on NA of hydrocarbons (Table 3-7). Additionally, the relatively low biodegradation rates for the E85-S column (5.4 μmol C m^{-3} s^{-1}) are consistent with the rates calculated from the E100 microcosms (within a factor of 2, Table 3-7), likely illustrating the toxicity effect of elevated ethanol concentrations, affecting the ability of microbes to degrade high ethanol content fuels. However, the biodegradation rates calculated for the Balaton (20 μmol C m^{-3} s^{-1}) and Cambria (33.5 μmol C m^{-3} s^{-1}) sites, contaminated with E95, are much higher than the E85-S degradation rates calculated in this study, likely resulting from an enhanced period of microbial acclimatization, in addition to the transient effects following spring snow melt, and a decline of the water table. This data suggests that high ethanol content spills may initially show slow degradation rates; however, over time higher degradation rates may evolve, as the toxicity is overcome. Not surprisingly, observed degradation rates in the column experiments were substantially higher than degradation rates seen at the crude oil spill in Bemidji, MN, with the exception of the E20 sand column. The reasons for the slow degradation progress in this column remain unclear.

3.6 Figures

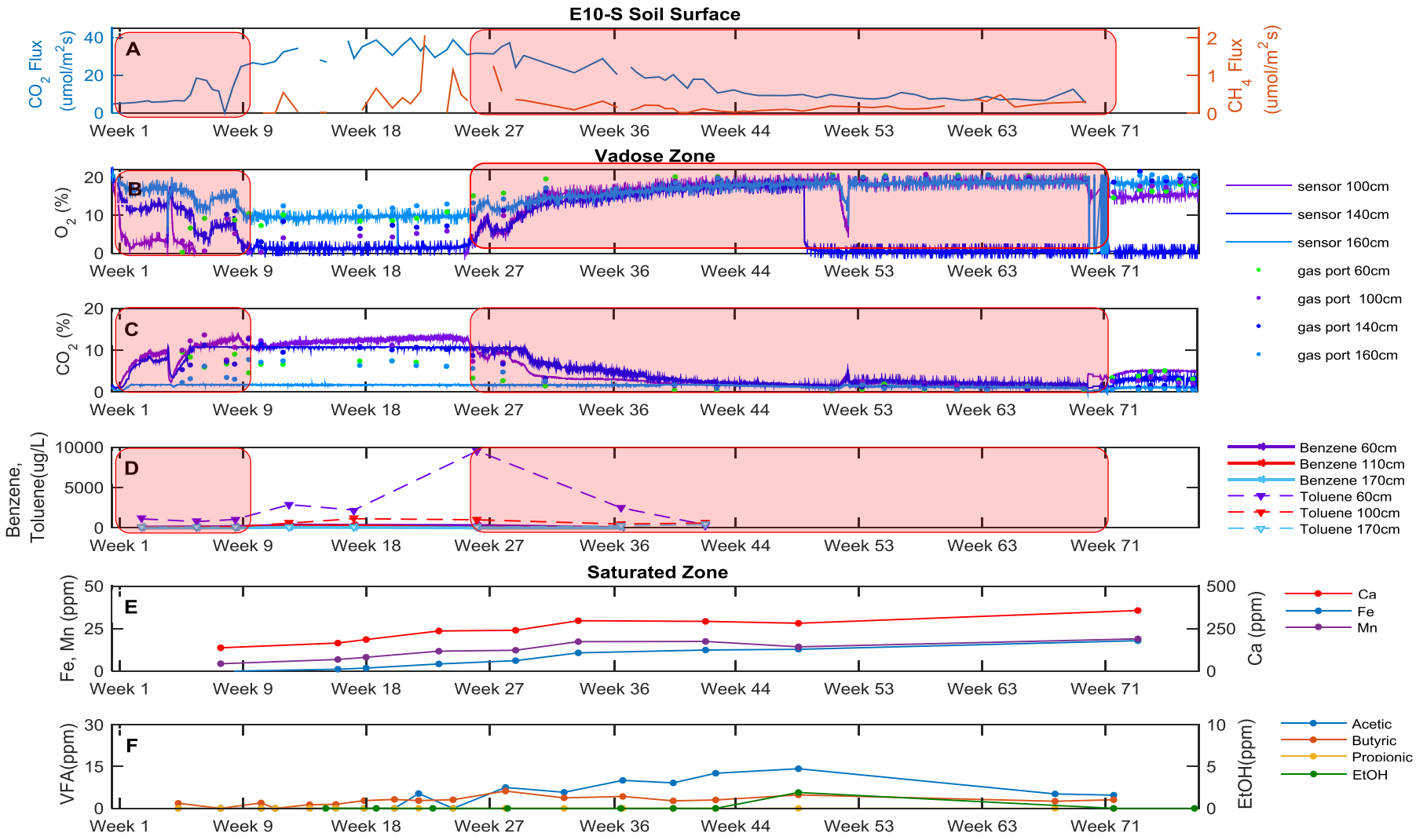

Figure 3-1 E10 sand column data plot. A) Surficial soil CO_2 and CH_4 flux (µmol/m^2.s). B) Soil column O_2 concentration profile (%). Vertically distributed gas sensor data plotted with gas chromatograph measurements from gas ports distributed vertically along the column. C) Soil column CO_2 concentration profile (%). Vertically distributed gas sensor data plotted with gas chromatograph measurements from gas ports distributed vertically along the column. D) Benzene and Toluene vadose zone concentration (µg/L). E) Dissolved metals in the saturated zone (ppm). F) Volatile fatty acids and dissolved ethanol in the saturated zone (ppm). Red zones indicate regions where data has been compromised due to leak development.

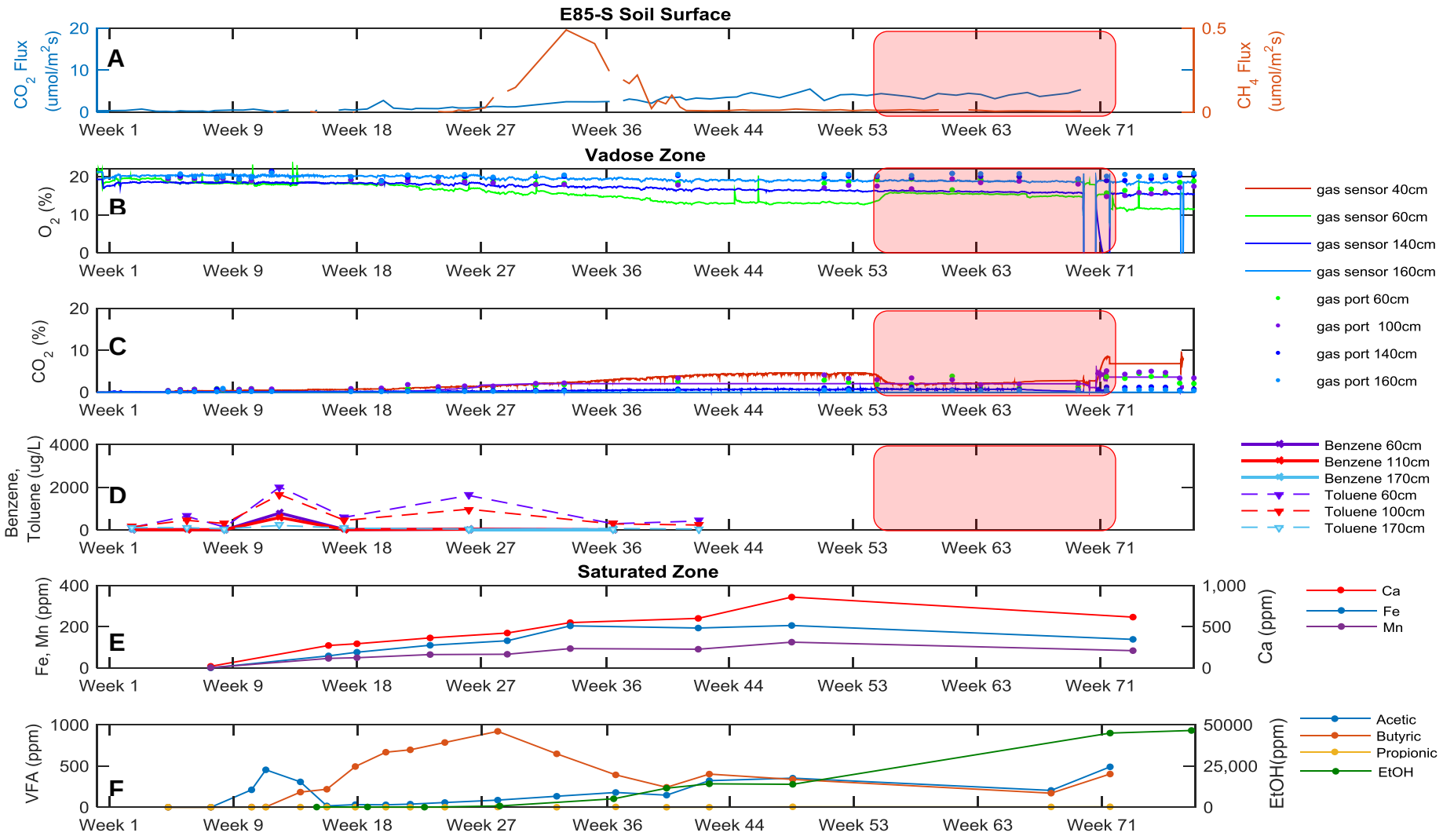

Figure 3-2 E85 sand column data plot. A) Surficial soil CO_2 and CH_4 flux (µmol/m^2.s). B) Soil column O_2 concentration profile (%). Vertically distributed gas sensor data plotted with gas chromatograph measurements from gas ports distributed vertically along the column. C) Soil column CO_2 concentration profile (%). Vertically distributed gas sensor data plotted with gas chromatograph measurements from gas ports distributed vertically along the column. D) Benzene and Toluene vadose zone concentration (µg/L). E) Dissolved metals in the saturated zone (ppm). F) Volatile fatty acids and dissolved ethanol in the saturated zone (ppm). Red zones indicate regions where data has been compromised due to leak development.

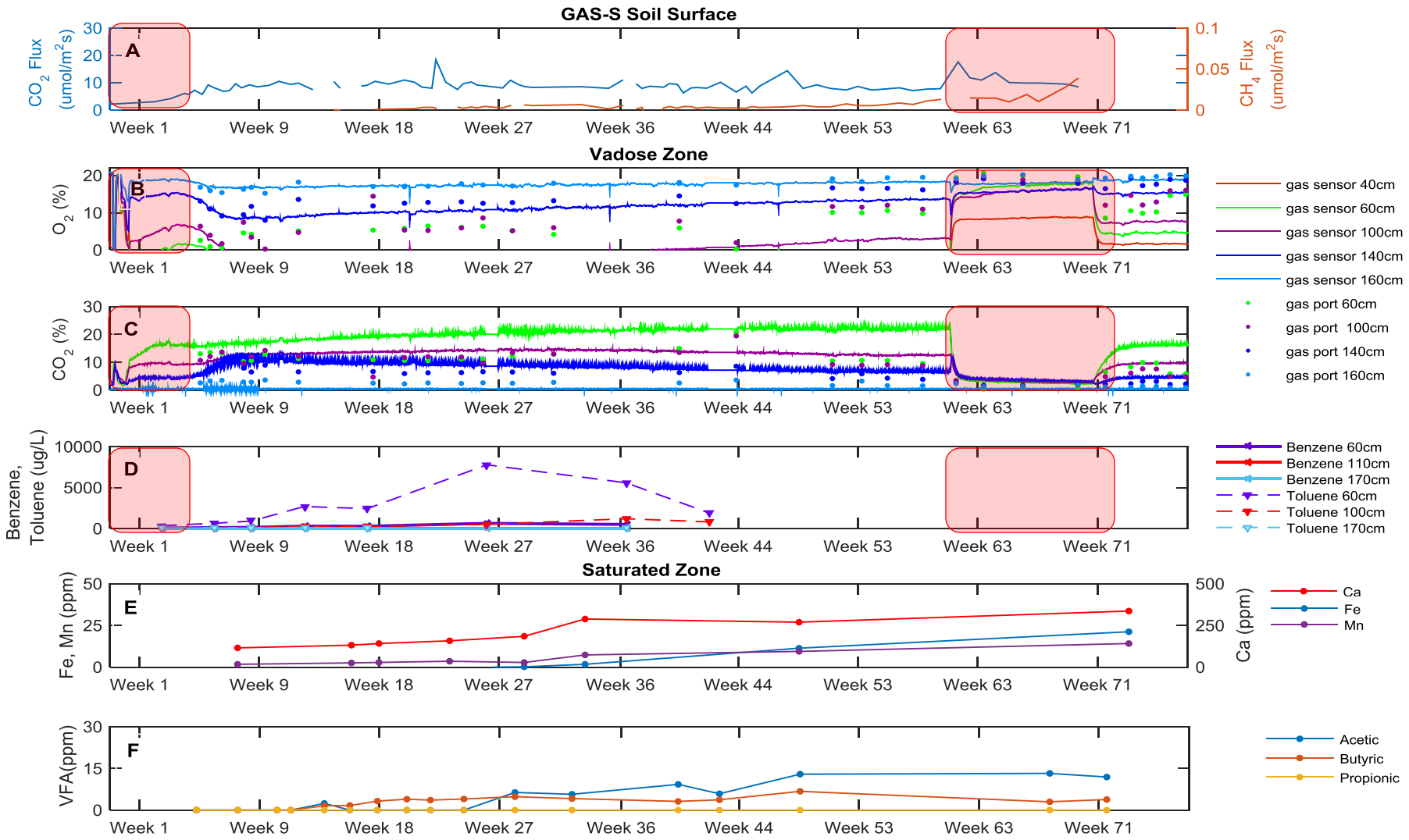

Figure 3-3 Gasoline sand column data plot. A) Surficial soil CO_2 and CH_4 flux (µmol/m^2.s). B) Soil column O_2 concentration profile (%). Vertically distributed gas sensor data plotted with gas chromatograph measurements from gas ports distributed vertically along the column. C) Soil column CO_2 concentration profile (%). Vertically distributed gas sensor data plotted with gas chromatograph measurements from gas ports distributed vertically along the column. D) Benzene and Toluene vadose zone concentration (µg/L). E) Dissolved metals in the saturated zone (ppm). F) Volatile fatty acids in the saturated zone (ppm). Red zones indicate regions where data has been compromised due to leak development.

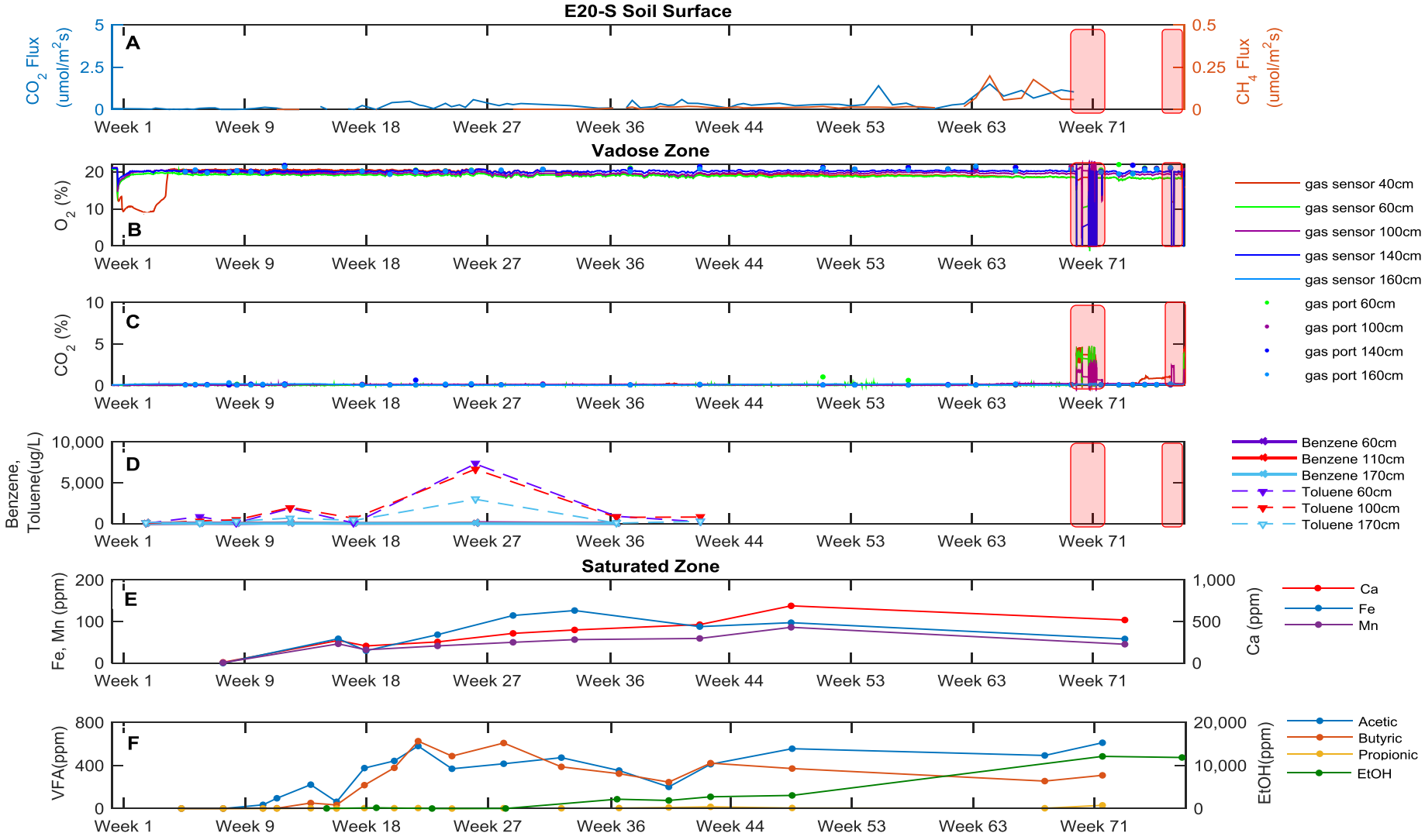

Figure 3-4 E20 sand column data plot. A) Surficial soil CO_2 and CH_4 flux (µmol/m^2.s). B) Soil column O_2 concentration profile (%). Vertically distributed gas sensor data plotted with gas chromatograph measurements from gas ports distributed vertically along the column. C) Soil column CO_2 concentration profile (%). Vertically distributed gas sensor data plotted with gas chromatograph measurements from gas ports distributed vertically along the column. D) Benzene and Toluene vadose zone concentration (µg/L). E) Dissolved metals in the saturated zone (ppm). F) Volatile fatty acids and dissolved ethanol in the saturated zone (ppm). Red zones indicate regions where data has been compromised due to pump removal.

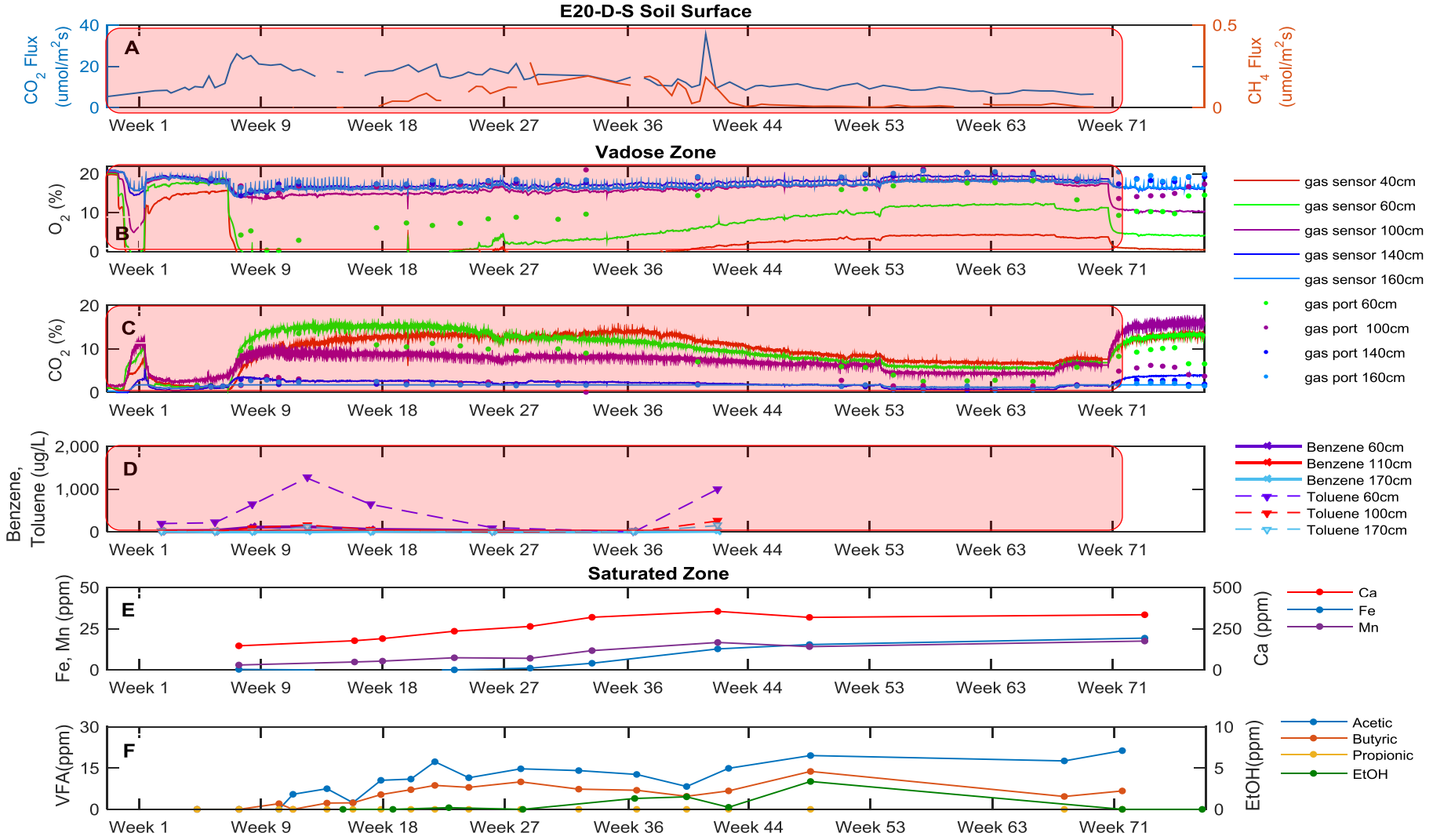

Figure 3-5 E20-delay sand column data plot. A) Surficial soil CO_2 and CH_4 flux (µmol/m^2.s). B) Soil column O_2 concentration profile (%). Vertically distributed gas sensor data plotted with gas chromatograph measurements from gas ports distributed vertically along the column. C) Soil column CO_2 concentration profile (%). Vertically distributed gas sensor data plotted with gas chromatograph measurements from gas ports distributed vertically along the column. D) Benzene and Toluene vadose zone concentration (µg/L). E) Dissolved metals in the saturated zone (ppm). F) Volatile fatty acids and dissolved ethanol in the saturated zone (ppm). Red zones indicate regions where data has been compromised due to pump removal.

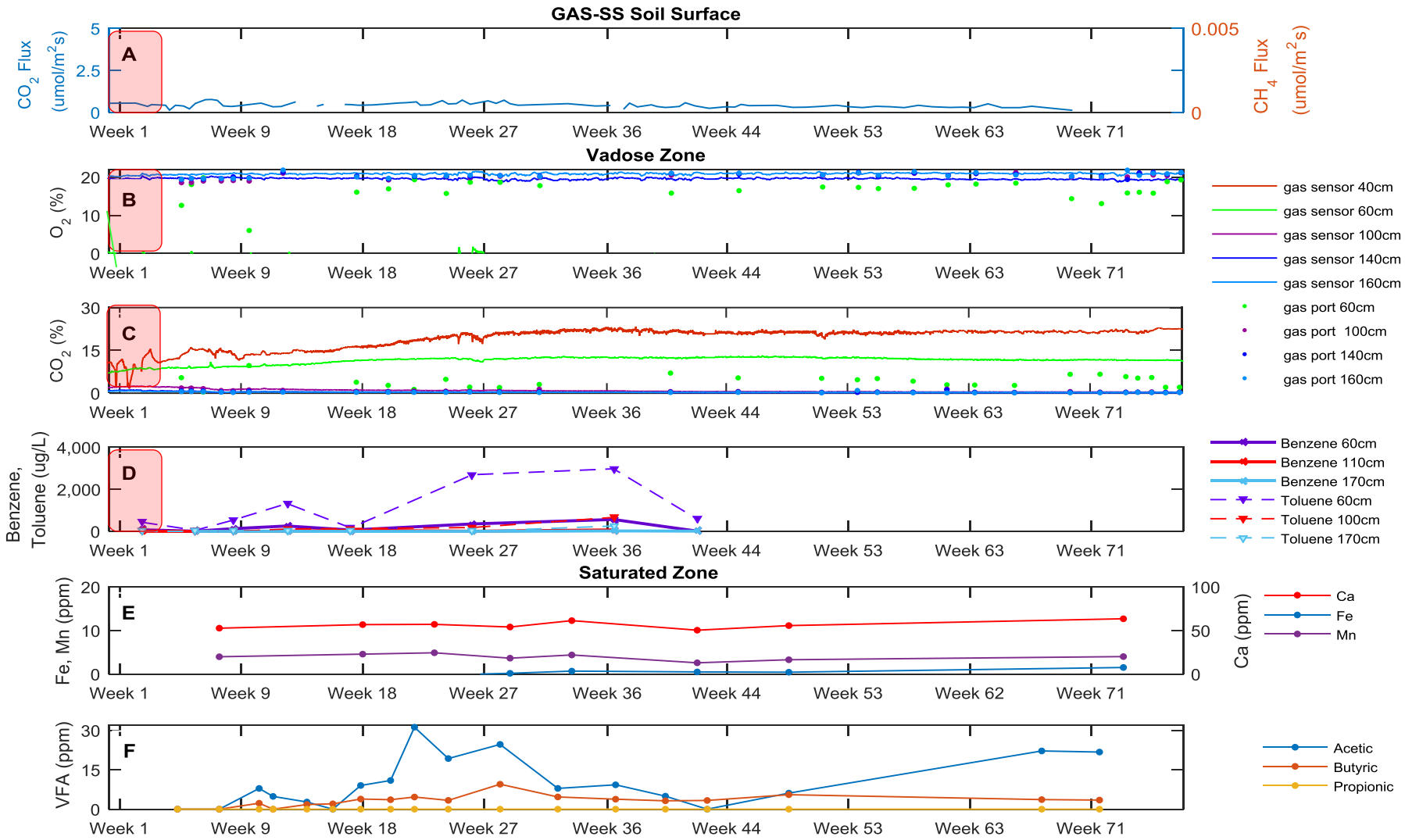

Figure 3-6 Gasoline silty-sand column data plot. A) Surficial soil CO_2 and CH_4 flux (µmol/m^2.s). B) Soil column O_2 concentration profile (%). Vertically distributed gas sensor data plotted with gas chromatograph measurements from gas ports distributed vertically along the column. C) Soil column CO_2 concentration profile (%). Vertically distributed gas sensor data plotted with gas chromatograph measurements from gas ports distributed vertically along the column. D) Benzene and Toluene vadose zone concentration (µg/L). E) Dissolved metals in the saturated zone (ppm). F) Volatile fatty acids in the saturated zone (ppm).

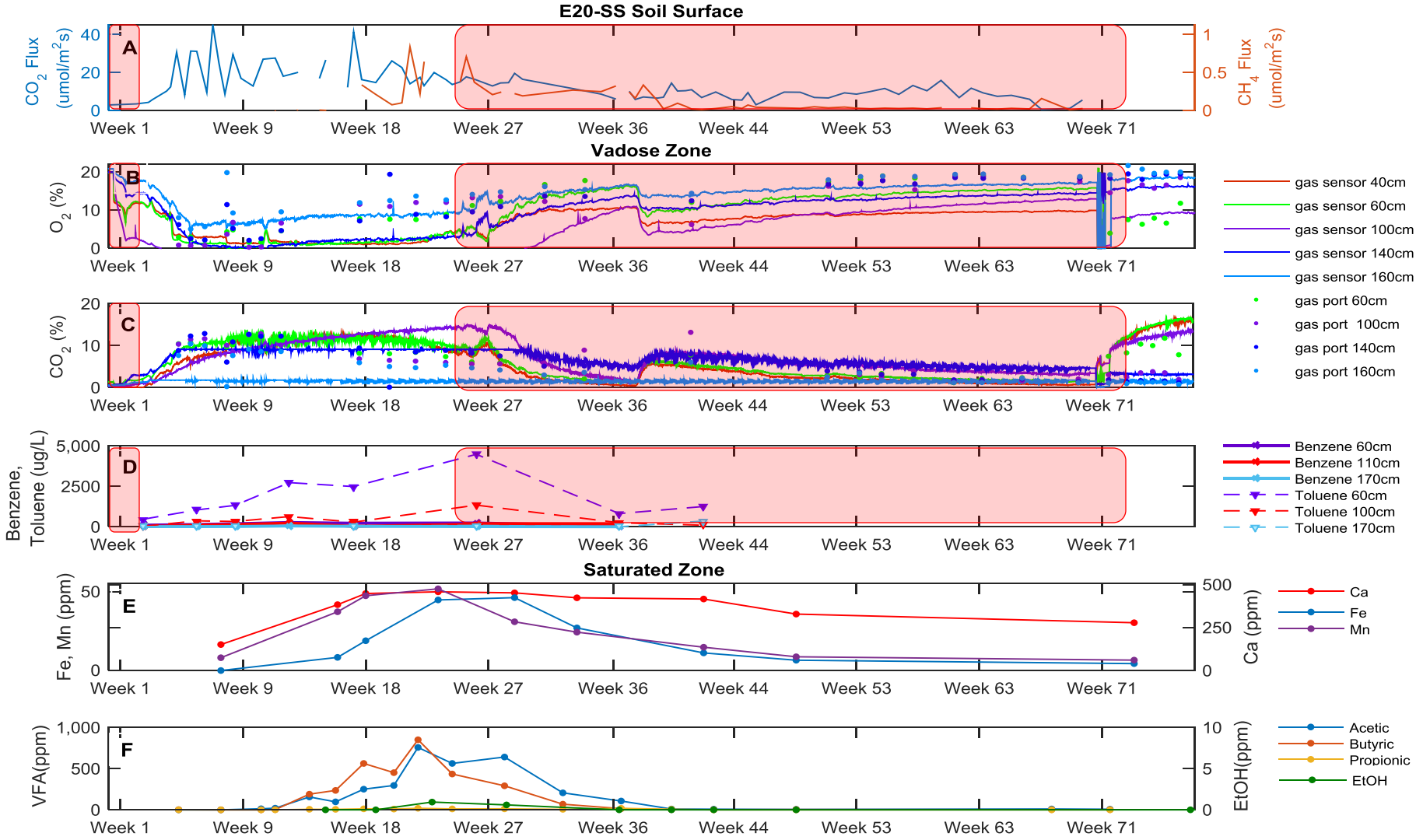

Figure 3-7 E20 silty-sand column data plot. A) Surficial soil CO_2 and CH_4 flux (µmol/m^2.s). B) Soil column O_2 concentration profile (%). Vertically distributed gas sensor data plotted with gas chromatograph measurements from gas ports distributed vertically along the column. C) Soil column CO_2 concentration profile (%). Vertically distributed gas sensor data plotted with gas chromatograph measurements from gas ports distributed vertically along the column. D) Benzene and Toluene vadose zone concentration (µg/L). E) Dissolved metals in the saturated zone (ppm). F) Volatile fatty acids and dissolved ethanol in the saturated zone (ppm). Red zones indicate regions where data has been compromised due to leak development.

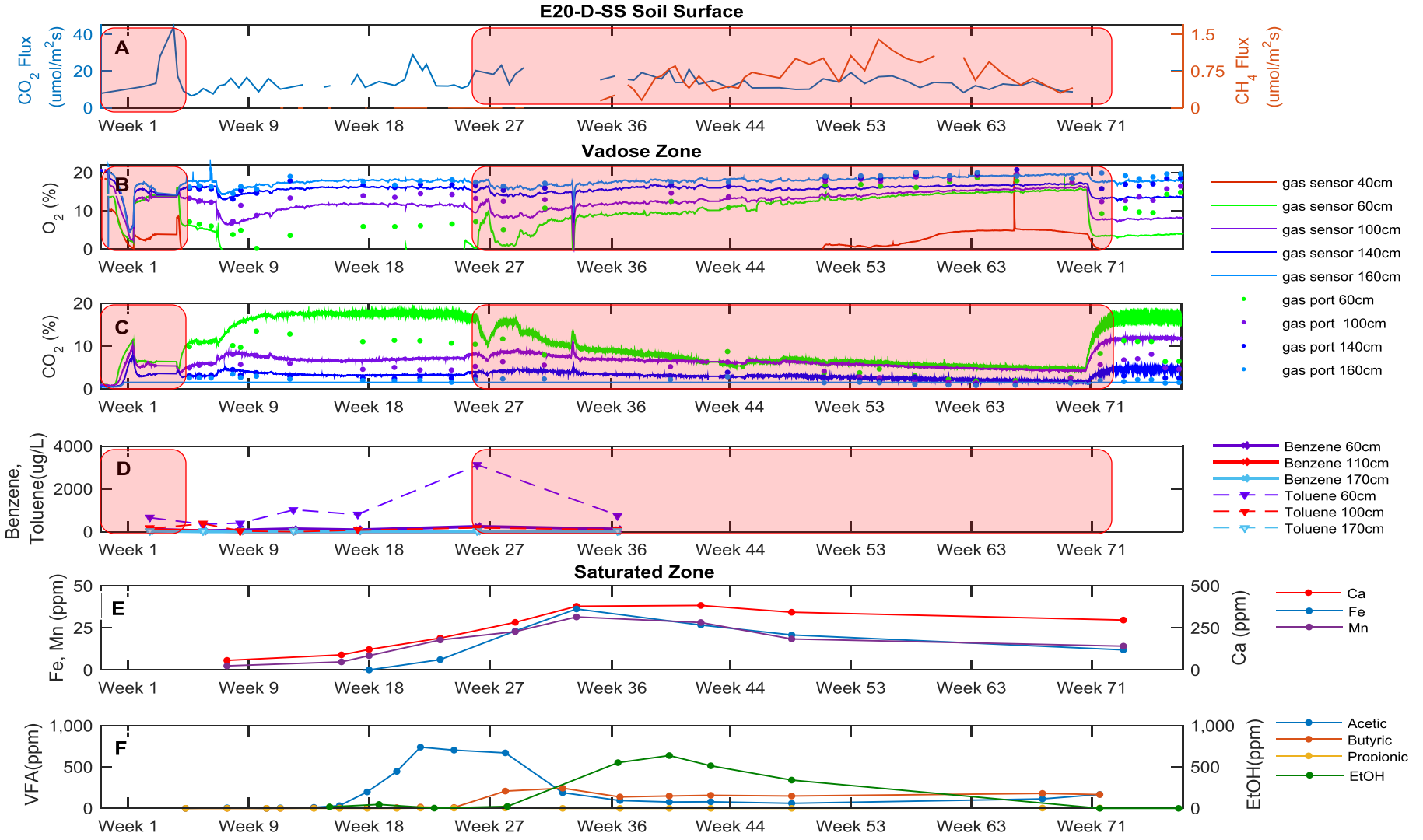

Figure 3-8 E20- delay silty- sand column data plot. A) Surficial soil CO_2 and CH_4 flux (µmol/m^2.s). B) Soil column O_2 concentration profile (%). Vertically distributed gas sensor data plotted with gas chromatograph measurements from gas ports distributed vertically along the column. C) Soil column CO_2 concentration profile (%). Vertically distributed gas sensor data plotted with gas chromatograph measurements from gas ports distributed vertically along the column. D) Benzene and Toluene vadose zone concentration (µg/L). E) Dissolved metals in the saturated zone (ppm). F) Volatile fatty acids and dissolved ethanol in the saturated zone (ppm). Red zones indicate regions where data has been compromised due to leak development.

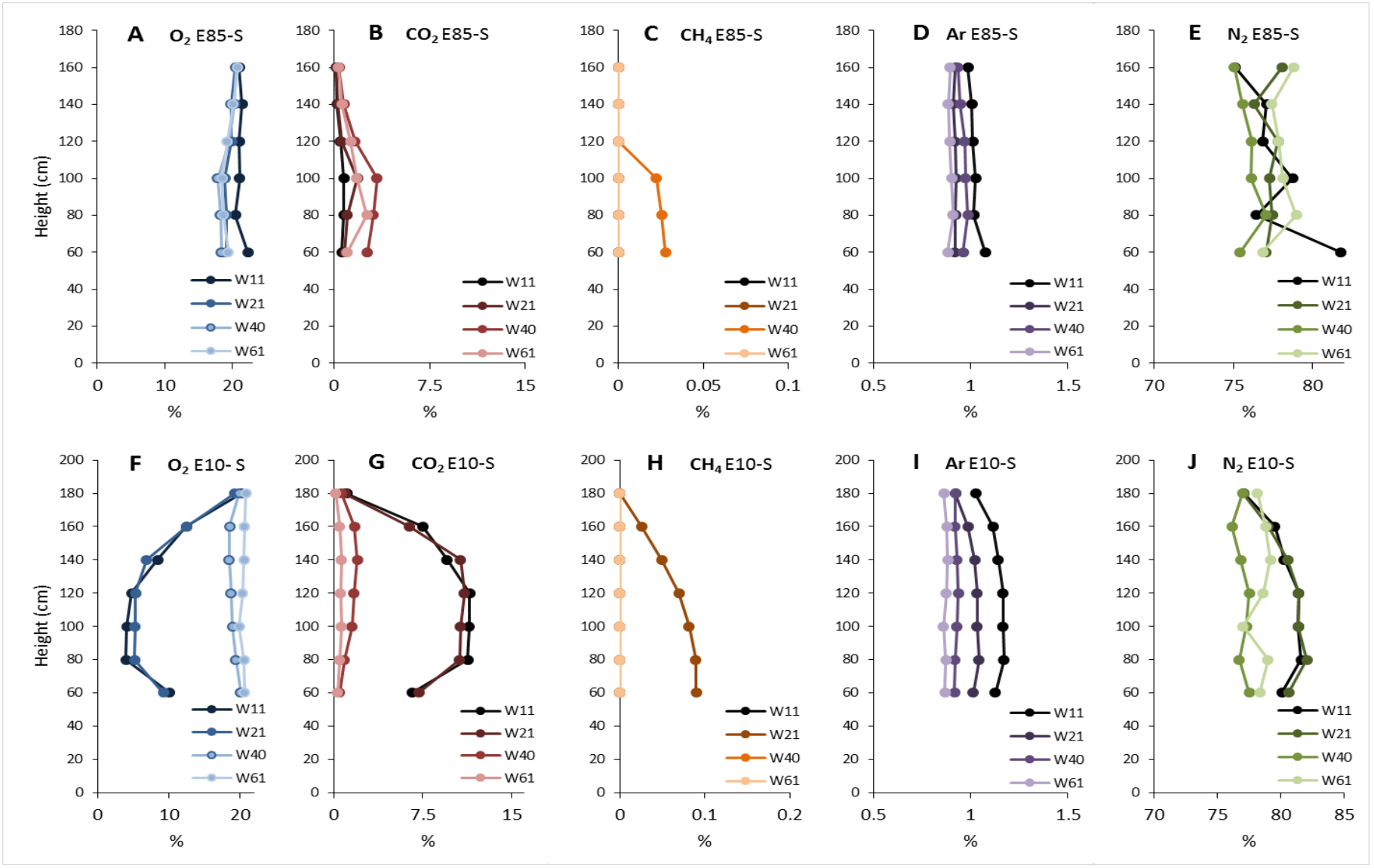

Figure 3-9 Vertical GC data on gas concentrations of O_2, CO_2, CH_4, Ar, and N_2 for the E85-S and E10-S columns for weeks 11, 21, 40 and 61.

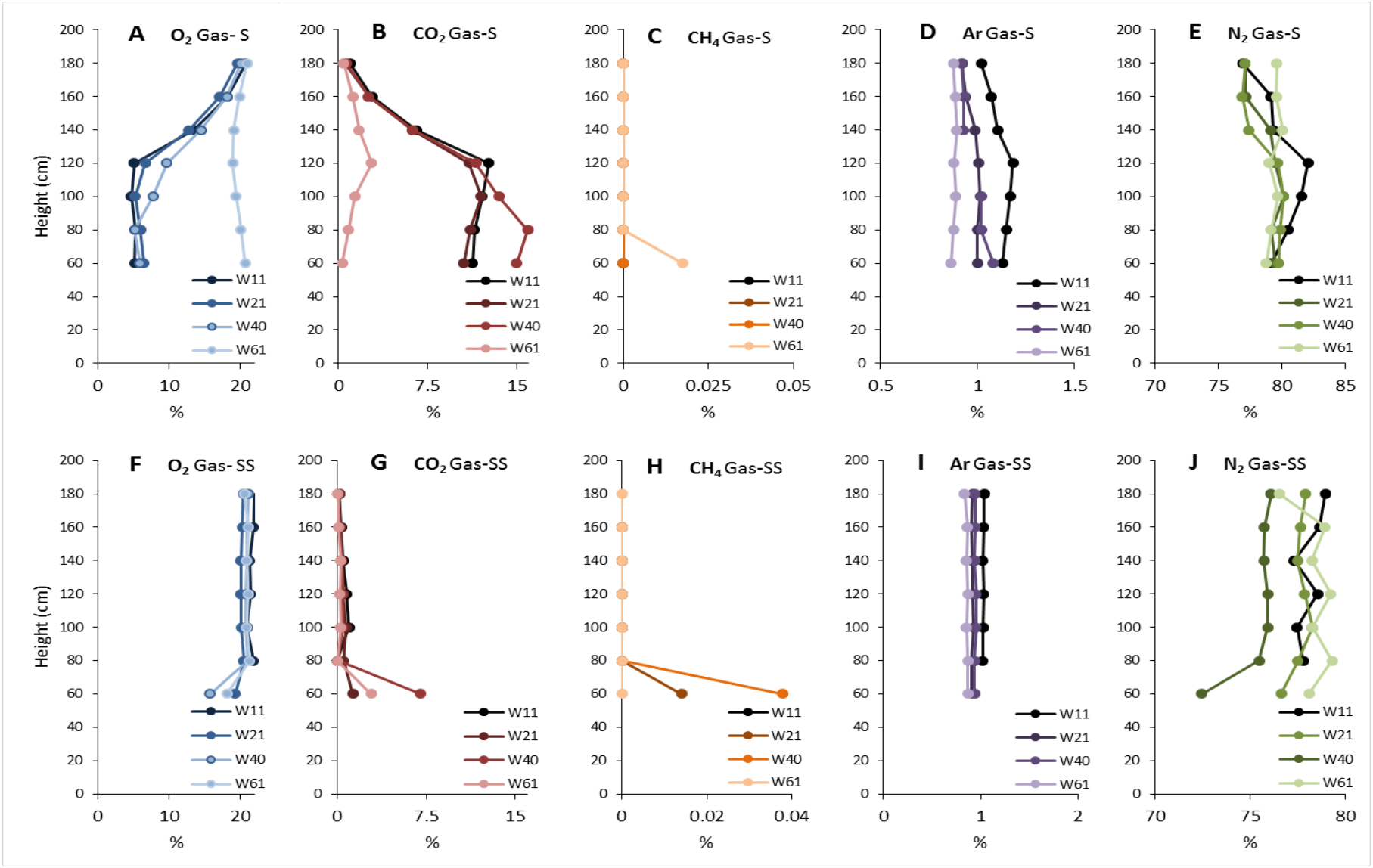

Figure 3-10 Vertical GC data on gas concentrations of O_2, CO_2, CH_4, Ar, and N_2 for the Gas-S and Gas-SS columns for weeks 11, 21, 40 and 61.

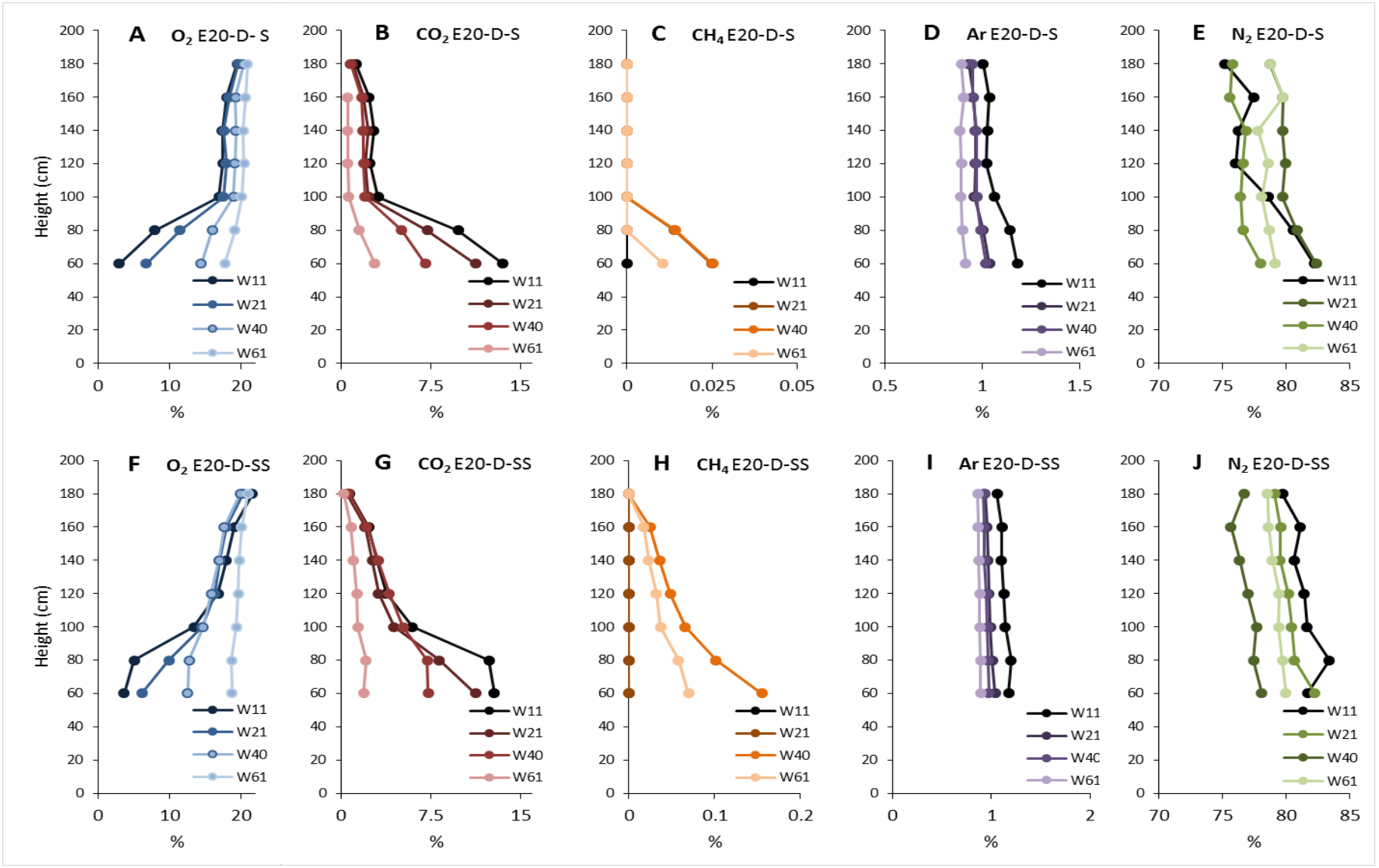

Figure 3-11 Vertical GC data on gas concentrations of O_2, CO_2, CH_4, Ar, and N_2 for the E20-D-S and E20-D-SS columns for weeks 11, 21, 40 and 61.

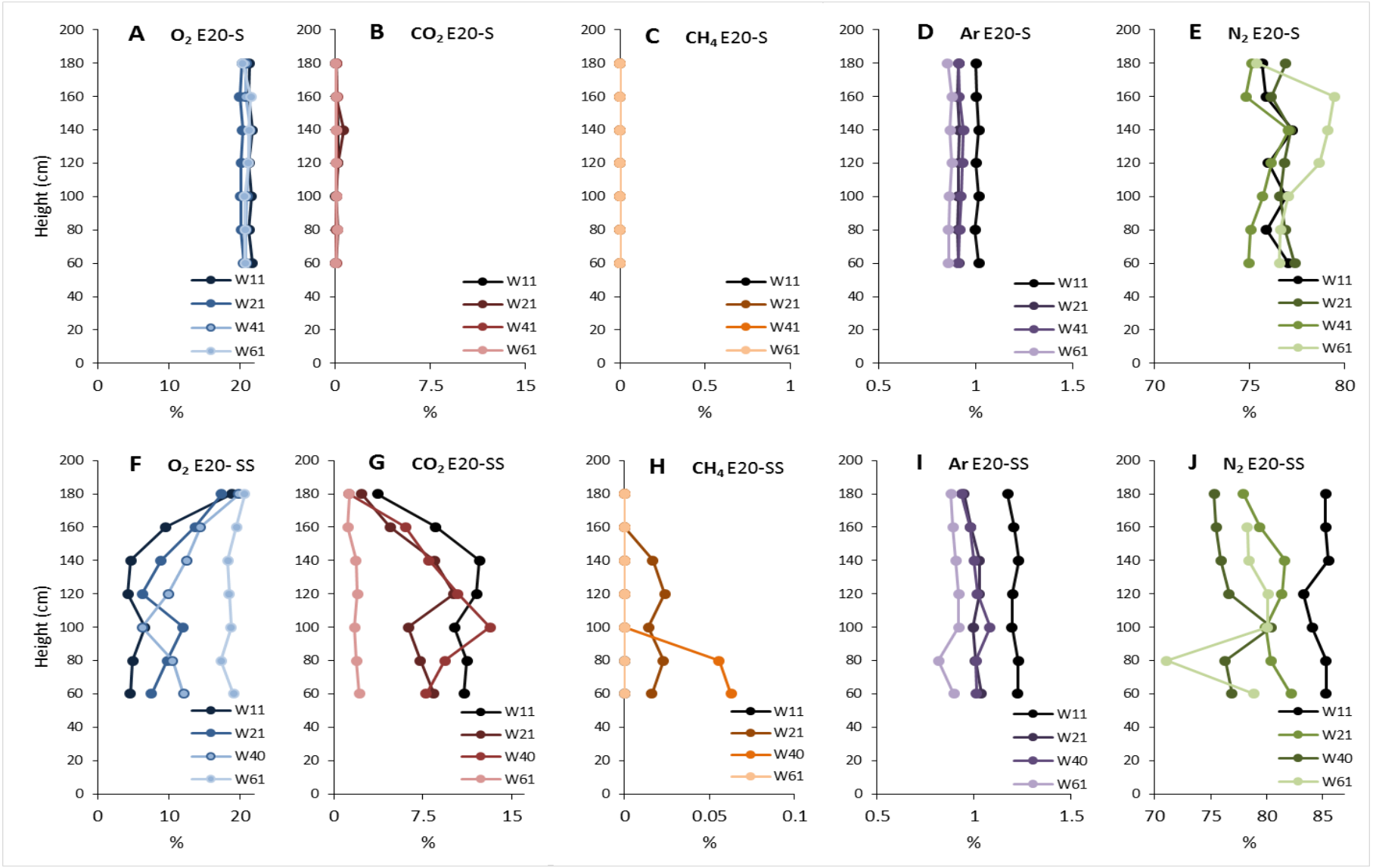

Figure 3-12 Vertical GC data on gas concentrations of O_2, CO_2, CH_4, Ar, and N_2 for the E20 -S and E20-SS columns for weeks 11, 21, 40 and 61.

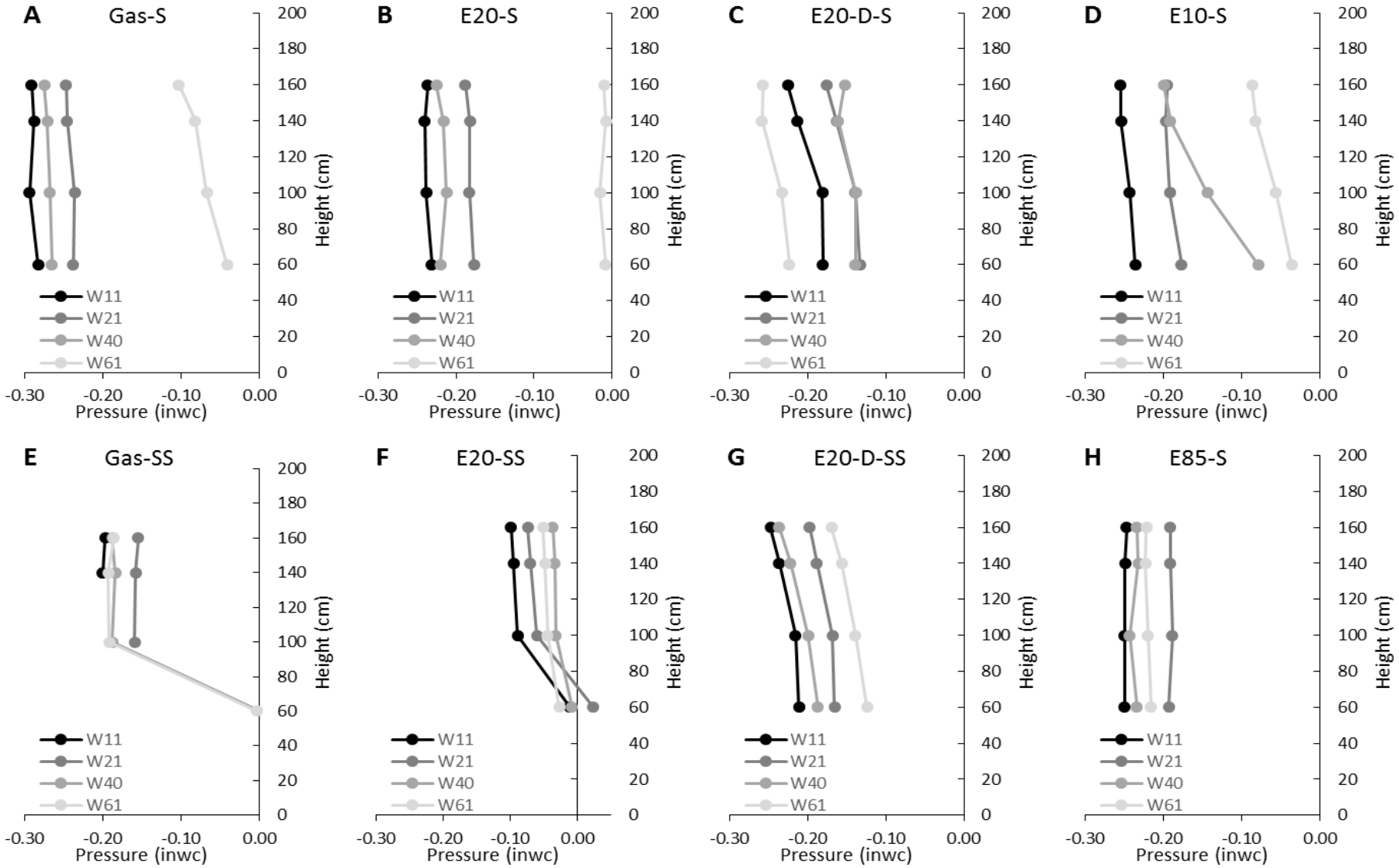

Figure 3-13 Vertical Pressure distribution of all columns during weeks 11, 21, 40 and 61.Pressure units are measured in inches of water (inwc).

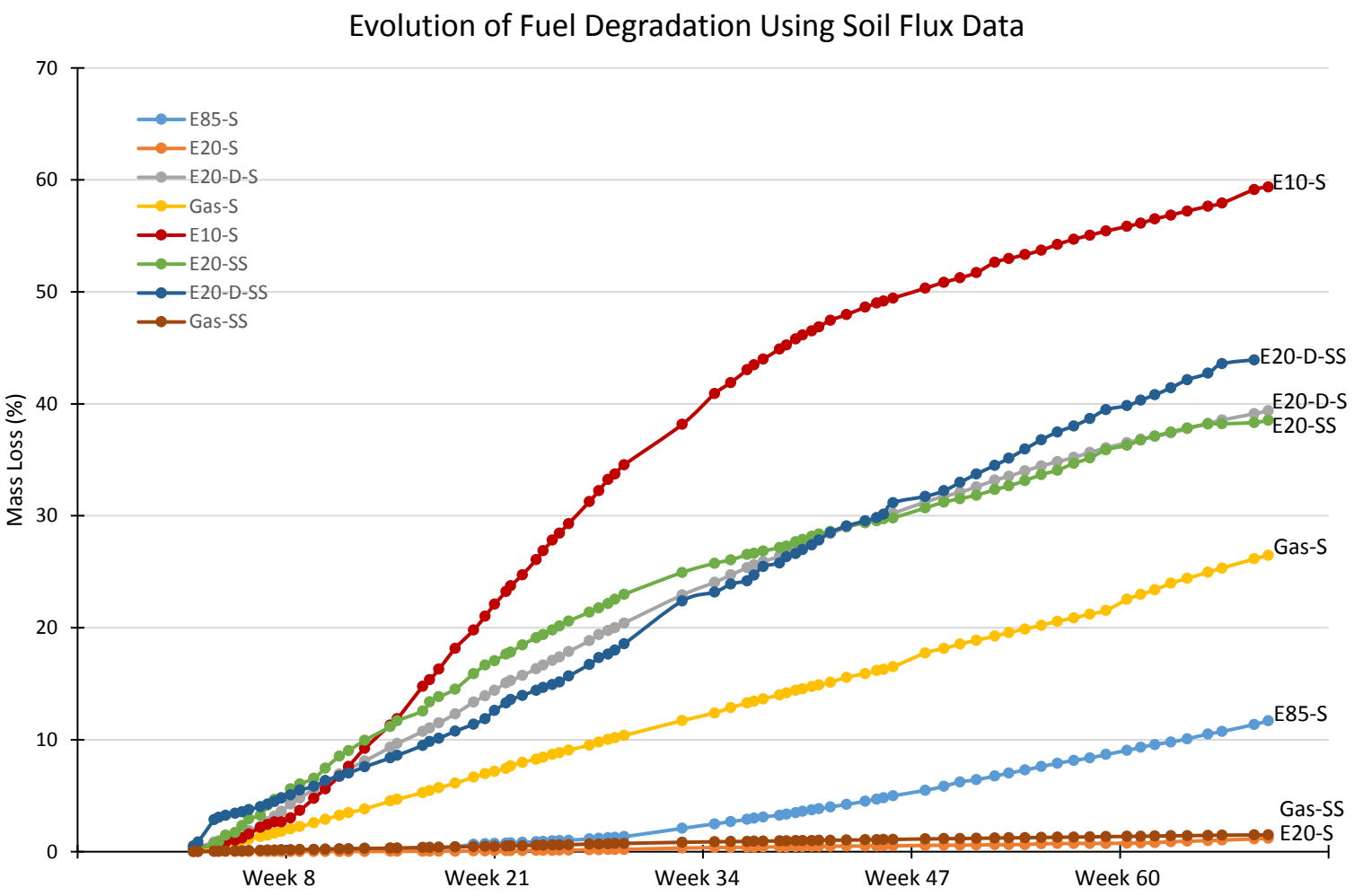

Figure 3-14 Fuel degradation plot shows the total accumulated mass loss (%), throughout the timeline of the experiment. The linear flux values obtained by the soil flux pro ® software was used to calculated mass loss of carbon through CO_2 and CH_4 soil effluxes. The total carbon efflux out of the columns is comparted to the total mass of C injected as fuel, which was calculated based on the proportions of ethanol and gasoline, whereby gasoline is represented as octane (C_8H_{18}).

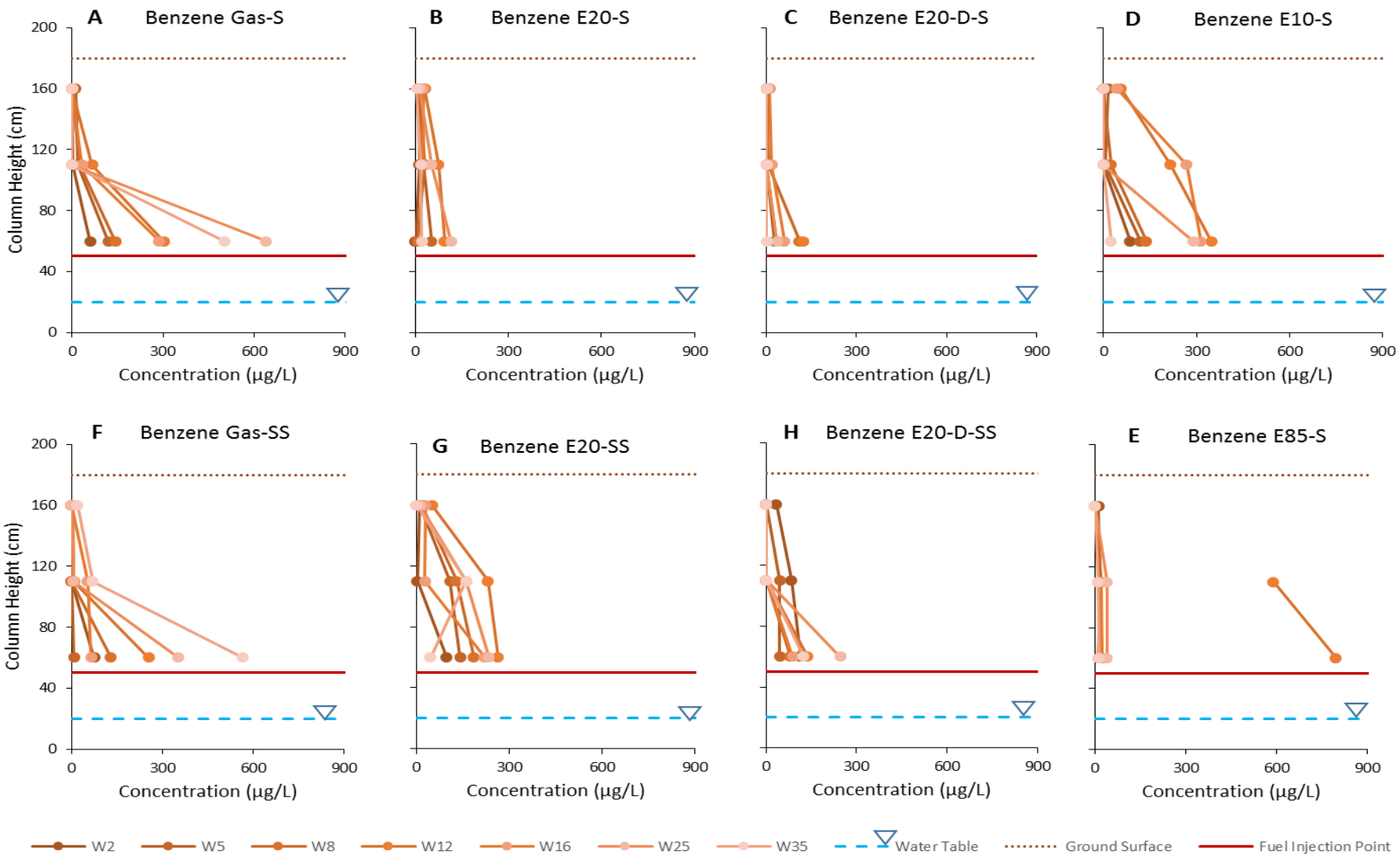

Figure 3-15 Vertical cross section of soil benzene concentrations (µg/L) progressing through each sample week.

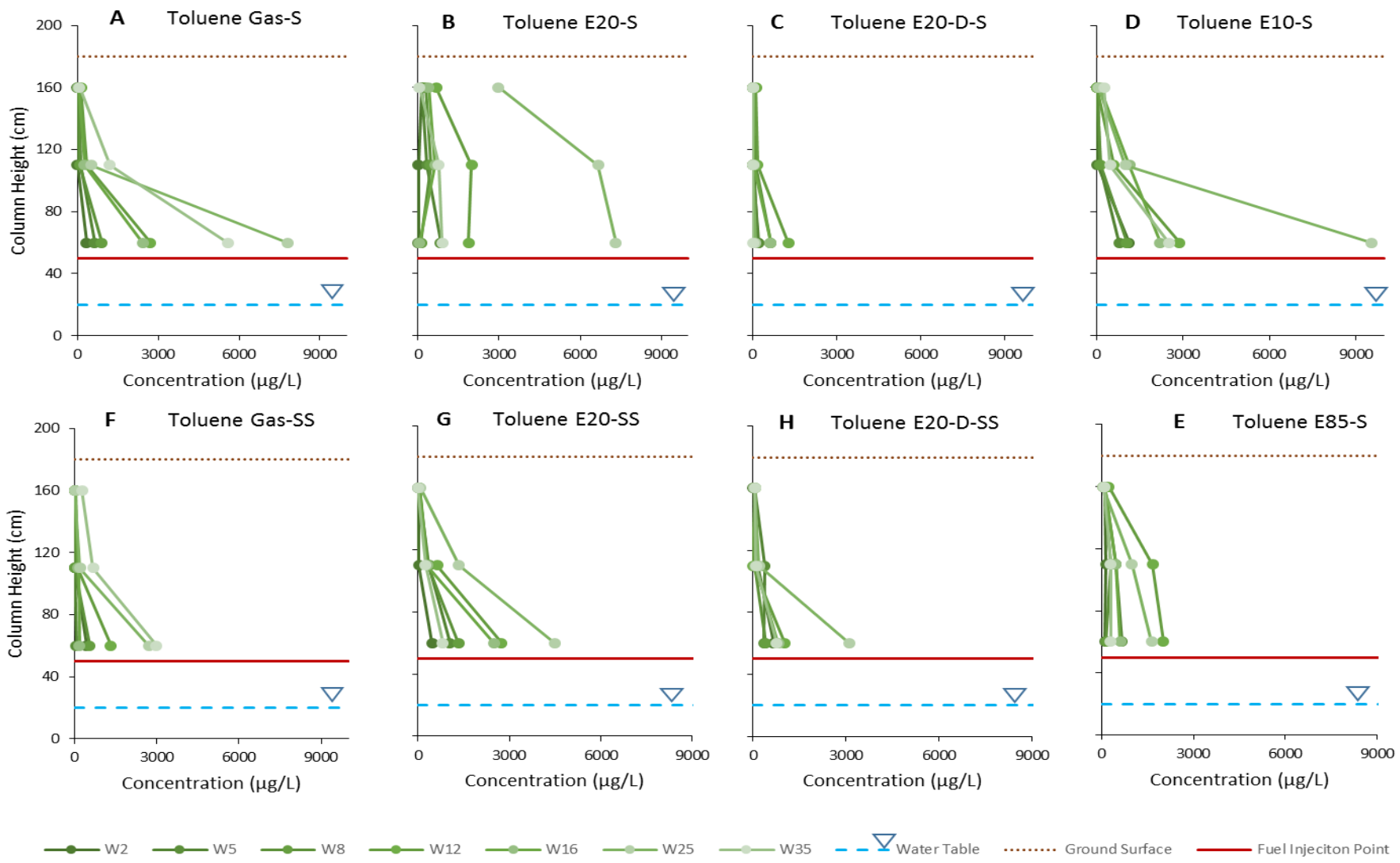

Figure 3-16 Vertical cross section of soil toluene concentrations (µg/L) progressing through each sample week.

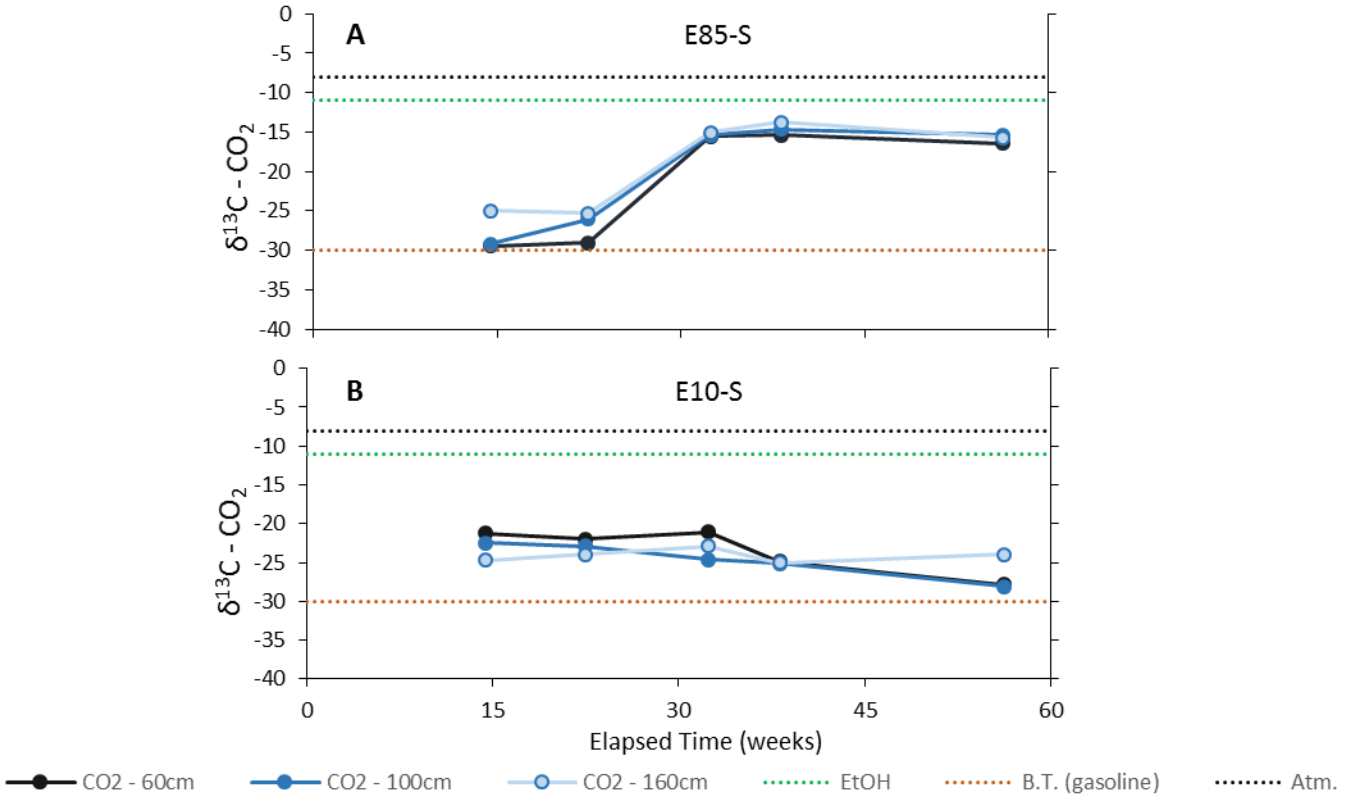

Figure 3-17 Stable isotopic results of CO_2, where CO2-60cm, 100cm, and 160cm represents measurements of ^{13}C of the CO_2 samples at the vertical height of 60cm, 100cm, and 160cm, respectively. . EtOH and B.T. (gasoline) represent the ^{13}C signature of the ethanol and gasoline used in the experiment, while Atm. represents the average composition of atmospheric CO_2 according to Friedli et al., (1986). Figure A is the evolution of the $\delta^{13}C$ in CO_2 in the E85. Figure B is the evolution of the $\delta^{13}C$ in CO_2 in the E10 column.

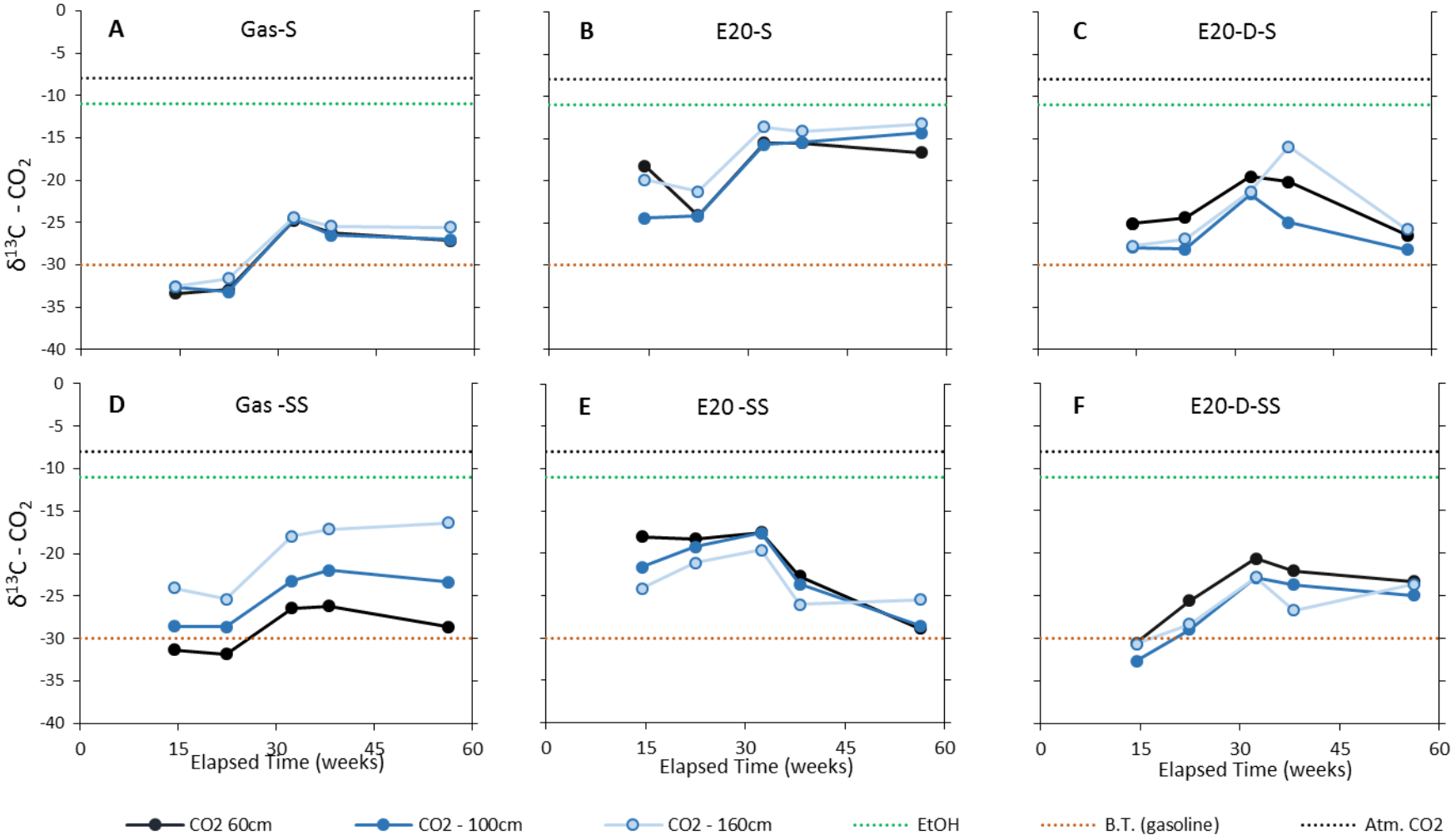

Figure 3-18 Stable isotopic results of CO_2, where CO2-60cm, 100cm, and 160cm represents measurements of ^{13}C of the CO_2 samples at the vertical height of 60cm, 100cm, and 160cm, respectively. . EtOH and B.T. (gasoline) represent the ^{13}C signature of the ethanol and gasoline used in the experiment, while Atm. represents the average composition of atmospheric CO_2 according to Friedli et al., (1986). Figure A is the evolution of the $\delta^{13}C$ in CO_2 in the Gas-Sand Column. Figure B is the evolution of the $\delta^{13}C$ in CO_2 in the E20-Sand column. Figure B is the evolution of the $\delta^{13}C$ in CO_2 in the E20-Sand column. Figure C is the evolution of the $\delta^{13}C$ in CO_2 in the E20-Delay-Sand column. Figure D is the evolution of the $\delta^{13}C$ in CO_2 in the Gas-Silty-Sand column. Figure E is the evolution of the $\delta^{13}C$ in CO_2 in the E20-Silty-Sand column. Figure F is the evolution of the $\delta^{13}C$ in CO_2 in the E20-Delay-Silty-Sand column.

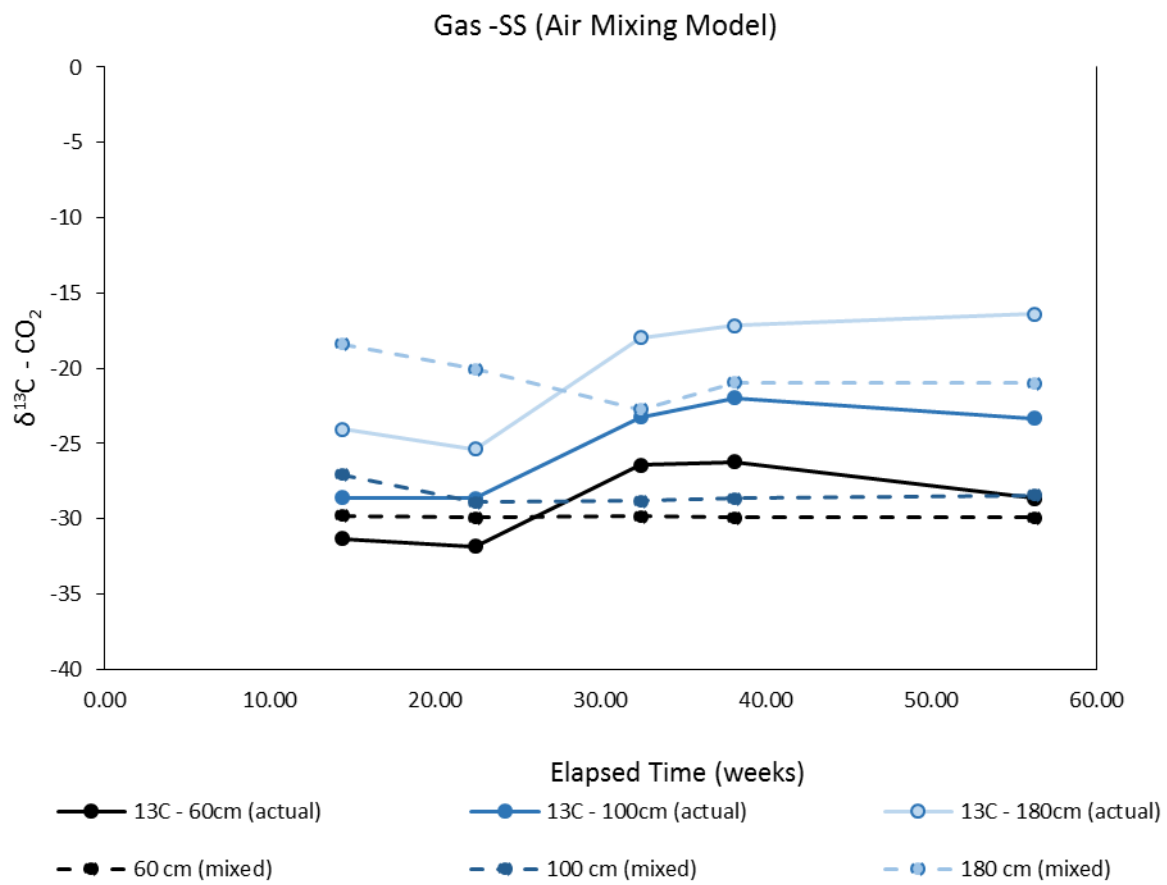

Figure 3-19 Actual Gas-S vertical distribution of δ ^{13}C- CO_2 compared to the "mixed" δ ^{13}C- CO_2 values generated through atmospheric CO_2 mixing. The atmospheric mixing model used the CO_2 concentration values to calculate the ^{13}C signature based on the proportion of atmospheric CO_2 influence on the total CO_2 concentration and by extension, the overall ^{13}C signature of the entire CO_2 signature).

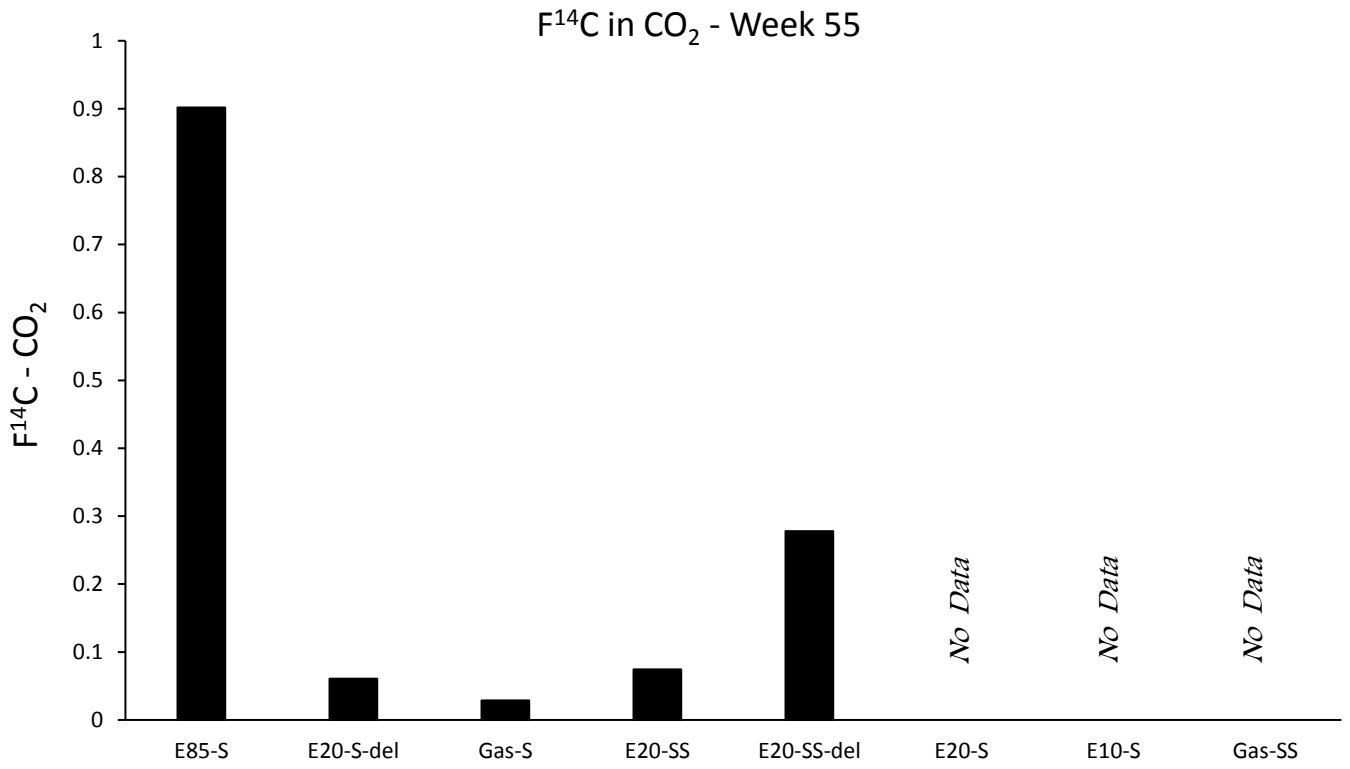

Figure 3-20 Radiocarbon data for the week 55 CO_2 samples taken at 60cm. Laboratory results of the ^{14}C in CO_2 were obtained for all columns except for the E20-S, E10-S, and Gas-SS columns.

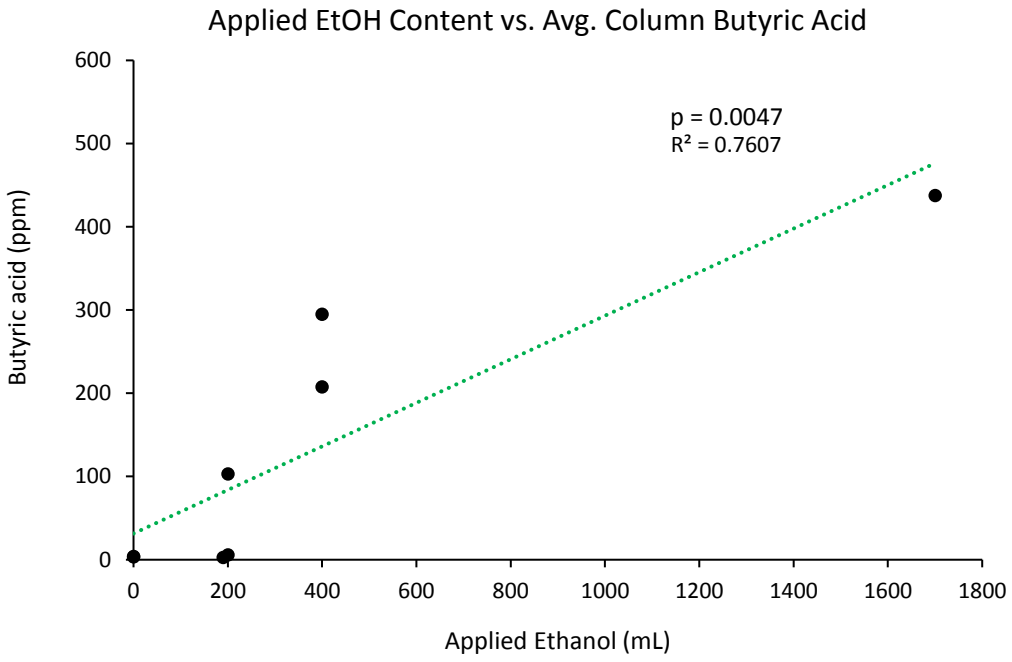

Figure 3-21 Total ethanol content applied to each experiment (mL) vs average butyric acid concentration (ppm).

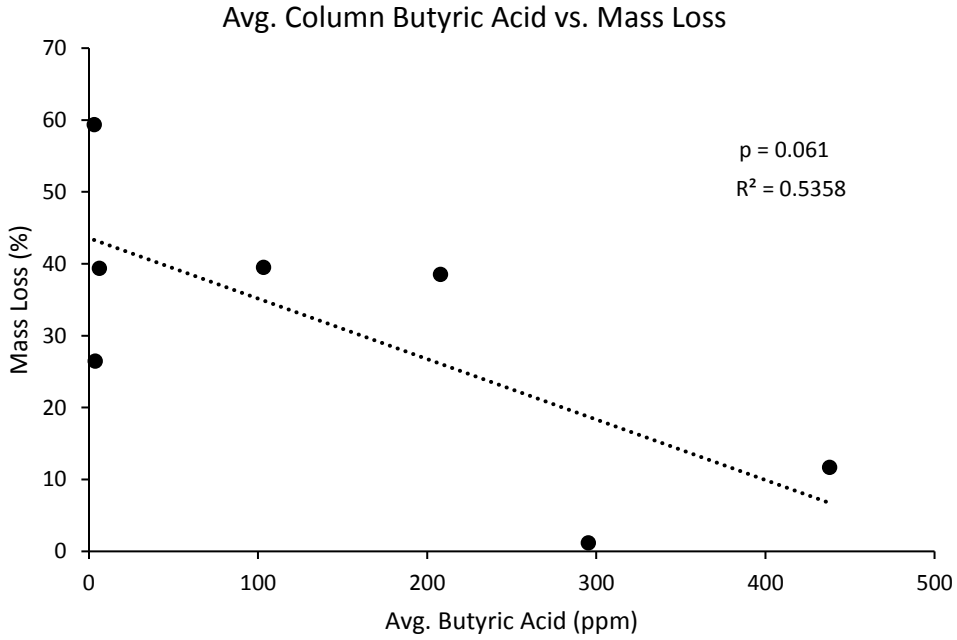

Figure 3-22 Average butyric acid concentration (ppm) vs calculated mass loss (%) based on soil surficial CO_2 effluxes.

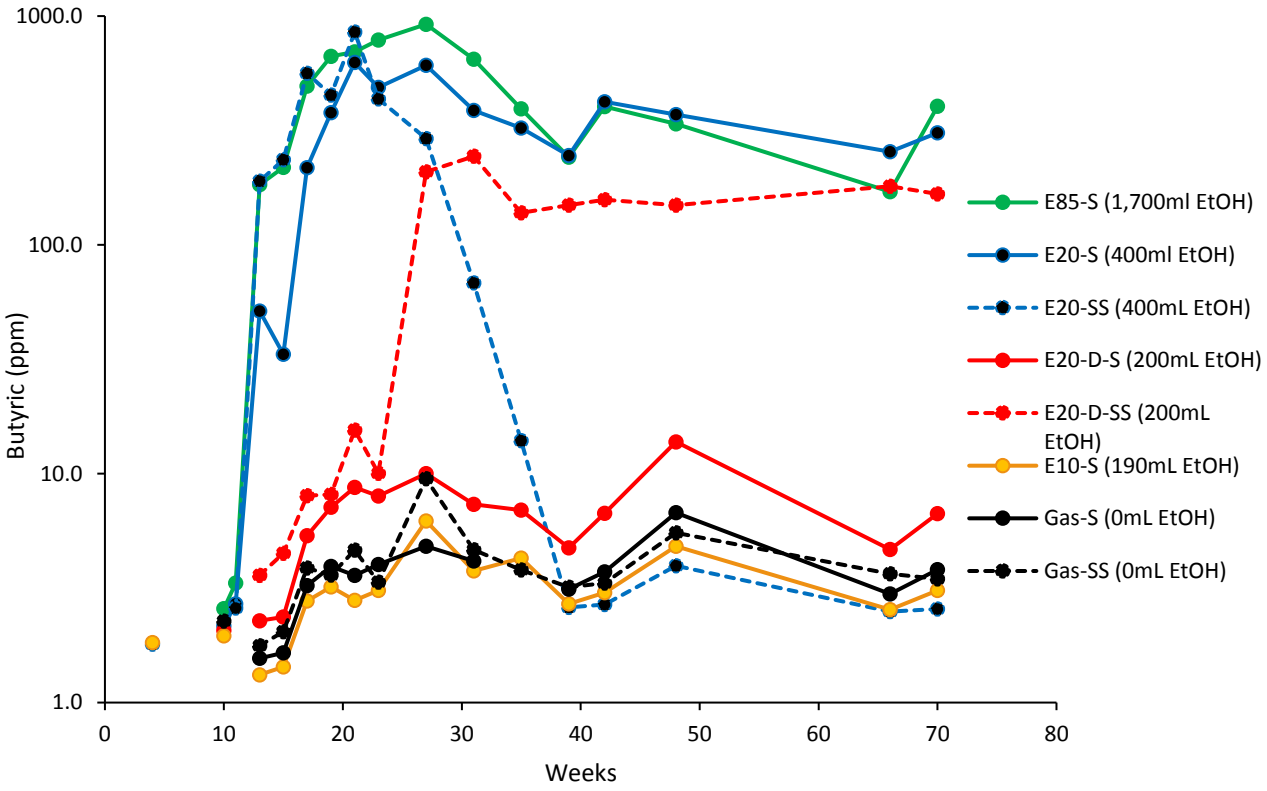

Figure 3-23 Evolution of butyric acid for each column.

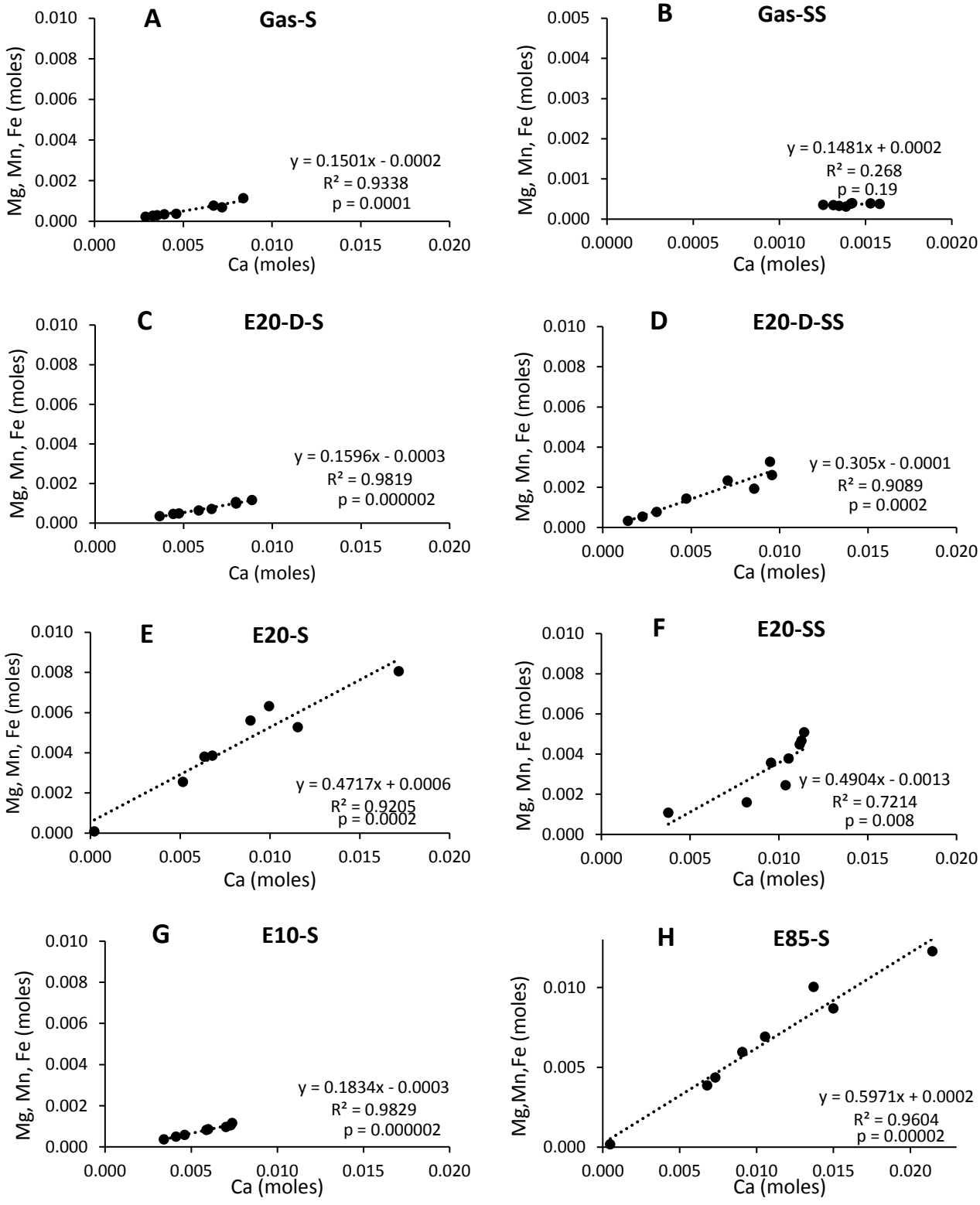

Figure 3-24 Cross-plots Ca moles vs (Mg,Mn,Fe) moles for each column.

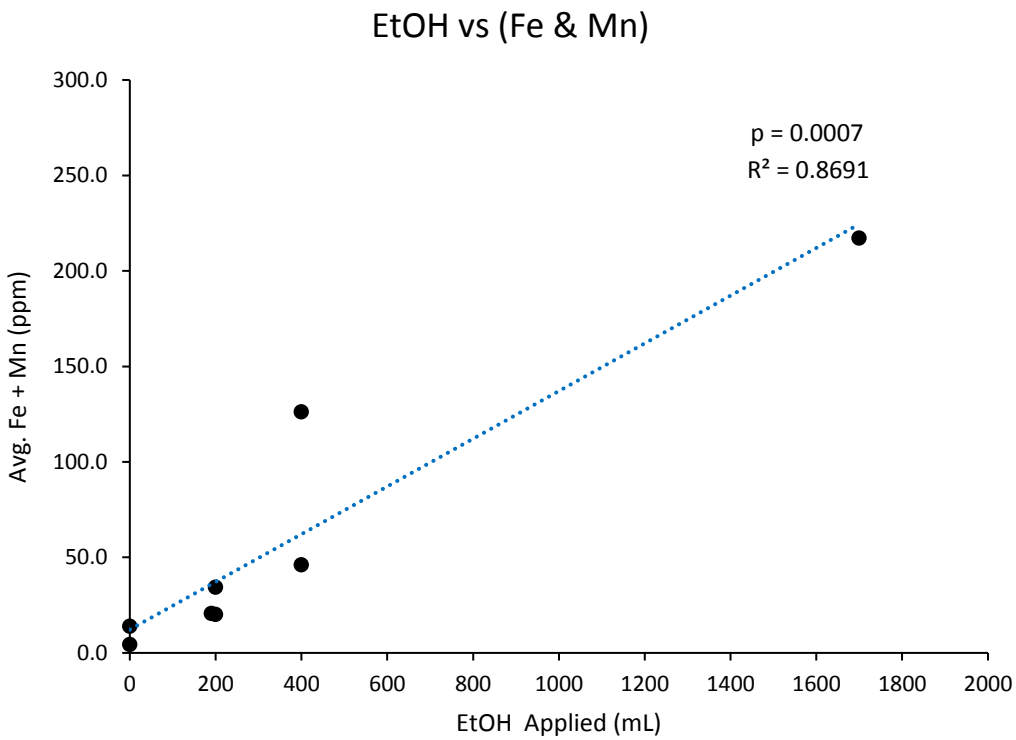

Figure 3-25 Cross-plot average Fe+Mn vs applied ethanol content.

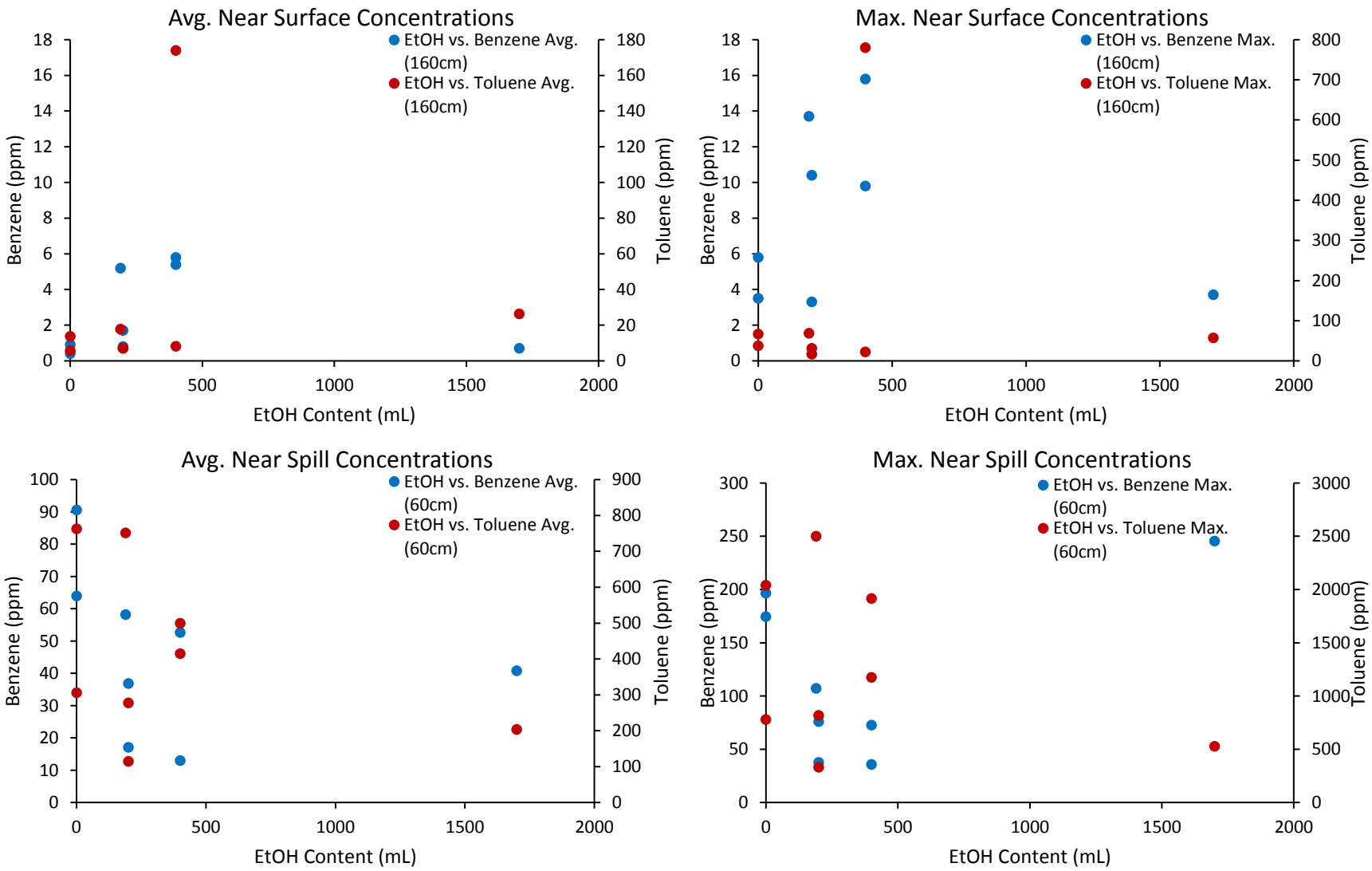

Figure 3-26 Near surface and near spill maximum and average benzene and toluene concentrations vs applied ethanol content.

3.7 Tables

Table 3-1 List of Microbial Reactions.

Process	Stoichiometry	Eqn #	Source
Ethanol Oxidation to CO_2 (Aerobic)	$CH_3CH_2OH + 3O_2 \rightarrow 2HCO_3^- + H_2O + 2H^+$	(1)	
Oxidation of Octane (Aerobic)	$2C_8H_{18} + 25O_2 \rightarrow 16HCO_3^- + 2H_2O + 16H^+$	(2)	Modified from (Sihota, 2014)
Benzene oxidation (Aerobic)	$C_6H_6 + 3H_2O + 7.5O_2 \rightarrow 6HCO_3^- + 6H^+$	(3)	Modified from (Vogt et al., 2011)
Toluene Oxidation (Aerobic)	$C_7H_8 + 9O_2 + 3H_2O \rightarrow 7HCO_3^- + 7H^+$	(4)	(Ghaly et al., 2007)
Methane oxidation (Aerobic)	$CH_4 + 2O_2 \rightarrow HCO_3^- + H^+ + H_2O$	(5)	Modified from (Ren et al., 1997)
Octane Fermentation to Glucose (Anaerobic – Hydrolysis)	$3C_8H_{18} + 24H_2O \rightarrow 4C_6H_{12}O_6 + 27H_2$	(6)	Modified from (Ostrem and Themelis, 2004)
Glucose Fermentation to Propionic Acid (Anaerobic – Acidicfication)	$C_6H_{12}O_6 + 2H_2 \rightarrow 2CH_3CH_2COOH + 2H_2O$	(7)	(Ostrem and Themelis, 2004)
Glucose Fermentation to Butyric Acid (Anaerobic – Acidicfication)	$2C_6H_{12}O_6 + 6H_2 \rightarrow 3CH_3CH_2CH_2COOH + 6H_2O$	(8)	Modified from (Ostrem and Themelis, 2004)
Glucose Fermentation to Ethanol (Anaerobic – Acidicfication)	$C_6H_{12}O_6 + 2H_2O \rightarrow 2CH_3CH_2OH + 2HCO_3^- + 2H^+$	(9)	Modification from (Priebe, 2013)
Benzene Oxidation (Anaerobic – Iron reduction)	$C_6H_6 + 30Fe(OH)_3 + 54H^+ \rightarrow 6HCO_3^- + 30Fe^{2+} + 72H_2O$	(10)	Modified from (Heider et al., 1998)
Toluene Oxidation (Anaerobic – Iron reduction)	$C_7H_8 + 36Fe(OH)_3 + 65H^+ \rightarrow 36Fe^{2+} + 7HCO_3^- + 87H_2O$	(11)	Modified from (Heider et al., 1998)

Process	Stoichiometry	Eqn #	Source
Ethanol Oxidation (Anaerobic – Mn Reduction)	$CH_3CH_2OH + 2MnO_2 + 3H^+ \rightarrow 2Mn^{2+} + CH_3COO^- + 3H_2O$	(12)	Modification of (Chen et al., 2008)
Acetate Oxidation (Anaerobic – Mn Reduction)	$CH_3COO^- + 4MnO_2 + 7H^+ \rightarrow 4Mn^{2+} + 2HCO_3^- + 4H_2O$	(13)	Modification of (Chen et al., 2008)
Ethanol Oxidation (Anaerobic – Fe Reduction)	$CH_3CH_2OH + 4Fe(OH)_3 + 7H^+ \rightarrow 4Fe^{2+} + CH_3COO^- + 11H_2O$	(14)	(Chen et al., 2008)
Acetate Oxidation (Anaerobic – Fe Reduction)	$CH_3COO^- + 8Fe(OH)_3 + 17H^+ \rightarrow 8Fe^{2+} + 2HCO_3^- + 20H_2O + 2H^+$	(15)	(Chen et al., 2008)
Ankerite Dissolution	$Ca(Fe^{2+}, Mn, Mg)(CO_3)_2 + 2H^+ \leftrightarrow Ca^{2+} + (Fe, Mn, Mg)^{2+} + 2HCO_3^-$	(16)	Modified from (Appelo and Postma, 2005) (Eq 5.27)
Butyrate to Acetate (Acetogenesis- Proton-Reducing Acetogens)	$CH_3CH_2CH_2COO^- + 2H_2O \rightarrow 2CH_3COO^- + 2H_2 + H^+$	(17)	(Ferry, 2011)
Propionate to Acetate (Acetogenesis- Proton-Reducing Acetogens)	$CH_3CH_2COO^- + 3H_2O \rightarrow CH_3COO^- + HCO_3^- + 3H_2 + H^+$	(18)	(Ferry, 2011)
Ethanol to Acetate (Acetogenesis- Proton-Reducing-Acetogens)	$CH_3CH_2OH + H_2O \rightarrow 2H_2 + CH_3COO^- + H^+$	(19)	(Freitas et al., 2010)
Bicarbonate to Acetate (Acetogenesis- Homoacetogens)	$2HCO_3^- + 4H_2 + H^+ \rightarrow CH_3COO^- + 4H_2O$	(20)	Modifired from (Ostrem and Themelis, 2004) Discussed in (Powers et al., 2001)
Acetate Fermentation to CH_4 & CO_2 (Methanogenesis -Acetoclastic Methanogens)	$CH_3COO^- + H_2O \rightarrow CH_4 + HCO_3^-$	(21)	Modified from (Freitas et al., 2010) (Whiticar, 1999)
CO_2 Reduction to CH_4 (Methanogenesis - Hydrogenotrphic Methanogens)	$H^+ + HCO_3^- + 4H_2 \rightarrow CH_4 + 3H_2O$	(22)	Modified from (Freitas et al., 2010) (Whiticar, 1999)
Calcite Dissolution	$CaCO_3 + 2H^+ \rightarrow Ca^{2+} + CO_2 + H_2O$	(23)	(Appelo and Postma, 2005)

Process	Stoichiometry	Eqn #	Source
Acetate to Butyrate (Stressed Conditions)	$2CH_3COO^- + H^+ + 2H_2 \leftrightarrow CH_3CH_2CH_2COO^- + 2H_2O$	(24)	Modified from (Freitas et al., 2010; Kim et al., 1994)(Wilson et al., 2016)(Wilson et al. 2016)
Mn^{2+} Oxidation	$Mn^{2+} + \frac{1}{2}O_2 + H_2O \rightarrow MnO_2 + 2H^+$	(25)	
Fe^{2+} Oxidation	$2Fe^{2+} + \frac{1}{2}O_2 + 5H_2O \rightarrow 2Fe(OH)_3 + 4H^+$	(26)	Modified from (Appelo and Postma, 2005)

Table 3-2 Summary of maximum and average VFA content.

Approximate Total Ethanol Content (mL)	Fuel Blend	Soil Type	Max. [Acetic] (ppm)	Avg. [Acetic] (ppm)	Max. [Butyric] (ppm)	Avg. [Butyric] (ppm)	Total Combined Avg. Dissolved Acetic & Butyric Content (ppm)
0	Gasoline	Sand	13.2	9.3	4.8	3.7	13.0
0	Gasoline	Silty-Sand	31.2	11.4	9.5	4.0	15.4
190	E10	Sand	14.2	7.5	6.2	2.9	10.4
200	Gasoline + E20	Sand	21.3	12.6	13.8	6.1	18.7
200	Gasoline + E20	Silty-Sand	740.1	239.4	243.8	103.1	342.6
400	E20	Sand	611	356.2	626	295.1	651.3
400	E20	Silty-Sand	757.4	196.7	850.5	207.7	404.4
1,700	E85	Sand	490	191.2	921	437.8	629.0

Table 3-3 Saturated zone ethanol data on maximum concentrations recorded, and average concentrations per column. Note week 14 represents the first sampling event for ethanol.

Applied Ethanol Content (mL)	Fuel Blend	Soil Type	First Appearance of EtOH (week)	Max. [EtOH] (ppm)	Avg. [EtOH] (ppm)
190	E10	Sand	48	1.9	0.2
200	Gasoline + E20	Sand	22	3.4	0.7
200	Gasoline + E20	Silty-Sand	14	638.3	213.6
400	E20	Sand	14	12119.2	3403.2
400	E20	Silty-Sand	22	0.9	0.2
1,700	E85	Sand	14	46568.8	13742.8

Table 3-4 Summary of redox indicators

Redox Indicators					
Column	Vadose Zone		Saturated Zone		Summary of Redox Conditions
	O_2	CH_4 Detected (60cm)	VFA's	Fe^{2+}/Mn^{2+}	
Gas-S	Anoxic < 100cm	Min: 0.017 % Max: 0.037% Average: 0.025% **10 samples detected CH_4**	(< 25 ppm)	(< 25 ppm)	Significant O_2 consumption - Strong Aerobic Activity Minimal Mn/Fe - Minimal Anaerobic Fe/Mn reduct'n Minimal CH_4 - Minimal Methanogenic Activity
Gas-SS	Anoxic < 80cm (below perched water table)	Min: 0.013 % Max: 0.073% Average: 0.027% **19 samples detected CH_4**	(< 25 ppm)	(< 25 ppm)	No O_2 consumption >80 cm Significant O_2 consumption <80 cm Overall - Minimum Aerobic Activity. Minimal Mn/Fe - Minimal Anaerobic Fe/Mn reduct'n Minimal CH_4- Minimal Methanogenic Activity
E10-S	Anoxic < 100cm (W1-W26) oxic (W30-W72)	Min: 0.010 % Max: 0.113% Average: 0.062% **18 samples detected CH_4**	(< 25 ppm)	(< 25 ppm)	Significant O_2 consumption - Strong Aerobic Activity Minimal Mn/Fe - Minimal Anaerobic Fe/Mn reduct'n Minimal CH_4- Minimal Methanogenic Activity
E20-D-S	Anoxic < 40cm (W7-W40) Ltd. O_2 @ 40cm(< 5% W40-70)	Min: 0.011 % Max: 0.124% Average: 0.039% **19 samples detected CH_4**	(< 25 ppm)	(< 25 ppm)	Significant O_2 consumption - Strong Aerobic Activity Minimal Mn/Fe - Minimal Anaerobic Fe/Mn reduct'n Minimal CH_4- Minimal Methanogenic Activity
E20-D-SS	Anoxic < 60cm (W7-W25) anoxic < 40cm (W25-70)	Min: 0.027 % Max: 0.546% Average: 0.127% **21 samples detected CH_4**	(100-500 ppm)	(< 25 ppm)	Significant O_2 consumption - Strong Aerobic Activity Moderate Mn/Fe-Moderate Anaerobic Fe/Mn reduct'n Moderate CH_4- Moderate Methanogenic Activity
E20-S	Oxic	Min: 0.84 % Max: 0.84 % Average: 0.84 % **1 sample detected CH_4**	(> 400 ppm)	(50-100 ppm)	Minimal O_2 consumption - Minimal Aerobic Activity Significant Mn/Fe-Significant Anaerobic Fe/Mn reduct'n Minimal CH_4- Minimal Methanogenic Activity
E20-SS	Anoxic < 60 cm (W5-W18) oxic (W18-W72)	Min: 0.012 % Max: 0.063% Average: 0.024% **18 samples detected CH_4**	(W18-W35) (200-900 ppm)	(< 50 ppm)	Significant O_2 consumption - Strong Aerobic Activity Significant Mn/Fe- Strong Anaerobic Fe/Mn reduct'n Minimal CH_4- Minimal Methanogenic Activity
E85-S	Oxic	Min: 0.013 % Max: 0.195% Average: 0.078% **6 samples detected CH_4**	(200- 1000 ppm)	(50-200 ppm)	Minimal O_2 consumption - Minimal Aerobic Activity Significant Mn/Fe- Strong Anaerobic Fe/Mn reduct'n Minimal CH_4- Minimal Methanogenic Activity

Table 3-5 Near surface maximum and average benzene and toluene concentrations 25 cm below soil surface.

Near Surface Maximum and Average Benzene and Toluene Concentrations (110 cm Above Spill) - 25 cm Below Surface							
Fuel Blend	**Soil Type**	**# of Benzene Samples >1 ppm**	**Max. Benzene**	**Avg. Benzene (ppm)**	**# of Toluene Samples >4 ppm**	**Max. Toluene**	**Avg. Toluene**
Gasoline	Sand	1/7 samples	**3.5 (ppm)** 11.2 (µg/L)	**0.4 (ppm)** 1.4 (µg/L)	5/7 samples	**37.5 (ppm)** 143 (µg/L)	**13.7 (ppm)** 52.1 (µg/L)
Gasoline	Silty-Sand	2/7 samples	**5.8 (ppm)** 18.9 (µg/L)	**0.9 (ppm)** 3.1 (µg/L)	1/7 samples	**66.6 (ppm)** 254.1 (µg/L)	**5.8 (ppm)** 40.7 (µg/L)
E10	Sand	3/7 samples	**13.7 (ppm)** 44.3 (µg/L)	**5.2 (ppm)** 16.9 (µg/L)	4/7 samples	**68.9 (ppm)** 263.0 (µg/L)	**17.8 (ppm)** 68.0 (µg/L)
Gasoline + E20	Sand	2/7 samples	**3.3 (ppm)** 10.7 (µg/L)	**0.8 (ppm)** 2.7 (µg/L)	4/7 samples	**31.2 (ppm)** 119.0 (µg/L)	**7.0 (ppm)** 26.5 (µg/L)
Gasoline + E20	Silty-Sand	1/7 samples	**10.4 (ppm)** 33.8 (µg/L)	**1.7 (ppm)** 5.6 (µg/L)	3/7 samples	**16.5 (ppm)** 63.1 (µg/L)	**7.1 (ppm)** 27.9 (µg/L)
E20	Sand	7/7 samples	**9.8 (ppm)** 31.6 (µg/L)	**5.4 (ppm)** 17.3 (µg/L)	7/7 samples	**780 (ppm)** 2974.0 (µg/L)	**174.0 (ppm)** 663.9 (µg/L)
E20	Silty-Sand	6/7 samples	**15.8 (ppm)** 51.1 (µg/L)	**5.8 (ppm)** 18.9 (µg/L)	4/7 samples	**22.4 (ppm)** 85.5 (µg/L)	**8.2 (ppm)** 31.3 (µg/L)
E85	Sand	2/7 samples	**3.7 (ppm)** 11.9 (µg/L)	**0.7 (ppm)** 70.7 (µg/L)	7/7 samples	**57.1 (ppm)** 218.0 (µg/L)	**26.3 (ppm)** 100.4 (µg/L)

Table 3-6 Summary comparing CH_4 and CO_2 effluxes results to previous field studies of E95 (DFE) and crude oil spills. Red highlighted columns represent data affected by leaks, and therefore represent conservative values for soil efflux.

Column	Depth to Water Table	CH_4 flux ($\mu mol\ m^{-2}\ s^{-1}$)	Max. CH_4 flux ($\mu mol\ m^{-2}\ s^{-1}$)	CO_2 flux ($\mu mol\ m^{-2}\ s^{-1}$)	Max. CO_2 flux ($\mu mol\ m^{-2}\ s^{-1}$)
Gas-S (2L spilled = 28L m^{-2})	1.6m	<0.5	0.5	5.0-10.0	18
Gas-SS (1.6L spilled = 23L m^{-2})	1.6m	0.0	0.0	<1.0	0.5
E10-S (1.9L spilled = 27L m^{-2})	1.6m	0.5-1.0	2.0	20.0 - 40.0 (W8-40) ~10.0 (W40-72)	38
E20-D-S (2L spilled = 28L m^{-2})	1.6m	<0.5	0.25	10.0 - 25.0	38
E20-D-SS (2L spilled = 28L m^{-2})	1.6m	0.5-1.5	1.4	10.0 - 20.0	42
E20-S (2L spilled = 28L m^{-2})	1.6m	<0.5	0.25	<2.5	2.4
E20-SS (2L spilled = 28L m^{-2})	1.6m	<0.5	0.8	10.0-40.0 (W5-30) ~10.0 (W30-72)	45
E85-S (2L spilled = 28L m^{-2})	1.6m	<1 (single event W27-36)	0.5	5.0	5

Previous Studies	Depth to Water Table	CH_4 flux ($\mu mol\ m^{-2}\ s^{-1}$)	Max. CH_4 flux ($\mu mol\ m^{-2}\ s^{-1}$)	CO_2 flux ($\mu mol\ m^{-2}\ s^{-1}$)	Max. CO_2 flux ($\mu mol\ m^{-2}\ s^{-1}$)
Bemidji, Minnesota 1979, 1,700,000L Crude Oil ~133L m^{-2} (Warren et al., 2014)	5.8-8.6 m	--	--	1.9-9.1	9.1
Balaton, Minnesota 2004, 150,000L E95 (DFE) ~15L m^{-2} (Sihota et al., 2013)	1.5-3.5m	non-detect - 9	9	0.6-178.4	178.4
Cambria, Minnesota 2006, 95,000L E95 (DFE) ~18.5L m^{-2} (Sihota et al., 2013)	<1m	0.2 - 393	393	0.5-174.7	174.7

Table 3-7 Summary of biodegradation rates per volume of contaminated soil (μmol m^{-3} s^{-1}) of this study in addition to previous lab and field studies.

Experimental Conditions	Site	Fuel Type	Average Estimated Rate of Carbon Loss	Reference
DFE spill site, shallow aquifer	Cambria, Minnesota	E95	Assumed thickness of spill zone = 0.6 m = **33.5 (μmol C m^{-3} s^{-1})**	(Sihota et al., 2013)
DFE spill site, shallow aquifer	Balaton, Minnesota	E95	Assumed thickness of spill zone = 0.6 m = **20 (μmol C m^{-3} s^{-1})**	(Sihota et al., 2013)
Crude oil spill site	Bemidji, Minnesota	Crude Oil	Assumed thickness of spill zone = 5 m (Essaid et al., 2011) **= 0.6 (μmol C m^{-3} s^{-1})**	(Sihota and Mayer, 2012)
Lab microcosms	Lab microcosms	Ethanol	**10.1 (μmol C m^{-3} s^{-1})**	(Wilson et al., 2016)
Lab microcosms	Lab microcosms	Ethanol	**9.0 (μmol C m^{-3} s^{-1})**	(Corseuil et al., 1998b)
Lab columns - gasoline sand column	Lab columns	Gasoline	**30.1 (μmol C m^{-3} s^{-1})**	This study
Lab columns - gasoline silty-sand column	Lab columns	Gasoline	**1.4 (μmol C m^{-3} s^{-1})**	This study
Lab columns - E10 sand column	Lab columns	E10	**110.3* (μmol C m^{-3} s^{-1})**	This study
Lab columns - gasoline + E20 sand column	Lab columns	Gasoline + E20	**45.4* (μmol C m^{-3} s^{-1})**	This study
Lab columns - gasoline + E20 silty-sand column	Lab columns	Gasoline + E20	**48.7* (μmol C m^{-3} s^{-1})**	This study
Lab columns - E20 sand column	Lab columns	E20	**1.0 (μmol C m^{-3} s^{-1})**	This study
Lab columns - E20 silty-sand column	Lab columns	E20	**73.8* (μmol C m^{-3} s^{-1})**	This study
Lab columns - E85 sand column	Lab columns	E85	**5.4 (μmol C m^{-3} s^{-1})**	This study

* columns affected by bioventing

Chapter 4: Conclusion

The emergence sustainable fuel alternatives in recent years in response to government and environmental initiatives have created a market for ethanol-blended fuels. An expanding global market has significantly elevated the risks for accidental release of ethanol-blended fuels. In response to recent legislature promoting higher ethanol content in gasoline, researchers have increased their efforts to understand the fate of ethanol-blended fuels in the subsurface. This work aimed to evaluate the evolution of biodegradation of different ethanol-blended fuels as well as the effect of soil media, as it relates to the risks posed to the environment and humans. These risks include: the potential for metal mobilization in groundwater, SVI risks for CH_4, benzene and toluene for different fuel blends and soil types, and microbial ethanol toxicity hindering NA processes. In addition, this study provides insights into the use of isotopic tools for investigating ethanol-blended fuel biodegradation.

The construction of 8 large experimental columns was completed to develop a 1D-proxy for the investigation of the fate of ethanol-blended fuels downgradient of a spill. A network of sampling ports and sensors allowed for the monitoring of soil gases in the vadose zone, as well as biodegradation intermediates, metals and ethanol in the groundwater. Data was collected over ~530 days and reported for each individual column. An inter-column comparison of the entire data set allowed for the evaluation of the effect of different variables (i.e. ethanol content, soil type). The primary findings of this research are highlighted below:

1. **Microbial toxicity in high-ethanol content fuels leads to increased butyric acid in the groundwater.**

   Elevated butyric acid, an indicator for microbial stress, was evident in columns with fuels higher in ethanol content. A correlation was observed between elevated butyric acid levels in groundwater and high-ethanol content fuels. In addition, the two columns

with the highest butyric acid levels experienced the lowest levels of mass loss, indicating a diminished biodegradation capability.

2. **Substantial delay in the appearance of dissolved ethanol.**

   In general, groundwater samples collected did not detect ethanol until late in the experiment. Observations suggest that ethanol remained trapped in the capillary region for an extended period due to its hydrophilic nature. In addition, infiltration into the groundwater zone did not appear to depend on soil type.

3. **Increased Mn^{2+} and Fe^{2+} mobilization in fuels with higher ethanol content.**

   Results show a statistically significant correlation between the degree of metal mobilization and ethanol content. It is likely that an increase in microbial Mn-oxide and Fe-oxide reduction reactions in response to an increase in available labile substrate (ethanol) resulted in the highest metal concentration in the column with the largest fraction of ethanol (E85).

4. **Sharp redox gradients exist on the scale of centimeters.**

   Study results indicate that aerobic degradation in the vadose zone dominates the biodegradation of ethanol-blended fuels. However, aerobic degradation occurred concurrently with anaerobic degradation processes, starting in the capillary fringe region and extending into the groundwater zone. Results show that in columns which remained oxic throughout in the vadose zone, anaerobic degradation was still occurring. This study confirms that the depletion of TEAs can occur on the scale of centimeters.

5. **Stable isotopes well suited for identifying primary microbial substrates.**

   Stable carbon isotope analysis of CO_2, produced by NA processes, proved to be a useful tool in identifying the evolution of the primary substrates undergoing degradation. The evolution of the isotopic signature of CO_2 revealed the substrate predominantly undergoing degradation, thereby highlighting delays in ethanol biodegradation and providing insights into the acclimatization periods of the microbial consortium.

6. **Ethanol content and soil type did not appear to significantly affect benzene or toluene degradation.**

   Contrary to prior studies, benzene or toluene degradation did not appear to be significantly inhibited by increasing ethanol content. In addition, soil type did not appear to affect the biodegradation or migration of benzene and toluene in the vadose zone. Nevertheless, it is important to recognize the potential role of column leaks and accidental air ingress, which may have had an influence vadose zone benzene and toluene concentrations.

7. **No significant risk for SVI of CH_4, benzene and toluene.**

   Biodegradation in some columns produced at times significant soil CO_2 fluxes. However, there did not appear to be a significant risk of SVI for CH_4, benzene, and toluene for the conditions in this study.

8. **Biodegradation rates were low in high EtOH-content fuels and bioventing elevates biodegradation regardless of ethanol content.**

   Biodegradation rates calculated for this study reveal that rates of biodegradation are hindered in columns with high ethanol content, as well as when natural oxygen ingress is inhibited due to an overlying impermeable layer. Unintended bioventing was shown

to significantly increase the rates of biodegradation in a number of columns with a variety of applied ethanol content.

This long-term (530 day) study contributes to the knowledge of the environmental impacts of fuel spills containing varying ethanol contents, and under different soil conditions. Field studies have also assessed the impacts of long term spills; however, it is uncommon for monitoring to be conducted days after an accidental release, therefore leaving a gap of knowledge for the early time processes. This study helps to fill that gap by providing information vital to assessing the immediate impacts resulting from accidental release of ethanol-blended fuels. Additionally, the highly instrumented columns managed to capture with significant detail, the vertical 1-D effects of bioventing on the soil gas profile. Columns which experienced the most substantial unintended bioventing, were also the columns with most significant mass loss. Conservative estimates of degradation ranged from 40-60% of the original fuel mass injected, confirming that bioventing is efficient in elevating rates of NA. This unintended result showed that bioventing can both increase NA rates and significantly decrease soil CO_2 concentrations.

Recommendations for future work include an improved column design to avoid the build-up of a negative air pressure in the column headspace. This can be achieved by fitting the column headspace with a larger diameter venting inlet. Using this revised design, it should be possible to eliminate unintended air ingress into the headspace or through leaky or open sampling ports. In addition to design modifications, sequential extractions and or scanning electron microscope (SEM) work should be done to better characterize the amorphous minerals in the soils. Lastly, periodic pH measurements would have been valuable to characterize processes controlling

biodegradation and for better assessing the role of ankerite dissolution on dissolved metals in groundwater.

Ongoing work outside the scope of this thesis includes a detailed study of the microbial communities and how they evolve during the degradation of the different fuel blends.

Bibliography

Abbott, T. (2016). Personal communication on the methods used for VFA analysis.

Aelion, C.M., Höhener, P., Hunkeler, D., and Aravena, R. (2009). Environmental Isotopes in Biodegradation and Bioremediation (CRC Press).

Agilent Technologies Agilent 7890A GC Operating Guide (Santa Clara, CA).

Air Force (1989). Gasoline. In:The installation restoration program toxicology guide (OH: Wright-Patteson Air Force Base). Available at http://www.dtic.mil/dtic/tr/fulltext/u2/a215002.pdf. Accessed March 8th, 2017.

Amos, R.T., Mayer, K.U., Bekins, B.A., Delin, G.N., and Williams, R.L. (2005). Use of dissolved and vapor-phase gases to investigate methanogenic degradation of petroleum hydrocarbon contamination in the subsurface. Water Resour. Res. *41*, W02001.

Apogee instruments (2015). SO-100-200-series-manual.pdf.

Appelo, C.A.J., and Postma, D. (2005). Geochemistry, Groundwater and Pollution (Amsterdam, the Netherlands: A.A. BALKEMA PUBLISHERS).

Atlas, R.M., and Bartha, R. (1972). Degradation and mineralization of petroleum in sea water: Limitation by nitrogen and phosphorous. Biotechnol. Bioeng. *14*, 309–318.

Atlas, R.M., and Bartha, R. (1998). Microbial ecology: fundamentals and applications (Menlo Park, Calif: Benjamin/Cummings).

ATSDR (1995). Toxicological Profile for Gasoline (U.S. Department of Health and Human Services). Available at https://www.atsdr.cdc.gov/toxprofiles/tp72.pdf. Accessed March 8th, 2016.

ATSDR (2007). Toxicological profile for benzene Agency for toxic substances and disease Registry, US Department of Health and Human Services (Atlanta: Agency for Toxic Substances and Disease Registry, Public Health Service, U.S. Department of Health and Humane Services).

AWWA (2006). Water Chlorination/Chloramination Practices and Principles - Manual of Water Supply Practices, M20 (2nd Edition) (American Water Works Association).

Bekins, B.A., Cozzarelli, I.M., Godsy, E.M., Warren, E., Essaid, H.I., and Tuccillo, M.E. (2001). Progression of natural attenuation processes at a crude oil spill site: II. Controls on spatial distribution of microbial populations. J. Contam. Hydrol. *53*, 387–406.

Blue Ribbon Panel (BRP) (1999). Executive summary and recommendations. (Washington DC), p. Available at https://www.epa.gov/sites/production/files/2014-10/documents/r99021.pdf. Accessed March 10th, 2016.

Cápiro, N.L., Stafford, B.P., Rixey, W.G., Bedient, P.B., and Alvarez, P.J.J. (2007). Fuel-grade ethanol transport and impacts to groundwater in a pilot-scale aquifer tank. Water Res. *41*, 656–664.

Chen, Y.D., Barker, J.F., and Gui, L. (2008). A strategy for aromatic hydrocarbon bioremediation under anaerobic conditions and the impacts of ethanol: A microcosm study. J. Contam. Hydrol. *96*, 17–31.

Conrad, M.E., Daley, P.F., Fischer, M.L., Buchanan, B.B., Leighton, T., and Kashgarian, M. (1997). Combined 14C and δ13C Monitoring of in Situ Biodegradation of Petroleum Hydrocarbons. Environ. Sci. Technol. *31*, 1463–1469.

Conrad, R., Phelps, T.J., and Zeikus, J.G. (1985). Gas Metabolism Evidence in Support of the Juxtaposition of Hydrogen-Producing and Methanogenic Bacteria in Sewage Sludge and Lake Sediments. Appl. Environ. Microbiol. *50*, 595–601.

Corseuil, H.X., Hunt, C.S., Ferreira dos Santos, R.C., and Alvarez, P.J.J. (1998a). The influence of the gasoline oxygenate ethanol on aerobic and anaerobic BTX biodegradation. Water Res. *32*, 2065–2072.

Corseuil, H.X., Hunt, C.S., Ferreira dos Santos, R.C., and Alvarez, P.J.J. (1998b). The influence of the gasoline oxygenate ethanol on aerobic and anaerobic BTX biodegradation. Water Res. *32*, 2065–2072.

Corseuil, H.X., Monier, A.L., Fernandes, M., Schneider, M.R., Nunes, C.C., do Rosario, M., and Alvarez, P.J. (2011). BTEX plume dynamics following an ethanol blend release: geochemical footprint and thermodynamic constraints on natural attenuation. Environ. Sci. Technol. *45*, 3422–3429.

Corwin, D.L. (2000). Evaluation of a simple lysimeter-design modification to minimize sidewall flow. J. Contam. Hydrol. *42*, 35–49.

Cozzarelli, I.M., Baedecker, M.J., Eganhouse, R.P., and Goerlitz, D.F. (1994). The geochemical evolution of low-molecular-weight organic acids derived from the degradation of petroleum contaminants in groundwater. Geochim. Cosmochim. Acta *58*, 863–877.

Decagon (2011). Decagon MPS-2 Manual Version 2.

Department of the Environment (2010). Renewable Fuels Regulations. Available at http://www.gazette.gc.ca/rp-pr/p1/2010/2010-04-10/pdf/g1-14415.pdf. Accessed March 15th, 2016.

Duetz, W.A., Marqués, S., de Jong, C., Ramos, J.L., and van Andel, J.G. (1994). Inducibility of the TOL catabolic pathway in Pseudomonas putida (pWW0) growing on succinate in continuous culture: evidence of carbon catabolite repression control. J. Bacteriol. *176*, 2354–2361.

Duetz, W.A., Marqués, S., Wind, B., Ramos, J.L., and van Andel, J.G. (1996). Catabolite repression of the toluene degradation pathway in Pseudomonas putida harboring pWW0 under various conditions of nutrient limitation in chemostat culture. Appl. Environ. Microbiol. *62*, 601–606.

Dynament (2011). Dynament Techinal Data Sheet TDS0036.

Elbehri, A., Segerstedt, A., and Liu, P. (2012). Biofuels And The Sustainability Challenge - A Global Assessment Of Sustainability Issues, Trends And Policies For Biofuels And Related Feedstocks (Rome, ITA: FAO).

Environment Canada and Health and Welfare Canada (1993). Canadian Environmental Protection Act Priority Substances List assessment report: Benzene (Ottawa, ON: Minister of Supply and Services Canada).

EPA (2011). Partial Grant of Clean Air Act Waiver Application Submitted by Growth Energy To Increase the Allowable Ethanol Content of Gasoline to 15 Percent; Decision of the Administrator. Fed. Regist. *76*. Available at https://www.federalregister.gov/articles/2011/01/26/2011-1646/partial-grant-of-clean-air-act-waiver-application-submitted-by-growth-energy-to-increase-the. Accessed March 15, 2016.

Essaid, H.I., Bekins, B.A., Herkelrath, W.N., and Delin, G.N. (2011). Crude Oil at the Bemidji Site: 25 Years of Monitoring, Modeling, and Understanding. Ground Water *49*, 706–726.

Federal Register (1985). (Washington DC,: US government Printing Office).

Ferry, J.G. (2011). Fundamentals of methanogenic pathways that are key to the biomethanation of complex biomass. Curr. Opin. Biotechnol. *22*, 351–357.

Foght, J. (2008). Anaerobic biodegradation of aromatic hydrocarbons: pathways and prospects. J. Mol. Microbiol. Biotechnol. *15*, 93–120.

Fredlund, D.G., and Rahardjo, H. (1993). Measurements of Soil Suction. In Soil Mechanics for Unsaturated Soils, (John Wiley & Sons, Inc.), pp. 64–106.

Freitas, J.G., and Barker, J.F. (2011). Monitoring Lateral Transport of Ethanol and Dissolved Gasoline Compounds in the Capillary Fringe. Ground Water Monit. Remediat. *31*, 95–102.

Freitas, J.G., Fletcher, B., Aravena, R., and Barker, J.F. (2010). Methane Production and Isotopic Fingerprinting in Ethanol Fuel Contaminated Sites. Ground Water *48*, 844–857.

Friedli, H., Lötscher, H., Oeschger, H., Siegenthaler, U., and Stauffer, B. (1986). Ice core record of the 13C/12C ratio of atmospheric CO2 in the past two centuries. Nature *324*, 237–238.

Ghaly, A.E., Rushton, D.G., and Martinell, K. (2007). Effect of Mixing on the Biological Degradation of Toluene under Aerobic Conditions. Am. J. Environ. Sci. *3*, 247–258.

Ghodrati, M., Chendorain, M., and Chang, Y.J. (1999). Characterization of Macropore Flow Mechanisms in Soil by Means of a Split Macropore Column. Soil Sci. Soc. Am. J. *63*, 1093.

Griffin, T.W., and Watson, K.W. (2002). A Comparison of Field Techniques for Confirming Dense Nonaqueous Phase Liquids. Ground Water Monit. Remediat. *22*, 48–59.

Gullick, R.W., and LeChevallier, M.W. (2000). Occurrence of MTBE in drinking water sources. J. Am. Water Works Assoc. *92*, 100–113.

Head, I.M., Jones, D.M., and Röling, W.F.M. (2006). Marine microorganisms make a meal of oil. Nat. Rev. Microbiol. *4*, 173–182.

Health Canada (2011). Residential Indoor Air Quality Guideline: Toluene. Available at https://www.canada.ca/en/health-canada/services/publications/healthy-living/residential-indoor-air-quality-guideline-toluene.html. Accessed May 18th, 2017.

Health Canada (2014). Guidance for Benzene in Residential Indoor Air. Available at https://www.canada.ca/en/health-canada/services/publications/healthy-living/guidance-benzene-residential-indoor-air.html. Accessed May 25th, 2017.

Heider, J., Spormann, A.M., and Beller, H.R. (1998). Anaerobic bacterial metabolism of hydrocarbons. FEMS Microbiol. Rev. *22*, 459–459.

Ingram, L.O., and Buttke, T.M. (1985). Effects of Alcohols on Micro-Organisms. In Advances in Microbial Physiology, A.H.R. and D.W. Tempest, ed. (Academic Press), pp. 253–300.

ITRC (2011). ITRC : Biofuels: Release Prevention, Environmental Behavior, and Remediation. (Washington DC, USA: ITRC). Available at http://www.itrcweb.org/GuidanceDocuments/biofuels/biofuels-1.pdf. Accessed March 23rd, 2016.

Kendall, C., and Caldwell, E. (1998). Isotope tracers in catchment hydrology (Amsterdam ; New York: Elsevier).

Kim, I.S., Young, J.C., and Tabak, H.H. (1994). Kinetics of Acetogenesis and Methanogenesis in Anaerobic Reactions under Toxic Conditions. Water Environ. Res. *66*, 119–132.

Klassen, M. (2014). Quantitative Phase Analysis of 3 Powder Samples Using the Rietveld Method and X-Ray Powder Diffraction Data. UBC.

Klute, A. (1986). Methods of Soil Analysis, Part 1. Physical and Mineralogical Methods (American Society of Agronomy).

Lewis, J., and Sjöstrom, J. (2010). Optimizing the experimental design of soil columns in saturated and unsaturated transport experiments. J. Contam. Hydrol. *115*, 1–13.

LI-COR (2007). Automated Soil CO2 Flux System & LI-8150 Multiplexer Instruction Manual. Fourth Ed.

Lovley, D. (1995). Microbial Reduction of Iron, Manganese, and other metals. Adv. Agron. VOL 54 *54*, 175–231.

Lovley, D.R. (1991). Dissimilatory Fe (III) and Mn (IV) reduction. Microbiol. Rev. *55*, 259–287.

Lovley, D.R., and Chapelle, F.H. (1995). Deep subsurface microbial processes. Rev. Geophys. *33*, 365–381.

Lovley, D.R., and Phillips, E.J.P. (1987). Competitive Mechanisms for Inhibition of Sulfate Reduction and Methane Production in the Zone of Ferric Iron Reduction in Sediments. Appl. Environ. Microbiol. *53*, 2636–2641.

Lovley, D.R., and Phillips, E.J.P. (1988). Novel Mode of Microbial Energy Metabolism: Organic Carbon Oxidation Coupled to Dissimilatory Reduction of Iron or Manganese. Appl. Environ. Microbiol. *54*, 1472–1480.

Ma, J., Xiu, Z., Monier, A.L., Mamonkina, I., Zhang, Y., He, Y., Stafford, B.P., Rixey, W.G., and Alvarez, P.J.J. (2011). Aesthetic Groundwater Quality Impacts from a Continuous Pilot-Scale Release of an Ethanol Blend. Ground Water Monit. Remediat. *31*, 47–54.

Ma, J., Rixey, W.G., and Alvarez, P.J. (2013). Microbial processes influencing the transport, fate and groundwater impacts of fuel ethanol releases. Curr. Opin. Biotechnol. *24*, 457–466.

Ma, J., Rixey, W.G., and Alvarez, P.J.J. (2015). Increased fermentation activity and persistent methanogenesis in a model aquifer system following source removal of an ethanol blend release. Water Res. *68*, 479–486.

Mackay, D.M., de Sieyes, N.R., Einarson, M.D., Feris, K.P., Pappas, A.A., Wood, I.A., Jacobson, L., Justice, L.G., Noske, M.N., Scow, K.M., et al. (2006). Impact of ethanol on the natural attenuation of benzene, toluene, and o-xylene in a normally sulfate-reducing aquifer. Environ. Sci. Technol. *40*, 6123–6130.

Madigan, M.T., Martinko, J.M., and Parker, J. (1997). Brock biology of microorganisms (Upper Saddle River, NJ: Prentice Hall).

McCarty, P.L. (1964). Anaerobic waste treatment fundamentals. Part three, toxic materials and their control.

McDowell, C.J., and Powers, S.E. (2003). Mechanisms Affecting the Infiltration and Distribution of Ethanol-Blended Gasoline in the Vadose Zone. Environ. Sci. Technol. *37*, 1803–1810.

Mitchell, J.J., and Lucas-Lenard, J.M. (1980). The effect of alcohols on guanosine 5'-diphosphate-3'-diphosphate metabolism in stringent and relaxed Escherichia coli. J. Biol. Chem. *255*, 6307–6313.

Moran, M.J., Zogorski, J.S., and Shermer, M. (1999). MTBE in ground water in the United States occurance, potential sources, and long-term range transport. In 1999 Water Resources Conference, (American Water Works Association).

Natural Resources Canada (2016). ecoENERGY for Biofuels Program | Natural Resources Canada. Available at http://www.nrcan.gc.ca/energy/alternative-fuels/programs/12358. Accessed March 15th, 2016.

Oliviera, I.B., Demond, A.H., and Salehzadeh, A. (1996). Packing of Sands for the Production of Homogeneous Porous Media. Soil Sci. Soc. Am. J. *60*, 49.

Österreicher-Cunha, P., Vargas Jr., E. do A., Guimarães, J.R.D., Lago, G.P., Antunes, F. dos S., and da Silva, M.I.P. (2009). Effect of ethanol on the biodegradation of gasoline in an unsaturated tropical soil. Int. Biodeterior. Biodegrad. *63*, 208–216.

Ostrem, K., and Themelis, N.J. (2004). Greening waste: Anaerobic digestion for treating the organic fraction of municipal solid wastes. Columbia University.

Osztovics, M., Igali, S., Antal, A., and Véghelyi, P. (1980). Alcohol is not mutagenic. Mutat. Res. Mutagen. Relat. Subj. *74*, 247.

Plummer, M.A., Hull, L.C., and Fox, D.T. (2004). Transport of Carbon-14 in a Large Unsaturated Soil Column. Vadose Zone J. *3*, 109.

Powers, S.E., Hunt, C.S., Heermann, S.E., Corseuil, H.X., Rice, D., and Alvarez, P.J.J. (2001). The Transport and Fate of Ethanol and BTEX in Groundwater Contaminated by Gasohol. Crit. Rev. Environ. Sci. Technol. *31*, 79–123.

Priebe, J.M. (2013). Is Methane Produced from a Fuel-Ethanol Spill Predictable? University of Minnesota.

Ren, T., Amaral, J.A., and Knowles, R. (1997). The response of methane consumption by pure cultures of methanotrophic bacteria to oxygen. Can. J. Microbiol. *43*, 925–928.

Ruiz-Aguilar, G. m. ., O'Reilly, K., and Alvarez, P. j. j. (2003). A Comparison of Benzene and Toluene Plume Lengths for Sites Contaminated with Regular vs. Ethanol-Amended Gasoline. Ground Water Monit. Remediat. *23*, 48–53.

Sentenac, P., Lynch, R. j., and Bolton, M. d. (2001). Measurement of a side-wall boundary effect in soil columns using fibre-optics sensing. Int. J. Phys. Model. Geotech. *1*, 35–41.

Seol, Y., and Lee, L.S. (2001). Coupled Effects of Treated Effluent Irrigation and Wetting–Drying Cycles on Transport of Triazines through Unsaturated Soil Columns. J. Environ. Qual. *30*, 1644.

Sihota, N. (2014). NOVEL APPROACHES FOR QUANTIFYING SOURCE ZONE NATURAL ATTENUATION OF FOSSIL AND ALTERNATIVE FUELS. The University of British Columbia.

Sihota, N.J., and Mayer, K.U. (2012). Characterizing Vadose Zone Hydrocarbon Biodegradation Using Carbon Dioxide Effluxes, Isotopes, and Reactive Transport Modeling. Vadose Zone J. *11*, 0.

Sihota, N.J., Mayer, K.U., Toso, M.A., and Atwater, J.F. (2013). Methane emissions and contaminant degradation rates at sites affected by accidental releases of denatured fuel-grade ethanol. J. Contam. Hydrol. *151*, 1–15.

Sluder, S., and West, B.H. (2011). Nmog Emissions Characterizations and Estimation for Vehicles Using Ethanol-Blended Fuels (Oak Ridge National Laboratory (ORNL); Fuels, Engines and Emissions Research Center). Available at http://www.osti.gov/scitech/biblio/1027841/. Accessed March 15th, 2016.

Smajstrla, A.G. (1985). A field lysimeter system for crop water use and water stress studies in humid regions. Proc. - Soil Crop Sci. Soc. Fla. USA.

Smith, D.P., and McCarty, P.L. (1989). Energetic and rate effects on methanogenesis of ethanol and propionate in perturbed CSTRs. Biotechnol. Bioeng. *34*, 39–54.

Spalding, R.F., Toso, M.A., Exner, M.E., Hattan, G., Higgins, T.M., Sekely, A.C., and Jensen, S.D. (2011). Long-term groundwater monitoring results at large, sudden denatured ethanol releases. Groundw. Monit. Remediat. *31*, 69–81.

TH., van G., M. (1980). A Closed-Form Equation for Predicting the Hydraulic Conductivity of Unsaturated Soils. Soil Sci Soc Am *44*, 892–898.

Todd, D.K. (1959). Ground water hydrology (New York: Wiley).

UC Davis Analysis of Methane (CH4) by GasBench-Precon-IRMS. Available at http://stableisotopefacility.ucdavis.edu/ch4.html. Accessed August 17th, 2016.

United Tech, Inc. (2003). Anaerobic digestion UTI Web design.

US EPA (1998). Carcinogenic Effects of Benzene: An Update (Washington DC: National Center for Environmental Assessment, Office of Research and Development, U.S. Environmental Protection Agency.).Available at https://cfpub.epa.gov/ncea/risk/recordisplay.cfm?deid=2806. Accessed May 18th, 2017

Vogt, C., Kleinsteuber, S., and Richnow, H. (2011). Anaerobic benzene degradation by bacteria. Microb. Biotechnol. *4*, 710–724.

Warren, E., Sihota, N.J., Hostettler, F.D., and Bekins, B.A. (2014). Comparison of surficial CO2 efflux to other measures of subsurface crude oil degradation. J. Contam. Hydrol. *164*, 275–284.

Whiticar, M.J. (1999). Carbon and hydrogen isotope systematics of bacterial formation and oxidation of methane. Chem. Geol. *161*, 291–314.

Whiticar, M.J., Faber, E., and Schoell, M. (1986). Biogenic methane formation in marine and freshwater environments: CO2 reduction vs. acetate fermentation—Isotope evidence. Geochim. Cosmochim. Acta *50*, 693–709.

Wilson, J.T., Adair, C., White, H., and Howard, R.L. (2016). Effect of Biofuels on Biodegradation of Benzene and Toluene at Gasoline Spill Sites. Groundw. Monit. Remediat. *36*, 50–61.

Wolfe, R.S. (1983). Fermentation and anaerobic respiration in anaerobic digestion. (Boston).

Wolin, M., and Miller, T. (1982). Interspecies hydrogen transfer: 15 years later. ASM Am. Soc. Microbiol. News *48*, 561–565.

Wu, M.M., and Hickey, R.F. (1996). n-Propanol production during ethanol degradation using anaerobic granules. Water Res. *30*, 1686–1694.

Appendices

Appendix A

Appendix A contains all supplementary information from the sediment characterization in

Chapter 2- Methodology

A.1 Cumulative Grain Size Analysis- Graphs

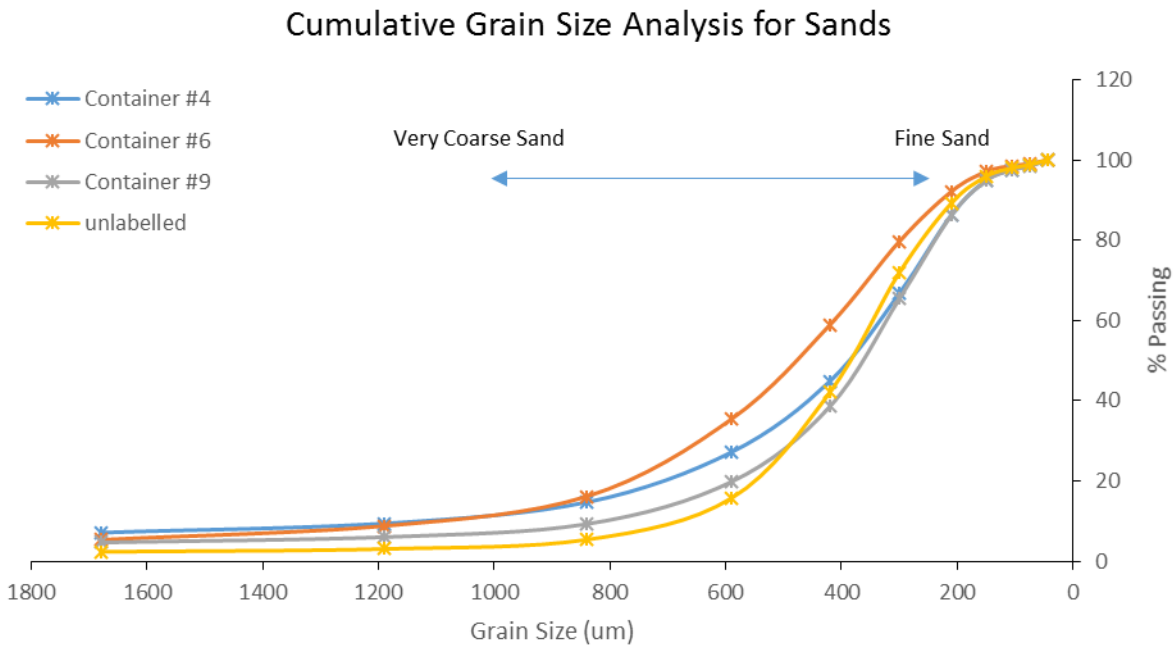

Figure A-1 Results of the sand grain size analysis presented as cumulative analysis. The Udden-Wentworth scale is used to overlay the results of the grain size analysis to provide a qualitative interpretation of the results. Results show the majority of the material consists of medium – fine sand.

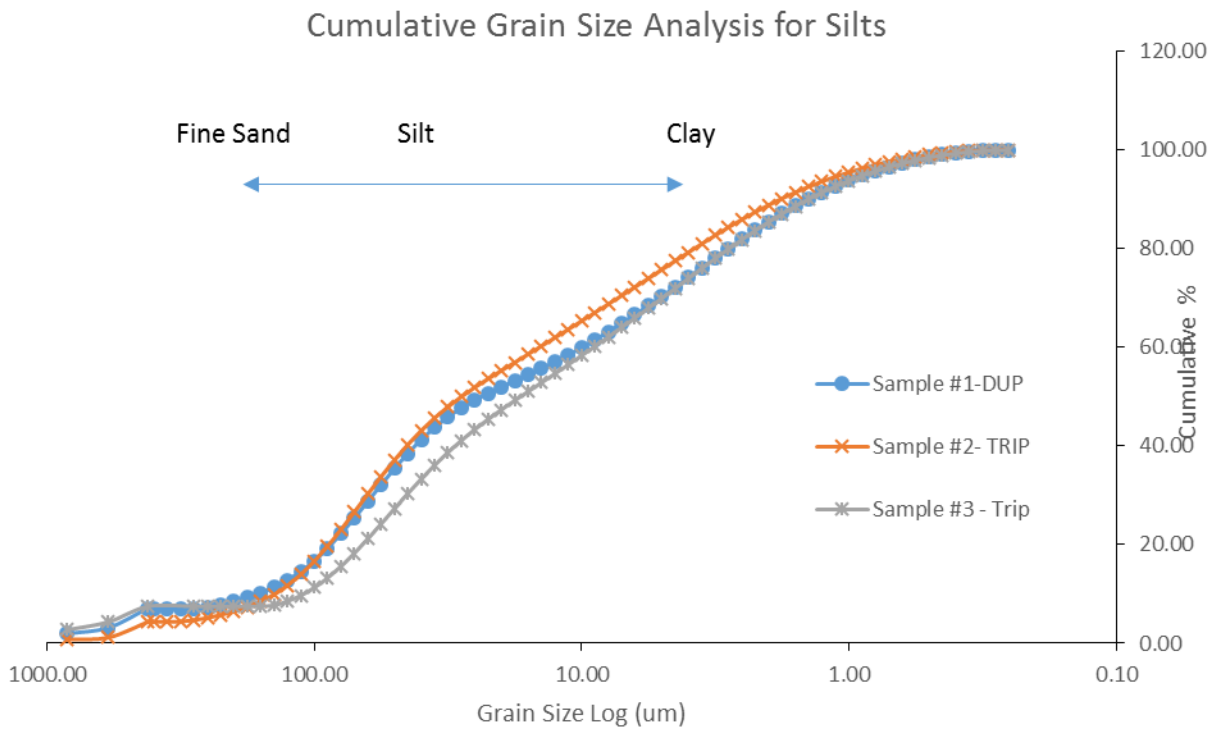

Figure A-2 Results from the silt grain size analysis presented as cumulative analysis. Silt samples were taken from all 3 Silt bags in equal proportions and then separated into 3 sample runs. The Udden-Wentworth scale is used to overlay the results of the grain size analysis to provide a qualitative interpretation of the results. Results show the majority of the material consists of fine sand to silt, with ~20% clay.

A.2 Grain Size Analysis – Raw Data

Table A-1 Cumulative percentage grain size analysis of 4 bags of sand, #4, #6, #9 and Unlabeled, taken from a local site in Burnaby.

Cumulative (%) grain size analysis - Sands #4, #6, #9, & Unlabeled					
U.S std. mesh No.	grain size (um)	#4 (%)	#6 (%)	#9 (%)	Unlabeled (%)
≥ 12	1680	7.17	5.39	4.71	2.40
16	1190	9.47	8.83	6.07	3.11
20	840	14.75	16.19	9.33	5.44
30	590	27.23	35.46	19.84	15.76
40	420	44.89	58.93	38.55	42.13
50	300	66.75	79.68	65.37	71.91
70	210	86.29	92.13	86.20	89.24
100	149	95.00	97.15	94.87	95.95
140	105	97.58	98.54	97.45	97.94
200	74	98.61	99.07	98.48	98.82
<200	44	100.00	100.00	100.00	100.00

Table A-2 The combined data from the sieve and Mastersizer results. This data represents the cumulative percent of grains from sample #1 which contained equal proportions from all 3 silt bags - "Unlabeled", "Container #1", and "Container #2".Once the sample was analyzed, the process was repeated in triplicate to evaluate the sampling technique. The results show a reliable sampling technique which provided consistent results.

Cumulative % Grain Size Analysis - Silts			
Sample #1- 3 min Ultrasonic treatment - Average			
Grain size (um)	Sample 1 (%)	Sample 1- DUP (%)	Sample 1- TRIP (%)
840.00	1.98	1.98	1.98
590.00	3.16	3.16	3.16
420.00	7.11	7.11	7.11
399.05	7.11	7.11	7.11
355.66	7.15	7.11	7.11
316.98	7.26	7.11	7.11
282.51	7.58	7.11	7.11
251.79	8.06	7.34	7.14
224.40	8.68	7.85	7.22
200.00	9.47	8.49	7.37
178.25	10.47	9.29	7.56
158.87	11.77	10.23	7.83
141.59	13.48	11.38	8.38
126.19	15.72	12.81	9.32
112.47	18.55	14.57	10.66
100.24	22.03	16.73	12.45
89.34	26.12	19.29	14.70
79.62	30.71	22.20	17.42
70.96	35.64	25.39	20.53
63.25	40.71	28.75	23.94
56.37	45.68	32.14	27.51
50.24	50.37	35.43	31.13
44.77	54.60	38.52	34.67
39.91	58.26	41.31	38.05
35.57	61.31	43.78	41.18
31.70	63.77	45.92	44.05
28.25	65.69	47.75	46.65
25.18	67.18	49.32	49.01
22.44	68.34	50.71	51.16
20.00	69.28	51.99	53.15
17.83	70.11	53.21	55.02
15.89	70.89	54.44	56.81
14.16	71.69	55.71	58.55
12.62	72.54	57.05	60.27
11.25	73.45	58.47	61.97
10.02	74.41	59.96	63.66
8.93	75.43	61.53	65.34
7.96	76.49	63.17	67.02
7.10	77.59	64.87	68.71
6.32	78.71	66.63	70.40
5.64	79.86	68.45	72.11
5.02	81.03	70.32	73.84
4.48	82.22	72.24	75.58
3.99	83.43	74.18	77.32

Cumulative % Grain Size Analysis - Silts			
Sample #1- 3 min Ultrasonic treatment - Average			
Grain size (um)	Sample 1 (%)	Sample 1- DUP (%)	Sample 1- TRIP (%)
3.56	84.64	76.14	79.06
3.17	85.84	78.09	80.78
2.83	87.03	80.02	82.46
2.52	88.20	81.90	84.10
2.24	89.33	83.72	85.68
2.00	90.42	85.47	87.19
1.78	91.45	87.13	88.63
1.59	92.44	88.69	89.98
1.42	93.36	90.14	91.24
1.26	94.22	91.49	92.41
1.12	95.01	92.73	93.49
1.00	95.75	93.86	94.49
0.89	96.42	94.88	95.39
0.80	97.03	95.81	96.21
0.71	97.59	96.64	96.95
0.63	98.09	97.37	97.60
0.56	98.53	98.01	98.18
0.50	98.91	98.56	98.68
0.45	99.24	99.02	99.09
0.40	99.50	99.39	99.43
0.36	99.71	99.67	99.69
0.32	99.87	99.87	99.87
0.28	99.96	99.96	99.97
0.25	100.00	100.00	100.00

Table A-3 The combined data from the sieve and Mastersizer results. This data represents the cumulative percent of grains from sample #2 which contained equal proportions from all 3 silt bags - "Unlabeled", "Container #1", and "Container #2".Once the sample was analyzed, the process was repeated in triplicate to evaluate the sampling technique. The results show a reliable sampling technique which provided consistent results.

Cumulative % Grain Size Analysis – (Silts cont'd)			
Sample #2- 3 min Ultrasonic treatment - Average			
Grain size (um)	Sample 2 (%)	Sample 2- DUP (%)	Sample 2- TRIP (%)
840.00	0.79	0.79	0.79
590.00	1.19	1.19	1.19
420.00	4.35	4.35	4.35
399.05	4.40	4.35	4.35
355.66	4.69	4.36	4.35
316.98	5.23	4.44	4.38
282.51	5.98	4.71	4.50
251.79	6.89	5.18	4.74
224.40	7.96	5.76	5.04
200.00	9.21	6.48	5.51
178.25	10.69	7.37	6.38
158.87	12.49	8.49	7.66
141.59	14.68	9.92	9.42
126.19	17.33	11.73	11.67
112.47	20.47	13.97	14.46
100.24	24.06	16.64	17.76
89.34	28.01	19.70	21.52
79.62	32.19	23.07	25.62
70.96	36.43	26.63	29.91
63.25	40.57	30.25	34.20
56.37	44.45	33.80	38.35
50.24	47.95	37.17	42.22
44.77	51.00	40.30	45.73
39.91	53.59	43.14	48.82
35.57	55.74	45.68	51.49
31.70	57.51	47.95	53.77
28.25	58.99	49.99	55.73
25.18	60.25	51.86	57.43
22.44	61.39	53.61	58.95
20.00	62.47	55.30	60.36
17.83	63.56	56.96	61.72
15.89	64.69	58.61	63.06
14.16	65.86	60.28	64.41
12.62	67.10	61.96	65.78
11.25	68.38	63.65	67.18
10.02	69.71	65.35	68.61
8.93	71.07	67.06	70.07
7.96	72.47	68.77	71.55
7.10	73.89	70.49	73.07
6.32	75.35	72.23	74.61

Cumulative % Grain Size Analysis – (Silts cont'd)			
Sample #2- 3 min Ultrasonic treatment - Average			
Grain size (um)	Sample 2 (%)	Sample 2- DUP (%)	Sample 2- TRIP (%)
5.64	76.83	73.98	76.18
5.02	78.33	75.75	77.77
4.48	79.84	77.51	79.37
3.99	81.36	79.27	80.97
3.56	82.87	81.00	82.55
3.17	84.35	82.70	84.10
2.83	85.79	84.34	85.61
2.52	87.18	85.92	87.06
2.24	88.52	87.43	88.45
2.00	89.78	88.85	89.76
1.78	90.98	90.19	90.99
1.59	92.09	91.43	92.13
1.42	93.13	92.58	93.19
1.26	94.09	93.64	94.17
1.12	94.97	94.61	95.06
1.00	95.78	95.49	95.88
0.89	96.51	96.28	96.61
0.80	97.17	97.00	97.27
0.71	97.77	97.64	97.86
0.63	98.29	98.20	98.37
0.56	98.74	98.68	98.81
0.50	99.12	99.09	99.19
0.45	99.43	99.42	99.49
0.40	99.68	99.68	99.72
0.36	99.86	99.86	99.88
0.32	99.96	99.96	99.97
0.28	100.00	100.00	100.00
0.25	100.00	100.00	100.00

Table A-4 The combined data from the sieve and Mastersizer results. This data represents the cumulative percent of grains from sample #3 which contained equal proportions from all 3 silt bags - "Unlabeled", "Container #1", and "Container #2".Once the sample was analyzed, the process was repeated in triplicate to evaluate the sampling technique. The results show a reliable sampling technique which provided consistent results.

Cumulative % Grain Size Analysis - Silts (cont'd)			
Sample #3- 3 min Ultrasonic treatment - Average			
Grain size (um)	Sample 3 (%)	Sample 3- DUP (%)	Sample 3- TRIP (%)
840.00	2.77	2.77	2.77
590.00	4.35	4.35	4.35
420.00	7.51	7.51	7.51
282.51	7.51	7.51	7.51
251.79	7.63	7.51	7.51
224.40	7.97	7.51	7.51
200.00	8.45	7.51	7.53
178.25	9.08	7.51	7.69
158.87	9.87	7.51	8.25
141.59	10.87	7.74	9.26
126.19	12.17	8.57	10.64
112.47	13.82	9.72	12.43
100.24	15.86	11.29	14.63
89.34	18.30	13.27	17.21
79.62	21.11	15.61	20.16
70.96	24.21	18.26	23.38
63.25	27.50	21.16	26.77
56.37	30.87	24.21	30.22
50.24	34.19	27.30	33.60
44.77	37.37	30.37	36.81
39.91	40.34	33.32	39.77
35.57	43.04	36.11	42.45
31.70	45.47	38.71	44.83
28.25	47.65	41.12	46.94
25.18	49.60	43.34	48.83
22.44	51.38	45.40	50.56
20.00	53.03	47.35	52.17
17.83	54.61	49.22	53.74
15.89	56.14	51.04	55.29
14.16	57.68	52.85	56.86
12.62	59.22	54.66	58.46
11.25	60.79	56.49	60.11
10.02	62.40	58.34	61.79
8.93	64.03	60.21	63.50

Cumulative % Grain Size Analysis - Silts (cont'd)			
Sample #3- 3 min Ultrasonic treatment - Average			
Grain size (um)	Sample 3 (%)	Sample 3-DUP (%)	Sample 3- TRIP (%)
7.96	65.69	62.10	65.24
7.10	67.38	64.02	67.01
6.32	69.11	65.96	68.79
5.64	70.87	67.94	70.60
5.02	72.66	69.93	72.43
4.48	74.48	71.95	74.27
3.99	76.32	73.98	76.12
3.56	78.15	76.00	77.96
3.17	79.96	78.00	79.78
2.83	81.74	79.95	81.57
2.52	83.47	81.85	83.30
2.24	85.13	83.68	84.97
2.00	86.71	85.42	86.57
1.78	88.21	87.08	88.09
1.59	89.62	88.63	89.52
1.42	90.94	90.07	90.85
1.26	92.15	91.41	92.09
1.12	93.27	92.64	93.22
1.00	94.30	93.77	94.26
0.89	95.23	94.79	95.21
0.80	96.08	95.72	96.07
0.71	96.84	96.55	96.84
0.63	97.51	97.29	97.52
0.56	98.11	97.94	98.12
0.50	98.62	98.50	98.64
0.45	99.05	98.97	99.07
0.40	99.39	99.35	99.41
0.36	99.66	99.64	99.68
0.32	99.86	99.85	99.87
0.28	99.96	99.96	99.96
0.251785	100.00	100.00	100.00

A.3 Summary of XRD Results

Table A-5 Soil mineralogical data obtained through XRD analysis.

Mineral	Ideal Formula	Sand 1 (%)	Sand 2 (%)	Silt 3 (%)
Quartz	SiO_2	43.9	44.9	36.1
Clinochlore	$(Mg,Fe^{2+})_5Al(Si_3Al)O_{10}(OH)_8$	1.9	1.1	2.7
Illite-Muscovite 2M1	$K_{0.65}Al_{2.0}Al_{0.65}Si_{3.35}O_{10}(OH)_2$ -$KAl_2AlSi_3O_{10}(OH)_2$	4.2	3.1	4.9
Plagioclase	$NaAlSi_3O_8 – CaAlSi_2O_8$	38.9	39.3	42.1
K-feldspar	$KAlSi_3O_8$	4.8	6.0	5.7
Ankerite-Dolomite	$Ca(Fe^{2+},Mg,Mn)(CO_3)_2$-$CaMg(CO_3)_2$	0.9	0.9	0.8
Actinolite	$Ca_2(Mg,Fe^{2+})_5Si_8O_{22}(OH)_2$	3.5	4.3	6.4
Marcasite ?	FeS_2	0.4		
Titanite ?	$CaTiSiO_5$	1.1		
Magnetite ?	Fe_3O_4	0.3	0.4	1.0
Zircon ?	$ZrSiO_4$			0.4
Total		100.0	100.0	100.0

A.4 XRD – Raw Data

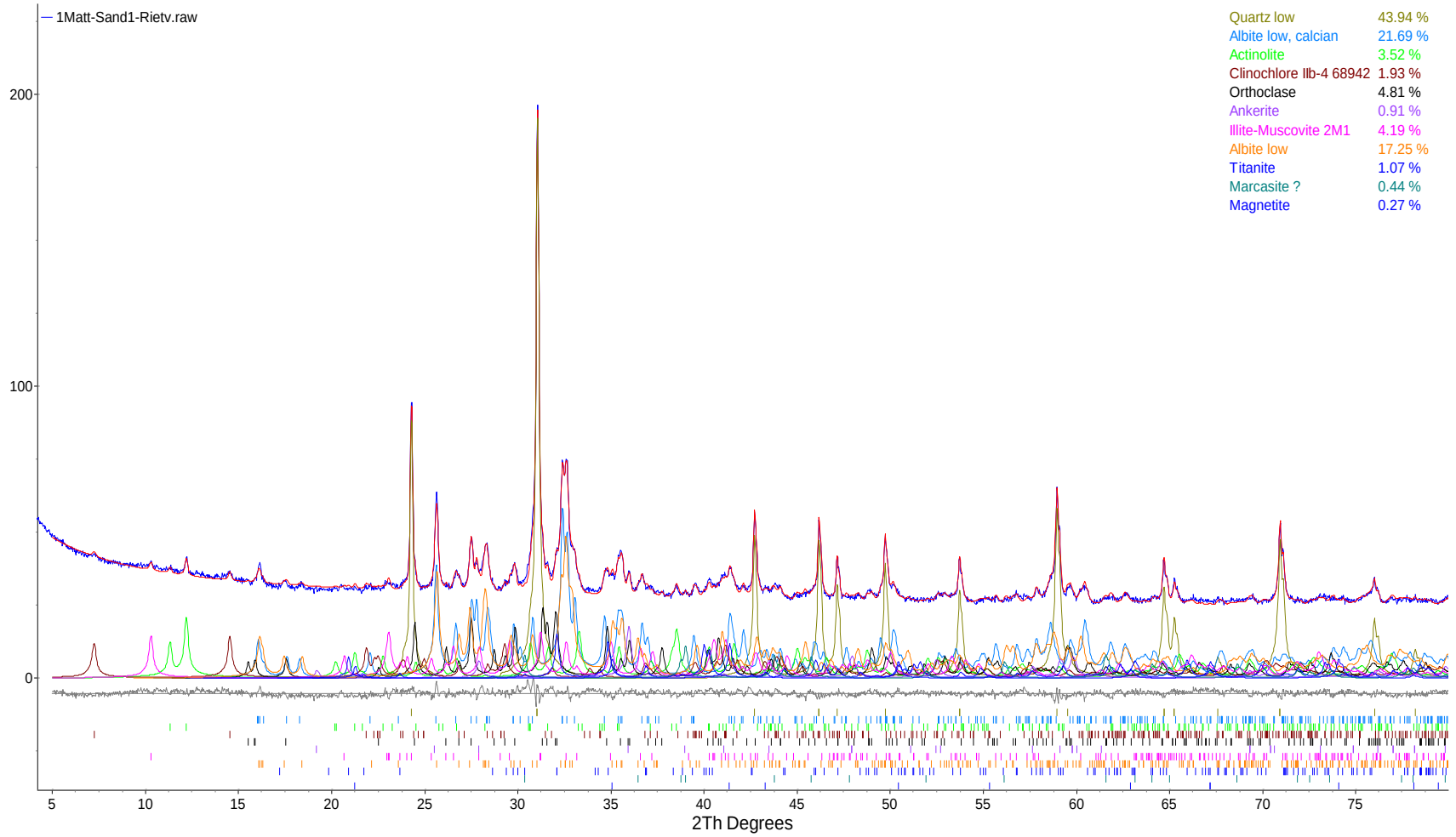

Figure A-3 Rietveld refinement plot of sample Sand 1. The blue lines are observed intensity at each step; red line is the calculated pattern; solid gray line (below), is the difference between observed and calculated intensities. The coloured lines are individual diffraction patterns of all phases. The small vertical bars (bottom) display the positions of all Bragg reflections.

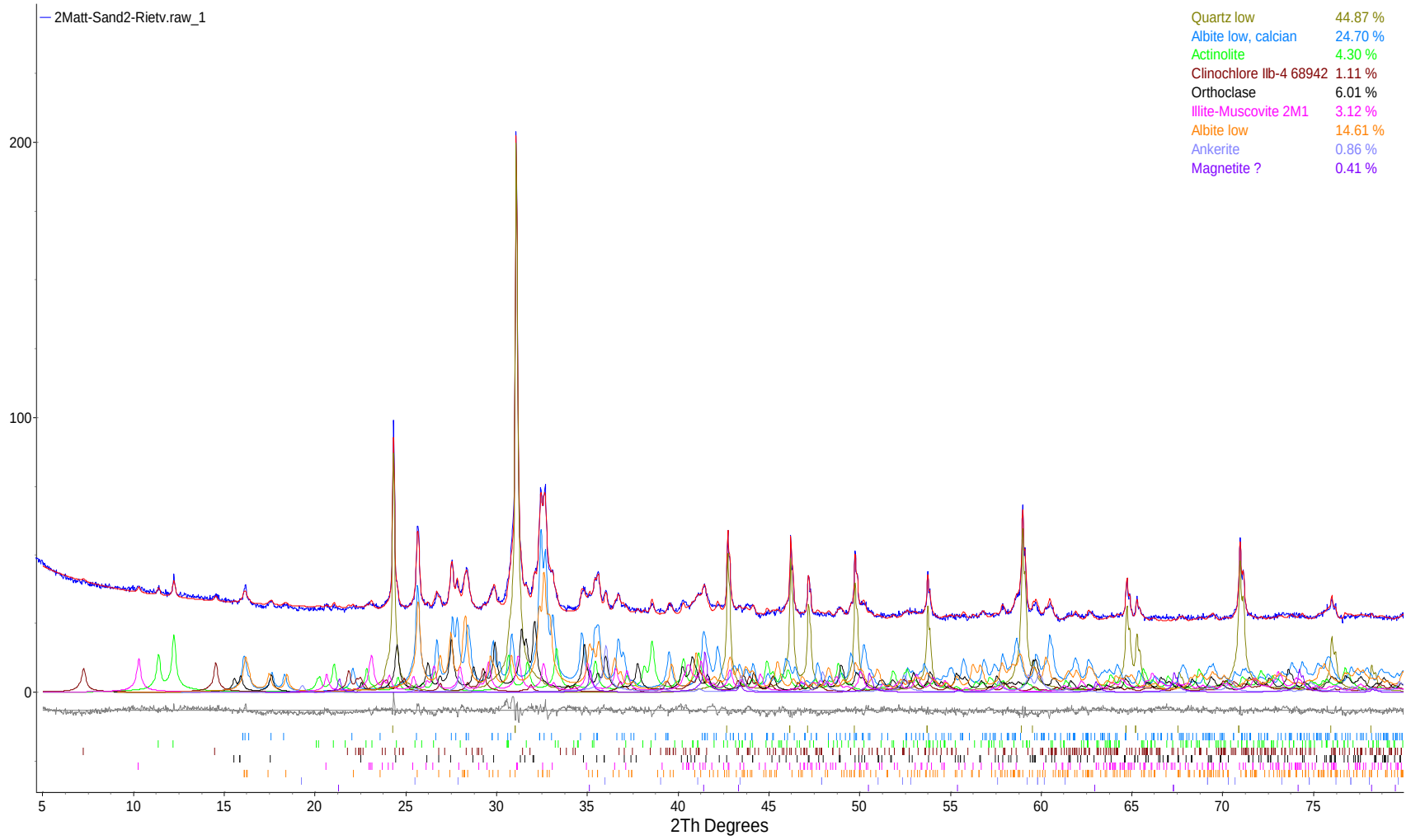

Figure A-4 Rietveld refinement plot of sample Sand 2. The blue lines are observed intensity at each step; red line is the calculated pattern; solid gray line (below), is the difference between observed and calculated intensities. The coloured lines are individual diffraction patterns of all phases. The small vertical bars (bottom) display the positions of all Bragg reflections.

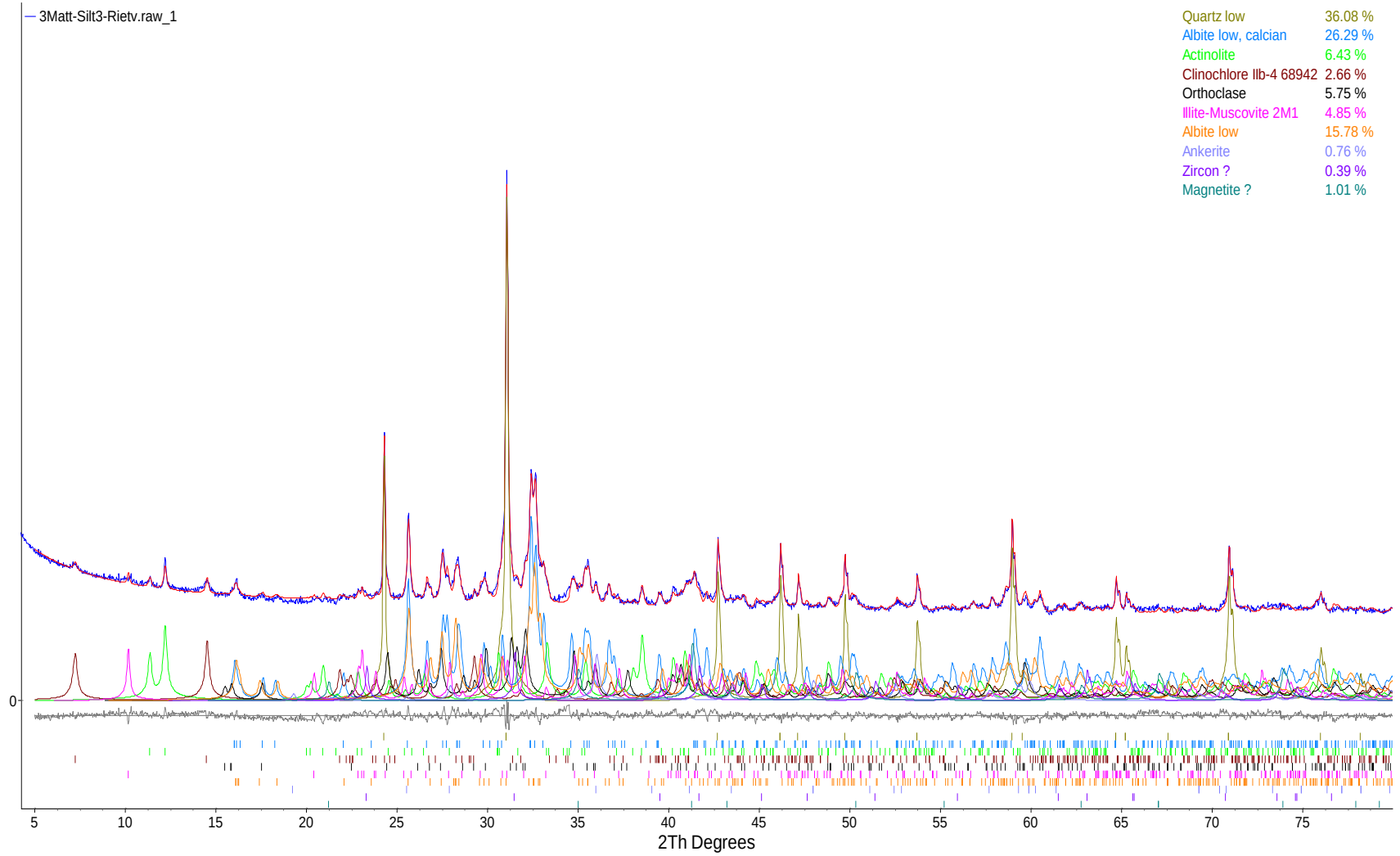

Figure A-5 Rietveld refinement plot of sample Silt -3. The blue lines are observed intensity at each step; red line is the calculated pattern; solid gray line (below), is the difference between observed and calculated intensities. The coloured lines are individual diffraction patterns of all phases. The small vertical bars (bottom) display the positions of all Bragg reflection.

A.5 Summary of Soil Geochemistry Data

Table A-6 Geochemical data on the sand, and silty-sand material. Tests which were performed include Total Carbon (C), Total Inorganic Carbon (TIC), and Metals by Multi-Acid Digestion with ICP-MS Finish.

Sample ID	C (Total)	TIC	TOC	Al	Ca	Fe	K	Mg	Mn	Na	P	S
	%	%	%	%	%	%	%	%	ppm	%	%	%
Method Code	CSA06V	CSV02B	Calc.	ICM40B	ICM40B	ICM40B	ICM40B	ICM40B	ICM40B	ICM40B	ICM40B	ICM40B
LOD	0.005	0.01	#N/A	0.01	0.01	0.01	0.01	0.01	2	0.01	0.005	0.01
UBC-Sand 1	0.056	<0.01	0.056	6.32	1.92	2.43	0.91	0.69	458	2.12	0.031	<0.01
UBC-Sand 2	0.084	<0.01	0.084	6.66	2.12	2.62	1	0.79	512	2.27	0.04	<0.01
UBC-Silt	0.211	0.11	0.101	7.31	2.87	3.61	1.11	1.43	680	2.13	0.058	0.01
UBC-Silt (DUP)	0.216	0.11		7.37	2.87	3.65	1.12	1.47	698	2.15	0.06	0.01
QC												
GTS-2A	1.99											
Certified Value	2.01											
Tolerance +/-	0.15											
SY-4		0.91										
Certified Value		0.95										
Tolerance +/-		0.06										
OREAS 901				7.2	0.09	4.06	3.89	0.63	283	0.04	0.06	0.04
Expected Values												
Tolerance (%)				6.81	0.092	4.03	3.67	0.6	290	0.042	620	0.036
				10.37	37.17	10.62	10.68	14.17	11.72	69.52	30.16	79.44

Appendix B

Appendix B contains all supplementary information from the hydrogeological characterization in Chapter 2- Methodology

B.1 Soil Water Retention Curves – Tempe Cell Data

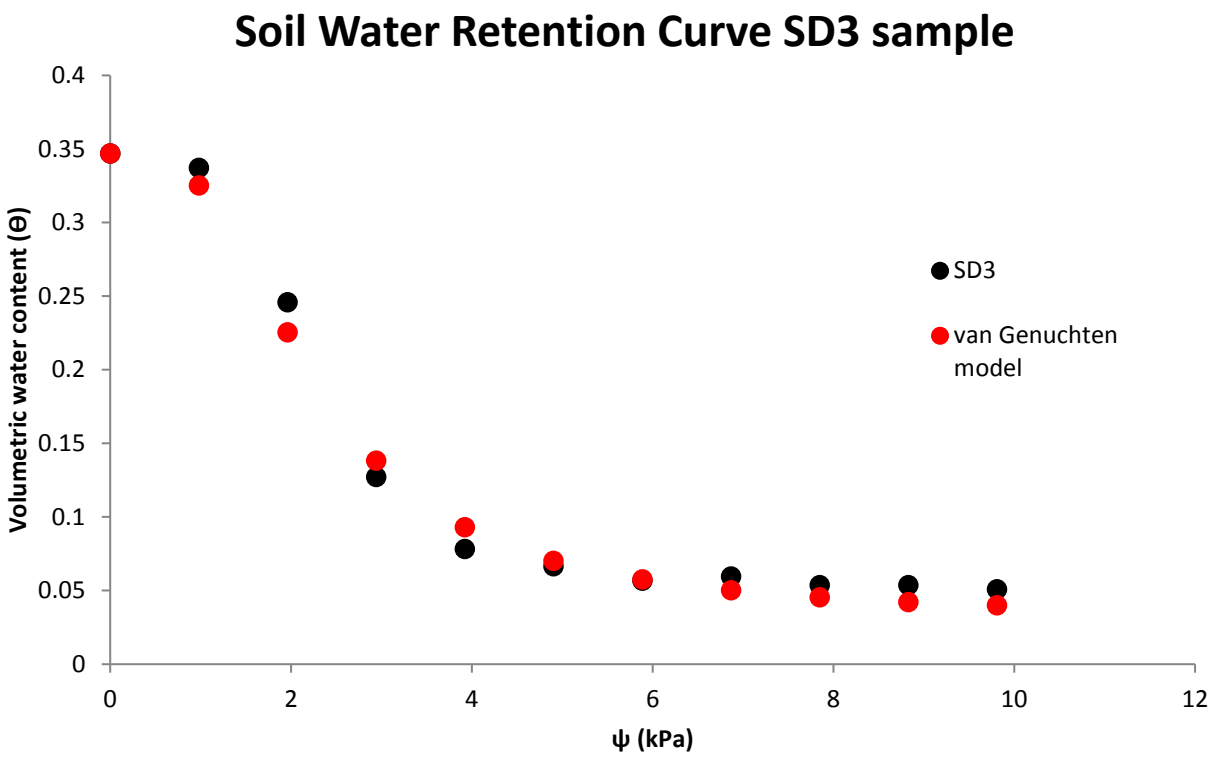

Figure B-1 Tempe cell results for SD3- sand sample. The empirical van Genuchten model is also displayed, and shows a good match between the model and the data.

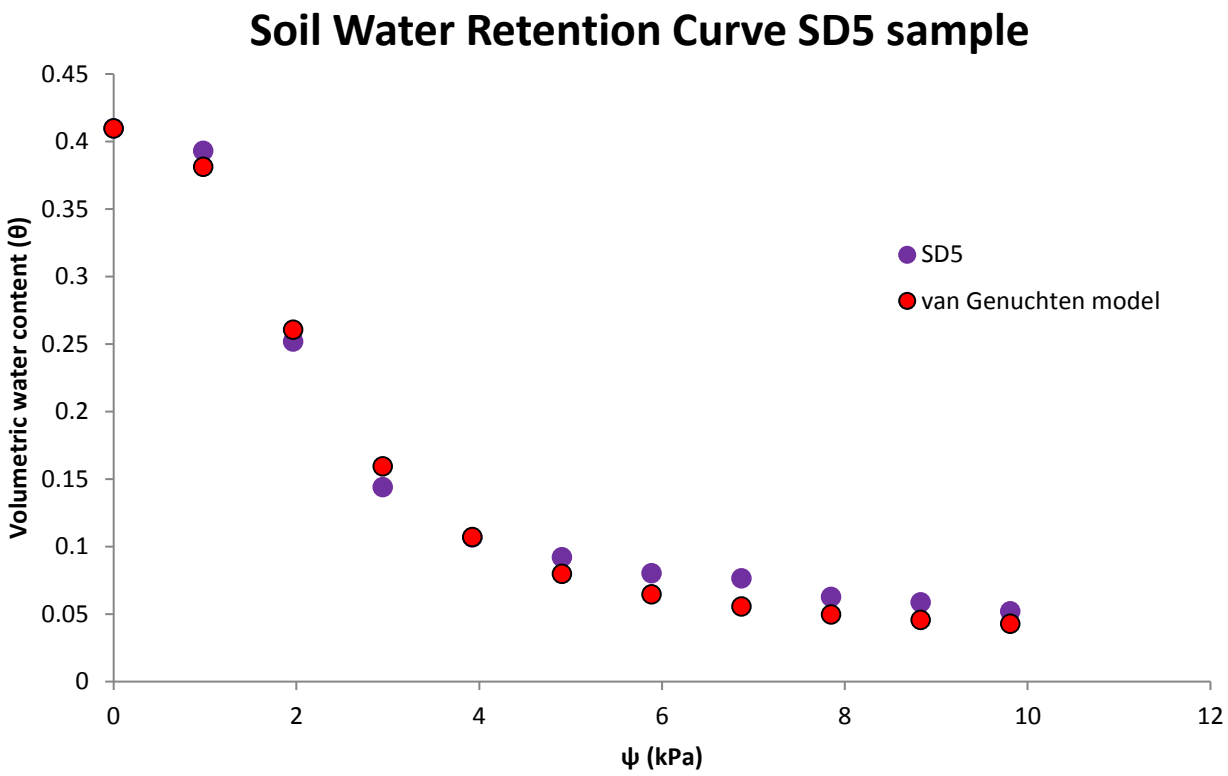

Figure B-2 Tempe cell results for SD5- sand sample. The empirical van Genuchten model is also displayed, and shows a good match between the model and the data.

B.2 Soil Water Characteristic Curves - Raw Data

Table B-1 Soil water characteristic curve data. A summary of the measured, modelled and model deviations between the van Genuchten (1980) empirical model and the Tempe cell experimental data. Relative hydraulic conductivity values are calculated based on the relationship derived by van Genuchten (1980) which calculated relative saturated hydraulic conductivity as a function of matric potential (ψ).

Soil Water Characteristic Curves - Measured and Modelled (van Genuchten)					
Sample Name	Tension ψ (kPa)	Θ (cm3/cm3) Measured	Θ (cm3/cm3) Model	Dev^2	K_r (ψ)= K(ψ)/ K_{sat}
SD3 (Sand)	0.00	0.347	0.347	3.08E-33	1
	0.98	0.337	0.325	1.39E-04	0.93
	1.96	0.246	0.226	4.19E-04	0.84
	2.94	0.127	0.138	1.20E-04	0.74
	3.92	0.078	0.093	2.19E-04	0.64
	4.91	0.067	0.070	1.35E-05	0.55
	5.89	0.057	0.058	8.60E-07	0.45
	6.87	0.060	0.050	8.98E-05	0.36
	7.85	0.054	0.046	6.95E-05	0.26
	8.83	0.054	0.042	1.33E-04	0.15
	9.81	0.051	0.040	1.17E-04	0.03
SD5 (Sand)	0.00	0.410	0.410	3.08E-33	1
	0.98	0.393	0.381	1.44E-04	0.91
	1.96	0.252	0.261	7.43E-05	0.79
	2.94	0.144	0.160	2.38E-04	0.68
	3.92	0.107	0.107	8.02E-09	0.57
	4.91	0.092	0.080	1.52E-04	0.47
	5.89	0.080	0.065	2.46E-04	0.37
	6.87	0.076	0.056	4.37E-04	0.26
	7.85	0.063	0.050	1.71E-04	0.15
	8.83	0.059	0.046	1.73E-04	0.02
	9.81	0.052	0.043	8.28E-05	-0.12

B.3 Summary of Van Genuchten Parameters

Table B-2 The curve fitting parameters n and α determined by using the empirical formula derived by van Genuchten (1980). The R^2 value shows a good fit between the model and the measured data. The table also shows the saturated water content Θ_s and the residual water content Θ_r.

Van Genuchten parameters for Sand					
Sample name	α (kPa^{-1})	n	Θ_r (cm^3/cm^3)	Θ_s (cm^3/cm^3)	R^2 fit to VG model
SD3 (Sand)	0.12	3.24	0.032	0.347	0.991
SD5 (Sand)	0.13	3.15	0.032	0.410	0.991

B.4 Hydraulic Conductivity

Table B-3 Saturated hydraulic conductivity for both soil materials; Sand, and Silty-Sand. The difference in saturated hydraulic conductivity is 2 orders of magnitude.

Silty-Sand K_{sat}		*Sand K_{sat}*	
Run	K (m/s)	Run	K (m/s)
1	1.20E-06	8	1.10E-04
2	1.20E-06	9	1.00E-04
3	1.23E-06	10	1.20E-04
4	1.25E-06	11	1.30E-04
5	1.33E-06	12	1.30E-04
6	1.21E-06		
Average	**1.2E-06**		**1.2E-04**

B.5 Soil Properties

Table B-4 Material properties for the two types of soil; sand and silty-sand. The bulk densities and porosities were calculated from the hydraulic conductivity data for the silts and the unsaturated conductivity data for the sands. Bulk densities were calculated from oven dried soil which was packed into their respective apparatuses. These apparatuses were then weighed once saturation was reached, and the porosity was back calculated.

Soil material properties							
	Trial #	wt. Sat (g)	wt. Unsat (g)	Bulk density ρ_b(g/cm^3)	Vol. water (cm^3)	Vol. sample (cm^3)	Porosity ϕ (cm^3/cm^3)
Sand	1	187.30	151.90	1.49	35.40	102.00	0.35
	2	194.10	152.30	1.49	41.80	102.00	0.41
Silty-Sand (5% silt)	1	212.00	177.90	1.70	34.10	104.55	0.33
	2	219.50	182.90	1.75	36.60	104.55	0.35
	3	214.50	176.50	1.69	38.00	104.55	0.36

Appendix C

Appendix C contains all supplementary information regarding data logging in Chapter 2-

Methodology

C.1 Relay Driver Code (Provided by N. Sihota) - Arduino MEGA CO_2 Control

```
#define RELAY_ON LOW //0
#define RELAY_OFF HIGH //1
#define Relay_1  4  // Arduino Digital I/O pin number
#define Relay_2  5
#define Relay_3  6
#define Relay_4  7
void setup()   /****** SETUP: RUNS ONCE ******/
{
//-------( Initialize Pins so relays are inactive at reset)----
  digitalWrite(Relay_1, RELAY_OFF);
  digitalWrite(Relay_2, RELAY_OFF);
  digitalWrite(Relay_3, RELAY_OFF);
  digitalWrite(Relay_4, RELAY_OFF);

//---( THEN set pins as outputs )----
  pinMode(Relay_1, OUTPUT);
  pinMode(Relay_2, OUTPUT);
  pinMode(Relay_3, OUTPUT);
  pinMode(Relay_4, OUTPUT);
  delay(4000); //Check that all relays are inactive at Reset
}//--(end setup )---

void loop()   /****** LOOP: RUNS CONSTANTLY ******/
{
//---( Turn all 4 relays ON in sequence)---
  digitalWrite(Relay_1, RELAY_ON);// set the Relay ON
  delay(1000);            // wait for a second
  digitalWrite(Relay_2, RELAY_ON);// set the Relay ON
  delay(1000);            // wait for a second
  digitalWrite(Relay_3, RELAY_ON);// set the Relay ON
  delay(1000);            // wait for a second
  digitalWrite(Relay_4, RELAY_ON);// set the Relay ON
  delay(300000);            // wait see all relays ON

//---( Turn all 4 relays OFF in sequence)---
  digitalWrite(Relay_1, RELAY_OFF);// set the Relay OFF
  delay(1000);            // wait for a second
```

```
  digitalWrite(Relay_2, RELAY_OFF);// set the Relay OFF
  delay(1000);              // wait for a second
  digitalWrite(Relay_3, RELAY_OFF);// set the Relay OFF
  delay(1000);              // wait for a second
  digitalWrite(Relay_4, RELAY_OFF);// set the Relay OFF
  delay(900000);              // wait see all relays OFF

}//--(end main loop )---
```

C.2 Columns Low-Level Code (Provided by N. Sihota) - Arduino MEGA Digita Logging

Code for Moisture Sensors.

```
//arduino low level sensor code
#include <SoftwareSerial.h>
#include <avr/wdt.h>
#define LED 13
#define num_sensors 10
#define txpin 2
#define rxpin 3
typedef struct
{
 int serial_address;
 int power_address;
 String data_in;
 int sensor_type; //1 = GS3, 2=MPS2
}
sensor;
sensor sensor_array[num_sensors];
int get_status_UART(int sensor_number){
 long start_time=millis();
 delay(100);
 sensor_array[sensor_number].data_in=" ";
 //Serial.println("Start of get_status");
 int flag = 1;
 char char_in;
 if(sensor_array[sensor_number].serial_address == 15){
 Serial3.begin(1200);
 }
 else if(sensor_array[sensor_number].serial_address == 17){
 Serial2.begin(1200);
 }
 else if(sensor_array[sensor_number].serial_address == 19){
 Serial1.begin(1200);
```

```
 }
 Serial1.flush();
 Serial2.flush();
 Serial3.flush();
 delay(100);
 digitalWrite(sensor_array[sensor_number].power_address,HIGH);
 while(flag){
 if(sensor_array[sensor_number].serial_address == 15){
 if(Serial3.available()){
 char_in = Serial3.read();
 }
 else{
 char_in = -1;
 }
 }
 else if(sensor_array[sensor_number].serial_address == 17){
 if(Serial2.available()){
 char_in = Serial2.read();
 }
 else{
 char_in = -1;
 }
 }
 else if(sensor_array[sensor_number].serial_address == 19){
 if(Serial1.available()){
 char_in = Serial1.read();
 }
 else{
 char_in = -1;
 }
 }
 if(char_in == 13){
 flag = 0;
 }
 else if(((char_in >= '0')&&(char_in <='9'))||(char_in ==' ')||(char_in =='.')||(char_in
==')){
 sensor_array[sensor_number].data_in+=char_in;
 }
 if(millis()-start_time>1500){
 if(sensor_array[sensor_number].sensor_type == 1){
 sensor_array[sensor_number].data_in = "NaN\tNaN\tNaN";
 }
 else if(sensor_array[sensor_number].sensor_type == 2){
 sensor_array[sensor_number].data_in = "NaN\tNaN";
 }
```

```
 else{
 sensor_array[sensor_number].data_in = "NaN";
 }
 flag = 0;
 }
 }
 digitalWrite(sensor_array[sensor_number].power_address,LOW);
 Serial.print(sensor_array[sensor_number].data_in);

 Serial1.end();
 Serial2.end();
 Serial3.end();
 delay(100);
 return(0);
}
int get_status(int sensor_number){
 sensor_array[sensor_number].data_in="";
int flag = 1;
 char char_in; //memory needed to store one byte of data (read returins one byte)
 SoftwareSerial serial_object(sensor_array[sensor_number].serial_address,txpin);
 serial_object.begin(1200);
 serial_object.listen();
 while(serial_object.available()){
 serial_object.read();
 }
 long start_time=millis();
 delay(200);
 pinMode(sensor_array[sensor_number].power_address,OUTPUT);
 digitalWrite(sensor_array[sensor_number].power_address,HIGH);
 while(flag){
 if(serial_object.available()){
 char_in = serial_object.read();
 }
 else{
 char_in = -1;
 delay(50);
 }
 if(char_in == 13){
 flag = 0;
 }
 else if(((char_in >= '0')&&(char_in <='9'))||(char_in ==' ')||(char_in =='.')||(char_in
=='-')){
 sensor_array[sensor_number].data_in+=char_in; //write data for sensor
 }
 if(millis()-start_time>2000){
```

```
 if(sensor_array[sensor_number].sensor_type == 1){
 sensor_array[sensor_number].data_in = "NaN\tNaN\tNaN";
 }
 else if(sensor_array[sensor_number].sensor_type == 2){
 sensor_array[sensor_number].data_in = "NaN\tNaN";
 }
 else{
 sensor_array[sensor_number].data_in = "NaN";
 }
 flag = 0;
 }
 }
Serial.print(sensor_array[sensor_number].data_in);
digitalWrite(sensor_array[sensor_number].power_address,LOW);
 delay(100);
 return(0);
}
void setup(){
 pinMode(LED,OUTPUT);
 Serial.begin(9600);
pinMode(14,OUTPUT);
 digitalWrite(14,LOW);
 int n=0;
//below are the sensor/pin IDs
sensor_array[0].power_address=55;//A1
 sensor_array[0].serial_address=62; //A8
 sensor_array[n].sensor_type = 1; //5TE
 n++; //1
sensor_array[n].power_address=57; // A3
 sensor_array[n].serial_address=64; // A10
 sensor_array[n].sensor_type = 1;
 n++; //2
sensor_array[n].power_address=59; //A5
 sensor_array[n].serial_address=67; //A13
 sensor_array[n].sensor_type = 1;
 n++; //3
sensor_array[n].power_address=60; //A6
 sensor_array[n].serial_address=69; //A15
 sensor_array[n].sensor_type = 1;
 n++; //4
sensor_array[n].power_address=61; //A7
 sensor_array[n].serial_address=68; //A14
 sensor_array[n].sensor_type = 1;
 n++;//5
sensor_array[n].power_address=56; //A2
```

```
 sensor_array[n].serial_address=63; //A9
 sensor_array[n].sensor_type = 2;
 n++;//6
sensor_array[n].power_address=58; //A4
 sensor_array[n].serial_address=65; //A11
 sensor_array[n].sensor_type = 2;
 n++;//7
sensor_array[n].power_address=18;
 sensor_array[n].serial_address=17;
 sensor_array[n].sensor_type = 2;
 n++;//8
sensor_array[n].power_address=9;
 sensor_array[n].serial_address=11;
 sensor_array[n].sensor_type = 2;
 n++;//9
sensor_array[n].serial_address=15;
 sensor_array[n].power_address=16;
 sensor_array[n].sensor_type = 2;
 for(int I=0;I<num_sensors;I++){
 pinMode(sensor_array[I].power_address,OUTPUT);
 pinMode(sensor_array[I].serial_address,INPUT);
}
}
void loop(){
 while(1){
 Serial.print(double(millis())/1000.);
 Serial.print("\t");
 for(int I=0;I<num_sensors;I++){
if((sensor_array[I].serial_address == 15)||(sensor_array[I].serial_address == 17)||
(sensor_array[I].serial_address == 19)){
 get_status_UART(I);
 }
 else{
 get_status(I);
 }
Serial.print("\t");
 delay(10);
 }
 Serial.print("\n");
 delay(15000);
 }
}
```

C.3 Columns High-Level Code (Provided by N. Sihota) - Arduino MEGA Digita

Read/Write Code for Interface with CPU.

```
import serial
import string
import time

print("HELLO WORLD (PYTHON)!")

s = serial.Serial(port='COM7',baudrate=9600)
s.flush()
if(s.isOpen()):
   print("Serial port open sucessful")
else:
   print("Could not open serial port!")

filename = "EtOH-column1_DecagonData_06-10-14.txt"
import os.path

save_path = 'C:\Users\Public\column data test\MPS2-GS3'
error_count = 0

while(1):
   line = s.readline()
   x = str(line)
   f = open(save_path+filename,'a')
   if (x.find('NaN') >= 0):
      error_count = error_count+1

   t = time.localtime()

   line = line.decode("UTF-8")
   line = line.strip()
   line = line.replace(' ',',')
   print(t.tm_sec)
   f.write("\n")
   f.write(str(t.tm_year))
   f.write(',')
   f.write(str(t.tm_mon))
   f.write(',')
   f.write(str(t.tm_mday))
   f.write(',')
   f.write(str(t.tm_hour))
   f.write(',')
```

```
f.write(str(t.tm_min))
f.write(',')
f.write(str(t.tm_sec))
f.write(',')
f.write(line)
f.write(',')
print(line)
f.close()
if(error_count > 5):
    error_count = 0
    print("ERROR THRESHOLD REACHED - RESETTING ARDUINO")
    s.flush()
    s.close()
    s.open()

   # error_count = 0
   # f.close()
```

Appendix D

Appendix D contains all supplementary information column testing in Chapter 2- Methodology

D.1 Sidewall Flow in Silty-Sand Column

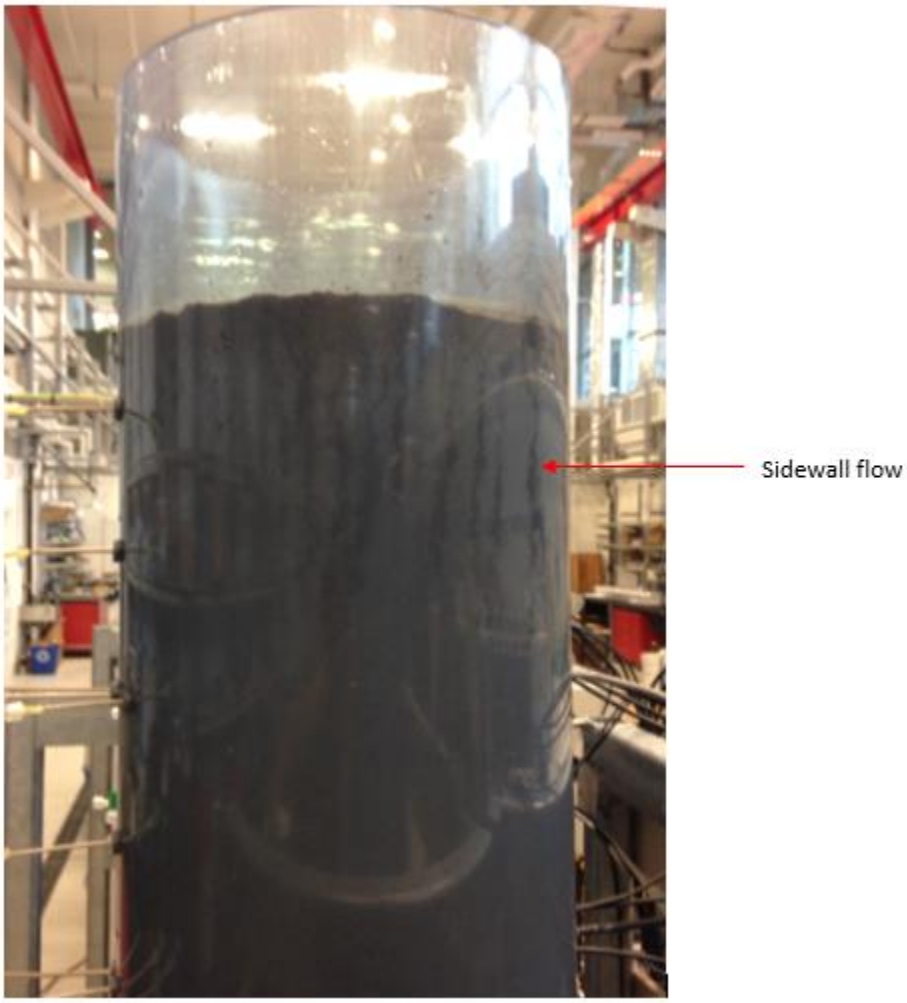

Figure D-1 Side wall flow as indicated by the fingering of the water front along the inner wall of the column.

D.2 Infiltration Testing

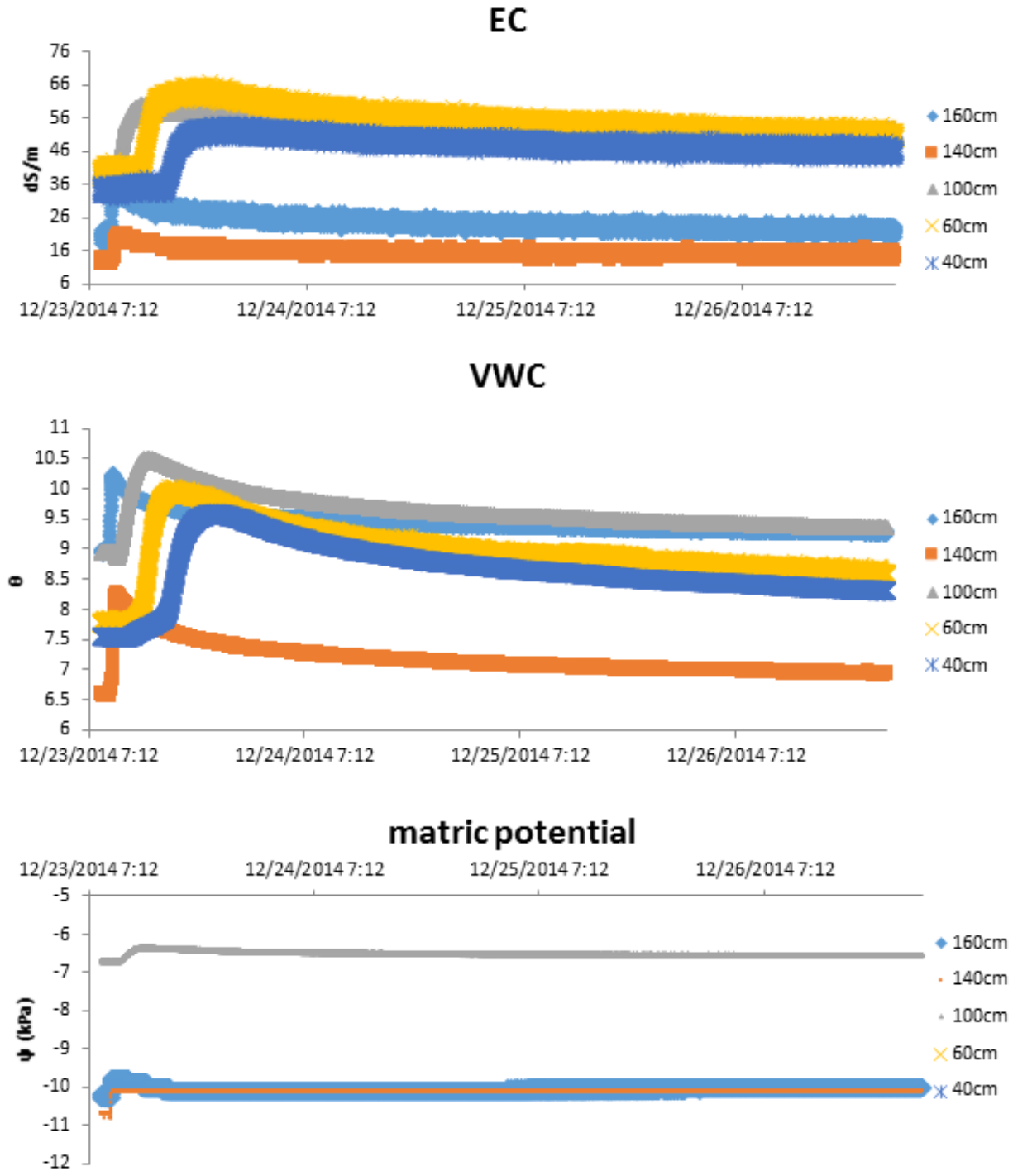

Figure D-2 Example data taken from water infiltration tests for E20-D-S. Data includes EC (dS/m), volumetric water content (cm3/cm3), and matric potential (kPa).

D.3 Observations of Perched Water Table in Gas-SS

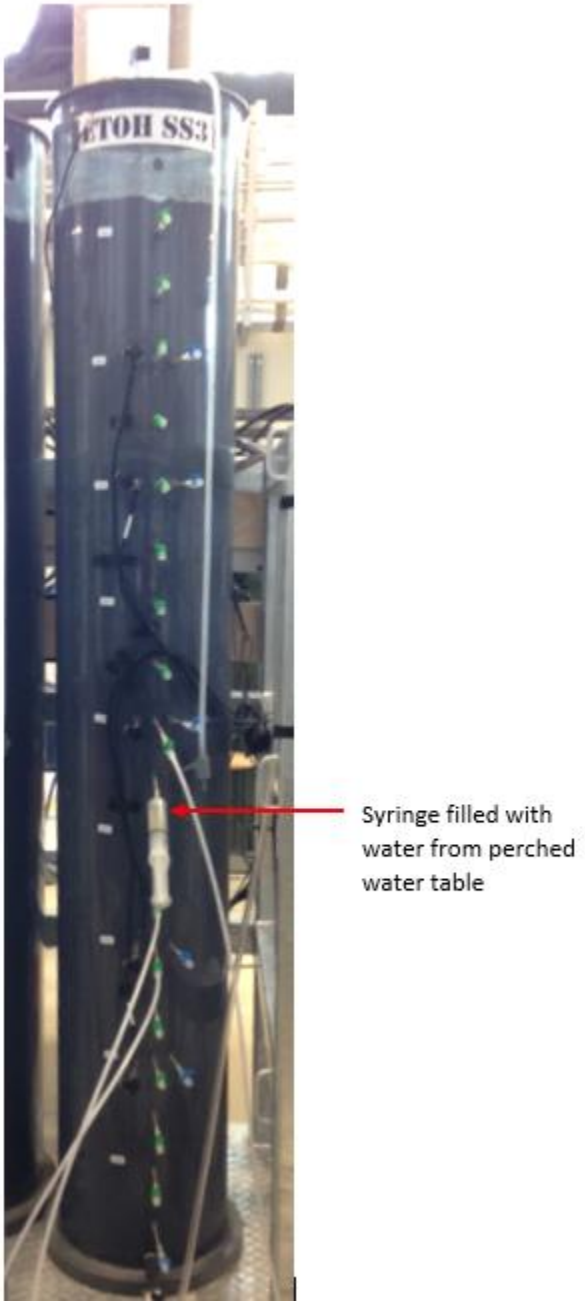

Figure D-3 A syringe was used to pull water from a perched water table that developed at 90-100cm in Gas-SS- during the water infiltration event.

D.4 Gas Injection Test

Figure D-4 Gas injection test. A gas of known composition is injected into the column at each sensor level.

D.5 O_2 and CO_2 Gas Sensor Calibration Data -Example

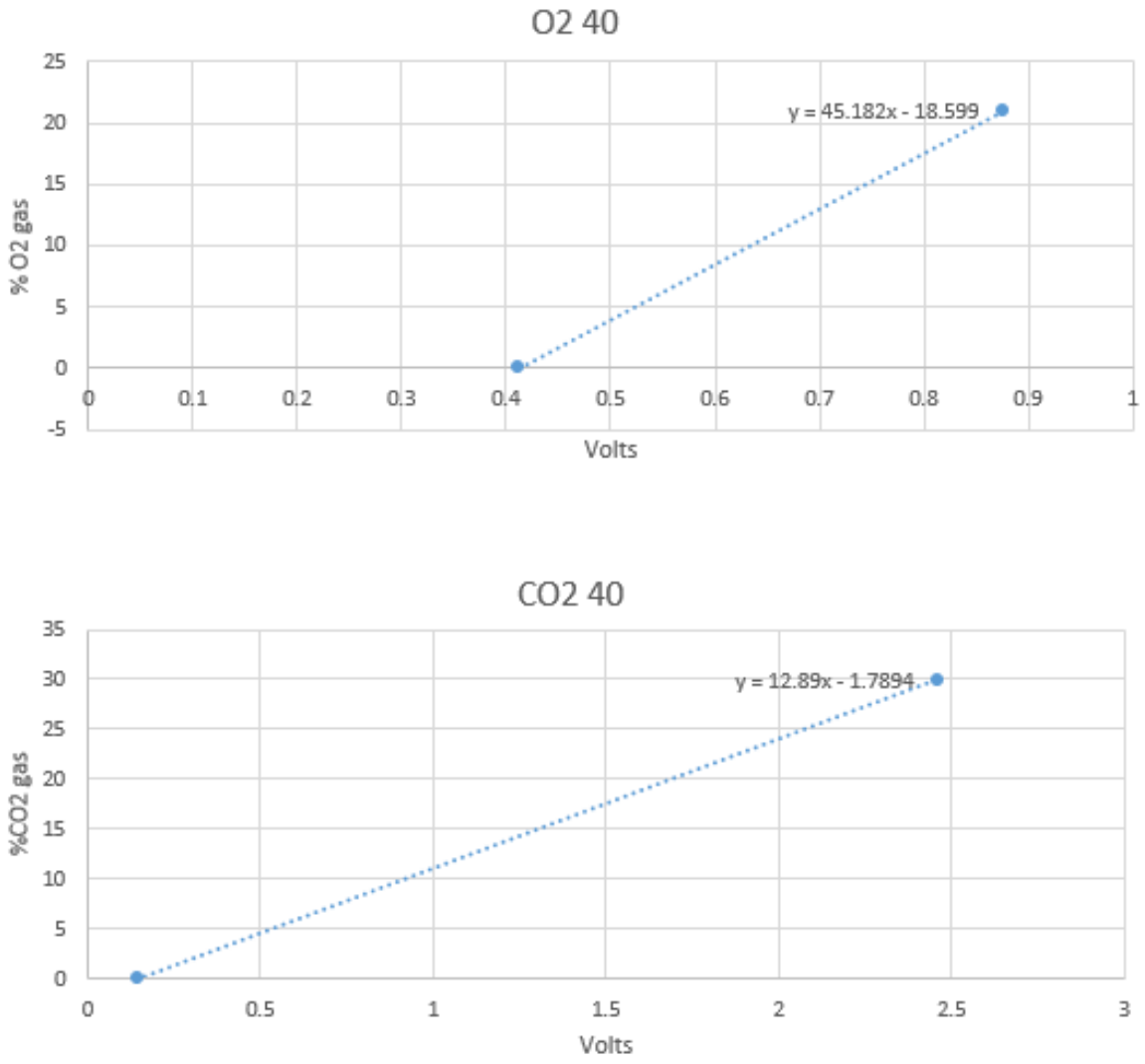

Figure D-5 Gas injection test data "Gas-SS" for O_2 and CO_2 sensors located at 40cm. Voltages were plotted against gas concentrations to obtain a linear regression equation. The linear equation is used to convert sensor voltages into real world gas concentrations.

D.6 Baseline Soil O_2 and CO_2 Concentrations

Table D-1 Baseline soil O2 and CO2 gas concentrations. The ranges are from all O_2 and CO_2 working sensors within each column.

Baseline Soil CO_2 and O_2 Ranges			
Column name	Experiment (Fuel Type)	O_2 (%)	CO_2 (%)
E85-S	E85	19.2 - 21.0	0.4 - 2
E20-S	E20	20.6 - 20.9	0.0
E20-D-S	Gasoline with delayed E20	19.6 - 20.66	0.2 - 1.97
GAS-S	Gasoline spill	20.67 - 20.8	0.29 - 1.48
E10-S	E10	20.7 - 20.8	0.2 - 2.42
E20-SS	E20	19.3 - 20.8	0.6 - 2.1
E20-D-SS	Gasoline with delayed E20	18.32 - 21.9	0.3 - 1.11
GAS-SS	Gasoline	20.05 - 20.1	no data

D.7 Baseline Soil CO_2 Flux

Table D-2 Data from baseline CO2 flux measurements.

Baseline Soil CO_2 Flux Data		
Column name	Experiment (Fuel Type)	Baseline Flux (umol/m^2/s)
E85-S	E85	0.07
E20-S	E20	0.09
E20-D-S	Gasoline with delayed E20	0.87
GAS-S	Gasoline spill	0.52
E10-S	E10	1.28
E20-SS	E20	0.92
E20-D-SS	Gasoline with delayed E20	1.04
GAS-SS	Gasoline	0.50

Appendix E

Appendix E contains all supplementary information from Chapter 3- Results and Discussion

E.1 CO_2 Isotopic Results with Concentration Data

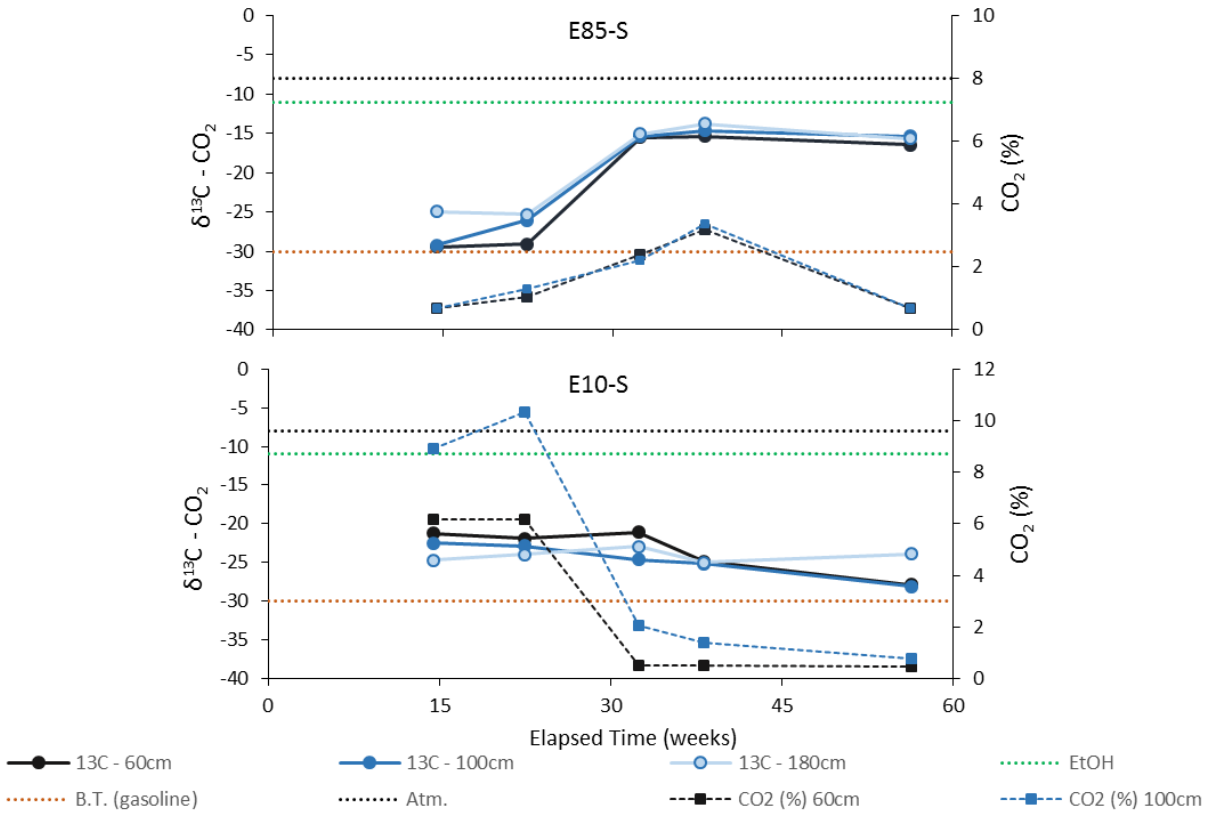

Figure E-1 Isotopic results for E85-S and E10-S with CO_2 concentration data.

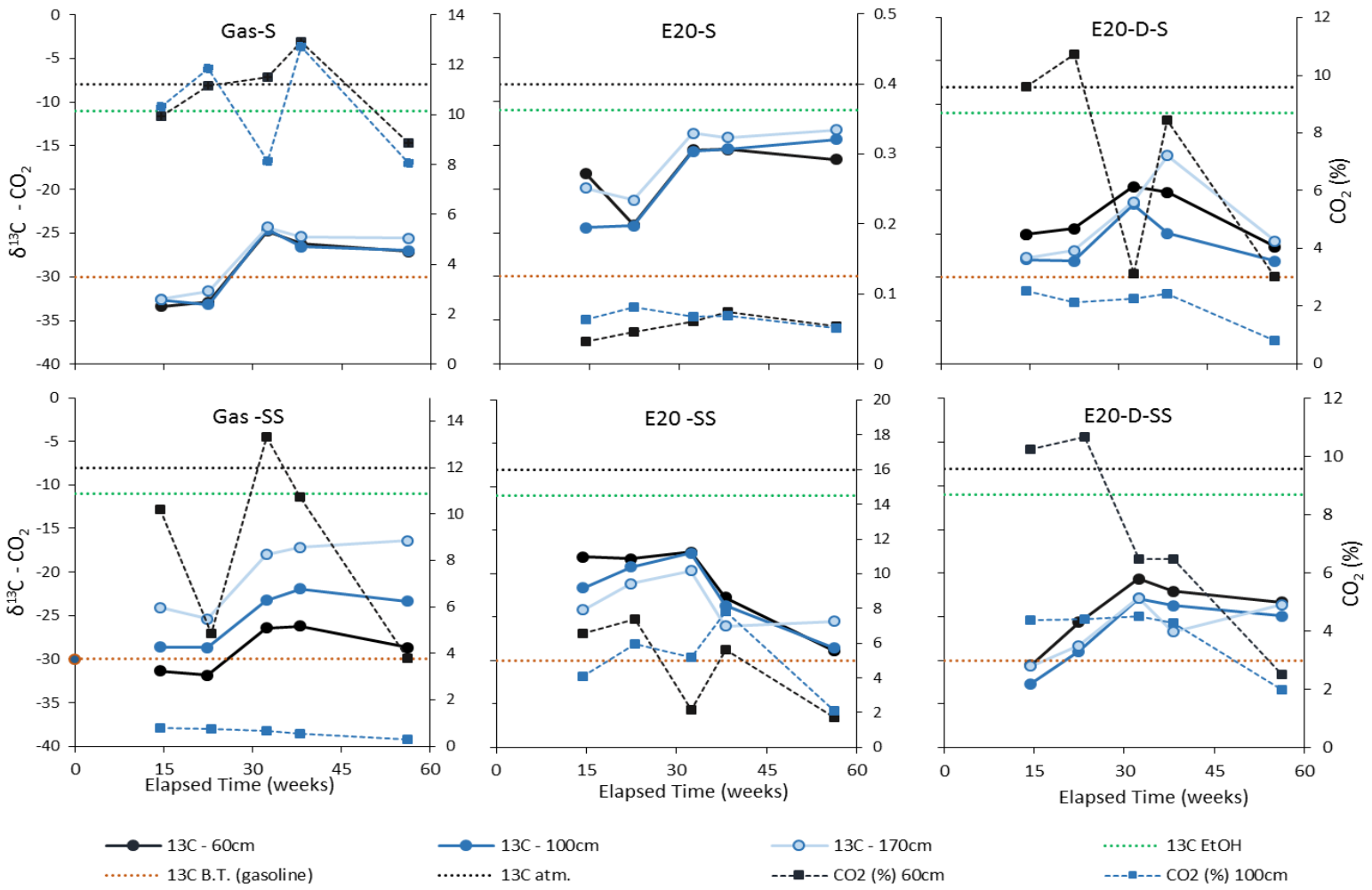

Figure E-2 Isotopic results combined with CO_2 concentration data for Gas-S, Gas-SS, E20-S,E20-SS, E20-D-S, and E20-D-SS columns.

E.2 Vadose Zone Benzene and Toluene – Raw Data

Table E-1 Vadose zone soil gas concentrations of benzene and toluene in the sand columns. Samples in red indicate questionable values due to extended sample storage before analysis. Data in red represents questionable date not included in thesis.

Column ID	Date	Week	Benzene 60cm (µg/L)	Toluene 60cm (µg/L)	Benzene 110cm (µg/L)	Toluene 110cm (µg/L)	Benzene 160cm (µg/L)	Toluene 160cm (µg/L)
E10-S	6/12/2015	2	86.4	1112.0	0.0	33.0	1.3	13.5
	7/9/2015	5	118.8	780.3	6.6	97.0	16.6	32.3
	7/28/2015	8	138.0	1040.0	24.2	139.0	0.0	0.0
	8/24/2015	12	347.0	2879.0	216.0	586.0	56.0	0.0
	9/25/2015	16	314.0	2212.0	267.0	1136.0	44.3	106.0
	11/25/2015	25	288.8	9542.0	0.0	999.0	0.0	61.0
	2/4/2016	35	24.3	2499.0	0.0	474.0	0.0	263.0
	3/17/2016	40	0.0	369.3	0.0	589.3	0.0	398.8
E85-S	6/12/2015	2	20.6	115.0	16.1	141.0	11.9	112.0
	7/9/2015	5	24.3	651.0	11.8	458.0	nd	112.0
	7/28/2015	8	10.3	135.6	20.9	310.0	3.6	56.6
	8/24/2015	12	794.0	2016.0	589.0	1664.0	nd	218.0
	9/25/2015	16	22.9	601.0	19.2	453.0	nd	90.6
	11/25/2015	25	39.4	1620.6	39.1	978.6	0.0	44.5
	2/4/2016	35	12.9	296.2	10.2	288.7	0.0	69.2
	3/17/2016	40	0.0	423.9	0.0	236.7	0.0	49.3
Gas-S	6/12/2015	2	58.9	341.0	1.0	3.2	0.0	2.4
	7/9/2015	5	119.0	641.0	18.1	124.0	11.2	59.9
	7/28/2015	8	143.2	913.0	24.9	103.7	0.0	33.2
	8/24/2015	12	302.0	2699.0	67.0	335.0	0.0	143.0
	9/25/2015	16	287.0	2425.0	33.7	262.0	0.0	41.7
	11/25/2015	25	639.0	7784.0	0.0	513.8	0.0	nd
	2/4/2016	35	502.1	5578.9	0.0	1199.6	0.0	84.5
	3/17/2016	40	0.0	1920.9	0.0	816.2	0.0	283.7
E20-S	6/12/2015	2	1.0	9.9	12.7	16.7	10.6	130.0
	7/9/2015	5	52.1	845.0	27.6	326.8	14.9	145.7
	7/28/2015	8	8.7	107.0	31.8	461.2	17.3	280.0
	8/24/2015	12	94.5	1866.0	74.2	1974.0	31.6	678.0
	9/25/2015	16	nd	49.1	25.4	641.3	25.8	386.3
	11/25/2015	25	115.4	7313.0	52.1	6656.0	15.4	2974.0
	2/4/2016	35	21.9	891.0	18.9	761.0	5.8	53.4
	3/17/2016	40	0.0	217.3	--	797.1	0.0	271.0

Column ID	Date	Week	Benzene 60cm (µg/L)	Toluene 60cm (µg/L)	Benzene 110cm (µg/L)	Toluene 110cm (µg/L)	Benzene 160cm (µg/L)	Toluene 160cm (µg/L)
E20-D-S	6/12/2015	2	27.4	196.0	0.0	32.8	8.1	15.3
	7/9/2015	5	34.1	214.2	0.0	0.0	0.0	0.0
	7/28/2015	8	109.8	641.8	6.9	98.1	0.0	0.0
	8/24/2015	12	122.0	1264.0	nd	164.0	0.0	119.0
	9/25/2015	16	58.9	645.9	17.3	47.8	10.7	25.6
	11/25/2015	25	33.9	101.0	0.0	0.0	0.0	25.8
	2/4/2016	35	0.0	0.0	0.0	0.0	0.0	0.0
	3/17/2016	40	0.0	1001.9	0.0	256.0	12.4	148.8

Table E-2 Vadose zone soil gas concentrations of benzene and toluene in the silty-sand columns. Samples in red indicate questionable values due to extended sample storage before analysis. Data in red represents questionable data not included in the thesis.

Column ID	Date	Week	Benzene 60cm (µg/L)	Toluene 60cm (µg/L)	Benzene 110cm (µg/L)	Toluene 110cm (µg/L)	Benzene 160cm (µg/L)	Toluene 160cm (µg/L)
Gas-SS	6/12/2015	2	74.2	435.0	2.0	8.1	nd	3.8
	7/9/2015	5	8.1	52.2	0.0	0.0	0.0	0.0
	7/28/2015	8	128.9	535.5	0.0	0.0	0.0	0.0
	8/24/2015	12	255.0	1324.0	8.6	109.7	2.5	26.7
	9/25/2015	16	64.4	164.9	53.3	131.6	0.0	0.0
	11/25/2015	25	353.1	2694.0	6.7	183.0	0.0	0.0
	2/4/2016	35	565.2	2974.9	69.7	664.8	18.9	254.1
	3/17/2016	40	11.0	583.9	0.0	0.0	11.0	0.0
E20-SS	6/12/2015	2	98.4	459.0	3.6	26.0	12.1	9.2
	7/9/2015	5	141.6	1042.0	108.4	368.0	10.8	36.7
	7/28/2015	8	186.2	1323.0	130.0	328.0	17.9	42.6
	8/24/2015	12	264.0	2731.0	232.0	632.0	51.1	nd
	9/25/2015	16	221.9	2486.0	28.1	286.5	29.1	45.3
	11/25/2015	25	235.0	4481.0	162.0	1339.0	11.1	85.5
	2/4/2016	35	45.7	816.3	162.0	248.2	0.0	0.0
	3/17/2016	40	0.0	1254.1	0.0	96.8	0.0	353.4
E20-D-SS	6/12/2015	2	115.0	657.0	84.6	148.7	33.8	7.6
	7/9/2015	5	46.7	348.3	45.3	375.7	0.0	46.1
	7/28/2015	8	81.7	408.1	0.0	35.1	0.0	nd
	8/24/2015	12	137.0	1028.0	0.0	0.0	0.0	63.1
	9/25/2015	16	89.7	804.1	0.0	78.6	0.0	nd
	11/25/2015	25	246.0	3117.0	0.0	182.0	0.0	44.8
	2/4/2016	35	123.9	762.1	0.0	95.2	0.0	57.4